Seismic structure along transitions from flat to normal subduction: central Mexico, southern Peru, and southwest Japan

Thesis by

Sara L. Dougherty

In Partial Fulfillment of the Requirements

for the Degree of

Doctor of Philosophy

California Institute of Technology

Pasadena, California

2014

(Defended May 23, 2014)

Acknowledgments

First and foremost, I would like to sincerely thank my advisors, Rob Clayton and Don Helmberger, without whom this thesis would not have been possible. Don taught me to appreciate every wiggle of a seismogram and introduced me to complex waveforms and the fine-scale structures they can resolve. Rob taught me to appreciate the bigger picture and to explore the possible tectonic implications of observed fine-scale structures. Their support and guidance throughout my time at Caltech has been immensely valuable. I greatly appreciate Rob's patience, encouragement, and accessibility, especially as this thesis was coming together.

I would like to thank my academic advisor, Jennifer Jackson, for her assistance with selecting courses and applying for candidacy and for the thought-provoking questions that she poses in my thesis committee meetings. I am also grateful to Joann Stock for serving on my committee and always providing insightful comments.

The former grad students and postdocs who helped me in the initial stages of my research and along the way deserve special thanks: Alex Song, Risheng Chu, Min Chen, YoungHee Kim, and Ting Chen. Shengji Wei has also been a great help. I would like to thank Xyoli Pérez-Campos and Steve Skinner for insightful comments and valuable discussions.

I am grateful for the support staff in the Seismo Lab and Tectonics Observatory, especially Rosemary Miller, Donna Mireles, Viola Carter, Evelina Cui, and Lisa Christiansen. Thanks also to Mike Black for all the IT support.

Special thanks to Jason Saleeby and Jean-Philippe Avouac for leading the Pahoehoe field trip to Hawaii and the division enrichment trip to Greece, respectively, both of which were great experiences.

Finally, my deep thanks to my husband, Walt Stelz, for his continuous support and understanding, especially during the busy times. His ability to always make me laugh has been invaluable, and the occasional coding advice didn't hurt either.

Abstract

The fine-scale seismic structure of the central Mexico, southern Peru, and southwest Japan subduction zones is studied using intraslab earthquakes recorded by temporary and permanent regional seismic arrays. The morphology of the transition from flat to normal subduction is explored in central Mexico and southern Peru, while in southwest Japan the spatial coincidence of a thin ultra-slow velocity layer (USL) atop the flat slab with locations of slow slip events (SSEs) is explored. This USL is also observed in central Mexico and southern Peru, where its lateral extent is used as one constraint on the nature of the flat-to-normal transitions.

In western central Mexico, I find an edge to this USL which is coincident with the western boundary of the projected Orozco Fracture Zone (OFZ) region. Forward modeling of the 2D structure of the subducted Cocos plate using a finite-difference algorithm provides constraints on the velocity and geometry of the slab's seismic structure in this region and confirms the location of the USL edge. I propose that the Cocos slab is currently fragmenting into a North Cocos plate and a South Cocos plate along the projection of the OFZ, by a process analogous to that which occurred when the Rivera plate separated from the proto-Cocos plate 10 Ma.

In eastern central Mexico, observations of a sharp transition in slab dip near the abrupt end of the Trans Mexican Volcanic Belt (TMVB) suggest a possible slab tear located within the subducted South Cocos plate. The eastern lateral extent of the USL is found to be coincident with these features and with the western boundary of a zone of decreased seismicity, indicating a change in structure which I interpret as evidence of a possible tear. Analysis of intraslab seismicity patterns and focal mechanism orientations and faulting types provides further support for a possible tear in the South Cocos slab. This potential tear, together with the tear along the projection of the

OFZ to the northwest, indicates a slab rollback mechanism in which separate slab segments move independently, allowing for mantle flow between the segments.

In southern Peru, observations of a gradual increase in slab dip coupled with a lack of any gaps or vertical offsets in the intraslab seismicity suggest a smooth contortion of the slab. Concentrations of focal mechanisms at orientations which are indicative of slab bending are also observed along the change in slab geometry. The lateral extent of the USL atop the horizontal Nazca slab is found to be coincident with the margin of the projected linear continuation of the subducting Nazca Ridge, implying a causal relationship, but not a slab tear. Waveform modeling of the 2D structure in southern Peru provides constraints on the velocity and geometry of the slab's seismic structure and confirms the absence of any tears in the slab.

In southwest Japan, I estimate the location of a possible USL along the Philippine Sea slab surface and find this region of low velocity to be coincident with locations of SSEs that have occurred in this region. I interpret the source of the possible USL in this region as fluids dehydrated from the subducting plate, forming a high pore-fluid pressure layer, which would be expected to decrease the coupling on the plate interface and promote SSEs.

Contents

List of Figures

List of Tables

Chapter 1

Introduction

Subduction zones are complex plate boundaries in which variable geometry and structure can be seismically observed. The along-strike transition from flat to normal subduction is one such geometric variation that is identified by changes in Wadati-Benioff zone seismicity. This transition may be accommodated by either a tear in the slab or a smooth contortion of the plate. Examination of the fine-scale seismic structure along this change in geometry can elucidate the nature of the transition and identify other features of the subducted plate. In this thesis, I investigate the seismic structure along transitions from flat to normal subduction located in central Mexico, southern Peru, and southwest Japan (Figure 1.1). A common feature of all three regions is a thin ultra-slow velocity layer (USL) atop the flat slab that is interpreted to consist of hydrous minerals and/or free water (*Song et al.*, 2009; *Kim et al.*, 2010). The presence of this layer is identified by the occurrence of complex P waveforms recorded by regional seismic arrays. The lateral extent of the USL is used as one constraint on the nature of the flat-to-normal transitions in central Mexico (Chapters 2 and 3) and southern Peru (Chapter 4). In southwest Japan, I explore the spatial coincidence of the USL with locations of slow slip events (SSEs) and the possible causal relationship between the two (Chapter 5).

In Chapter 2, I study the fine-scale seismic structure of the central Mexico subduction zone along the western transition from flat to normal subduction. Fragmentation of the subducting Cocos plate has been proposed to be actively occurring along the projected continuation of the Orozco Fracture Zone (OFZ), which overlies this transition, based on recent tectonic observations.

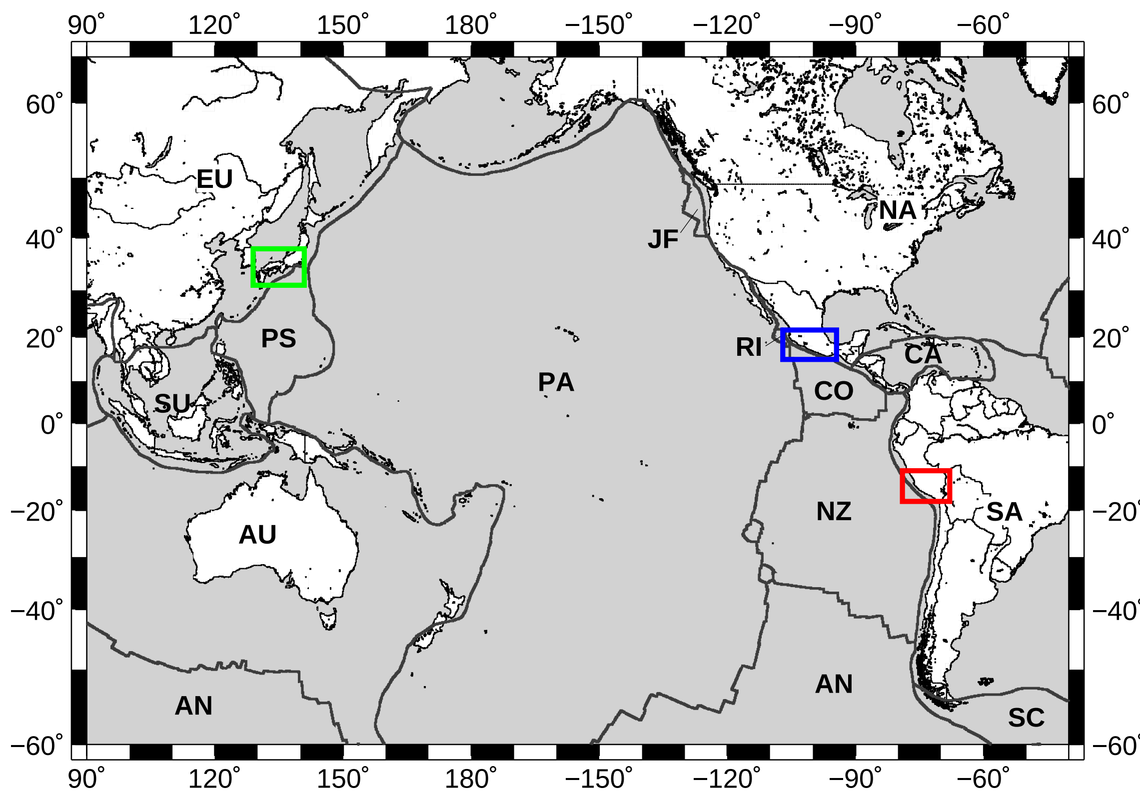

Figure 1.1: Map showing study locations in central Mexico (blue box), southern Peru (red box), and southwest Japan (green box). Major plate boundaries from *Bird* (2003) are shown in dark grey lines. The Rivera (RI), Cocos (CO), North American (NA), Nazca (NZ), South American (SA), Pacific (PA), Philippine Sea (PS), and Eurasian (EU) plates are indicated. Other plates labeled are the Australian (AU), Sunda (SU), Antarctic (AN), Scotia (SC), Caribbean (CA), and Juan de Fuca (JF).

I use intraslab earthquakes recorded by the regional Mapping the Rivera Subduction Zone (MARS) seismic array to test this hypothesis and further explore the subduction zone structure. Observed waveform complexities are used to map the western lateral extent of the USL that was imaged atop the flat Cocos slab by the Meso America Subduction Experiment (MASE) array (*Pérez-Campos et al.*, 2008; *Song et al.*, 2009; *Kim et al.*, 2010) to test if it ends along a lineament related to the landward projection of the OFZ. The edge of the USL is found to be approximately coincident with the western margin of the projected OFZ region, implying a structural boundary which I interpret as a tear in the Cocos plate. Forward modeling of the 2D structure of the subduction zone using a finite-difference algorithm provides constraints on the velocity and geometry of the slab's seismic structure and confirms the location of the USL edge. An analysis of seismicity and slab dip across the USL edge reveals a sharp transition in slab dip within the projected OFZ region and a significant decrease in seismicity west of the edge. On the basis of these results and tectonic observations, I propose a slab tear model, wherein the Cocos slab is currently fragmenting into a North Cocos plate and a South Cocos plate along the projection of the OFZ by a pivoting subduction process similar to that which occurred when the Rivera plate separated from the proto-Cocos plate.

Chapter 3 is a similar study to that presented in Chapter 2, now applied to the flat-to-normal transition that occurs in eastern central Mexico. Here, observations of a sharp transition in slab dip coupled with the abrupt end of the Trans Mexican Volcanic Belt (TMVB) suggest a second possible tear located within the subducted South Cocos plate. I use intraslab earthquakes recorded by the MASE, Veracruz-Oaxaca (VEOX), Servicio Sismológico Nacional (SSN), and Oaxaca Network (OXNET) seismic arrays to study the fine-scale structure of the subduction zone along this transition and elucidate the nature of the slab morphology (i.e., tear or contortion). Mapping the eastern lateral extent of the USL reveals an end to this layer which is coincident with the western boundary of a zone of decreased seismicity and the end of the TMVB near the sharp transition in slab dip. The coincidence of these features implies a change in structure which I interpret as evidence of a possible tear. Waveform modeling of the 2D structure in this region confirms the location of the USL. Analysis of intraslab seismicity patterns reveals clustering, sudden increase in depth, variable focal mechanism orientations and faulting types, and alignment of source mechanisms along the sharp transition in slab dip, further supporting the possibility of a slab tear. I propose the subduction of parallel ridges of seamounts and/or stress due to the abrupt change in geometry as potential causes of the possible slab tear in the South Cocos plate. This potential tear, together with the tear along the projection of the OFZ to the northwest, indicates a slab rollback mechanism in which separate slab segments move independently, allowing for mantle flow between the segments.

In Chapter 4, I investigate the slab morphology along the transition from flat to normal subduction in southern Peru. Previous studies of this transition region have suggested both tearing and continuous curvature of the subducted Nazca plate, with a recent receiver function study indicating a continuous slab with no clear breaks (*Phillips and Clayton*, 2014). In order to test this conclusion and expand on investigations of this region, I use regional intraslab earthquakes recorded by the Peru Subduction Experiment (PeruSE) and Central Andes Uplift and Geodynamics of High Topography (CAUGHT) seismic arrays to study the fine-scale structure of the southern Peru subduction zone along the flat-to-normal transition. I also analyze seismicity patterns and focal mechanism orientations for any indications of fragmentation or contortion of the subducted plate. Examination of the lateral variation in slab dip across the transition reveals a gradual increase with no sharp transitions, suggesting a smooth contortion of the Nazca plate. A lack of any gaps or vertical offsets in the intraslab seismicity, coupled with concentrations of focal mechanisms at orientations which are indicative of slab bending, further support this conclusion. The presence of a thin USL like that observed in central Mexico is also identified and located atop the horizontal Nazca slab. The lateral extent of this USL is coincident with the margin of the projected linear continuation of the subducting Nazca Ridge, implying a causal relationship. Unlike in central Mexico, the lateral extent of the USL in southern Peru does not suggest a tear in the slab due to its location and the lack of coincident tear indicators. Waveform modeling of the 2D structure in southern Peru provides constraints on the velocity and geometry of the slab's seismic structure and confirms the absence of any tears in the slab. In summary, the seismic and structural evidence suggests smooth contortion of the Nazca plate along the flat-to-normal transition. I also estimate the along-strike strain experienced by the continuous Nazca and torn Cocos slabs across their respective transitions, finding values of 10% for the Nazca slab and 15% for the Cocos slab in both western and eastern central Mexico.

Chapter 5 explores the fine-scale seismic structure of the transition from flat to normal subduction in southwest Japan in a manner different than that of the previous three chapters. Here, rather than focusing on the nature of the transition, I focus on the USL and its possible causal relationship with SSEs. *Song et al.* (2009)'s study on subduction beneath central Mexico indicated that there is a relationship between the location of SSEs and the location of intraslab earthquakes that generate complex P-waves. Simple P waveforms indicate normal slab conditions with no occurrences of SSEs, whereas complex P waveforms imply the presence of the USL atop the slab and the occurrence of SSEs. I further test this hypothesis in a region of southwest Japan that experiences SSEs and has a similar geometry to that studied in central Mexico. I use intraslab earthquakes recorded by the Hi-net array to estimate the location of a possible USL along the Philippine Sea slab surface and find this region of low velocity to be coincident with locations of SSEs. The fluid-rich composition of the USL would be expected to greatly reduce the effective normal stress on the plate interface, decreasing the coupling, and promoting SSEs. I interpret the source of the possible USL in this region as fluids dehydrated from the subducting plate, forming a high pore-fluid pressure layer.

References

Bird, P. (2003), An updated digital model of plate boundaries, *Geochem. Geophys. Geosyst.*, *4*, 1027, doi:10.1029/2001GC000252.

Kim, Y., R. W. Clayton, and J. M. Jackson (2010), Geometry and seismic properties of the subducting Cocos plate in central Mexico, *J. Geophys. Res.*, *115*, B06310, doi:10.1029/2009JB006942.

Pérez-Campos, X., Y. Kim, A. Husker, P. M. Davis, R. W. Clayton, A. Iglesias, J. F. Pacheco, S. K. Singh, V. C. Manea, and M. Gurnis (2008), Horizontal subduction and truncation of the Cocos Plate beneath central Mexico, *Geophys. Res. Lett.*, *35*, L18303, doi:10.1029/2008GL035127.

Phillips, K., and R. W. Clayton (2014), Structure of the subduction transition region from seismic array data in southern Peru, *Geophys. J. Int.*, *196*, 1889–1905.

Song, T. A., D. V. Helmberger, M. R. Brudzinski, R. W. Clayton, P. Davis, X. Pérez-Campos, and S. K. Singh (2009), Subducting slab ultra-slow velocity layer coincident with silent earthquakes in southern Mexico, *Science*, *324*, 502–506.

Chapter 2

Seismic structure in central Mexico: Implications for fragmentation of the subducted Cocos plate

Originally published in:

Dougherty, S. L., R. W. Clayton, and D. V. Helmberger (2012), Seismic structure in central Mexico: Implications for fragmentation of the subducted Cocos plate, *Journal of Geophysical Research*, *117*, B09316, doi:10.1029/2012JB009528.

2.1 Abstract

The fine-scale seismic structure of the central Mexico subduction zone is studied using moderate-sized (M4-6) intraslab earthquakes. Regional waveforms from the Mapping the Rivera Subduction Zone (MARS) seismic array are complicated and contain detailed information about the subduction zone structure, including evidence of lateral heterogeneity. This waveform information is used to model the structure of the subducted plates, particularly along the transition from flat to normal subduction, where recent studies have shown evidence for possible slab-tearing along the eastern projection of the Orozco Fracture Zone (OFZ). The lateral extent of a thin ultra-slow velocity layer (USL) imaged atop the Cocos slab in recent studies along the Meso America Subduction Experiment array is examined here using MARS waveforms. We find an edge to this USL which is coincident with the western boundary of the projected OFZ region. Forward modeling of the 2D structure of

the subducted Rivera and Cocos plates using a finite-difference algorithm provides constraints on the velocity and geometry of each slab's seismic structure in this region and confirms the location of the USL edge. We propose that the Cocos slab is currently fragmenting into a North Cocos plate and a South Cocos plate along the projection of the OFZ, in agreement with observations of variable Cocos plate motion on either side of the OFZ. This tearing event may be a young analogy to the 10 Ma Rivera-Cocos plate boundary, and may be related to the slab rollback in central Mexico.

2.2 Introduction

The tectonic evolution of the northeast Pacific has been characterized by the fragmentation of lithospheric plates as segments of spreading centers approached the trench off the west coast of North America. During the last 55 million years, the Farallon plate and its remnants have been fragmenting into progressively smaller plates as the Pacific-Farallon ridge approached the subduction zone, with each new plate moving independently and becoming less stable through time (*Wortel and Cloetingh*, 1981, 1983; *Atwater*, 1989; *Lonsdale*, 1991; *Stock and Lee*, 1994). These fragmentation events generally occurred along a fracture zone that represented a line of weakness between areas of the plate experiencing driving forces of differing magnitude or direction (*Lonsdale*, 1991). The most recent of these fragmentation events occurred when the Rivera plate separated from the proto-Cocos plate about 10 Ma (*Klitgord and Mammerickx*, 1982; *DeMets and Traylen*, 2000).

The Rivera and Cocos plates are subducting beneath the North American plate along the Middle American Trench (MAT) in central Mexico with convergence rates increasing from 1.1 cm/yr at 106.5°W to 2.4 cm/yr at 105°W and from 4.8 cm/yr at 104.5°W to 7.5 cm/yr at 94°W, respectively (*DeMets et al.*, 1990). The age of the oceanic crust being subducted at the MAT also increases from about 10 Ma in the west to about 23 Ma in the east (*Pardo and Suárez*, 1995). These young oceanic plates exhibit large lateral variations in slab dip, with a shallow subhorizontal segment bounded by segments that dip much more steeply (*Pardo and Suárez*, 1995). Receiver functions and seismic velocity tomography along the Meso America Subduction Experiment (MASE) array show that the Cocos slab is horizontal for about 250 km beneath the North American plate in the Guerrero region, before steeply subducting with a dip of 75° at the southern margin of the Trans Mexican Volcanic Belt (TMVB) and truncating at a depth of 500 km (*Pérez-Campos et al.*, 2008; *Husker and Davis*, 2009; *Kim et al.*, 2010). To the north and south, the dip angle of the Cocos slab increases gradually from 0° to ~50° and ~30°, respectively, whereas the Rivera plate subducts at a dip of about 50° (*Pardo and Suárez*, 1995).

Although the location and nature of the Rivera-Cocos plate boundary has long been contested (e.g., *Nixon*, 1982; *Eissler and McNally*, 1984; *Bourgois and Michaud*, 1991; *DeMets and Wilson*, 1997), recent studies have shown that it lies beneath the Colima Graben on land and its offshore extension to the southwest, the El Gordo Graben (e.g., *Stock and Lee*, 1994; *Bandy et al.*, 1995, 2000; *Serrato-Díaz et al.*, 2004). These prominent extensional structures likely formed in response to divergence between the subducting Rivera and Cocos plates (*Ferrari et al.*, 1994; *Bandy et al.*, 1995, 1998, 2000; *Serrato-Díaz et al.*, 2004). Seismic tomography imaging using data from the Mapping the Rivera Subduction Zone (MARS) array shows a clear gap between the Rivera and Cocos slabs starting at a depth of about 150 km and increasing with depth (*Yang et al.*, 2009). This tear between the plates occurs beneath the Colima Graben and is suggested to be responsible for the location of Colima volcano and the graben itself (*Soto et al.*, 2009; *Yang et al.*, 2009).

Further fragmentation of the Cocos plate has been proposed to be actively occurring along the Orozco Fracture Zone (OFZ) based on variations in plate motions observed on either side of the OFZ (*DeMets et al.*, 1990; *DeMets and Wilson*, 1997; *Bandy et al.*, 2000), the approach of the Pacific-Cocos spreading center towards the MAT (*Bandy and Hilde*, 2000), and the presence of a possible rift-rift-rift triple junction overlying the landward projection of the OFZ (*Bandy et al.*, 2000). This ongoing fragmentation event may be occurring by a process analogous to that which occurred when the Rivera plate separated from the proto-Cocos plate. The tearing of the plate may provide a short-cut mechanism related to the trench-parallel flow associated with the rollback of the slab in central Mexico (*Russo and Silver*, 1994; *Ferrari*, 2004). In order to test this hypothesis, we use regional earthquakes recorded by the MARS array to study the fine-scale structure of the central Mexico subduction zone along the transition from flat to normal subduction, where the eastern projection of the OFZ lies (Figure 2.1) (*Blatter and Hammersley*, 2010). We perform 1D and 2D waveform modeling to image the structure of the slab and overriding plate. We also use observed waveform complexities to map the lateral extent of a thin ultra-slow velocity layer (USL) that was imaged atop the flat Cocos slab by the MASE array (*Pérez-Campos et al.*, 2008; *Song et al.*, 2009; *Kim et al.*, 2010) to test if the USL ends along a lineament related to the landward projection of the OFZ.

2.3 Data Analysis

2.3.1 Data

The seismic data used in this study were provided by the MARS array, which consisted of 50 broadband seismic instruments deployed from January 2006 to June 2007 in a 2D geometry in the Jalisco and Michoacan regions with an average station spacing of ∼40 km (Figure 2.1). The goal of the MARS experiment was to understand the forces that are controlling the tectonics of the Jalisco block and the behaviors of the Rivera and adjacent Cocos plates (*Yang et al.*, 2009). In this study, we analyze seismograms from 24 regional intraslab earthquakes recorded by the MARS array. These events are within the magnitude range of 4.0 to 6.2, and the depths vary from 40 km to 85 km (Table 2.1). The locations of these events are shown in Figure 2.1.

2.3.2 1D Velocity Modeling

The shallow seismic structure of the central Mexico subduction zone is analyzed in 1D using frequency-wavenumber forward modeling techniques. The sensitivity of observed waveforms to the subduction zone structure is tested using five different P- and S-wave velocity models: (1) standard Southern California (SoCal) crustal velocity model from *Dreger and Helmberger* (1993) (Figure 2.2a); (2) modified SoCal model with thickened crustal layers (SoCalx) to place the Moho at 45 km depth (Figure 2.2b); (3) central Mexico velocity model from receiver function study along the MASE array by *Kim et al.* (2010) (Figure 2.2c); (4) central Mexico velocity model from waveform modeling study

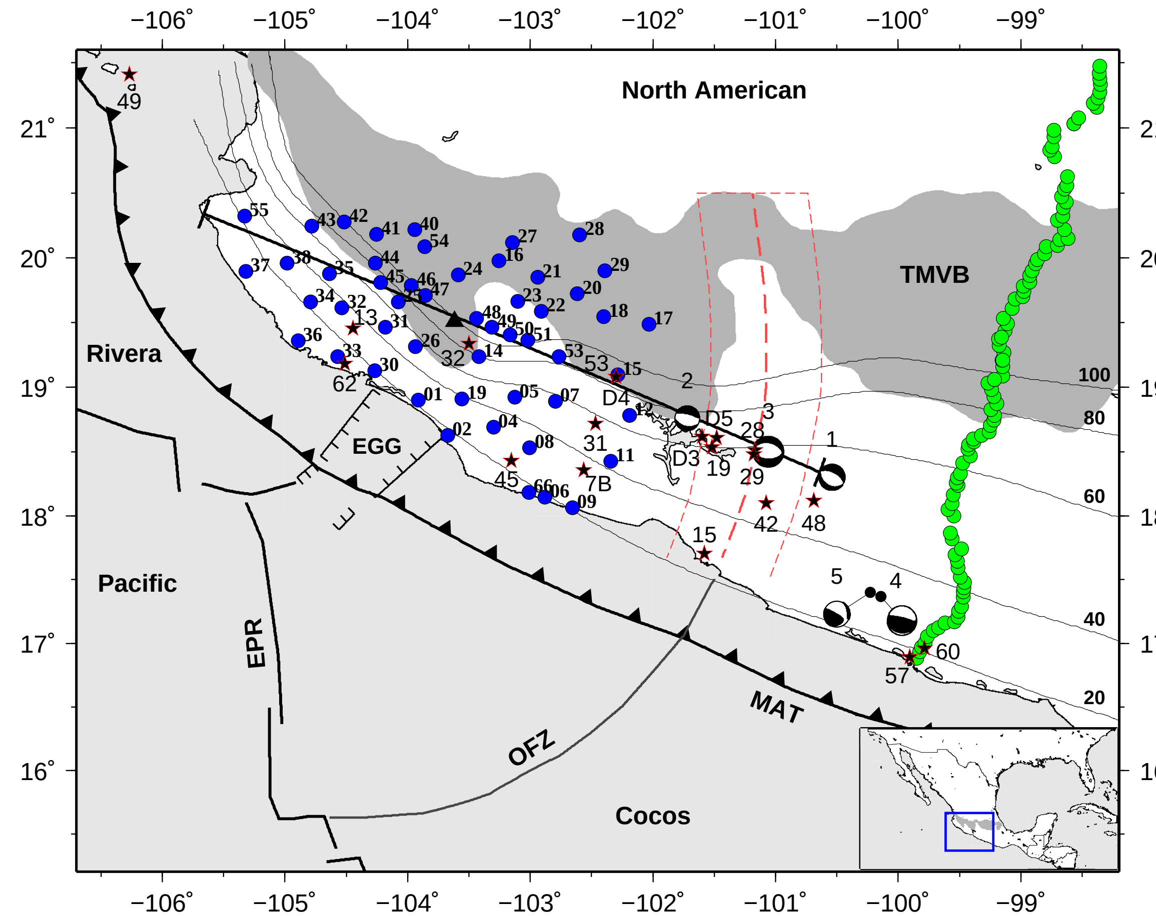

Figure 2.1: Map showing the MARS stations (blue dots) and events (stars, focal mechanisms) used in this study. Locations of MASE (green dots) stations are also shown for reference. The dark grey shaded area indicates the Trans Mexican Volcanic Belt (TMVB), and the black triangle denotes Colima Volcano. Slab isodepth contours from *Pardo and Suárez* (1995) are shown in thin lines. The projected path of the Orozco Fracture Zone (OFZ) beneath the North American plate is shown as a thick, red dashed line, with thinner, red dashed lines to either side delineating the estimated 100 km width of the fracture zone (*Blatter and Hammersley*, 2010). The thick northwest-southeast trending line marks the location of the data profile and 2D velocity model cross-section. Other abbreviations shown in the map are EPR, East Pacific Rise; MAT, Middle America Trench; EGG, El Gordo Graben.

Table 2.1: Events used in western central Mexico and their source parameters.

Event ID	Date	Lat (°)	Lon (°)	Depth (km)	Mag	Mechanism Strike/Dip/Rake	Source
1	2006/02/20	18.30	-100.54	56	5.2	297/57/-93	1
2	2006/03/20	18.76	-101.72	64	4.9	282/59/-91	1
3	2006/08/11	18.50	-101.06	68	6.2	281/41/-83	2
4	2007/04/13	17.37	-100.14	43	6.0	284/73/92	1
5	2007/04/13	17.40	-100.23	67	5.3	297/90/119	1
7B	2006/02/17	18.35	-102.56	44	4.3	—	3
13	2006/03/30	19.46	-104.44	85	4.2	—	4
15	2006/05/16	17.71	-101.58	43	4.1	—	4
19	2006/06/07	18.54	-101.52	63	4.2	—	4
28	2006/08/11	18.51	-101.17	64	5.4	—	5^b
29	2006/08/11	18.48	-101.18	64	4.9	—	5^b
31	2006/08/17	18.72	-102.47	60	4.6	—	5^d
32	2006/10/14	19.34	-103.50	43	4.0	—	5^d
42	2006/12/17	18.10	-101.08	66	4.7	—	3
45	2006/12/27	18.43	-103.15	41	4.1	—	4
48	2007/02/06	18.12	-100.69	65	4.4	—	3
49	2007/02/11	21.41	-106.27	47	5.1	—	3
53	2007/03/08	19.09	-102.30	78	4.1	—	4
57	2007/03/31	16.90	-99.91	42	4.4	314/86/119	6
60	2007/04/28	16.96	-99.79	40	4.8	307/75/118	6
62	2007/05/28	19.18	-104.51	42	4.0	—	4
D3	2007/03/13	18.62	-101.60	85	4.1	—	3
D4	2007/03/08	19.09	-102.30	79	4.1	—	4
D5	2007/02/03	18.61	-101.48	72	4.3	—	5^d

Sources are 1) location, focal mechanism, M_w, and depth from the Global CMT catalog; 2) focal mechanism, M_w, and depth from V. Andrews [personal communication, 2010], location from CMT; 3) location, m_b, and depth from the Bulletin of the International Seismological Centre (ISC); 4) location, M_D, and depth from the Servicio Sismològico Nacional (SSN) catalog; 5) location, ${}^b m_b$, ${}^d M_D$, and depth from the National Earthquake Information Center (NEIC); 6) focal mechanism, M_w, and depth from *Pacheco and Singh* (2010), location from ISC.

along the MASE array by *Song et al.* (2009) (Figure 2.2d); (5) new central Mexico (ncM) velocity model from this study (Figure 2.2e). The SoCal and SoCalx models do not include slab structure, while the other models contain a multi-layered, somewhat complex slab that includes the USL that was imaged by the MASE array (Figure 2.2). *Kim et al.* (2010)'s receiver function results are used to constrain the depth of the Moho to 45 km in the SoCalx and ncM models. The overriding plate velocities in the ncM model are taken from the *Song et al.* (2009) model, with the crustal layers thinned to place the Moho at the constrained depth (Figure 2.2e). The subducted plate structure in this model is modified from *Kim et al.* (2010) and consists of a 3-km-thick USL atop a 3-km-thick lower oceanic crust and a 4-km-thick high velocity layer, overlying oceanic mantle (Figure 2.2e). The SoCal and SoCalx crustal models test the sensitivity of the observed waveforms to the crustal structure only, while the *Kim et al.* (2010) model tests waveform sensitivity to the slab structure only. The *Song et al.* (2009) and ncM models test the sensitivity of the observed waveforms to combined crustal and slab structure. The SoCal and SoCalx models were selected for their robust representations of simple crustal structure, not for their affinities with Mexican subduction zone structure.

A comparison of the synthetics produced for each of these five models to the data for event 3 at three stations is shown in Figure 2.3. The waveforms have been bandpass filtered to 0.01–0.1 Hz in order to increase the signal-to-noise ratio and accentuate the major phases (e.g., P, sP, S, multiple S). Overall, the ncM model provides the most accurate prediction of the data, with the best fits to P, sP, and SH phases at all distances, along with an S-wave multiple at large distances (Figures 2.3-2.4). The SoCal model provides a comparable fit to these phases, but fails to predict some of the waveform complexities seen in both the data and the ncM model synthetics, such as the shoulder following SV (Figure 2.3). The uppermost slab structure in the ncM model, particularly the USL, is likely responsible for reproducing the observed waveform complexities that the simpler SoCal model fails to predict. The complete 1D modeling results for the SoCal, SoCalx, *Kim et al.* (2010), and *Song et al.* (2009) velocity models are shown in Supplemental Figures 2.13-2.16, respectively.

A NW-SE trending profile across the MARS array (see Figure 2.1 for location) of the ncM

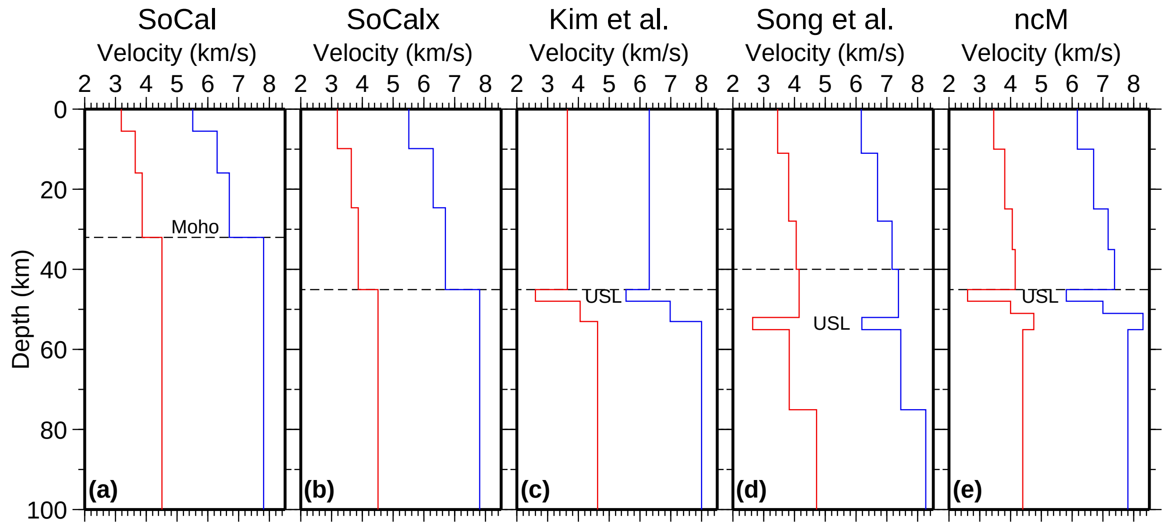

Figure 2.2: 1D P (blue) and S (red) wave velocity models tested in this study. (a) Southern California velocity model (*Dreger and Helmberger*, 1993). (b) Modified southern California model with thickened crustal layers that place the Moho (black dashed line) at 45 km depth. (c) Central Mexico velocity model from receiver function study by *Kim et al.* (2010) using the MASE array. Ultra-slow velocity layer (USL) is indicated at the top of the subducted plate. (d) Central Mexico velocity model from waveform modeling study along the MASE array by *Song et al.* (2009). (e) New central Mexico (ncM) velocity model from this study.

modeling results for event 3 illustrates some lateral variation in the structure of this region (Figure 2.5). For the stations located within the TMVB, complexities in the waveforms are observed after the arrival of the S-wave in the data and are most prevalent on the transverse component. These complexities are not predicted by the ncM model synthetics and may be indicative of a change in crustal structure within the TMVB region.

2.3.3 Ultra-slow Velocity Layer

The USL atop the flat Cocos slab was imaged as a thin, 3–5-km-thick layer with a V_P of 5.4–6.2 km/s and a V_S of 2.0–3.4 km/s (*Song et al.*, 2009; *Kim et al.*, 2010). For the ncM model, we set these parameters to 3 km thick, V_P of 5.8 km/s, and V_S of 2.6 km/s. The exact nature of the USL is not known, but its anomalously low shear wave velocity suggests a relationship with fluids, specifically free water or hydrous minerals, in the subduction zone. *Song et al.* (2009) proposed that the USL represents part of the oceanic crust that is fluid-saturated, forming a high pore-fluid pressure (HPFP) layer that is sealed by some low permeability layer, possibly fine-grained blueschist, directly above

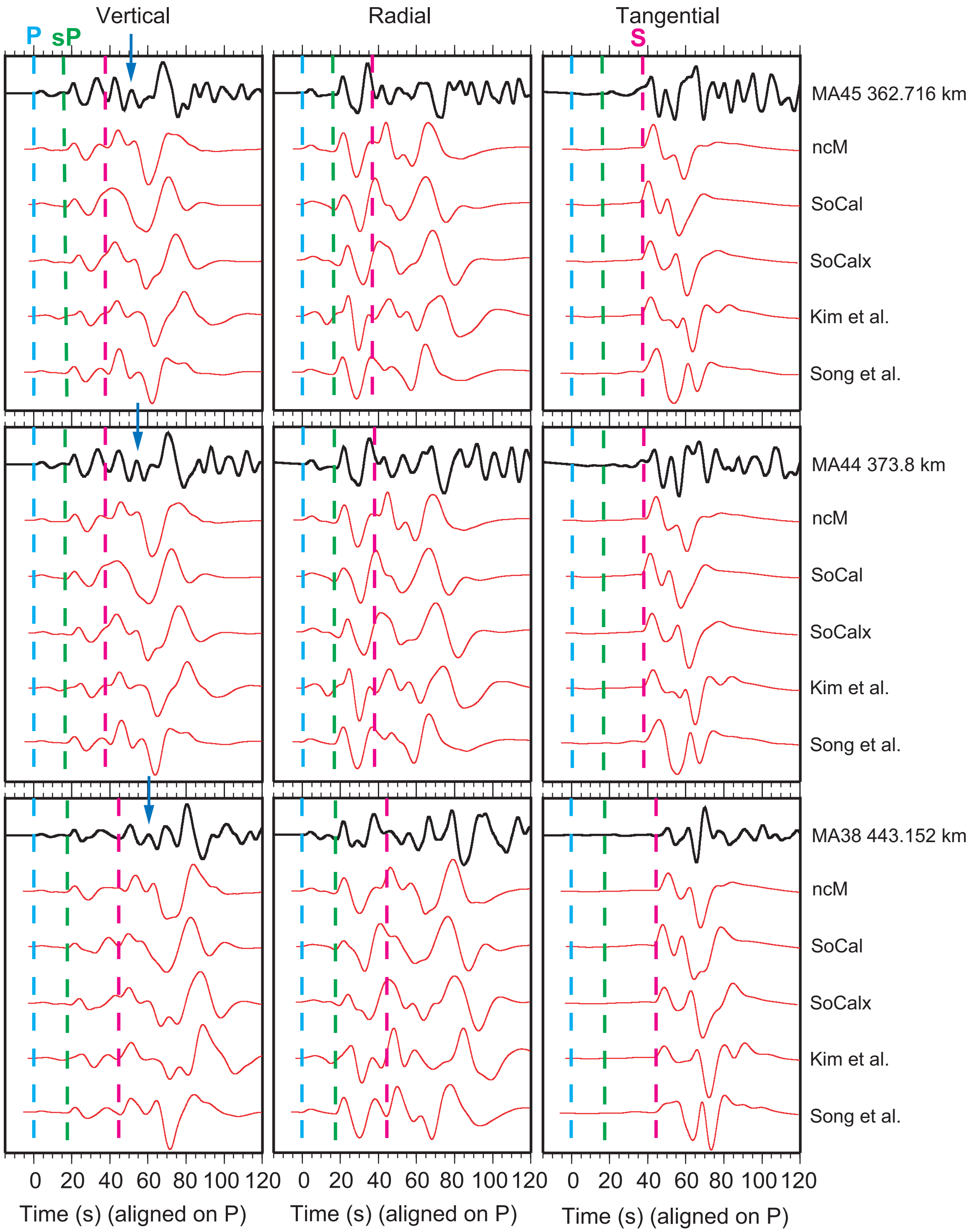

Figure 2.3: Comparison of 1D modeling results of event 3 for the five models tested at three stations. Waveforms are filtered to 0.01–0.1 Hz. Data are in black, synthetics are in red. P, sP, and S phases are indicated by dashed lines. Blue arrows indicate the shoulder following SV. Of the 1D models tested, ncM is preferred because it produces synthetics that accurately predict the waveshapes and arrival times of the P, sP, S, and SV shoulder phases in addition to the arrival time of the S-wave multiple. This model, however, fails to predict the waveshape of the S multiple and some post S multiple complexities, necessitating the development of a 2D model.

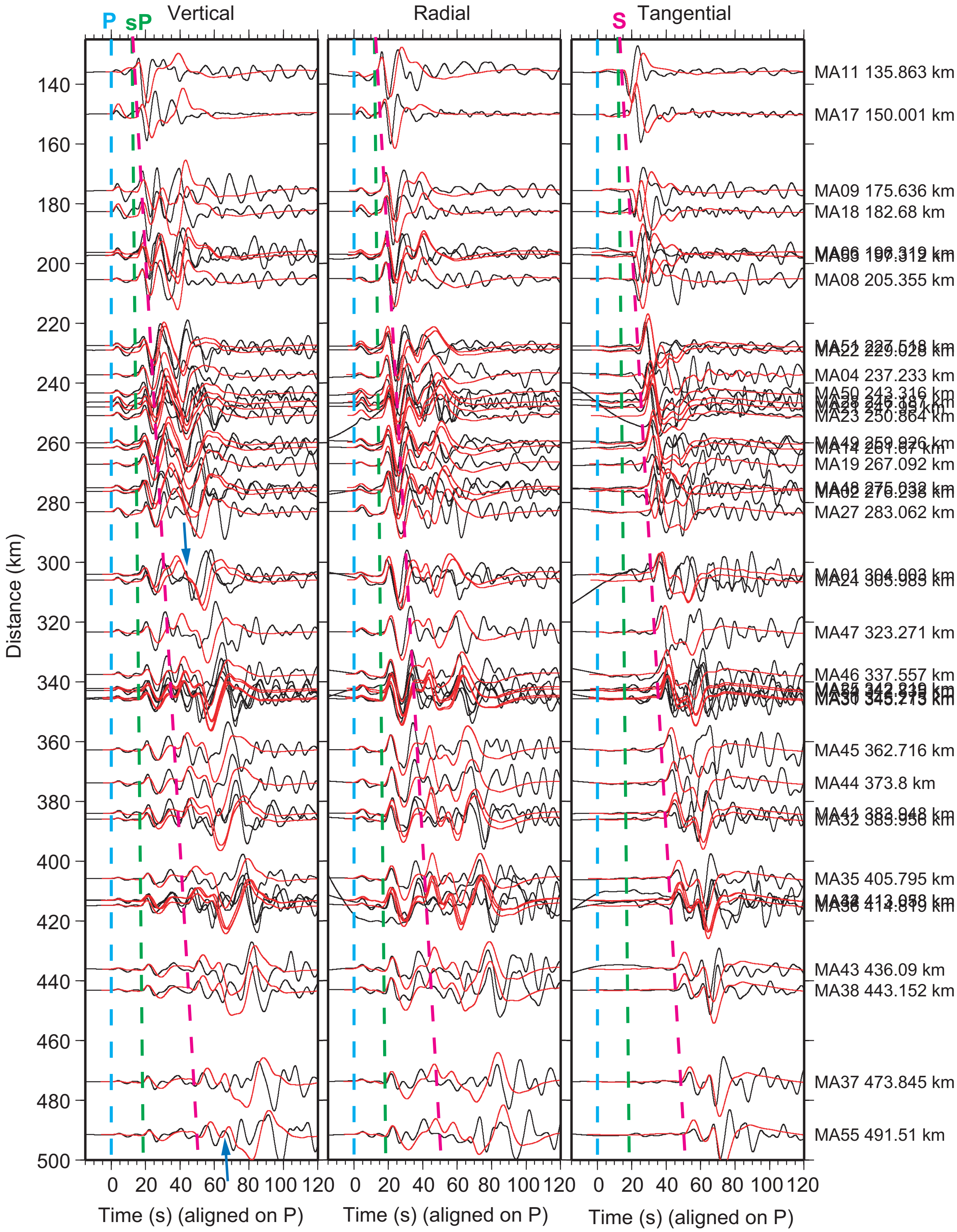

Figure 2.4: 1D modeling results of event 3 for the ncM velocity model filtered to 0.01–0.1 Hz. Data and synthetics are as in Figure 2.3. P, sP, and S phases are indicated and are predicted well by the ncM model. Blue arrows indicate the shoulder following SV.

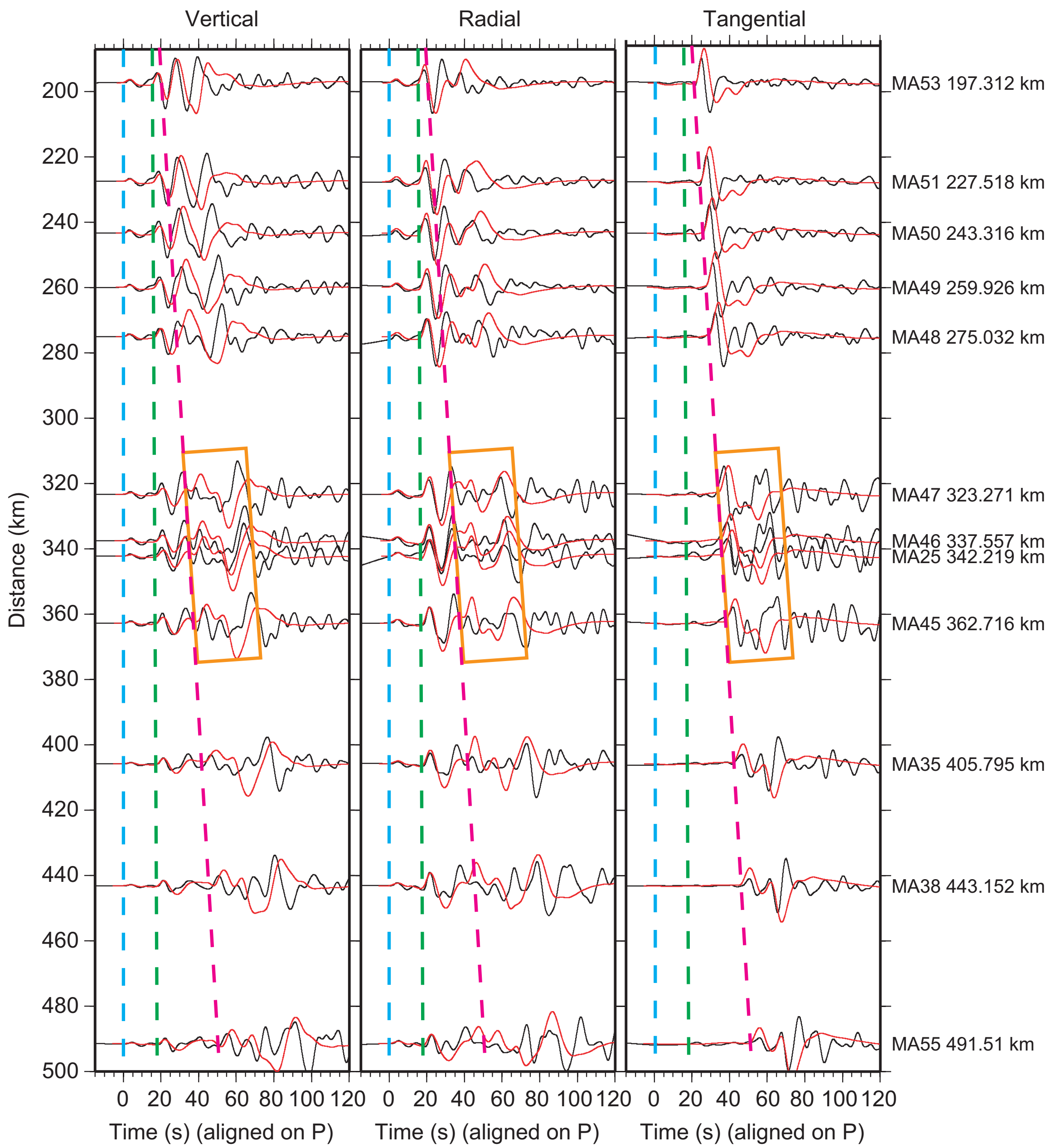

Figure 2.5: Profile across the MARS array along the NW-SE line in Figure 2.1. Data and synthetics are as in Figure 2.3. For the stations located within the TMVB, complexities in the waveforms are observed after the arrival of the S-wave in the data (indicated by orange box) and are not predicted by the model.

it. In their thermal modeling of the central Mexico subduction zone, *Manea et al.* (2004) found a high pore pressure ratio of 0.98 along the subduction interface, consistent with *Song et al.* (2009)'s HPFP layer, based on the extent of the coupled zone (450°C isotherm) from the trench. *Kim et al.* (2010) proposed that the USL is upper oceanic crust that is highly heterogeneous and composed of mechanically weak hydrous minerals (talc) that might be under high pore pressure. The hydrous minerals or high pore pressure of the USL is a likely explanation for the observed decoupling of the flat slab from the overriding plate, as evidenced by the lack of compressional seismicity in the North American plate (*Singh and Pardo*, 1993) and GPS observations (*Franco et al.*, 2005), and may be responsible for the flat subduction geometry, shown to be facilitated and sustained by such a low strength layer (*Manea and Gurnis*, 2007; *Kim et al.*, 2010).

The presence of the USL atop the Cocos slab is identified by the existence of complex P waveforms (*Song et al.*, 2009) recorded by the MARS array. These complex P waveforms consist of three locally converted S-to-P phases (A, B, C) that arrive within 4 sec after the P-wave (Figure 2.6). Phase A converts at the bottom of the USL and appears as a negative pulse at local stations. Phase B arrives immediately after phase A as a positive pulse, indicative of an S-to-P wave that converted at the top of the USL. Phase C converts at the bottom of the high velocity layer, arriving before phase A and ~1.0–1.5 sec after the direct P-wave. These three phases are searched for on the recordings of the intraslab earthquakes analyzed in this study. P waveforms on these recordings are categorized as complex, possibly complex, or simple based on the existence or absence and nature of phases A, B, and C. Examples of these waveforms from event 1 are shown in Figure 2.6. The waveforms have been bandpass filtered to 0.01–0.6 Hz, with the shorter periods in the frequency band allowing for the identification of the three S-to-P phases. When all three of the phases are clearly visible, the waveform is deemed complex. If one of the phases is not easily identified due to an uncharacteristic pulse shape and/or amplitude, but the other two phases are clearly present, then the waveform is possibly complex. Simple waveforms lack the shoulder in the direct P pulse indicative of the C phase and also have uncharacteristically shaped and/or low amplitude A and B phases. These features of the simple P waveforms indicate that there is no USL present.

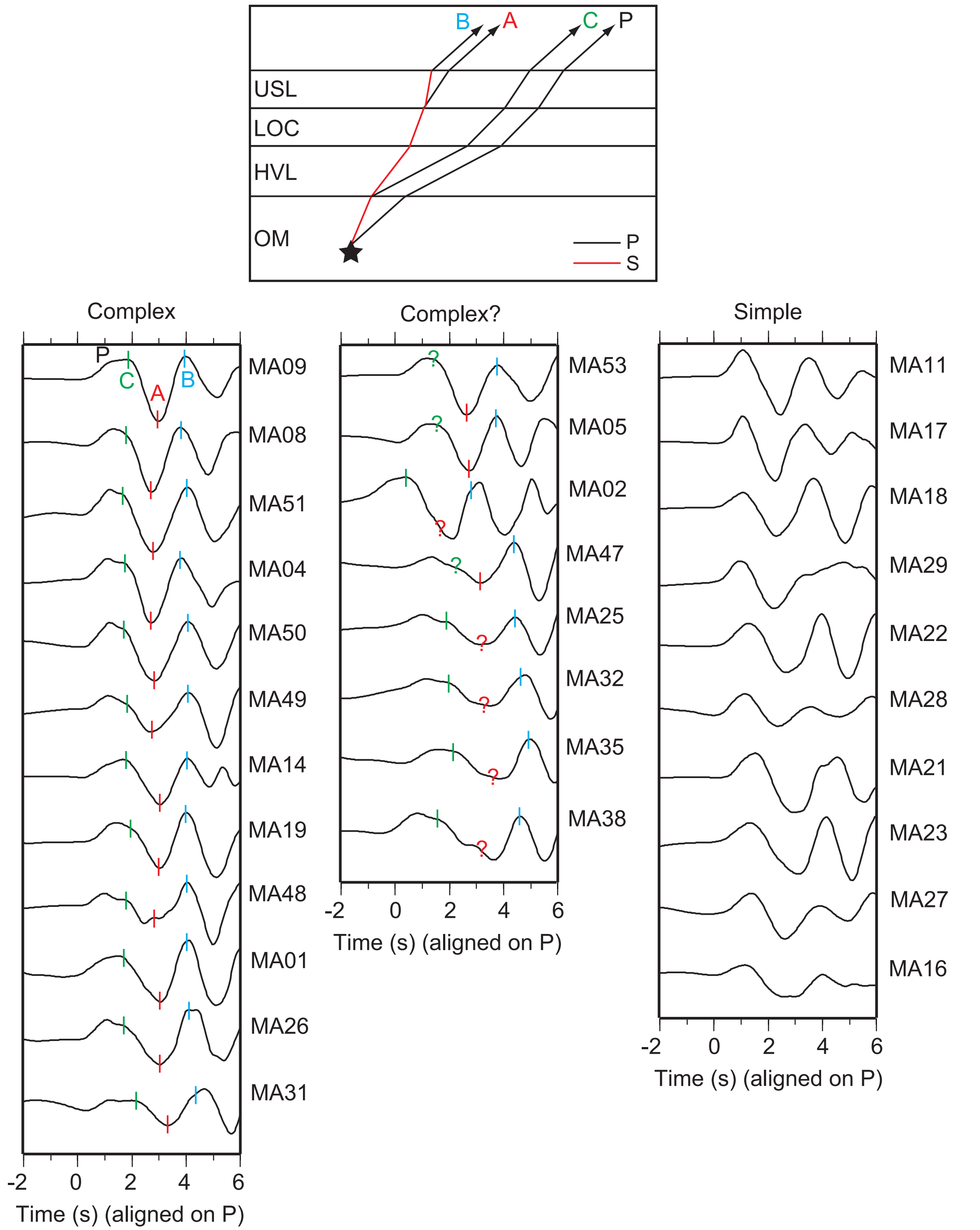

Figure 2.6: (Top) Schematic illustrating the ray paths of the P-wave and the three S-to-P phases (A, B, C) that comprise the complex P waveform. Abbreviations are USL, ultra-slow velocity layer; LOC, lower oceanic crust; HVL, high velocity layer; OM, oceanic mantle. (Bottom) Examples of complex (left), possibly complex (middle), and simple (right) P waveforms from event 1 recorded on the vertical component and filtered to 0.01–0.6 Hz. S-to-P phases A, B, and C are indicated by red, blue, and green tick marks, respectively. All three of these phases are visible in the complex waveforms within 4 sec of the P-wave. Question marks on the possibly complex waveforms indicate a phase that is not easily identified due to an uncharacteristic pulse shape and/or amplitude. Simple waveforms lack the shoulder in the direct P pulse indicative of the C phase and also have uncharacteristically shaped and/or low amplitude A and B phases, indicating there is no USL present.

The lateral extent of the USL is examined by mapping the locations of the S-to-P conversion points from the top of the Cocos slab for the eight events which exhibited complexity in their P waveforms (Figure 2.7). The locations of these conversion points are estimated using the TauP Toolkit (*Crotwell et al.*, 1999) with the ncM velocity model. The intermingling of S-to-P conversion points for stations that recorded complex, possibly complex, and simple P waveforms indicates that the USL is likely laterally heterogeneous, consistent with the observations of *Song et al.* (2009) and *Kim et al.* (2010). An approximate location for the western edge of the USL atop the slab is proposed based on the locations of these conversion points. This edge is located between the conversion points for the westernmost event which exhibited P complexity (event 19) and the nearest neighboring event which produced simple waveforms (event 2). The USL edge is arbitrarily mapped as a linear feature normal to the trench, but its exact orientation or curvature may vary. This boundary of the USL is approximately coincident with the western margin of the projected OFZ region.

2.3.4 2D Velocity Modeling

To further investigate the shallow structure of the subducted Rivera and Cocos plates, we produce synthetic seismograms with a 2D finite-difference wave propagation algorithm for particular velocity and slab geometry models and compare these to the data for event 3 (the largest magnitude event). The preferred model is a NW-SE oriented profile across the MARS array (see Figure 2.1 for profile location) consisting of P- and S-wave velocities from the ncM model and subducted slab geometries estimated from the isodepth contours of *Pardo and Suárez* (1995) (Figure 2.8). The USL in this model ends at the approximate edge location. The synthetics produced from this model are compared to the data in Figure 2.9. The model predicts the P and sP phases reasonably well at all distances and the S-wave at most distances. A later large amplitude phase, presumed to be an S-wave multiple, is predicted reasonably well by the model at distances greater than $\sim$320 km.

In order to test the effect of the presence or absence of the USL, the location of its edge, and the geometry of the subducted slabs on the synthetic seismograms produced, we examine four other models with the same velocity structure: (1) no USL, but a thicker lower oceanic crust layer to

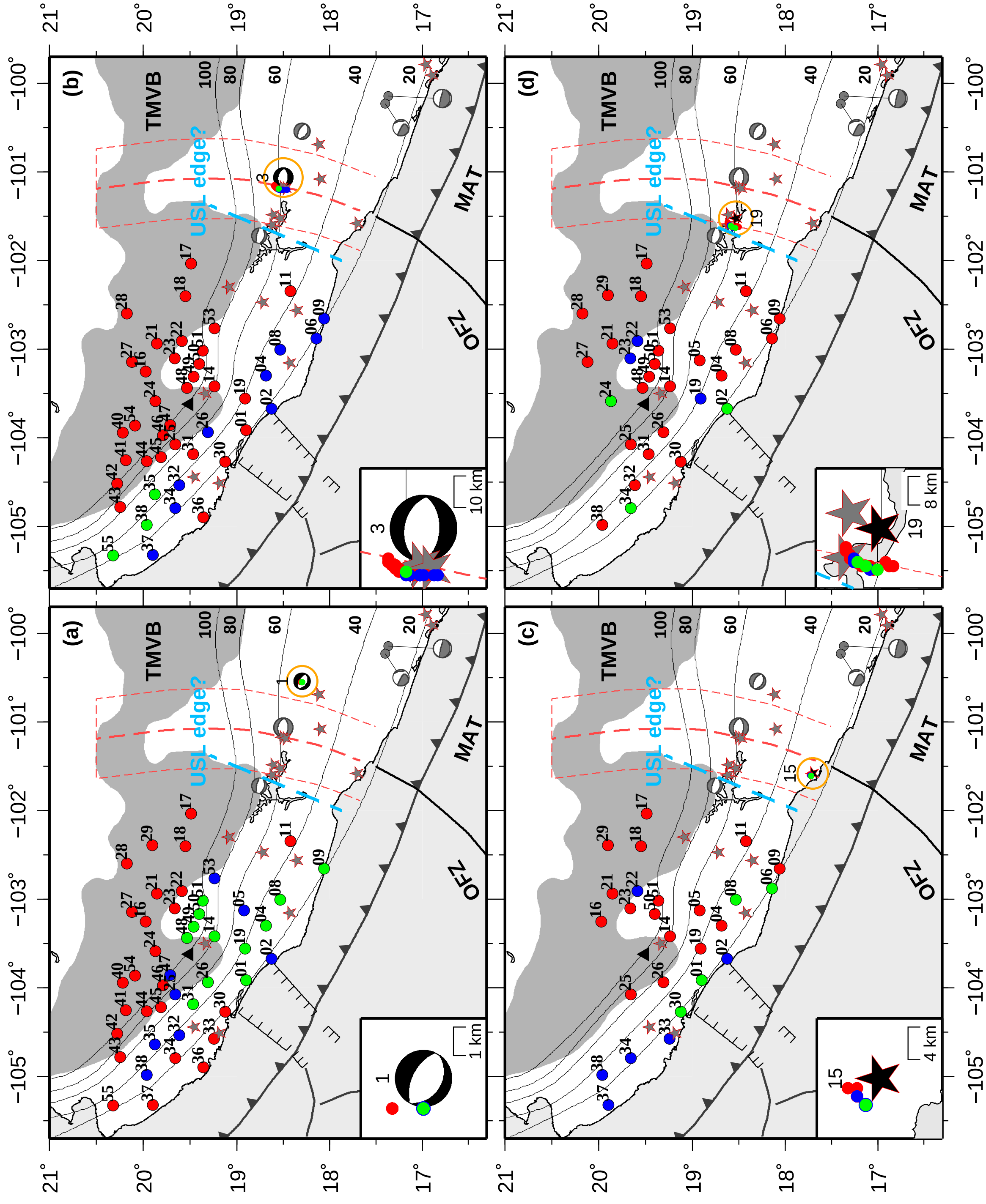

Figure 2.7: Local S-to-P conversion points from the top of the Cocos slab (small dots) for MARS stations which recorded complex (large green dots), possibly complex (large blue dots), or simple (large red dots) P waveforms for eight events which exhibited complexity (conversion points are colored corresponding to station). An approximate location for the western edge of the USL atop the slab is proposed (blue dashed line) based on the locations of these conversion points. The events shown are (by event number) (a) 1, (b) 3, (c) 15, (d) 19, (e) 28, (f) 29, (g) 42, and (h) 48. The location of each of these events is shown in black and highlighted with an orange circle. Insets show enlarged view of event and conversion point locations. Other events are shown in grey.

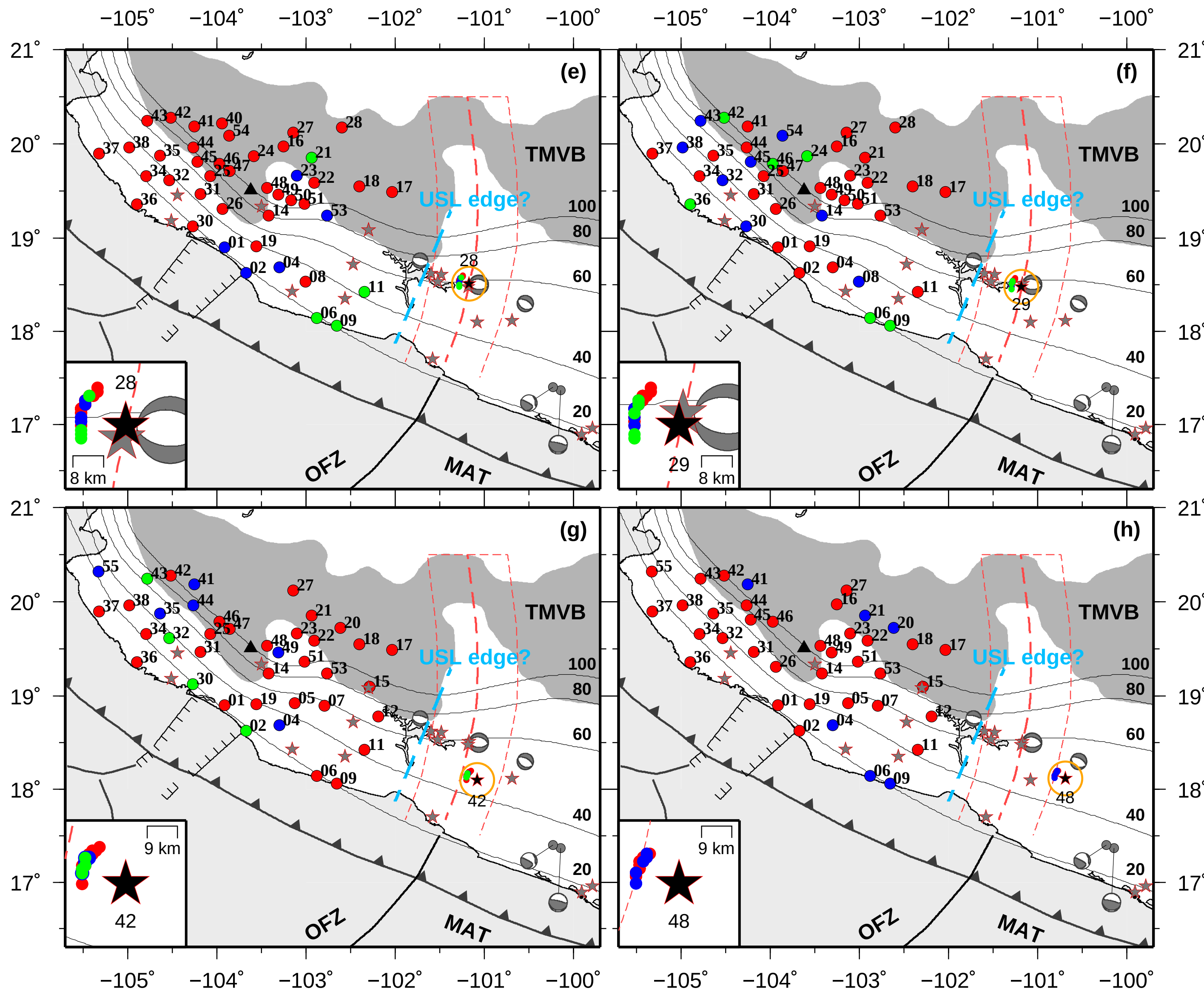

Figure 2.7: (continued).

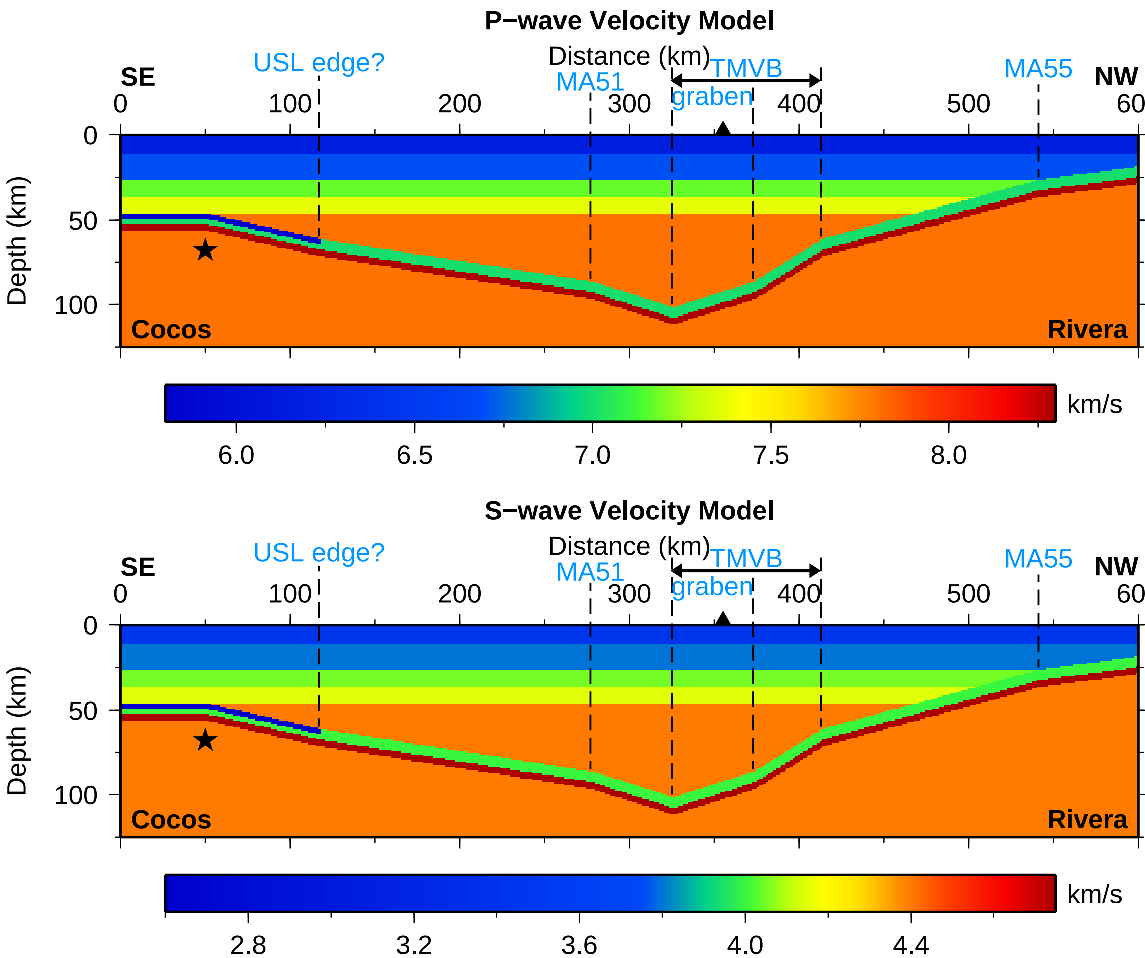

Figure 2.8: 2D velocity model of the shallow subduction zone structure across the MARS array along the NW-SE profile in Figure 2.1. P- and S-wave velocities are from the ncM model. Subducted slab shape is estimated from the isodepth contours of *Pardo and Suárez* (1995). Locations of the approximate USL edge, stations MA51 and MA55, Colima graben, TMVB, and Colima volcano (black triangle) are indicated for reference. The location of event 3 used in the modeling is shown by the black star.

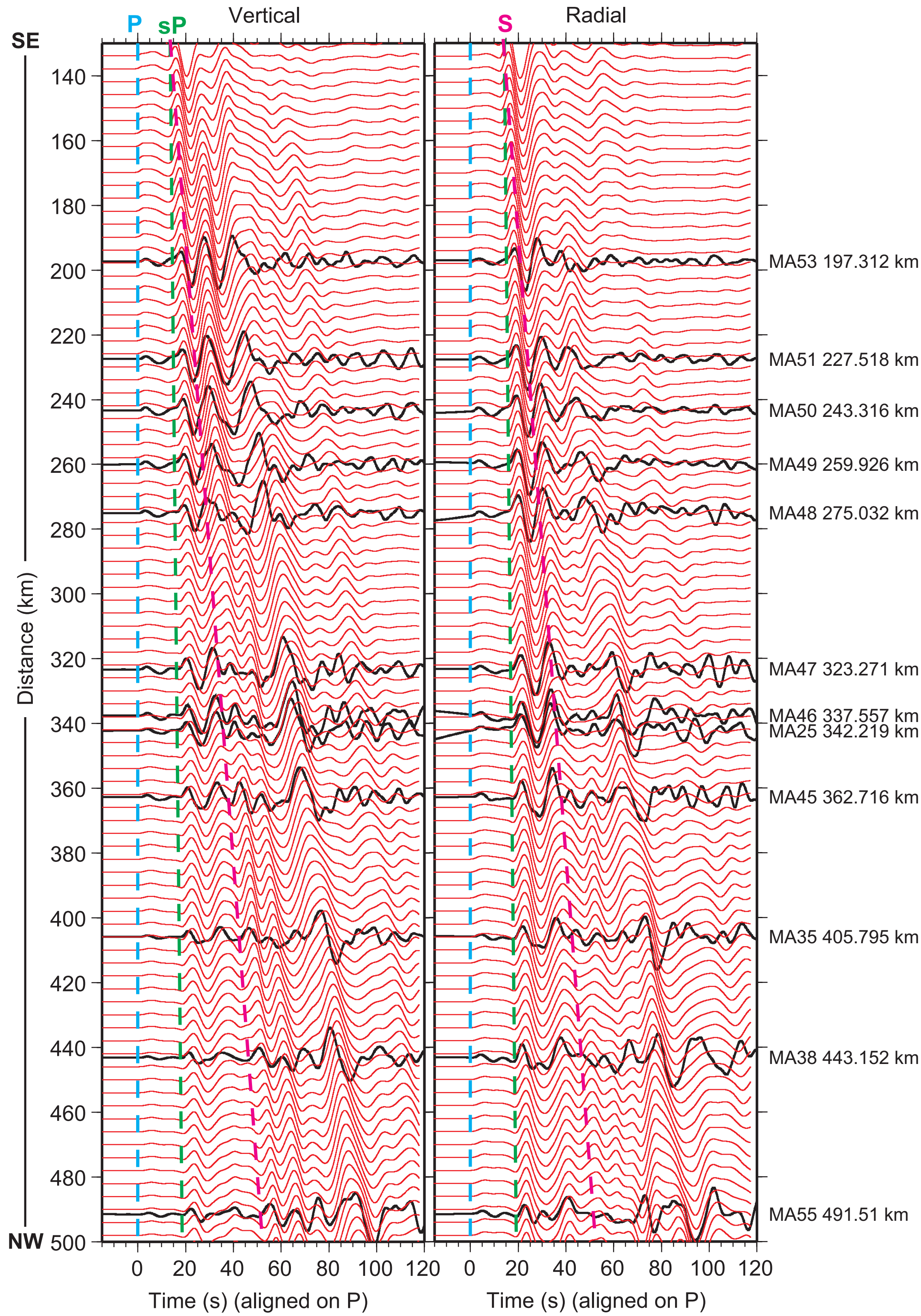

Figure 2.9: 2D modeling results of event 3 along the NW-SE profile filtered to 0.01–0.1 Hz. Data are in black, synthetics are in red. P, sP, and S phases are indicated.

maintain overall slab thickness (no USL); (2) USL continues across entire width of model without an edge (full USL); (3) USL edge shifted 100 km to the northwest (edge +100); (4) USL edge at approximated location, but subducted Rivera slab geometry is horizontal (or flat) northwest of the TMVB (edge fltRiv). We tested a variety of shift amounts for the edge +100 model (−30 km, −20 km, −10 km, +10 km, +20 km, +30 km, +40 km, +50 km, +100 km), but found no appreciable difference in the synthetics produced for shifts <100 km when compared to the edge model (i.e., unshifted) synthetics. A comparison of the synthetics produced for each of the four models and the preferred (edge) model to the data at four stations is shown in Figure 2.10. A ∼48 sec segment of the waveform after the S-wave that includes the large amplitude, presumed S-wave multiple illustrates the greatest variance among the models, indicating that this phase is most sensitive to the USL. The synthetic waveform for each model is cross-correlated with the data for this segment. The insignificant difference in correlation coefficients for the edge and edge fltRiv models show that the shape of the subducted Rivera slab is poorly resolved in our preferred model. While there is some variance between the vertical and radial components, in general, the correlation coefficients indicate that the edge model synthetics are better representations of the data than the no USL and full USL models. The correlation coefficients for the majority of the twelve stations located along the profile clearly indicate that the edge model synthetics fit the data better than those produced by the edge +100 model. In Figure 2.10, this finding is illustrated at stations MA45, MA48, and MA49 (radial component), while at station MA25, an exception to this result, the edge +100 model more accurately predicts the data.

Figure 2.10 *(following page)*: Comparison of 2D modeling results for five different models at four stations. The primary variance among the models was the USL: no USL = no USL present, thicker lower oceanic crust to compensate; full USL = USL continues across entire width of model without an edge; edge = USL stops at approximated edge location; edge +100 = USL edge shifted 100 km to the northwest; edge fltRiv = USL edge at approximated location, subducted Rivera slab shape made horizontal (or flat) northwest of the TMVB. Segment of waveform illustrating greatest variance among the models is shaded grey. Cross-correlation coefficients (X) for each model with the data for the selected segment are shown.

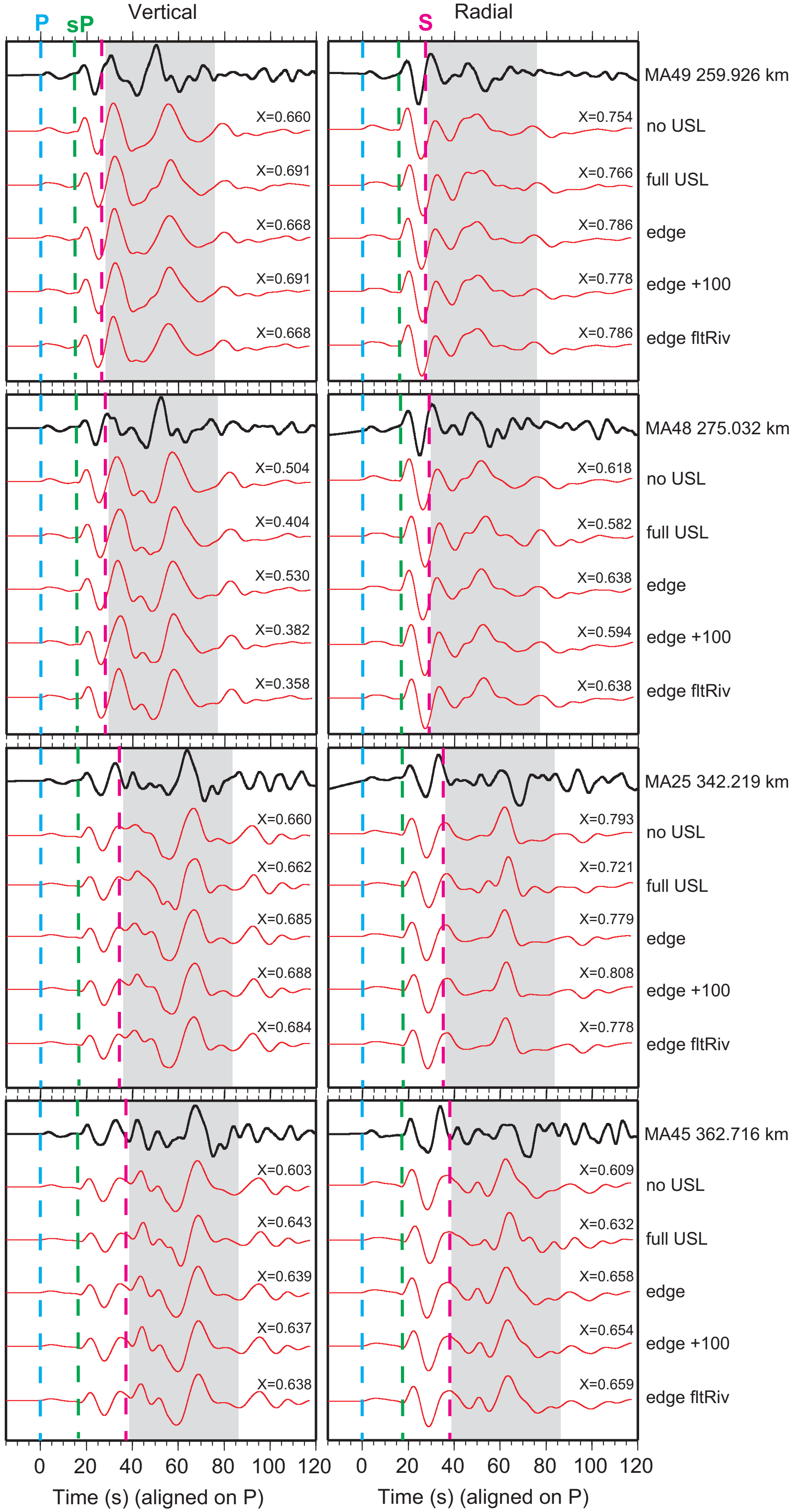

P
sP
Vertical
S
Radial
MA49 259.926 km
no USL
full USL
edge
edge +100
edge fltRiv
X=0.660
X=0.691
X=0.668
X=0.691
X=0.668
X=0.754
X=0.766
X=0.786
X=0.778
X=0.786
MA48 275.032 km
X=0.504
X=0.404
X=0.530
X=0.382
X=0.358
X=0.618
X=0.582
X=0.638
X=0.594
X=0.638
MA25 342.219 km
X=0.660
X=0.662
X=0.685
X=0.688
X=0.684
X=0.793
X=0.721
X=0.779
X=0.808
X=0.778
MA45 362.716 km
X=0.603
X=0.643
X=0.639
X=0.637
X=0.638
X=0.609
X=0.632
X=0.658
X=0.654
X=0.659
0 20 40 60 80 100 120
Time (s) (aligned on P)
0 20 40 60 80 100 120
Time (s) (aligned on P)

2.3.5 Seismicity and Slab Dip Across USL Edge

The variation in slab dip across the USL edge is examined in detail to locate any abrupt changes in geometry which could be indicative of a possible plate boundary. Epicenters for earthquakes located between 16.5°N and 20.5°N from the January 2001–May 2011 event catalog of the Servicio Sismológico Nacional (SSN) are mapped and divided into four 50-km-wide trench-normal bins parallel to the USL edge (Figure 2.11a). The locations of events furnished by the SSN have been carefully revised by an analyst and checked against the locations provided by the Global Centroid Moment Tensor (GCMT) and National Earthquake Information Center (NEIC) catalogs (*Noriega-Manzanedo and Pérez-Campos*, 2010). Bins 1 and 2 are located east of the USL edge and include the majority of the projected OFZ region. Bins 3 and 4 are located west of the USL edge. There is a significant decrease in the seismicity in the western bins compared to the eastern bins, which is indicative of a structural change across the USL edge. Cross-sections of the seismicity in each bin illustrate variations in the Benioff zone across the region and are used to estimate the slab dip in each bin (Figure 2.11b). The dip angle is estimated by visually selecting hypocenter locations that are downdip of the trench and are not within the overriding plate, then performing a linear regression of the selected locations. There is a considerable difference in slab dip between bins 1 (25°) and 2 (39°), while the slab dip is constant across bins 3 and 4 (41°) (Figure 2.11c). Using an estimated maximum error of ±5° for each bin, the errors on these dip estimates are weighted by the number of earthquakes in each bin, such that fewer events in a bin produces a larger error, with values ranging from ±2.5° (bin 1) to ±4.5° (bin 4). These dip estimates indicate a significant change in slab geometry across the projected OFZ region, which the USL continues through, and constant geometry west of the USL edge.

2.4 Discussion

Previous evidence suggestive of the ongoing fragmentation of the Cocos plate has been purely tectonic in nature, while in this study we provide evidence based on seismic observations and modeling of the velocity structure of the central Mexico subduction zone. From mapping the locations of S-to-P conversion points, we find the location of the USL edge to be approximately coincident with the western margin of the projected OFZ region. Although indicated as a linear feature, we have minimal constraints on the orientation and shape of the USL edge due to limited earthquakes in the region, so it is possible that it could instead follow a curved path parallel to the projected OFZ. The 2D finite-difference modeling confirmed the location of the USL edge where it intersects the NW-SE profile across the MARS array. The coincidence of the confirmed USL edge with the western margin of the projected OFZ region indicates that this margin is a sharp structural boundary. On the basis of these results, we propose a slab tear model, wherein the Cocos slab is currently fragmenting into a North Cocos plate and a South Cocos plate along the projection of the OFZ by a process similar to that which occurred when the Rivera plate separated from the proto-Cocos plate (Figure 2.12). The presence and location of this slab tear are consistent with the anisotropy pattern found by *Stubailo et al.* (2012) using Rayleigh wave phase velocity dispersion measurements. The continuation of the USL across the projected OFZ region indicates that the N Cocos and S Cocos slabs are not currently separated by a significant gap, but rather that the OFZ region may be acting as a transition zone (*Blatter et al.*, 2007) in this young tear. This is contrary to the mature tear along the Rivera-Cocos plate boundary where a distinct gap between the slabs has been observed (*Yang et al.*, 2009).

The variations in observed seismicity and slab dip across the USL edge from the SSN catalog data provide further evidence for a distinct N Cocos-S Cocos plate boundary along the western margin of the projected OFZ region and can be used to explain why the USL terminates here. The S Cocos seismicity bins (1 and 2) overly the OFZ and contain more than three times the events in

---

Figure 2.11 *(following page)*: Seismicity and slab dip across the USL edge. (a) Map showing epicenters (stars) for earthquakes located between 16.5°N and 20.5°N from the 1/2001 – 5/2011 SSN catalog. Data in four 50-km-wide bins parallel to the USL edge (blue dashed line) are analyzed for changes in slab dip across this region. Bins 1 and 2 (yellow) are on the South Cocos plate, and bins 3 and 4 (peach) are on the North Cocos plate. Note the decreased seismicity in bins 3 and 4 relative to bins 1 and 2. (b) Cross-sections of seismicity in the S Cocos slab (top) and N Cocos slab (bottom). Note the significant change in slab dip between bins 1 and 2 and the constant slab dip across bins 3 and 4. (c) Plot of slab dip across the four data bins. Error bars are weighted by the number of events in each bin, such that fewer events produces a larger error.

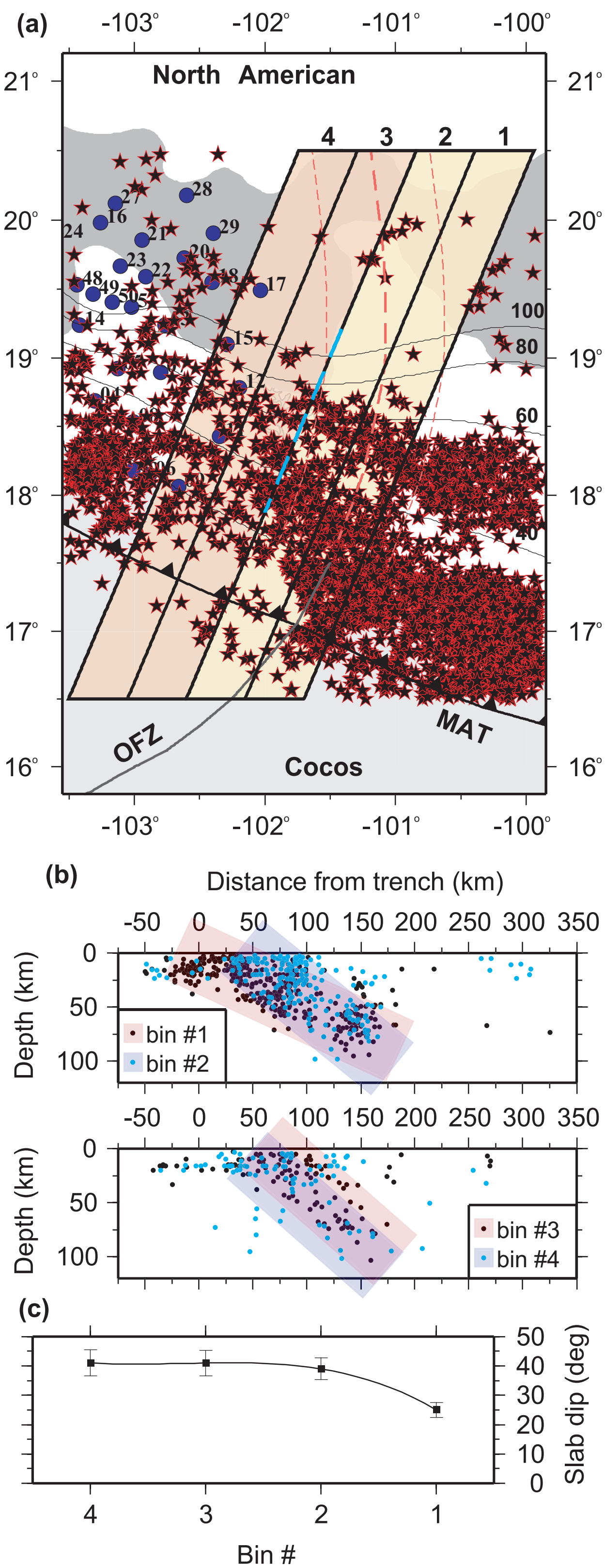
(a)
North American
Cocos
OFZ
MAT
4
3
2
1
100
80
60
40
-103°
-102°
-101°
-100°
21°
20°
19°
18°
17°
16°
(b)
Distance from trench (km)
Depth (km)
bin #1
bin #2
bin #3
bin #4
(c)
Slab dip (deg)
Bin #

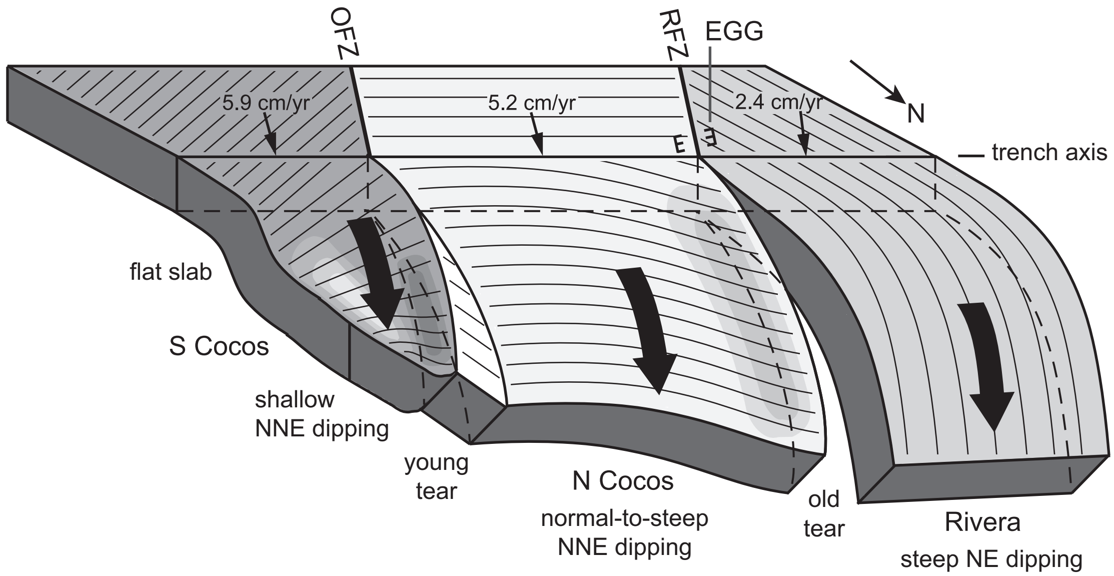

Figure 2.12: 3D schematic of the two-tear model illustrating the geometry of the S Cocos, N Cocos, and Rivera plates, along with the Orozco (OFZ; young tear) and Rivera (RFZ; old tear) fracture zones. Plate convergence rates and directions (small arrows) are shown at the trench (from *DeMets et al.* (1990)).

the N Cocos bins (3 and 4). This large variation in observed seismicity on either side of the USL edge indicates that this is a marked structural boundary. The observed change in slab dip across the S Cocos bins and the constant slab dip across the N Cocos bins is consistent with the interpretation that the OFZ region is a transition zone of changing geometry, while the N Cocos exhibits stable geometry. This result also signifies that the USL edge is a distinct structural boundary, which we interpret as the N Cocos-S Cocos plate boundary. Based on this interpretation, the OFZ transition zone is structurally S Cocos, which explains why the USL ends along its western margin. If the presence of the USL was controlled simply by slab geometry, then we would expect its lateral extent to lie along the eastern margin of the projected OFZ region where the slab ceases to underplate the North American plate in a flat geometry. The low permeability fine-grained blueschist cap layer of *Song et al.* (2009) would likely be lost as the slab dip increased and the subsequently larger pressures and temperatures of the subduction zone metamorphosed the blueschist to coarse-grained eclogite, which would not be capable of sealing the water in the HPFP USL. As the USL continues across the transition from flat to normal subduction and across the OFZ, its lateral extent is clearly not controlled by a change in geometry. The USL appears to be purely a feature of the S Cocos plate with the location of its edge caused by the end of the S Cocos slab at the N Cocos-S Cocos plate tear along the western margin of the projected OFZ region. The USL ends due to the structural change from one plate to another, which may be related to the tear itself. It can be theorized that the plate tear breaks the USL, allowing entrained water from the hydrous minerals and/or pore spaces to be released, which effectively prevents the USL from continuing.

The fragmentation of a lithospheric plate, such as the Cocos plate, along a fracture zone can be related to the subduction and inherent structure of the fracture zone itself. A fracture zone is usually of lower density than the surrounding oceanic plate and, as such, it tends to resist subduction or subduct in a different way (*Chung and Kanamori*, 1978; *Rosenbaum et al.*, 2008; *Blatter and Hammersley*, 2010), modifying the geometry of the subduction zone (*Vogt et al.*, 1976; *McCann and Habermann*, 1989; *Franke et al.*, 2008). This increased resistance against subduction due to buoyancy coupled with the bathymetric relief of the fracture zone likely enhances downdip extensional stress in the slab (*Chung and Kanamori*, 1978) and increases vertical and horizontal stresses on the overriding plate, creating or reactivating preexisting fractures (*McCann and Habermann*, 1989). The subduction of a fracture zone causes some degree of local decoupling of the oceanic plate from the overriding plate and/or creates a zone of extension within the slab (*Eissler and Kanamori*, 1982; *Huchon and Bourgois*, 1990), illustrating its nature as a weaker interface compared to the surrounding lithosphere (*Lowrie et al.*, 1986; *Kostoglodov and Ponce*, 1994; *Hall and Gurnis*, 2005; *Lonsdale*, 2005; *Porritt et al.*, 2011). A fracture zone, as a line of weakness, is therefore an ideal place for a lithospheric tear to develop, resulting in the fragmentation of the subducted oceanic plate into distinct segments, each behaving as an individual unit (*Sillitoe*, 1974; *Vogt et al.*, 1976; *Nixon*, 1982; *Burbach et al.*, 1984; *Lonsdale*, 1991; *Rosenbaum et al.*, 2008; *Sigloch*, 2011). The proposed fragmentation of the Cocos plate along the OFZ is an example of this process. The tectonic history of the northeast Pacific supports this theory of the OFZ as a plate boundary. From about 11 Ma to 6.5 Ma, the OFZ was the location of the Rivera-Cocos plate boundary before the Pacific-Rivera spreading center migrated northward and the Pacific-Cocos spreading center jumped north to the

Rivera Fracture Zone (RFZ) (*Klitgord and Mammerickx*, 1982; *Mammerickx and Klitgord*, 1982). As a previously active plate boundary, it is certainly possible and highly feasible for the OFZ to become reactivated as a plate boundary with the fragmentation of the Cocos plate.

A fracture zone like the OFZ reflects discontinuities in the underlying subduction zone (*Sillitoe*, 1974; *Lowrie et al.*, 1986; *Lonsdale*, 1991; *Hall and Gurnis*, 2005; *Porritt et al.*, 2011) such as contrasting lithosphere age, buoyancy, slab dip, topography, and convergence rate, which can be used to explain the plate tearing process. The age of the lithosphere at the OFZ is 17.6 Ma on the N Cocos and 14.5 Ma on the S Cocos (*Pardo and Suárez*, 1995). The older, colder, and therefore, denser N Cocos slab subducts at a steeper angle than the younger, more buoyant S Cocos slab which is nearly horizontal (*Blatter et al.*, 2007; *Blatter and Hammersley*, 2010). This drastic change in slab dip ($\sim$10–15° to $\sim$30°) (*Pardo and Suárez*, 1995) could be contributing to the tearing along the OFZ, although *Pardo and Suárez* (1995) argue for smooth contortions between these geometries, rather than tear faults. The convergence rate on either side of the OFZ is a constant 5.6 cm/yr, but this rate slows to the north and speeds up to the south (*DeMets et al.*, 1990), indicating an overall slower convergence rate for the N Cocos plate relative to the S Cocos. This slower convergence may be related to the rugged topography of the oceanic crust that was observed between the OFZ and the RFZ, relative to the smooth topography south of the OFZ (*Kostoglodov and Ponce*, 1994; *Ramírez-Herrera et al.*, 2011). The rougher topography offers greater resistance to subduction, resulting in a slower convergence rate. This difference in resistance against the oceanic lithosphere to the north and south of the OFZ may result in differential motion between these two lithospheres (*Chung and Kanamori*, 1978; *Lonsdale*, 2005), leading to a tear. In *Wortel and Cloetingh* (1981, 1983)'s plate fragmentation model, the lateral variation in the age of the slab across the OFZ ($\sim$3 Ma) would produce significant tensional stresses in the plate, possibly causing fragmentation of the oceanic plate (*Burkett and Billen*, 2010). These stresses would result from the variable slab-pull forces and trench resistance forces which depend on the age of the subducting lithosphere, where slab-pull forces are greater for older lithosphere and trench resistance forces are greater for young lithosphere (*Wortel and Cloetingh*, 1981, 1983). If these tensional stresses exceed the strength of the lithosphere, then tearing or stretching of the plate may occur (*Wortel and Cloetingh*, 1981, 1983; *Burkett and Billen*, 2010).

A special case of the more general plate fragmentation mechanism proposed by *Wortel and Cloetingh* (1981, 1983) is the process of pivoting subduction (*Menard*, 1978), which emphasizes the role of differences in the direction of motion rather than differences in the relative rate of motion between segments of a plate in the course of a fragmentation event (*Lonsdale*, 1991, 2005; *Bandy et al.*, 2000). Pivoting subduction involves a pinned geometry in which a ridge and a trench approach one another obliquely and the young buoyant lithosphere near the point where they meet resists subduction so that the plate pivots about the point (*Menard*, 1978; *Burkett and Billen*, 2010). This is the process by which the proto-Cocos plate fragmented into the Rivera and Cocos plates (*Bandy et al.*, 2000). In response to the collision of the East Pacific Rise (EPR) with the MAT off the southern tip of Baja California (e.g., *Mammerickx and Klitgord*, 1982; *Atwater*, 1989; *Lonsdale*, 1991), a small part of the proto-Cocos plate near the point of collision began to pivot about a new pole located close to this point (*Bandy et al.*, 2000). The motion of the remainder of the proto-Cocos plate to the south was unaffected by the ridge-trench collision, and this differing response of the two parts of the plate produced extensional stresses within the plate which resulted in a zone of extensional deformation, or tearing, (*Burkett and Billen*, 2010) along the present Rivera-Cocos plate boundary (*Bandy et al.*, 2000). Plate motions suggest that the stresses were greatest at the northeast extent of the subducted Rivera-Cocos boundary, and the tearing propagated to the southwest towards the EPR (*Bandy et al.*, 1998, 2000; *Serrato-Díaz et al.*, 2004). This extensional deformation along the Rivera-Cocos plate boundary is consistent with the location and formation of the Colima Graben and its offshore extension to the southwest, the El Gordo Graben. The propagation of tearing from northeast to southwest is also consistent with the seismic tomography images of *Yang et al.* (2009), which show a clear gap between the subducted Rivera and Cocos plates that widens in the downdip (northeast) direction.

The Cocos plate is proposed to be fragmenting along the OFZ by a recently initiated (0.9 Ma) (*Bandy et al.*, 2000) pivoting subduction process analogous to that which occurred when the Rivera plate separated from the proto-Cocos plate. The wedge-shaped Cocos plate includes curved fracture zone traces, fanning magnetic anomalies (*Lynn and Lewis*, 1976; *Atwater*, 1989), and a Pacific-Cocos spreading rate that increases southward along the EPR (*Klitgord and Mammerickx*, 1982; *Atwater*, 1989). The northern terminus of the Pacific-Cocos spreading center is approaching the MAT (*Bandy and Hilde*, 2000), with the pole of opening located nearby to the north (*Mammerickx and Klitgord*, 1982). When all of these features are taken into account, it becomes clear that the present Cocos plate is a good approximation of the pinned geometry described by *Menard* (1978). The younger, more buoyant lithosphere of the northern Cocos plate resists subduction and pivots about the nearby Pacific-Cocos pole, while the motion of the southern Cocos plate remains unchanged. This difference in the direction of motion of the two parts of the plate produces extensional stresses in the plate, which result in the ongoing tearing, or fragmentation, into a N Cocos plate and a S Cocos plate along the landward projection of the OFZ.

There are several tectonic observations which support the theory that the Cocos plate is fragmenting along the OFZ by a process analogous to the Rivera-Cocos tear event. The variations in plate motions on either side of the boundary are one example of such an observation. *DeMets et al.* (1990) and *DeMets and Wilson* (1997) noted a systematic misfit of ~3 mm/yr of Pacific-Cocos spreading rates relative to magnetic anomalies from the EPR north of the OFZ. They attributed this misfit to seafloor north of the OFZ which moves relative to the rigid Pacific and Cocos plates. *Bandy et al.* (2000) report the results of a statistical F-Test which was performed to test for the presence of a N Cocos plate. This test passed at the 5% risk level, suggesting that the motion of the Cocos plate north of the OFZ is different than that to the south (*Bandy et al.*, 2000). The 5°–9° change in strike of the Pacific-Cocos spreading center segment on either side of the OFZ further suggests that the motion of the Cocos plate changes at this boundary (*Bandy et al.*, 2000). These observations of variable plate motions on either side of the OFZ indicate the presence of separate N Cocos and S Cocos plates, which are fragmenting from one another along the eastward projection of the OFZ. Evidence for this landward projection lies in the existence of an embayment in the TMVB along its path (*Blatter et al.*, 2007; *Blatter and Hammersley*, 2010). The subduction of fracture zones is known to produce an interruption or offset of a volcanic chain (e.g., *Sillitoe*, 1974; *Vogt et al.*, 1976; *Eissler and Kanamori*, 1982), such as that observed in the TMVB along the projection of the RFZ, or Rivera-Cocos plate boundary, (*Nixon*, 1982) and the Tzitzio Gap in the TMVB along the projection of the OFZ (*Blatter et al.*, 2007; *Blatter and Hammersley*, 2010).

The observation of a possible rift-rift-rift triple junction overlying the projected OFZ region (*Bandy et al.*, 2000) provides further support for the fragmenting Cocos plate theory. This triple junction is comprised of broad river valleys (*Kostoglodov and Ponce*, 1994) with the eastern and southern rifts containing the Rio Balsas (*Ramírez-Herrera et al.*, 2011), the western rift containing the Rio Tepalcatepec, and Lake Presa del Infiernillo lying at their juncture (*Bandy et al.*, 2000). This triple junction overlying the proposed zone of separation between the N Cocos and S Cocos plates is similar to the Colima-Chapala-Zacoalco rift-rift-rift triple junction which overlies the Rivera-Cocos plate boundary (*Bandy et al.*, 2000; *Bourgois and Michaud*, 2002). The rifts of the Rivera-Cocos system contain the Colima Graben in the south, Lake Chapala in the east (part of the Chapala Graben), and the Zacoalco Graben in the northwest (*Luhr et al.*, 1985; *Allan*, 1986). Both of these triple junctions reflect the response of the overriding plate to divergence of the plate below. In the Rivera-Cocos plate boundary case, the divergence is that between the Rivera and N Cocos slabs, while in the OFZ case, the divergence is that between the N Cocos and S Cocos slabs. The OFZ triple junction is of a smaller scale than that of the Rivera-Cocos boundary, with less developed rifts or grabens, indicative of the young age of the N Cocos-S Cocos plate tear relative to the mature Rivera-Cocos tear.

The apparent tear along the OFZ may play an important role in the rollback dynamics of the slab in central Mexico. The age of volcanism north of Mexico City shows that the slab has been rolling back from 20 Ma to present (*Ferrari*, 2004). This would necessitate trench parallel flow in order to move material from the backarc to the forearc (*Russo and Silver*, 1994; *Schellart et al.*, 2007; *Burkett and Billen*, 2010). This flow is presumably currently accommodated by the tear between the Cocos and Rivera plates (*Soto et al.*, 2009). A tear along the OFZ would significantly short-cut this process, and it may be that tearing is a natural part of this process.

2.5 Conclusions

We have studied the seismic structure of the central Mexico subduction zone along the transition from flat to normal subduction using 1D and 2D waveform modeling techniques and an analysis of P waveform complexities. The results show that the subducted Cocos plate is a complicated, multi-layered structure with a thin USL atop the slab. The lateral extent of this USL is approximately coincident with the western margin of the projected OFZ region, implying a structural boundary which we interpret as a tear in the Cocos plate. Recent tectonic observations in the region of variable plate motions on either side of the OFZ and a small-scale rift-rift-rift triple junction overlying the landward projection of the OFZ have suggested that the Cocos plate is fragmenting along this fracture zone. On the basis of our seismic results and these tectonic observations, we propose a slab tear model, wherein the Cocos slab is currently fragmenting into a N Cocos plate and a S Cocos plate along the projection of the OFZ by a pivoting subduction process similar to that which occurred when the Rivera plate separated from the proto-Cocos plate. This ongoing fragmentation event presents the opportunity to observe and study a young tearing process in action.

Acknowledgments

This study was supported in part by the Gordon and Betty Moore Foundation through the Tectonics Observatory at California Institute of Technology. This is contribution number 207 from the Caltech Tectonics Observatory. We are grateful to the Incorporated Research Institutions for Seismology Data Management Center (IRIS-DMC) for making the waveform data available. We thank Arturo Iglesias for providing the Servicio Sismológico Nacional event catalog. We also thank Editor Robert Nowack and two anonymous reviewers for helpful comments which greatly improved the manuscript.

2.6 Supplemental Figures

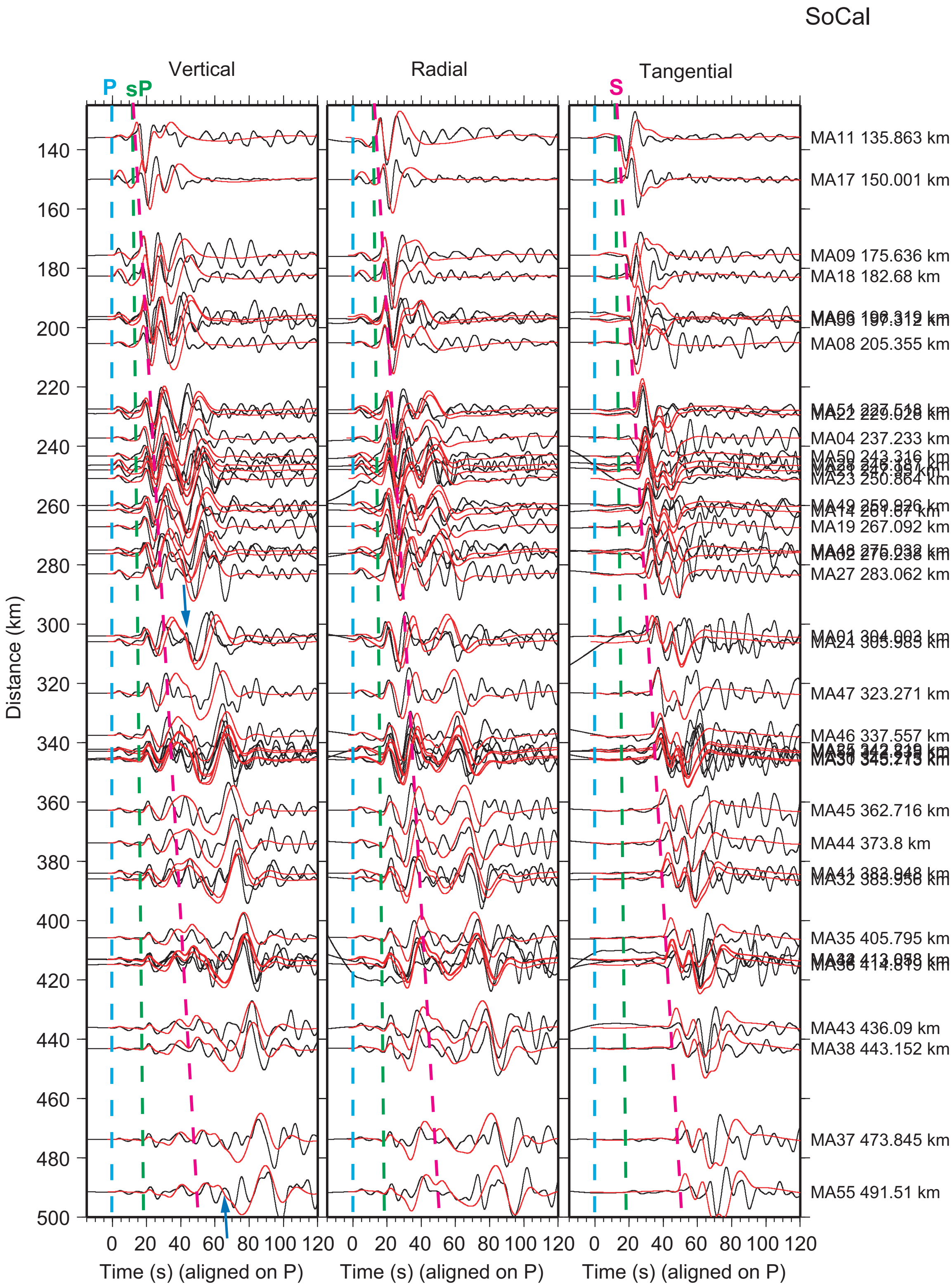

Figure 2.13: 1D modeling results of event 3 for the SoCal velocity model filtered to 0.01–0.1 Hz. Data are in black, synthetics are in red. P, sP, and S phases are indicated by dashed lines. Blue arrows indicate the shoulder following SV in the data.

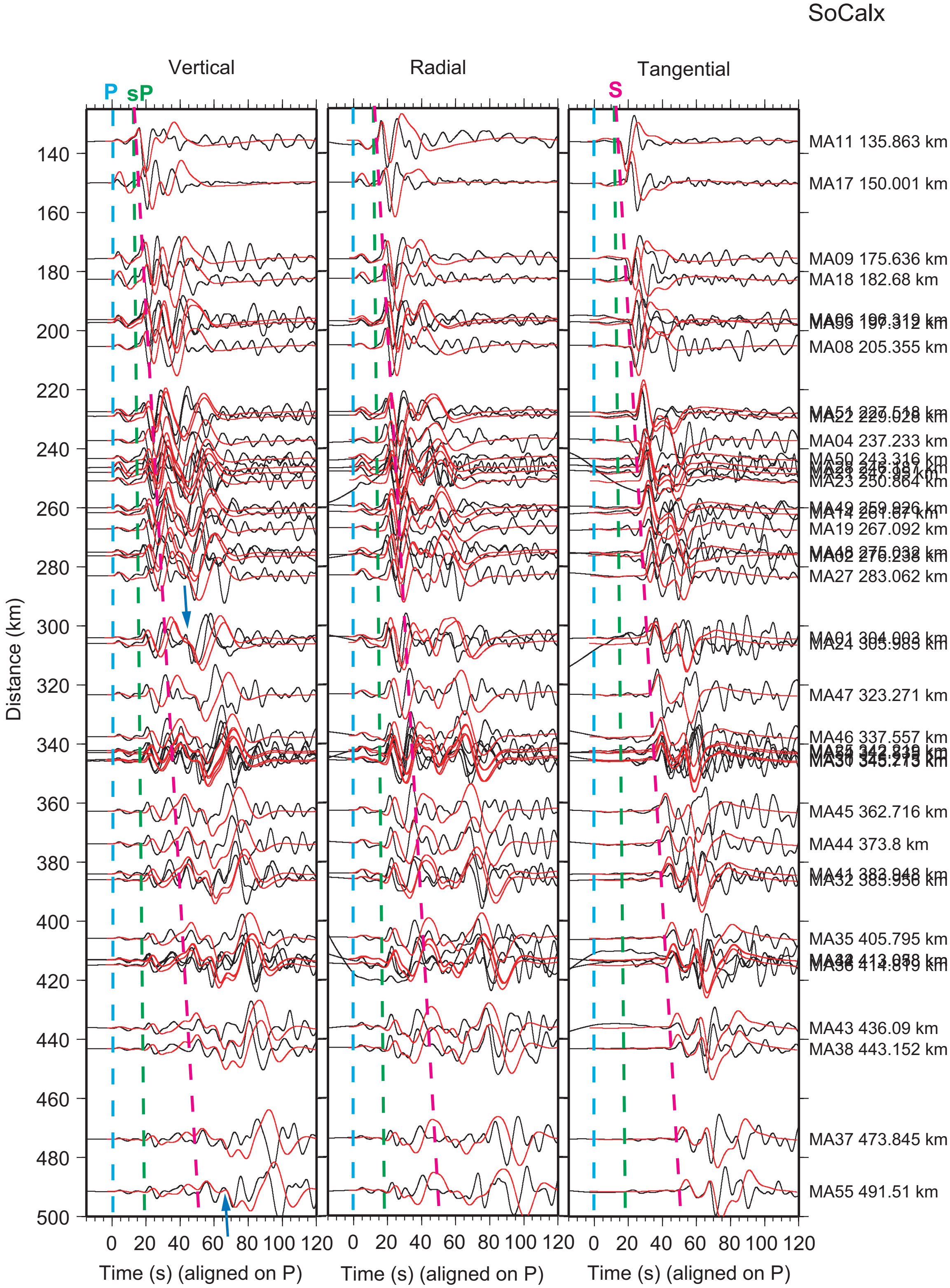

Figure 2.14: 1D modeling results of event 3 for the SoCalx velocity model filtered to 0.01–0.1 Hz. Data are in black, synthetics are in red. P, sP, and S phases are indicated by dashed lines. Blue arrows indicate the shoulder following SV.

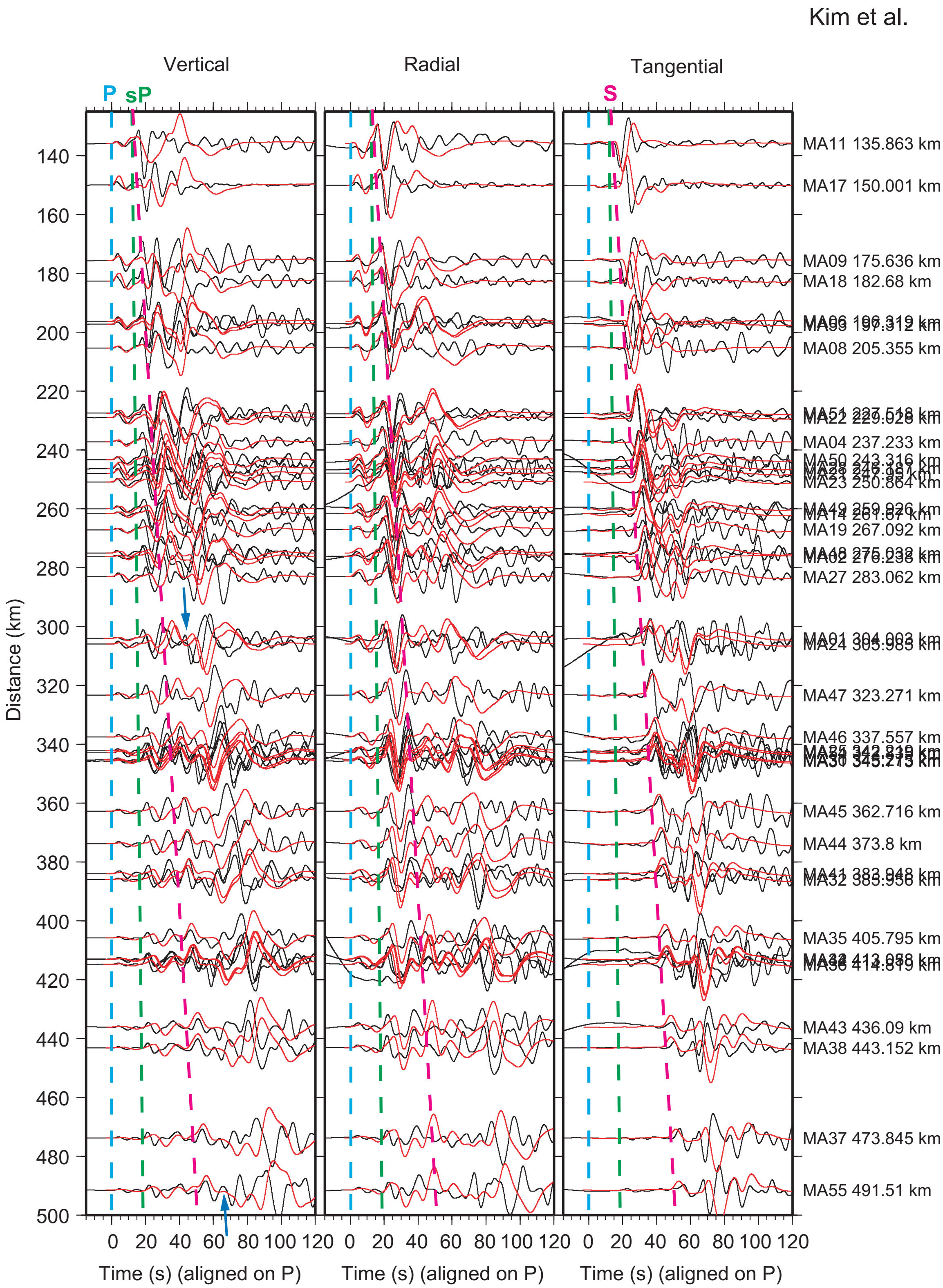

Figure 2.15: 1D modeling results of event 3 for the *Kim et al.* (2010) velocity model filtered to 0.01–0.1 Hz. Data are in black, synthetics are in red. P, sP, and S phases are indicated by dashed lines. Blue arrows indicate the shoulder following SV.

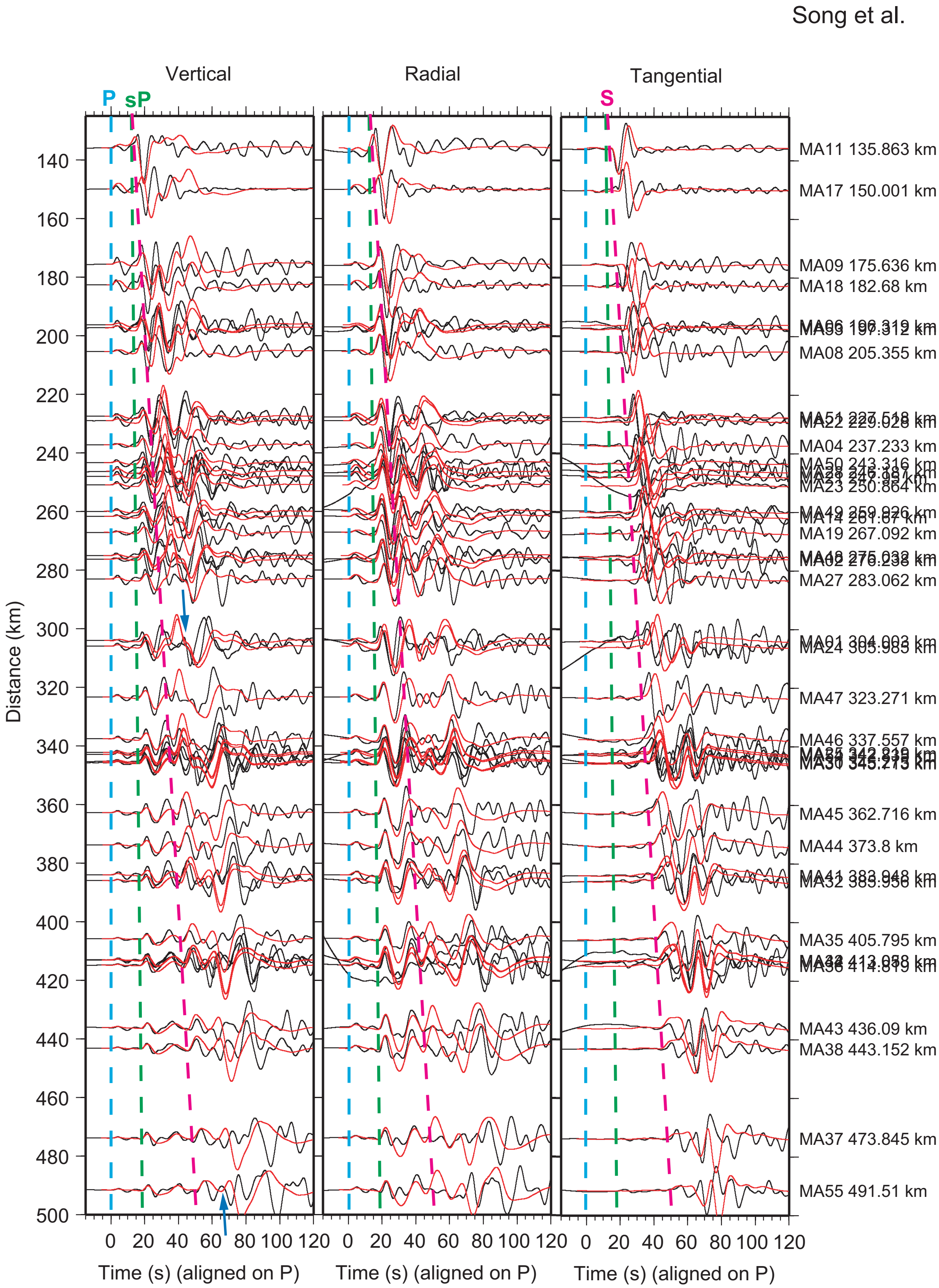

Figure 2.16: 1D modeling results of event 3 for the *Song et al.* (2009) velocity model filtered to 0.01–0.1 Hz. Data are in black, synthetics are in red. P, sP, and S phases are indicated by dashed lines. Blue arrows indicate the shoulder following SV.

References

Allan, J. F. (1986), Geology of the Northern Colima and Zacoalco Grabens, southwest Mexico: Late Cenozoic rifting in the Mexican Volcanic Belt, *Geol. Soc. Am. Bull.*, *97*, 473–485.

Atwater, T. (1989), Plate tectonic history of the northeast Pacific and western North America, in *The Eastern Pacific Ocean and Hawaii*, *The Geology of North America*, vol. N, edited by E. L. Winterer, D. M. Hussong, and R. W. Decker, pp. 21–72, GSA, Boulder, Colorado.

Bandy, W., C. Mortera-Gutierrez, J. Urrutia-Fucugauchi, and T. W. C. Hilde (1995), The subducted Rivera-Cocos plate boundary: Where is it, what is it, and what is its relationship to the Colima rift?, *Geophys. Res. Lett.*, *22*, 3075–3078.

Bandy, W. L., and T. W. C. Hilde (2000), Morphology and recent history of the ridge propagator system located at 18°N, 106°W, in *Cenozoic Tectonics and Volcanism of Mexico*, *Geol. Soc. Am. Spec. Pap.*, vol. 334, edited by H. Delgado-Granados, G. Aguirre-Díaz, and J. M. Stock, pp. 29–40, GSA, Boulder, Colorado.

Bandy, W. L., V. Kostoglodov, and C. A. Mortera-Gutiérrez (1998), Southwest migration of the instantaneous Rivera-Pacific euler pole since 0.78 Ma, *Geofís. Int.*, *37*, 153–169.

Bandy, W. L., T. W. C. Hilde, and C.-Y. Yan (2000), The Rivera-Cocos plate boundary: Implications for Rivera-Cocos relative motion and plate fragmentation, in *Cenozoic Tectonics and Volcanism of Mexico*, *Geol. Soc. Am. Spec. Pap.*, vol. 334, edited by H. Delgado-Granados, G. Aguirre-Díaz, and J. M. Stock, pp. 1–28, GSA, Boulder, Colorado.

Blatter, D. L., and L. Hammersley (2010), Impact of the Orozco Fracture Zone on the central Mexican Volcanic Belt, *J. Volcanol. Geotherm. Res.*, *197*, 67–84, doi:10.1016/j.volgeores.2009.08.002.

Blatter, D. L., G. L. Farmer, and I. S. E. Carmichael (2007), A North-South transect across the Central Mexican Volcanic Belt at ∼100°W: Spatial distribution, petrological, geochemical, and isotopic characteristics of Quaternary volcanism, *J. Petrol.*, *48*, 901–950, doi:10.1093/petrology/egm006.

Bourgois, J., and F. Michaud (1991), Active fragmentation of the North America plate at the Mexican triple junction area off Manzanillo, *Geo-Mar. Lett.*, *11*, 59–65.

Bourgois, J., and F. Michaud (2002), Comparison between the Chile and Mexico triple junction areas substantiates slab window development beneath northwestern Mexico during the past 12-10 Myr, *Earth Planet. Sci. Lett.*, *201*, 35–44.

Burbach, G. V., C. Frohlich, W. D. Pennington, and T. Matumoto (1984), Seismicity and tectonics of the subducted Cocos plate, *J. Geophys. Res.*, *89*, 7719–7735.

Burkett, E. R., and M. I. Billen (2010), Three-dimensionality of slab detachment due to ridge-trench collision: Laterally simultaneous boudinage versus tear propagation, *Geochem. Geophys. Geosyst.*, *11*, Q11012, doi:10.1029/2010GC003286.

Chung, W.-Y., and H. Kanamori (1978), Subduction process of a fracture zone and aseismic ridges the focal mechanism and source characteristics of the New Hebrides earthquake of 1969 January 19 and some related events, *Geophys. J. R. astr. Soc.*, *54*, 221–240.

Crotwell, H. P., T. J. Owens, and J. Ritsema (1999), The TauP Toolkit: Flexible seismic travel-time and ray-path utilities, *Seis. Res. Lett.*, *70*, 154–160.

DeMets, C., and S. Traylen (2000), Motion of the Rivera plate since 10 Ma relative to the Pacific and North American plates and the mantle, *Tectonophysics*, *318*, 119–159.

DeMets, C., and D. S. Wilson (1997), Relative motions of the Pacific, Rivera, North American, and Cocos plates since 0.78 Ma, *J. Geophys. Res.*, *102*, 2789–2806.

DeMets, C., R. G. Gordon, D. F. Argus, and S. Stein (1990), Current plate motions, *Geophys. J. Int.*, *101*, 425–478.

Dreger, D. S., and D. V. Helmberger (1993), Determination of source parameters at regional distances with three-component sparse network data, *J. Geophys. Res.*, *98*, 8107–8125.

Eissler, H., and H. Kanamori (1982), A large normal-fault earthquake at the junction of the Tonga trench and the Louisville ridge, *Phys. Earth Planet. Inter.*, *29*, 161–172.

Eissler, H. K., and K. C. McNally (1984), Seismicity and tectonics of the Rivera plate and implications for the 1932 Jalisco, Mexico, earthquake, *J. Geophys. Res.*, *89*, 4520–4530.

Ferrari, L. (2004), Slab detachment control on mafic volcanic pulse and mantle heterogeneity in central Mexico, *Geology*, *32*, 77–80, doi:10.1130/G19887.1.

Ferrari, L., G. Pasquaré, S. Venegas, D. Castillo, and F. Romero (1994), Regional tectonics of western Mexico and its implications for the northern boundary of the Jalisco block, *Geofís. Int.*, *33*, 139–151.

Franco, S. I., V. Kostoglodov, K. M. Larson, V. C. Manea, M. Manea, and J. A. Santiago (2005), Propagation of the 2001-2002 silent earthquake and interplate coupling in the Oaxaca subduction zone, Mexico, *Earth Planets Space*, *57*, 973–985.

Franke, D., M. Schnabel, S. Ladage, D. R. Tappin, S. Neben, Y. S. Djajadihardja, C. Muller, H. Kopp, and C. Gaedicke (2008), The great Sumatra-Andaman earthquakes - Imaging the boundary between the ruptures of the great 2004 and 2005 earthquakes, *Earth Planet. Sci. Lett.*, *269*, 118–130, doi:10.1016/j.epsl.2008.01.047.

Hall, C. E., and M. Gurnis (2005), Strength of fracture zones from their bathymetric and gravitational evolution, *J. Geophys. Res.*, *110*, B01402, doi:10.1029/2004JB003312.

Huchon, P., and J. Bourgois (1990), Subduction-induced fragmentation of the Nazca Plate off Peru: Mendana Fracture Zone and Trujillo Trough revisited, *J. Geophys. Res.*, *95*, 8419–8436.

Husker, A., and P. M. Davis (2009), Tomography and thermal state of the Cocos plate subduction beneath Mexico City, *J. Geophys. Res.*, *114*, B04306, doi:10.1029/2008JB006039.

Kim, Y., R. W. Clayton, and J. M. Jackson (2010), Geometry and seismic properties of the subducting Cocos plate in central Mexico, *J. Geophys. Res.*, *115*, B06310, doi:10.1029/2009JB006942.

Klitgord, K. D., and J. Mammerickx (1982), Northern East Pacific Rise: Magnetic anomaly and bathymetric framework, *J. Geophys. Res.*, *87*, 6725–6750.

Kostoglodov, V., and L. Ponce (1994), Relationship between subduction and seismicity in the Mexican part of the Middle America trench, *J. Geophys. Res.*, *99*, 729–742.

Lonsdale, P. (1991), Structural patterns of the Pacific floor offshore of peninsular California, in *The Gulf and Peninsular Province of the Californias*, *AAPG Memoir*, vol. 47, edited by J. P. Dauphin and B. R. T. Simoneit, pp. 87–125, AAPG, Tulsa, Oklahoma.

Lonsdale, P. (2005), Creation of the Cocos and Nazca plates by fission of the Farallon plate, *Tectonophysics*, *404*, 237–264, doi:10.1016/j.tecto.2005.05.011.

Lowrie, A., C. Smoot, and R. Batiza (1986), Are oceanic fracture zones locked and strong or weak?: New evidence for volcanic activity and weakness, *Geology*, *14*, 242–245.

Luhr, J. F., S. A. Nelson, J. F. Allan, and I. S. E. Carmichael (1985), Active rifting in southwestern Mexico: Manifestations of an incipient eastward spreading-ridge jump, *Geology*, *13*, 54–57.

Lynn, W. S., and B. T. R. Lewis (1976), Tectonic evolution of the northern Cocos plate, *Geology*, *4*, 718–722.

Mammerickx, J., and K. D. Klitgord (1982), Northern East Pacific Rise: Evolution from 25 m.y. B.P. to the present, *J. Geophys. Res.*, *87*, 6751–6759.

Manea, V., and M. Gurnis (2007), Subduction zone evolution and low viscosity wedges and channels, *Earth Planet. Sci. Lett.*, *264*, 22–45, doi:10.1016/j.epsl.2007.08.030.

Manea, V. C., M. Manea, V. Kostoglodov, C. A. Currie, and G. Sewell (2004), Thermal structure, coupling and metamorphism in the Mexican subduction zone beneath Guerrero, *Geophys. J. Int.*, *158*, 775–784, doi:10.1111/j.1365-246X.2004.02325.x.

McCann, W. R., and R. E. Habermann (1989), Morphologic and geologic effects of the subduction of bathymetric highs, *Pure Appl. Geophys.*, *129*, 41–69.

Menard, H. W. (1978), Fragmentation of the Farallon Plate by pivoting subduction, *J. Geology*, *86*, 99–110.

Nixon, G. T. (1982), The relationship between Quaternary volcanism in central Mexico and the seismicity and structure of subducted ocean lithosphere, *Geol. Soc. Am. Bull.*, *93*, 514–523.

Noriega-Manzanedo, F., and X. Pérez-Campos (2010), Comparación de catálogos sísmicos públicos para sismos mexicanos, *GEOS, Unión Geofísica Mexicana*, *30*(1), 165.

Pacheco, J. F., and S. K. Singh (2010), Seismicity and state of stress in Guerrero segment of the Mexican subduction zone, *J. Geophys. Res.*, *115*, B01303, doi:10.1029/2009JB006453.

Pardo, M., and G. Suárez (1995), Shape of the subducted Rivera and Cocos plates in southern Mexico: Seismic and tectonic implications, *J. Geophys. Res.*, *100*, 12,357–12,373.

Pérez-Campos, X., Y. Kim, A. Husker, P. M. Davis, R. W. Clayton, A. Iglesias, J. F. Pacheco, S. K. Singh, V. C. Manea, and M. Gurnis (2008), Horizontal subduction and truncation of the Cocos Plate beneath central Mexico, *Geophys. Res. Lett.*, *35*, L18303, doi:10.1029/2008GL035127.

Porritt, R. W., R. M. Allen, D. C. Boyarko, and M. R. Brudzinski (2011), Investigation of Cascadia segmentation with ambient noise tomography, *Earth Planet. Sci. Lett.*, *309*, 67–76, doi:10.1016/j.epsl.2011.06.026.

Ramírez-Herrera, M. T., V. Kostoglodov, and J. Urrutia-Fucugauchi (2011), Overview of recent coastal tectonic deformation in the Mexican subduction zone, *Pure Appl. Geophys.*, *168*, 1415–1433, doi:10.1007/s00024-010-0205-y.

Rosenbaum, G., M. Gasparon, F. P. Lucente, A. Peccerillo, and M. S. Miller (2008), Kinematics of slab tear faults during subduction segmentation and implications for Italian magmatism, *Tectonics*, *27*, TC2008, doi:10.1029/2007TC002143.

Russo, R. M., and P. G. Silver (1994), Trench-parallel flow beneath the Nazca plate from seismic anisotropy, *Science*, *263*, 1105–1111.

Schellart, W. P., J. Freeman, D. R. Stegman, L. Moresi, and D. May (2007), Evolution and diversity of subduction zones controlled by slab width, *Nature*, *446*, 308–311, doi:10.1038/nature05615.

Serrato-Díaz, G. S., W. L. Bandy, and C. A. Mortera-Gutiérrez (2004), Active rifting and crustal thinning along the Rivera-Cocos plate boundary as inferred from mantle bouguer gravity anomalies, *Geofís. Int.*, *43*, 361–381.

Sigloch, K. (2011), Mantle provinces under North America from multifrequency P wave tomography, *Geochem. Geophys. Geosyst.*, *12*, Q02W08, doi:10.1029/2010GC003421.

Sillitoe, R. H. (1974), Tectonic segmentation of the Andes: implications for magmatism and metallogeny, *Nature*, *250*, 542–545.

Singh, S. K., and M. Pardo (1993), Geometry of the Benioff zone and state of stress in the overriding plate in central Mexico, *Geophys. Res. Lett.*, *20*, 1483–1486.

Song, T. A., D. V. Helmberger, M. R. Brudzinski, R. W. Clayton, P. Davis, X. Pérez-Campos, and S. K. Singh (2009), Subducting slab ultra-slow velocity layer coincident with silent earthquakes in southern Mexico, *Science*, *324*, 502–506.

Soto, G. L., J. F. Ni, S. P. Grand, E. Sandvol, R. W. Valenzuela, M. G. Speziale, J. M. G. González, and T. D. Reyes (2009), Mantle flow in the Rivera-Cocos subduction zone, *Geophys. J. Int.*, *179*, 1004–1012, doi:10.1111/j.1365-246X.2009.04352.x.

Stock, J. M., and J. Lee (1994), Do microplates in subduction zones leave a geological record?, *Tectonics*, *13*, 1472–1487.

Stubailo, I., C. Beghein, and P. M. Davis (2012), Structure and anisotropy of the Mexico subduction zone based on Rayleigh-wave analysis and implications for the geometry of the Trans-Mexican Volcanic Belt, *J. Geophys. Res.*, *117*, B05303, doi:10.1029/2011JB008631.

Vogt, P. R., A. Lowrie, D. R. Bracey, and R. N. Hey (1976), *Subduction of Aseismic Oceanic Ridges: Effects on Shape, Seismicity, and Other Characteristics of Consuming Plate Boundaries*, *Geol. Soc. Am. Spec. Pap.*, vol. 172, GSA, Boulder, Colorado.

Wortel, R., and S. Cloetingh (1981), On the origin of the Cocos-Nazca spreading center, *Geology*, *9*, 425–430.

Wortel, R., and S. Cloetingh (1983), A mechanism for fragmentation of oceanic plates, in *Studies in Continental Margin Geology*, *AAPG Memoir*, vol. 34, edited by J. S. Watkins and C. L. Drake, pp. 793–801, AAPG, Tulsa, Oklahoma.

Yang, T., S. P. Grand, D. Wilson, M. Guzman-Speziale, J. M. Gomez-Gonzalez, T. Dominguez-Reyes, and J. Ni (2009), Seismic structure beneath the Rivera subduction zone from finite-frequency seismic tomography, *J. Geophys. Res.*, *114*, B01302, doi:10.1029/2008JB005830.

Chapter 3

Seismicity and structure in central Mexico: Evidence for a possible slab tear in the South Cocos plate

Originally published in:

Dougherty, S. L., and R. W. Clayton (2014), Seismicity and structure in central Mexico: Evidence for a possible slab tear in the South Cocos plate, *Journal of Geophysical Research*, *119*, 3424-3447, doi:10.1002/2013JB010883.

3.1 Abstract

The morphology of the transition from flat to normal subduction in eastern central Mexico is explored using intraslab earthquakes recorded by temporary and permanent regional seismic arrays. Observations of a sharp transition in slab dip near the abrupt end of the Trans Mexican Volcanic Belt (TMVB) suggest a possible slab tear located within the subducted South Cocos plate. The eastern lateral extent of a thin ultra-slow velocity layer (USL) imaged atop the Cocos slab in recent studies along the Meso America Subduction Experiment array is examined here using additional data. We find an end to this USL which is coincident with the western boundary of a zone of decreased seismicity and the end of the TMVB near the sharp transition in slab dip. Waveform modeling of the 2D structure in this region using a finite-difference algorithm provides constraints on the velocity and geometry of the slab's seismic structure and confirms the location of the USL. Analysis of intraslab seismicity patterns reveals clustering, sudden increase in depth, variable focal

mechanism orientations and faulting types, and alignment of source mechanisms along the sharp transition in slab dip. The seismicity and structural evidence suggests a possible tear in the S Cocos slab. This potential tear, together with the tear along the Orozco Fracture Zone to the northwest, indicates a slab rollback mechanism in which separate slab segments move independently, allowing for mantle flow between the segments.

3.2 Introduction

Slab tears are tectonically important morphological features of subducted plates that have been proposed to occur in numerous subduction zones. These tears can propagate horizontally, resulting in lateral slab detachment, or vertically, both of which produce observable gaps between slab segments. A slab tear can occur due to subduction of seafloor heterogeneities (e.g., *Bonnardot et al.*, 2009), a transition from subduction to strike-slip motion along the plate boundary (e.g., *Clark et al.*, 2008), along-strike changes in slab geometry (e.g., *Miller et al.*, 2004), lateral variation in slab rollback (e.g., *Govers and Wortel*, 2005), variable plate motion along strike (e.g., *Bandy et al.*, 2000), and/or a change in plate structure, temperature, and/or age (e.g., *Lonsdale*, 2005; *Burkett and Billen*, 2010). Locations where a slab tear has been suggested include Tonga (*Millen and Hamburger*, 1998; *Bonnardot et al.*, 2009), southern Izu-Bonin arc (*Miller et al.*, 2004), southern Mariana arc (*Fryer et al.*, 2003; *Miller et al.*, 2006), Costa Rica (*Johnston and Thorkelson*, 1997; *Abt et al.*, 2010), western central Mexico (*Dougherty et al.*, 2012; *Stubailo et al.*, 2012), Colombia (*Vargas and Mann*, 2013), Chile (*Cahill and Isacks*, 1992; *Pesicek et al.*, 2012), southern and northern Lesser Antilles (*ten Brink*, 2005; *Clark et al.*, 2008; *Meighan et al.*, 2013a), and the Mediterranean (*Wortel and Spakman*, 2000; *Gasparon et al.*, 2009; *Suckale et al.*, 2009) among others. The occurrence of a possible slab tear can be indicated by observations of seismic anisotropy from SKS splitting directions (e.g., *Peyton et al.*, 2001; *Soto et al.*, 2009), upper plate deformation (e.g., rifting) (e.g., *Yang et al.*, 2009; *Vargas and Mann*, 2013), abrupt changes in Wadati-Benioff zone seismicity (e.g., *Protti et al.*, 1994; *Dougherty et al.*, 2012), focal mechanism orientations (e.g., *Millen and Hamburger*, 1998; *Gutscher et al.*, 1999), seismicity patterns (e.g., clusters or gaps) (e.g., *Miller et al.*, 2004; *Meighan* *et al.*, 2013b), holes in tomographic images (e.g., *Miller et al.*, 2005; *Pesicek et al.*, 2012), and/or changes in arc volcanism (e.g., composition, orientation, and/or gap) (e.g., *Ferrari*, 2004; *Lin et al.*, 2004).

Tearing of the subducted oceanic lithosphere creates a gap in the plate through which asthenospheric mantle may flow, explaining both observed changes in seismic anisotropy and surface volcanism. The abrupt rotation of trench-parallel SKS fast directions to trench-perpendicular near a slab tear (or a circular pattern of anisotropy around a slab edge) indicate 3D toroidal flow of mantle material through the gap (*Peyton et al.*, 2001; *Kneller and van Keken*, 2008; *Zandt and Humphreys*, 2008) that has important implications for rollback of the subducted plate. A tear in the plate would short-cut the trench-parallel flow that occurs beneath the slab as it rolls back, providing a conduit for the transfer of material into the overlying mantle wedge (*Russo and Silver*, 1994; *Schellart*, 2004; *Jadamec and Billen*, 2010). The addition of this less dense asthenosphere to the wedge would also enhance rollback of the slab segment (*Schellart et al.*, 2007; *Soto et al.*, 2009). The upwelling of hot asthenospheric mantle to shallower depths also warms the mantle wedge, which may promote uplift, extension, and magmatism of the overriding plate (*Bandy et al.*, 1995; *Zandt and Humphreys*, 2008; *Nolet*, 2009; *Yang et al.*, 2009) or produce anomalous melting patterns at the slab edge (i.e., adakites) (*Yogodzinski et al.*, 2001). The Rivera-Cocos plate boundary in the Mexican subduction zone is an example locality where such a seismic anisotropy pattern indicative of toroidal flow is spatially coincident with observed rifting (i.e., Colima Graben and El Gordo Graben) and magmatism (i.e., Colima Volcano) in the overriding North American plate along a tomographically imaged gap between the two slabs (*Soto et al.*, 2009; *Yang et al.*, 2009). This tear between the plates was the result of the first fragmentation of the Cocos plate, when the Rivera plate separated from the proto-Cocos plate about 10 Ma (*Klitgord and Mammerickx*, 1982; *DeMets and Traylen*, 2000).

The transitions from flat to normal subduction of the Cocos plate that occur in western and eastern central Mexico are ideal locations for possible slab tear development. On the basis of structural modeling results and seismic and tectonic observations in the west, *Dougherty et al.* (2012) proposed that the Cocos slab is currently fragmenting into a North Cocos plate and a South Cocos plate along the projection of the Orozco Fracture Zone (OFZ) by a process analogous to that which occurred when the Rivera plate separated from the proto-Cocos plate. In the east, observations of a sharp transition in slab dip coupled with the abrupt end of the Trans Mexican Volcanic Belt (TMVB) suggest a second possible slab tear located within the subducted S Cocos plate. In order to test this hypothesis, we use regional earthquakes recorded by the Meso America Subduction Experiment (MASE) (*MASE*, 2007), Veracruz-Oaxaca (VEOX) (*VEOX*, 2010), Servicio Sismológico Nacional (SSN), and Oaxaca Network (OXNET) seismic arrays to study the fine-scale structure of the central Mexico subduction zone along the eastern transition from flat to normal subduction (Figure 3.1). We use observed waveform complexities to map the lateral extent of a thin ultra-slow velocity layer (USL) that was imaged atop the flat Cocos slab by the MASE array (*Pérez-Campos et al.*, 2008; *Song et al.*, 2009; *Kim et al.*, 2010) to test if the USL ends along a lineament related to the end of the TMVB or the sharp transition in slab dip. We also analyze seismicity patterns and focal mechanism orientations for any indications of fragmentation of the subducted plate. Additionally, we perform 1D and 2D waveform modeling to image the structure of the S Cocos slab and overriding plate in this region.

3.3 Tectonic Setting

The Cocos plate is subducting beneath the North American plate along the Middle America Trench (MAT) in central Mexico with convergence rate and plate age (11–23 Ma) increasing towards the east. This young oceanic plate exhibits large lateral variations in slab dip, with a shallow subhorizontal segment bounded by segments that dip much more steeply: ∼50° near the Rivera-Cocos plate boundary and ∼30° near the Isthmus of Tehuantepec (*Pardo and Suárez*, 1995). Receiver functions and seismic velocity tomography along the MASE array show that the subducted Cocos plate is horizontal for about 250 km beneath the North American plate in the Guerrero region, before transitioning to a much steeper dip of 75° at the southern margin of the TMVB and truncating at a depth of 500 km (*Pérez-Campos et al.*, 2008; *Husker and Davis*, 2009; *Kim et al.*, 2010). Along the transition from flat to normal subduction to the west of this region, waveform modeling and

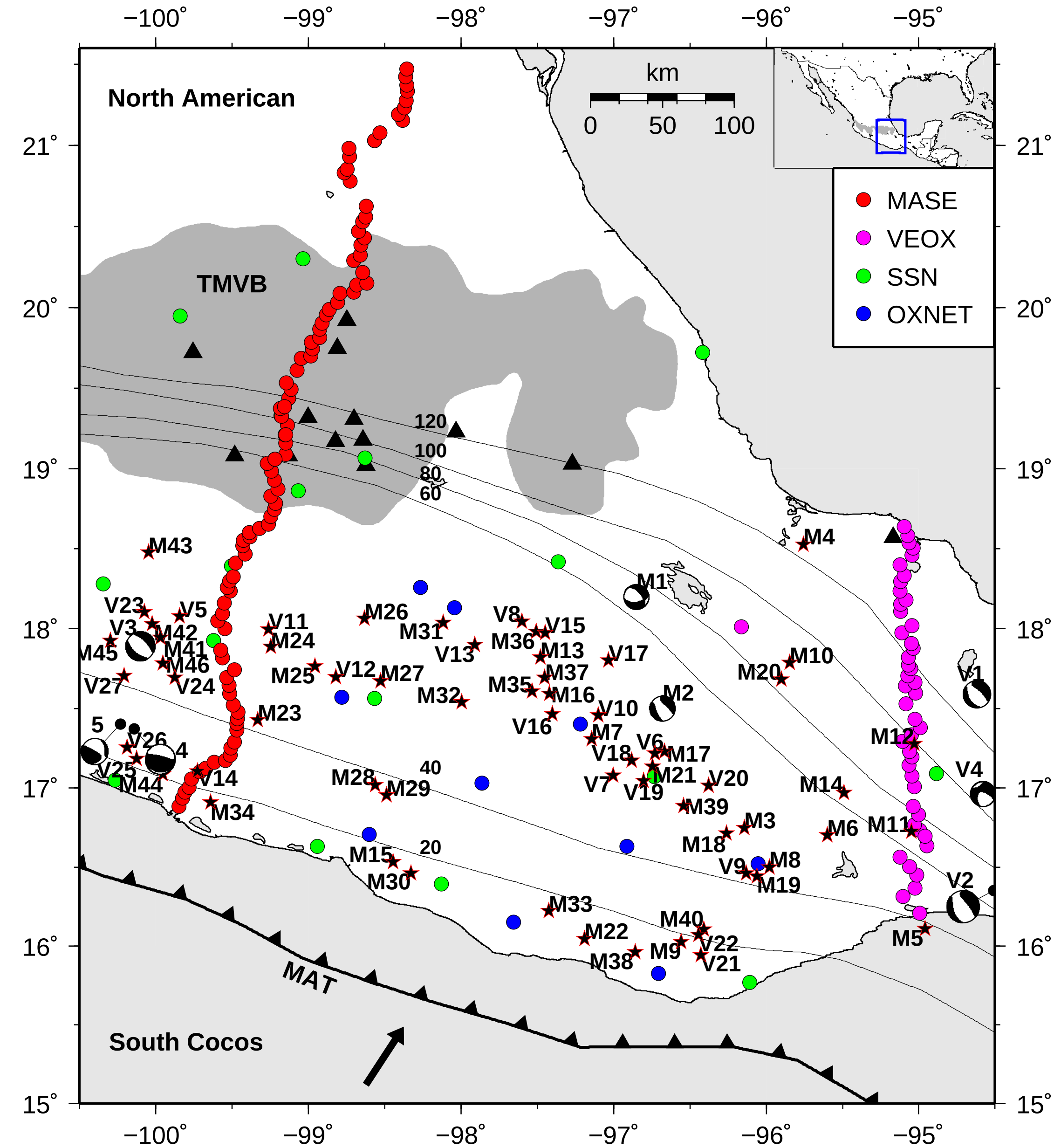

Figure 3.1: Map showing the locations of MASE, VEOX, SSN, and OXNET stations along with events (stars, focal mechanisms) used in this study. Event labels indicate whether the earthquake occurred during the MASE (M) or VEOX (V) array deployment. Focal mechanisms are from the Global CMT catalog (Table 3.1). The dark grey shaded area indicates the Trans Mexican Volcanic Belt (TMVB), and the black triangles denote active volcanoes. Slab isodepth contours based on local seismicity and teleseismic receiver functions (*Pérez-Campos et al.*, 2008; *Kim et al.*, 2010, 2011; *Melgar and Pérez-Campos*, 2011) are shown in thin lines. The convergence direction of the South Cocos plate near the Middle America Trench (MAT) is indicated by the black arrow (*DeMets et al.*, 2010). See Figure 3.16 of the auxiliary material for station names.

seismic anisotropy analysis suggest a tear in the Cocos slab along the landward projection of the OFZ (*Dougherty et al.*, 2012; *Stubailo et al.*, 2012). This tear is proposed to indicate ongoing fragmentation of the Cocos slab into N Cocos and S Cocos plates, respectively (*Dougherty et al.*, 2012).

The along-strike variation in slab dip is evident in the $\sim$16° oblique to the trench orientation of the TMVB, unlike volcanic arcs in most other subduction zones which are oriented trench-parallel. The TMVB is comprised of nearly 8000 volcanic structures, including large stratovolcanoes, monogenetic cones, shield volcanoes, calderas, lava flows, and domes (*Macías*, 2007), covering a region about 1000 km long and 80–230 km wide (*Gómez-Tuena et al.*, 2007). Trenchward migration of the volcanic front since the late Miocene suggests ongoing rollback of the slab (*Ferrari et al.*, 2011). In the east, the TMVB abruptly ends near the Gulf of Mexico, accompanied by a steep topographic gradient between the high peaks of large stratovolcanoes and the coastal Veracruz Basin (Figure 3.2a). Post-10 Ma volcanism in the region between the eastern end of the TMVB and the Central America arc is discontinuous, including only a few isolated volcanic features, such as the Los Tuxtlas Volcanic Field (LTVF) near the Gulf of Mexico coast (Figure 2a) (*Ferrari et al.*, 2011). LTVF volcanism began $\sim$7 Ma, but the mechanisms of its origin are unclear (e.g., *Nelson et al.*, 1995; *Ferrari et al.*, 2005; *Verma*, 2006). If the S Cocos slab is projected beneath the LTVF it would lie at $\sim$250 km depth, or deeper if truncated as suggested by observations of a southward-dipping Yucatán slab (*Kim et al.*, 2011; *Chen and Clayton*, 2012). This truncation at $\sim$120–150 km depth constricts flow in the mantle wedge for both systems and may explain the unusual configuration of arc volcanism in the region (*Kim et al.*, 2011; *Chen and Clayton*, 2012).

In the oceanic domain, the S Cocos plate morphology is characterized by several tectonic structures, such as fracture zones, seamounts, and faults. Linear zones of weakness in the oceanic plate will be discussed in section 3.5. The O'Gorman Fracture Zone (OGFZ) intersects the MAT off the coast of Oaxaca (*Singh and Mortera*, 1991) and has been suggested to be the remnant of a small offset of spreading segments of the short-lived Mathematician ridge (*Mammerickx and Klitgord*, 1982) that is identified as a deep trough (*Klitgord and Mammerickx*, 1982). Other studies of the OGFZ

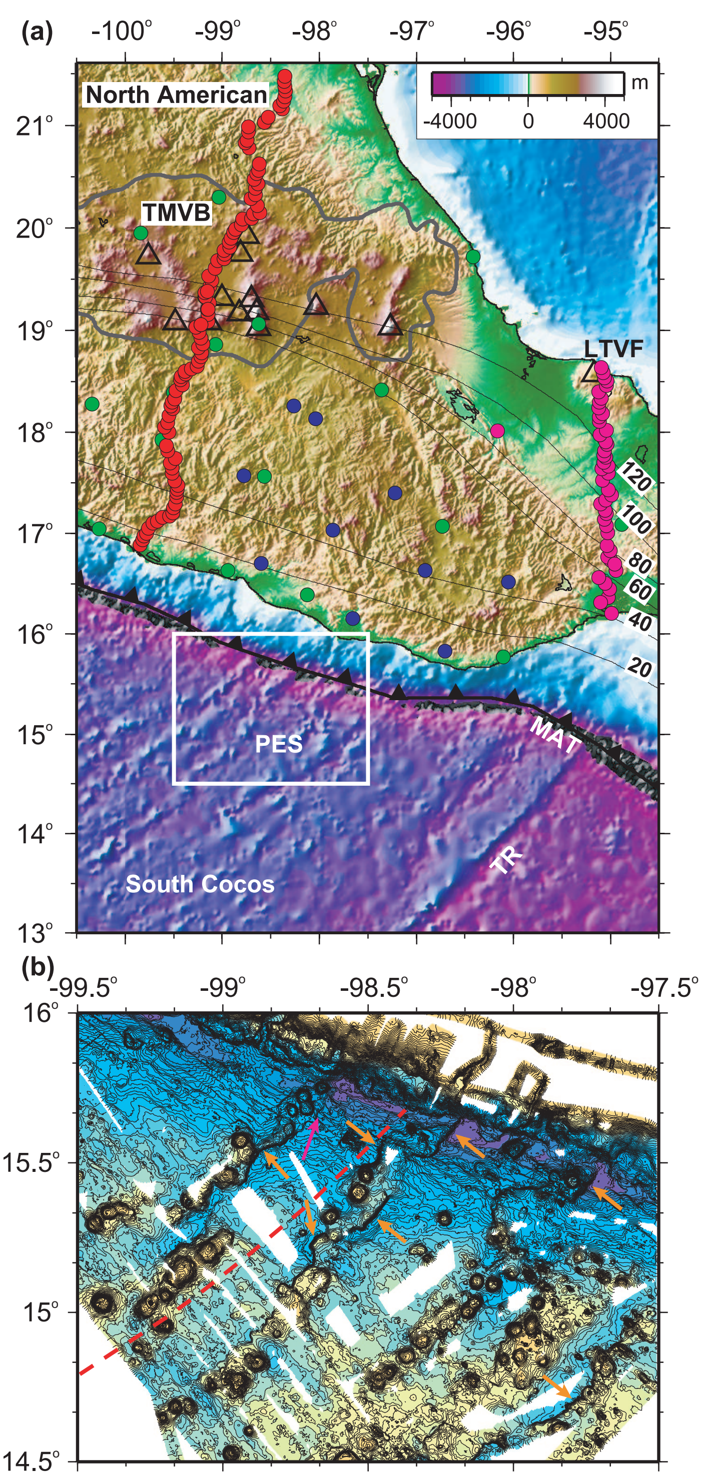

Figure 3.2: (a) Topographic-bathymetric map illustrating the abrupt end of the TMVB (outlined in grey) with a steep gradient in elevation and the interruption of arc volcanism. The locations of Los Tuxtlas Volcanic Field (LTVF) and the Puerto Escondido seamounts (PES) (*Kanjorski*, 2003) are indicated. Station locations are as in Figure 3.1 and open triangles denote active volcanoes. The Tehuantepec Ridge (TR) is also shown. (b) Enlarged bathymetric map of the region outlined by a white box in (a) showing lines of seamounts entering the MAT (dark blue region oriented NW-SE) (modified from *Kanjorski* (2003)). Large seamounts can be seen to enter the trench unbroken (pink arrow). Examples of seamount-parallel faulting are indicated by orange arrows. The previously identified location of the O'Gorman Fracture Zone is also shown (red dashed line).

in the vicinity of the East Pacific Rise argue that it is not a fracture zone at all, but simply a chain of seamounts that extends 50–200 km from the ridge axis (*Batiza et al.*, 1989; *McClain and Wright*, 1990). This is in agreement with *Kanjorski* (2003)'s finding that no OGFZ exists at the MAT, based on the lack of significant age offsets across the proposed fracture zone. Rather, *Kanjorski* (2003) identified several parallel ridges composed of small-to-medium-sized (up to ∼20 km diameter and 1700 m high) seamounts created as off-axis volcanism entering the MAT in this region, with the larger seamounts remaining physically intact throughout the subduction process (Figure 3.2b). Included in this zone is the Puerto Escondido seamount cluster, a broad volcanic feature littered with >100 volcanic cones and accompanying lava flows (Figure 3.2) (*Kanjorski*, 2003). Observed seamount-parallel normal faulting (Figure 3.2b) is shown to be seismically active (*Kanjorski*, 2003).

3.4 Data Analysis

3.4.1 Data

The seismic data used in this study were recorded by the MASE, VEOX, SSN, and OXNET arrays. The MASE array consisted of 100 broadband seismic instruments deployed from January 2005 to June 2007 in a trench-perpendicular line in the Guerrero region with a station spacing of ∼5 km (Figure 3.1). Across the Isthmus of Tehuantepec, the 45 broadband seismometers of the VEOX array were deployed in a 300-km-long line from August 2007 to March 2009 (Figure 3.1). The goal of these experiments was to image the structure of the Mexican subduction zone in the flat slab and normal dipping regions, respectively. The permanent SSN array consists of 37 broadband seismic instruments located throughout Mexico, of which, 16 are utilized in this study (Figure 3.1). In the Oaxaca region, located between the MASE and VEOX arrays, 10 broadband seismometers were installed in a 2D geometry in 2006 as part of the OXNET array (Figure 3.1) in an effort to detect and monitor non-volcanic tremor and microseismicity signals in this region (*Brudzinski et al.*, 2010). A map of the station names for all four arrays is shown in Figure 3.16 of the auxiliary material.

We analyze seismograms from 75 regional intraslab earthquakes recorded by these arrays. These events have magnitudes within the range of 3.8 to 6.5 and occur at depths between 30 km and 149 km (Table 3.1). The locations of these events are shown in Figure 3.1. Earthquakes that occurred during the MASE deployment have identifiers that begin with 'M', while those that occurred during the VEOX deployment begin with 'V' (Figure 3.1, Table 3.1). Events 4 and 5 were also part of the *Dougherty et al.* (2012) dataset, so their identifiers have been maintained for clarity. Note that both of these events occurred during the MASE deployment (Table 3.1).

Table 3.1. Events used in eastern central Mexico and their source parameters.

Event ID	Date	Lat (°)	Lon (°)	Depth (km)	Mag (M_w)	Mechanism Strike/Dip/Rake	Source[a]
4	2007/04/13	17.37	-100.14	39	5.99	279/42/86	1[b]
				43	6.0	284/73/92	2
				41	5.9	303/79/98	3
				20	5.7	267/61/85	4
5	2007/04/13	17.40	-100.23	30	5.30	70/41/2	1[b]
				67	5.3	28/29/0	2
				36	5.3	39/17/6	3
				35	5.3	117/84/-101	4
M1	2005/09/24	18.20	-96.85	68	5.17	316/64/-66	1[b]
				61	5.0	320/56/-46	2
				104	5.1	329/57/-42	3
M2	2007/05/04	17.50	-96.68	59	5.08	139/32/-75	1[b]
				60	5.0	176/46/-46	2
				70	5.0	192/51/-40	3
M3	2007/02/14	16.749	-96.142	67	4.71	9/70/-58	1[c]
				81	4.7	327/66/-65	3
M4	2005/11/14	18.528	-95.757	64	4.81	335/50/-60	1[c]
				28	4.4	320/34/-77	3
M5	2006/01/26	16.111	-94.957	82	4.73	255/71/-62	1[c]
M6	2007/06/02	16.701	-95.600	80	4.74	9/47/46	1[c]
M7	2005/09/08	17.306	-97.145	70	4.82	345/35/4	1[c]
M8	2005/09/29	16.500	-95.980	67	4.36	246/61/-49	1[c]
				76	4.2	174/24/10	3
M9	2006/11/08	16.027	-96.558	43	5.23	348/36/-44	1[c]
				38	5.1	352/35/-44	2
				45	4.9	288/85/98	3
M10	2006/03/17	17.786	-95.844	124	4.52	204/16/-43	1[c]
M11	2005/12/17	16.725	-95.048	99	4.73	180/71/-84	1[c]
M12	2007/03/01	17.279	-95.029	142	4.70	45/67/-20	1[c]
M13	2005/09/07	17.820	-97.480	72	4.20	149/50/-64	1[c]
M14	2006/02/22	16.969	-95.489	123	4.53	121/64/-1	1[c]
M15	2005/06/06	16.534	-98.444	59	4.42	281/45/-40	1[c]
M16	2006/09/18	17.593	-97.422	69	4.35	140/31/51	1[c]
M17	2006/06/08	17.228	-96.666	86	4.45	328/78/-26	1[c]
M18	2005/12/22	16.713	-96.259	84	4.50	350/43/-81	1[c]
M19	2006/12/21	16.443	-96.060	77	5.25	36/19/-5	1[c]
M20	2006/02/09	17.684	-95.901	104	4.62	226/56/-86	1[c]
M21	2006/01/19	17.134	-96.743	55	4.60	146/81/5	1[c]

Table 3.1. (continued).

Event ID	Date	Lat (°)	Lon (°)	Depth (km)	Mag (M_w)	Mechanism Strike/Dip/Rake	Source[a]
M22	2005/11/01	16.044	-97.192	54	4.28	70/59/-60	1[c]
M23	2005/05/20	17.428	-99.330	38	4.39	195/48/74	1[c]
M24	2006/09/01	17.888	-99.244	61	4.54	74/64/-44	1[c]
M25	2006/09/22	17.763	-98.958	45	4.43	298/47/21	1[c]
M26	2006/09/07	18.064	-98.633	56	4.15	113/65/36	1[c]
M27	2006/11/12	17.673	-98.528	64	4.44	331/70/-72	1[c]
M28	2005/10/03	17.020	-98.561	35	4.05	350/69/-41	1[c]
M29	2006/11/30	16.954	-98.488	56	4.28	198/84/47	1[c]
M30	2005/06/06	16.461	-98.327	54	4.34	279/81/6	1[c]
M31	2006/06/09	18.038	-98.117	57	4.23	290/87/53	1[c]
M32	2006/07/24	17.539	-97.995	70	4.27	132/67/-20	1[c]
M33	2006/11/28	16.223	-97.426	59	4.06	241/51/-75	1[c]
M34	2007/01/02	16.910	-99.640	45	4.62	345/75/69	1[c]
M35	2005/02/11	17.607	-97.534	54	4.38	36/43/-22	1[c]
M36	2007/02/09	17.981	-97.505	79	3.90	70/50/-60	1[c]
M37	2007/06/05	17.694	-97.453	70	4.26	10/44/-31	1[c]
M38	2006/03/12	15.962	-96.859	54	4.35	83/61/-57	1[c]
M39	2006/03/22	16.886	-96.541	63	4.38	350/54/-87	1[c]
M40	2006/11/08	16.106	-96.409	52	4.30	99/44/60	1[c]
M41	2005/05/26	17.946	-99.970	53	5.00	13/61/-60	1[c]
				62	4.8	296/41/-80	3
				50	4.6	289/34/-76	4
M42	2006/06/26	18.032	-100.023	51	4.65	345/58/-28	1[c]
				50	4.3	293/35/-79	4
M43	2007/05/28	18.478	-100.046	52	4.45	217/76/-83	1[c]
M44	2007/06/18	17.086	-99.953	42	4.21	57/40/18	1[c]
M45	2005/11/21	17.925	-100.295	56	4.19	26/76/26	1[c]
M46	2005/04/30	17.784	-99.952	77	4.45	16/61/-40	1[c]
V1	2007/09/15	17.59	-94.62	149	5.44	308/65/-85	1[b]
				144	5.4	309/61/-108	2
V2	2008/02/12	16.35	-94.51	86	6.52	155/42/-81	1[b]
				87	6.5	178/35/-54	2
V3	2008/04/28	17.89	-100.10	64	5.80	175/54/-51	1[b]
				56	5.8	129/42/-96	2
				52	5.8	131/46/-97	3
				50	5.4	138/40/-88	4
V4	2009/02/18	16.96	-94.58	117	4.99	174/41/-55	1[b]
				121	4.9	193/54/-22	2
V5	2007/10/12	18.078	-99.845	52	4.13	256/68/-3	1[c]
V6	2007/12/13	17.218	-96.728	80	4.57	210/74/-58	1[c]
V7	2008/12/15	17.078	-97.004	69	4.38	209/54/-46	1[c]
				65	4.4	154/43/-82	3
V8	2009/01/27	18.047	-97.602	66	4.28	20/40/-49	1[c]
V9	2007/11/04	16.460	-96.131	75	4.47	56/61/25	1[c]
V10	2007/11/12	17.457	-97.102	66	4.37	209/63/-29	1[c]
V11	2008/08/21	17.996	-99.263	50	4.31	8/22/-49	1[c]
V12	2008/03/08	17.699	-98.819	42	4.46	298/75/69	1[c]
V13	2008/04/05	17.899	-97.909	61	4.17	341/67/39	1[c]
				54	4.0	310/46/-78	3
V14	2007/08/18	17.106	-99.725	78	4.48	110/60/-16	1[c]
V15	2008/07/18	17.976	-97.447	57	4.21	7/36/-25	1[c]

Table 3.1. (continued).

Event ID	Date	Lat (°)	Lon (°)	Depth (km)	Mag (M_w)	Mechanism Strike/Dip/Rake	Source[a]
V16	2008/12/11	17.466	-97.402	56	4.15	196/40/-61	1[c]
V17	2008/03/18	17.802	-97.032	90	4.49	195/86/-73	1[c]
V18	2007/11/28	17.174	-96.881	83	3.96	190/65/-70	1[c]
V19	2008/06/01	17.046	-96.805	50	3.80	134/61/-79	1[c]
V20	2008/01/09	17.016	-96.377	79	4.25	11/84/19	1[c]
V21	2009/02/02	15.944	-96.429	47	4.13	180/41/7	1[c]
V22	2008/06/20	16.071	-96.442	49	4.10	230/55/-85	1[c]
V23	2009/01/14	18.104	-100.073	46	4.40	120/41/-80	1[c]
				46	4.3	129/49/-100	3
V24	2008/05/18	17.694	-99.874	73	4.36	191/70/-25	1[c]
V25	2008/10/08	17.184	-100.126	47	4.26	188/81/19	1[c]
V26	2009/02/01	17.253	-100.189	36	3.91	312/76/59	1[c]
V27	2008/02/23	17.703	-100.208	63	4.38	175/85/-56	1[c]

[a]Sources are 1) focal mechanism, M_w, and depth from this study; 2) focal mechanism, M_w, and depth from the Global CMT (GCMT) catalog (*Dziewonski et al.*, 1981; *Ekström et al.*, 2012); 3) focal mechanism, M_w, and depth from the Servicio Sismológico Nacional (SSN) catalog; 4) focal mechanism, M_w, and depth from *Pacheco and Singh* (2010).
[b]Location from GCMT catalog.
[c]Location from SSN catalog.

3.4.2 Slab Dip

The lateral variation in slab dip across the transition from flat to normal subduction in eastern central Mexico is examined in detail to assess if this change in geometry is accommodated by a smooth contortion of the slab or if there is an abrupt transition which could be indicative of a possible tear. Epicenters for earthquakes from the January 2001–May 2011 event catalog of the SSN are mapped and divided into twenty-one 25-km-wide trench-normal bins (Figure 3.3a). The locations of events furnished by the SSN have been carefully revised by an analyst, and the accuracy of the catalog is confirmed by a relocation study (*Alberto*, 2010). Bin 1 overlies the flat slab region located along the MASE array and bin 21 overlies the normal dipping region across the VEOX array (Figure 3.3a). Cross-sections of the seismicity in each bin illustrate variations in the Wadati-Benioff zone across the region and are used to estimate the slab dip in each bin. Examples from bins 2, 13, and 14 are shown in Figure 3.3b-d. The dip angle is estimated by visually selecting hypocenter locations that are downdip of the trench and not within the overriding plate (as defined by teleseismic receiver

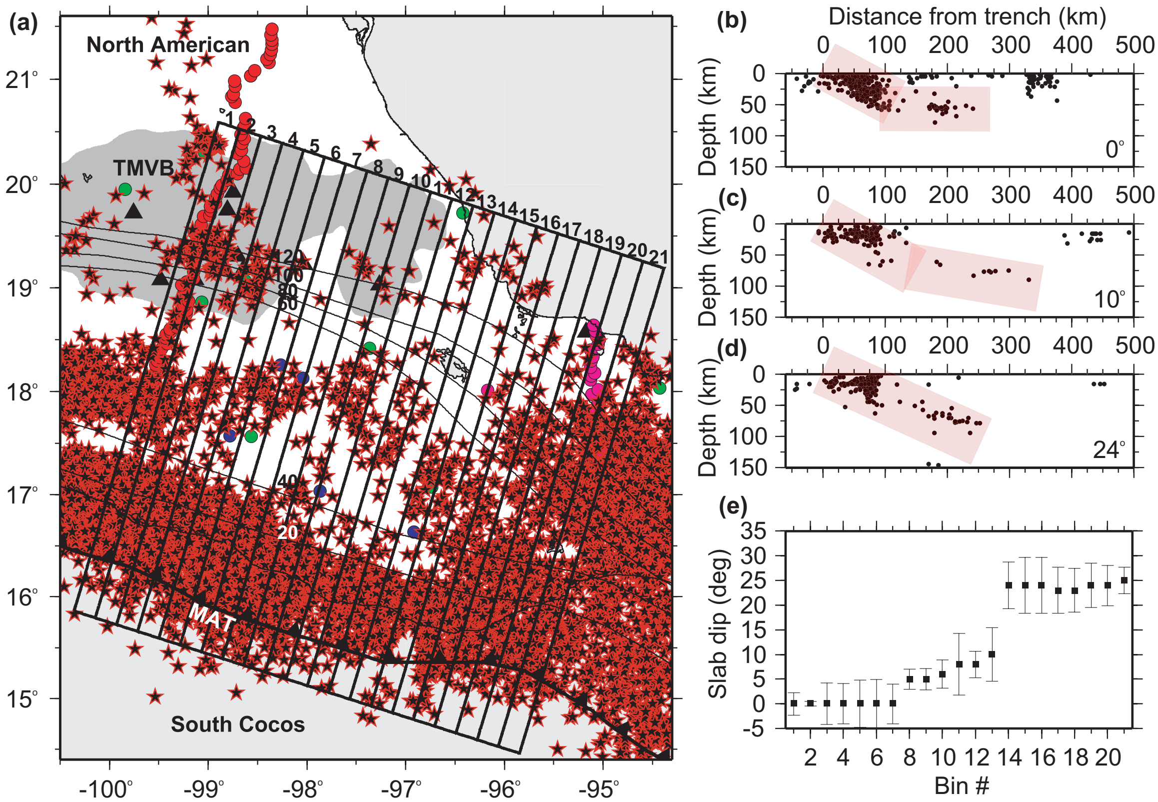

Figure 3.3: Seismicity and slab dip across the transition from flat to normal subduction located to the east of the MASE array. (a) Map showing epicenters (stars) for earthquakes from the 1/2001–5/2011 SSN event catalog. Data in twenty-one 25-km-wide bins roughly perpendicular to the MAT are analyzed for changes in slab dip across this region. Cross-sections of seismicity in bins (b) 2, (c) 13, and (d) 14 are shown along with their respective estimated slab dips. Note the significant change in slab dip between bins 13 and 14. (e) Plot of slab dip across the data bins. Error bars are weighted by the number of events in each bin, such that fewer events produces a larger error.

functions (*Pérez-Campos et al.*, 2008; *Kim et al.*, 2010, 2011; *Melgar and Pérez-Campos*, 2011)), and then performing a linear regression of the selected locations. The estimated slab dip in each of the twenty-one bins is shown in Figure 3.3e. The errors on these dip estimates (calculated from the standard deviation in dip) are weighted by the number of earthquakes in each bin, such that fewer events in a bin produces a larger error, with values ranging from ±0.49° (bin 2) to ±6.3° (bin 11). The slab is flat beneath the MASE array with its dip gradually increasing across the easternmost TMVB region to 10° by bin 13 (Figure 3.3). Between bins 13 and 14, there is a sharp 14° increase in slab dip, followed by an approximately constant dip (23–25°) across the remainder of the bins to the east (Figure 3.3).

3.4.3 Ultra-slow Velocity Layer

The USL that was imaged atop the flat Cocos slab beneath the MASE array is a 3–5-km-thick layer with a V_P of 5.4–6.2 km/s and a V_S of 2.0–3.4 km/s (*Song et al.*, 2009; *Kim et al.*, 2010). The exact nature of the USL is not known, but its anomalously low shear wave velocity suggests a relationship with fluids, specifically free water or hydrous minerals, in the subduction zone. *Song et al.* (2009) proposed that the USL represents a fluid-saturated portion of the oceanic crust, forming a high pore fluid pressure (HPFP) layer that is sealed by some low permeability layer, such as fine-grained blueschist, directly above it. In their thermal modeling of the central Mexico subduction zone, *Manea et al.* (2004) found a high pore pressure ratio of 0.98 along the subduction interface, consistent with *Song et al.* (2009)'s HPFP layer. *Kim et al.* (2010), on the other hand, proposed that the USL is upper oceanic crust that is highly heterogeneous and composed of mechanically weak hydrous minerals (talc) that might be under high pore pressure. With or without free fluid, *Kim et al.* (2013) demonstrate that a talc-rich ultramafic layer is required to explain the observed USL velocities and suggest that this talc originates from the mantle wedge during the slab flattening process. Similarly, *Manea et al.* (2013) propose that the USL represents a remnant of mantle wedge that experienced significant serpentinization since the slab flattened. The hydrous minerals and/or high pore pressure of the USL can explain the observed decoupling of the flat slab from the overriding plate, as evidenced by the lack of compressional seismicity in the North American plate (*Singh and Pardo*, 1993) and GPS observations (*Franco et al.*, 2005), and may be responsible for the flat subduction geometry, shown to be facilitated and sustained by such a low strength layer (*Manea and Gurnis*, 2007; *Kim et al.*, 2010).

The presence of the USL atop the S Cocos slab is identified by the existence of complex P waveforms (*Song et al.*, 2009) recorded by the MASE or VEOX, SSN, and OXNET arrays. As described by *Dougherty et al.* (2012), these complex P waveforms consist of three locally converted S-to-P phases (A, B, C) that arrive within 4 sec after the P-wave (Figure 3.4). Phase A converts at the bottom of the USL and appears as a negative pulse at local stations. Phase B arrives immediately after phase A as a positive pulse, indicative of an S-to-P wave that converted at the top of the USL.

Phase C converts at the base of the high velocity layer, arriving before phase A and ∼1.0–1.5 sec after the direct P-wave. These three phases are searched for in the seismograms of the intraslab earthquakes analyzed in this study. P waveforms in these seismograms are categorized as complex, possibly complex, or simple based on the existence or absence and nature of phases A, B, and C. Examples of these waveforms from event M2 recorded at MASE, SSN, and OXNET stations are shown in Figure 3.4. The waveforms have been bandpass filtered to 0.01–0.6 Hz, with the shorter periods in the frequency band allowing for the identification of the three S-to-P phases. When all three of the phases are readily observed, the waveform is deemed complex. If one of the phases is not easily identified due to an uncharacteristic pulse shape and/or amplitude, but the other two phases are clearly visible, then the waveform is possibly complex. Simple waveforms lack the shoulder in the direct P pulse representative of the C phase and also have uncharacteristically shaped and/or low amplitude A and B phases, indicating that there is no USL present.

The eastern lateral extent of the USL is mapped by examining the status of the layer at each epicentral event location (Figure 3.5). We identify ten events which indicate the presence of the USL from their P waveforms. Another 28 events possibly indicate the presence of the USL. The remaining 37 events in our dataset indicate that no USL is present at their locations. An enlarged USL status map that includes event labels can be found in Figure 3.17. In general, the events which suggest (or possibly suggest) the occurrence of the USL are concentrated in the western portion of the study region, south of the TMVB, while those that suggest the USL is lacking are concentrated in the east, where the slab dip increases. A handful of possible USL locations overlap the predominantly no USL region near the location of the sharp transition in slab dip, marked by the boundary between bins 13 and 14 of Figure 3.3a (Figure 3.5). Concentrating on the area east of the MASE array, we draw shaded contours of the USL, possible USL, and no USL zones for clarity of observation (Figure 3.5). Note that the boundary between the USL and no USL zones is approximately coincident with the eastern end of the TMVB along a trench-normal transect.

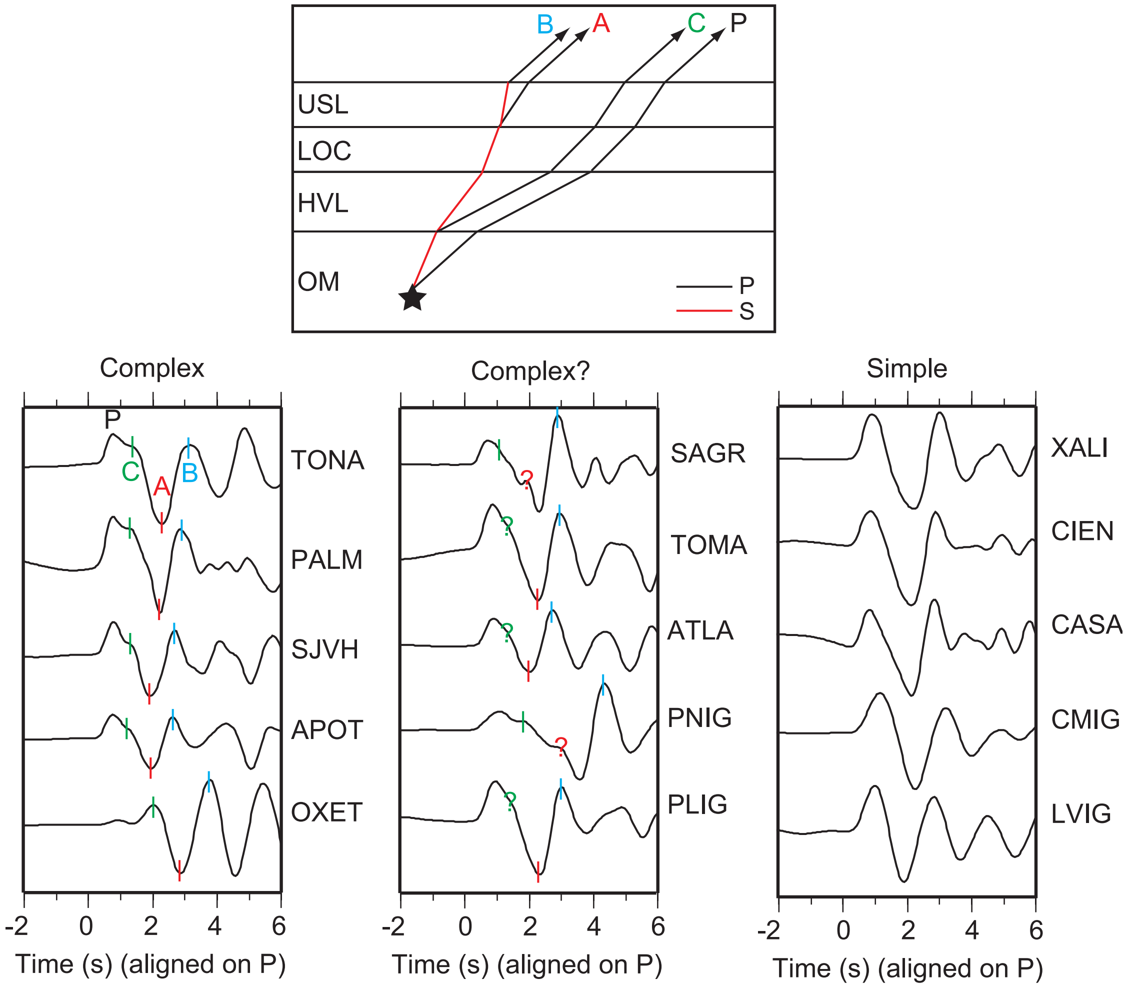

Figure 3.4: (top) Schematic illustrating the raypaths of the P-wave and the three S-to-P phases (A, B, C) that comprise the complex P waveform. Abbreviations are USL, ultra-slow velocity layer; LOC, lower oceanic crust; HVL, high velocity layer; OM, oceanic mantle. (bottom) Examples of (left) complex, (middle) possibly complex, and (right) simple P waveforms from event M2 recorded on the vertical component by MASE, SSN, and OXNET stations and filtered to 0.01–0.6 Hz. S-to-P phases A, B, and C are indicated by red, blue, and green tick marks, respectively. All three of these phases are visible in the complex waveforms within 4 sec of the P-wave. Question marks on the possibly complex waveforms indicate a phase that is not easily identified due to an uncharacteristic pulse shape and/or amplitude. Simple waveforms lack the shoulder in the direct P pulse indicative of the C phase and also have uncharacteristically shaped and/or low amplitude A and B phases, indicating there is no USL present. Modified from *Dougherty et al.* (2012).

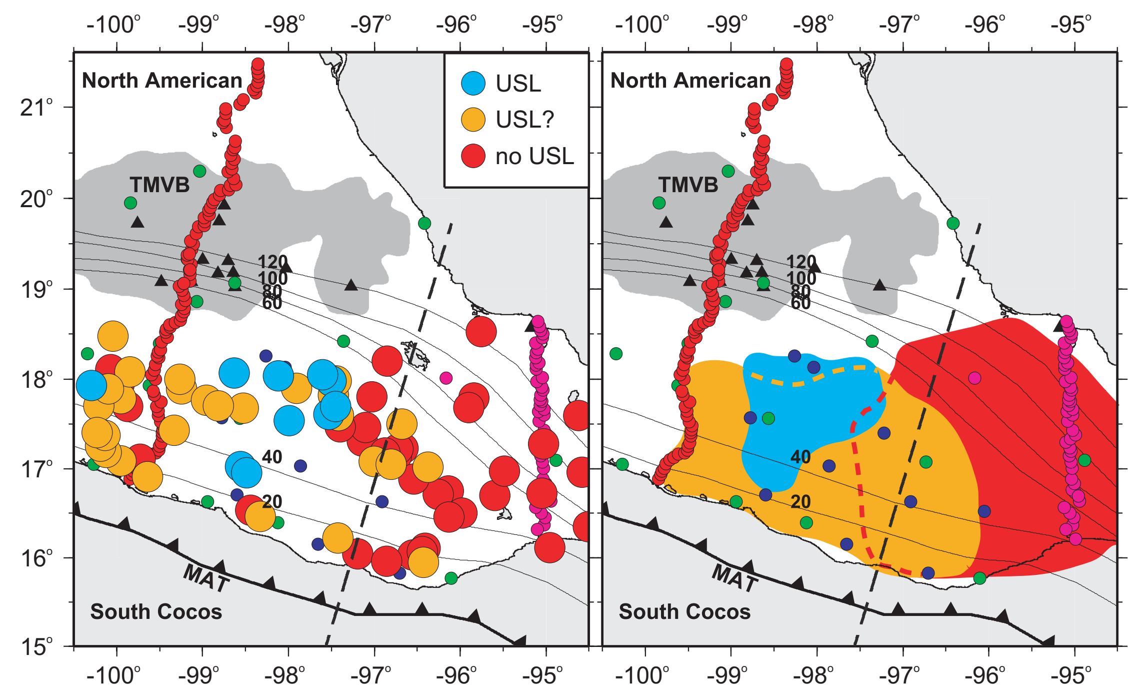

Figure 3.5: Mapping the eastern lateral extent of the USL using MASE, VEOX, SSN, and OXNET P waveforms. (left) Events which indicate the presence of the USL are shown in cyan. Those which possibly indicate the USL is present are shown in orange. Red events indicate no USL is present. See Figure 3.17 of the auxiliary material for enlarged map including event labels. (right) Shaded contours of USL, possible USL, and no USL zones. The boundary between bins 13 and 14 of Figure 3.3, demarking the significant change in slab dip, is denoted by the black dashed line.

3.4.4 Seismicity

Intraslab seismicity across the study region is analyzed for any changes, gaps, or patterns that could elucidate the nature of the transition from flat to normal subduction of the S Cocos plate. Epicentral locations of 40–80-km-depth earthquakes from the 1960–2012 International Seismological Centre (ISC) Bulletin event catalog (*International Seismological Centre*, 2011) are mapped and divided into the same twenty-one 25-km-wide bins used to estimate the lateral variation in slab dip (Figure 3.6). Examination of the number of earthquakes in each bin, in conjunction with the event map, reveals a ~75-km-wide zone of decreased intraslab seismicity (bins 11-13), which is indicative of a structural change, located immediately west of the sharp transition in slab dip. The western limit of this decreased seismicity zone encompasses the easternmost tip of the TMVB. While the three bins that comprise this zone each contain a low number of earthquakes, the spatial distribution of the seismicity in bins 12 and 13 is noticeably sparser than that in bin 11 (Figure 3.6). In particular, downdip seismicity in bins 12 and 13 is concentrated near 97.25°W, 17.25°N, extending linearly to the northeast, with gaps in the seismicity observed along either side. Additionally, seismicity updip is concentrated in a small area between the coast and the 20-km isodepth contour. This scattered distribution suggests that the events in these bins may be occurring in clusters.

The broadscale distribution of intraslab seismicity west of the VEOX array can be described by two overall trends: (1) a WNW-ESE oriented band along the coast; (2) an E-W oriented downdip zone that rotates to a NW-SE orientation at the eastern end of the TMVB (Figure 3.6a). The downdip zone is spatially offset from the coastal band by a seismicity gap that increases in width from west to east. At the point of rotation in the downdip zone orientation, a general increase in the depth of the intraslab seismicity can be observed. Coincidentally, the coastal band exhibits decreased seismicity.

Focal mechanisms of intraslab earthquakes in eastern central Mexico are also examined for details of the S Cocos slab structure. Source mechanisms of 40–170-km-depth events from the January 1976–November 2012 Global Centroid Moment Tensor (GCMT) catalog (*Dziewonski et al.*, 1981; *Ekström et al.*, 2012) and the January 2000–November 2012 SSN CMT catalog are mapped in Figure 3.7a. For

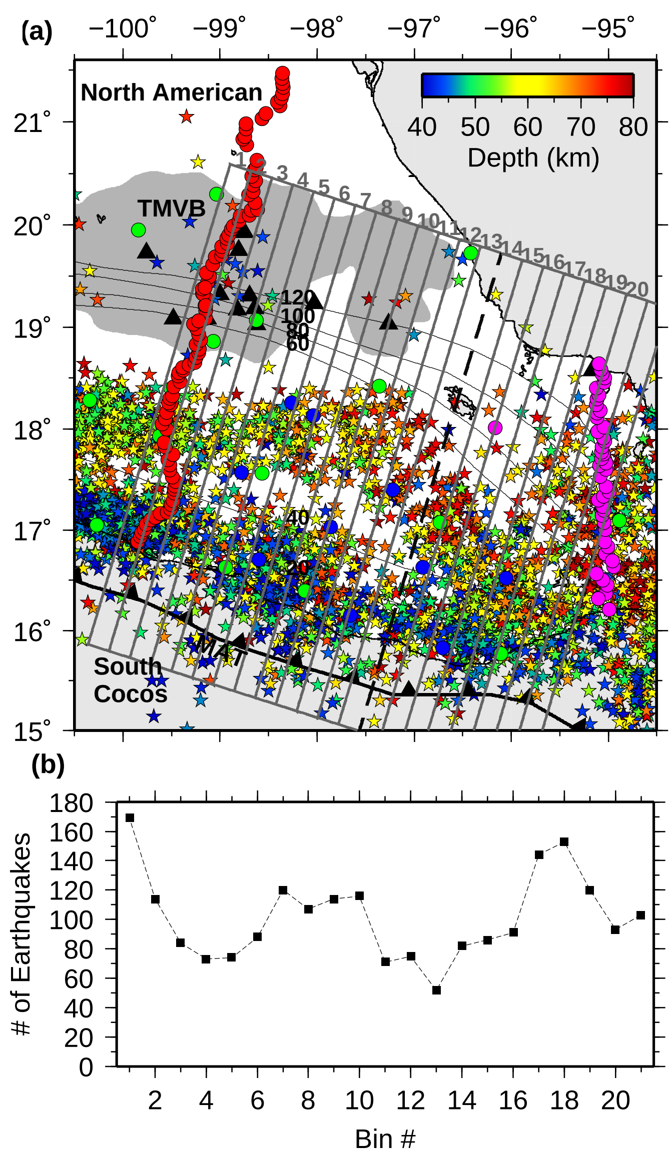

Figure 3.6: Intraslab seismicity across the study region. (a) Map of epicenters (stars) for 40–80-km-depth earthquakes from the 1960–2012 International Seismological Centre (ISC) Bulletin event catalog (*International Seismological Centre*, 2011). Epicenters are color-coded by event depth. Data in the same 25-km-wide bins as Figure 3.3 are analyzed for changes in intraslab seismicity across this region. (b) Plot of number of earthquakes per bin for the twenty-one bins analyzed. Note the ∼75-km-wide zone of decreased seismicity immediately west of the sharp transition in slab dip (black dashed line), encompassing bins 11–13.

events which can be found in both catalogs, only the GCMT solution is shown. West of the VEOX array, in the flat slab and transitional dip regions, there is a predominance of normal faulting events north of the 40-km isodepth contour, although the overall seismicity is scarce. This preponderance of normal faulting events is consistent with the observed decoupling of the slab from the overriding plate (*Singh and Pardo*, 1993; *Franco et al.*, 2005) due to the low strength USL. It is also consistent with the typical faulting type (i.e., normal) of earthquakes which occur in the oceanic lithosphere due to bending of the slab and/or slab pull (e.g., *Isacks and Barazangi*, 1977; *Manea et al.*, 2006). Across the sharp transition in slab dip, a group of events can be seen to abruptly decrease in depth from west (shallowly dipping slab) to east (more steeply dipping slab), contrary to what would be expected for this change in geometry. The deeper events in the west are coincident with the location of increased intraslab seismicity depth noted above for the ISC catalog data. The focal planes across this zone are oriented roughly normal or oblique to the change in dip line.

In addition to the GCMT and SSN CMT catalog data, we perform source mechanism inversions for the 75 earthquakes of interest in this study using the Cut and Paste (CAP) source estimation technique. This waveform modeling method, detailed in *Zhao and Helmberger* (1994) and *Zhu and Helmberger* (1996), divides broadband seismograms into body wave and surface wave segments and inverts them independently in an effort to maximize the benefits and minimize the limitations of using long- and short-period portions of broadband records. The source mechanism is obtained by applying a direct grid search of strike, dip, rake, magnitude, and depth through all possible solutions to find the global minimum of misfit between the observations and synthetics, allowing time shifts between portions of seismograms and synthetics (*Zhu and Helmberger*, 1996). One of the advantages of this technique is that it proves insensitive to velocity models and lateral crustal

Figure 3.7 *(following page)*: Focal mechanism maps for intraslab earthquakes which occurred in the study region. (a) Map of focal mechanisms from the 1/1976–11/2012 Global CMT (GCMT) catalog (*Dziewonski et al.*, 1981; *Ekström et al.*, 2012) and the 1/2000–11/2012 SSN CMT catalog. Events analyzed in this study are labeled for comparison. (b) Map of focal mechanisms inverted for using the Cut and Paste (CAP) technique in this study for the 75 earthquakes of interest. Source parameters can be found in Table 3.1. The black dashed lines mark the locations of trench-perpendicular (at the sharp transition in slab dip) and trench-parallel cross-sections. Mechanisms are color-coded by event depth.

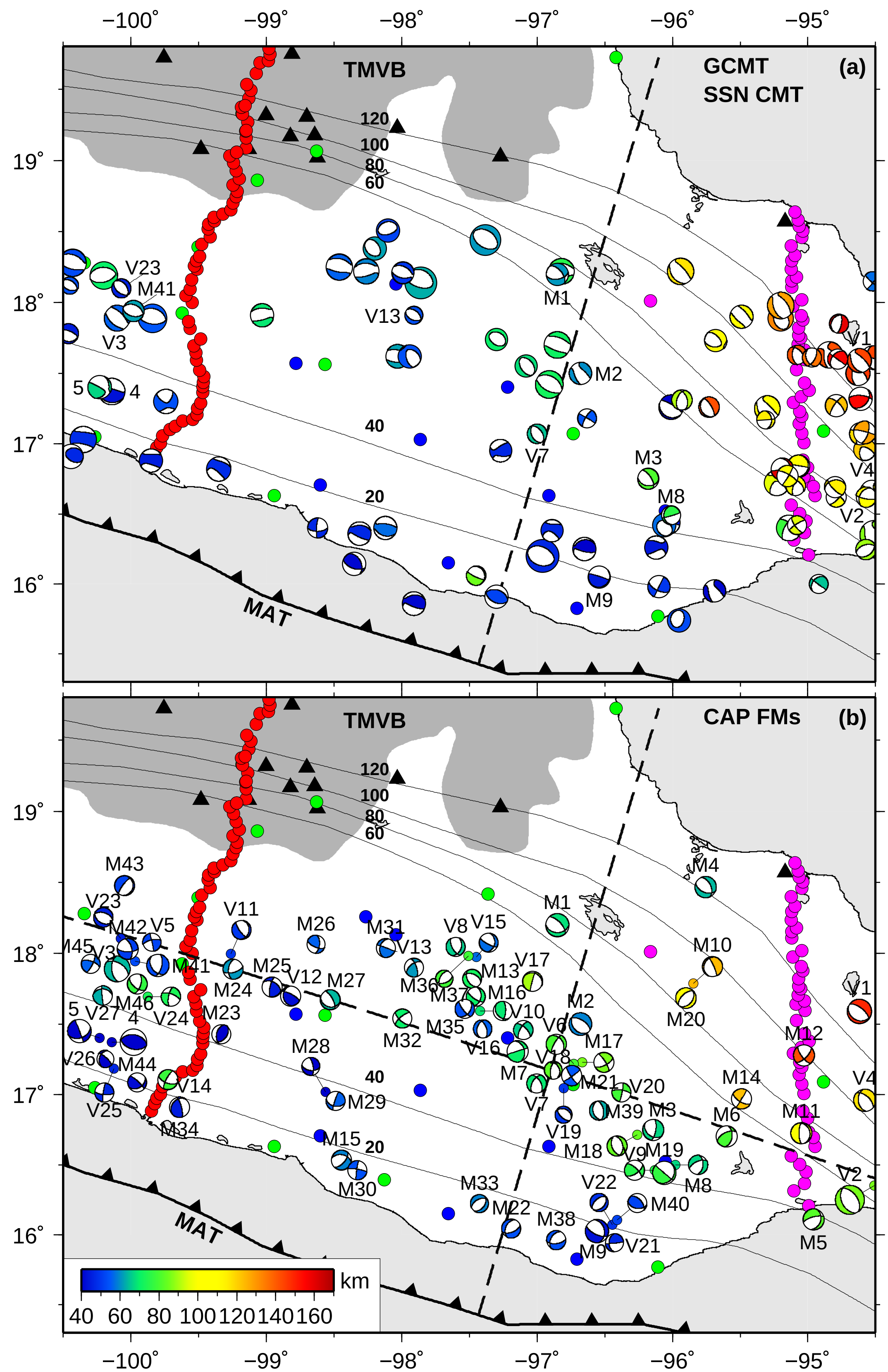
−100°
−99°
−98°
−97°
−96°
−95°
19°
18°
17°
16°
TMVB
GCMT
SSN CMT
(a)
120
100
80
60
40
20
MAT
CAP FMs
(b)
km
40 60 80 100 120 140 160

variation, making it possible to generate accurate source mechanisms with less than perfect Green's functions (*Zhao and Helmberger*, 1994; *Zhu and Helmberger*, 1996; *D'Amico et al.*, 2010, 2011). The focal mechanisms obtained using CAP are shown in Figure 3.7b and detailed in Table 3.1. As with the GCMT and SSN CMT catalog data, the CAP focal mechanisms show a general predominance of normal faulting events in the flat slab and transitional dip regions, although a few thrust and several strike-slip faulting events can also be seen. The patch of deeper events west of the sharp transition in slab dip also recurs in our data; however, the eastward shallowing is not as abrupt. Contrary to the catalog data, a few of the CAP source mechanisms located near the sharp transition in slab dip show focal planes orientated roughly parallel to the change in dip line, which may have important implications for the morphology of the S Cocos slab in this region.

Cross-sections of the CAP focal mechanisms along trench-normal (i.e., change in dip line) and trench-parallel transects that sample the transition from flat to normal subduction are analyzed for additional details of the slab morphology (Figure 3.8). Hypocenters located within 50 km of each respective transect are projected on vertical planes with focal mechanisms shown as viewed from the side. For clarity, mechanisms are distinguished by faulting type following the classification of *Zoback* (1992), which is based on the plunge of P, T, and B axes. The faulting types include normal faulting (NF), predominantly normal faulting with a component of strike-slip (NS), strike-slip faulting (SS), predominantly thrust faulting with a component of strike-slip (TS), thrust faulting (TF), and unknown (U). The unknown faulting type describes events which do not clearly fit into any of other categories and generally applies to smaller and/or less well constrained focal mechanisms (*Zoback*, 1992). The trench-normal and trench-perpendicular cross-sections further demonstrate the predominance of normal (NF and NS) mechanisms in this region that was noted above. Near the point of intersection of these two cross-sections, a slight vertical spread in the distribution of events can be observed, which may be related to the nature of the sharp transition in slab dip located here. From the trench-parallel profile (Figure 3.8b), a concentration of strike-slip mechanisms can also be observed near the abrupt dip change, which may have further implications for the nature of this zone.

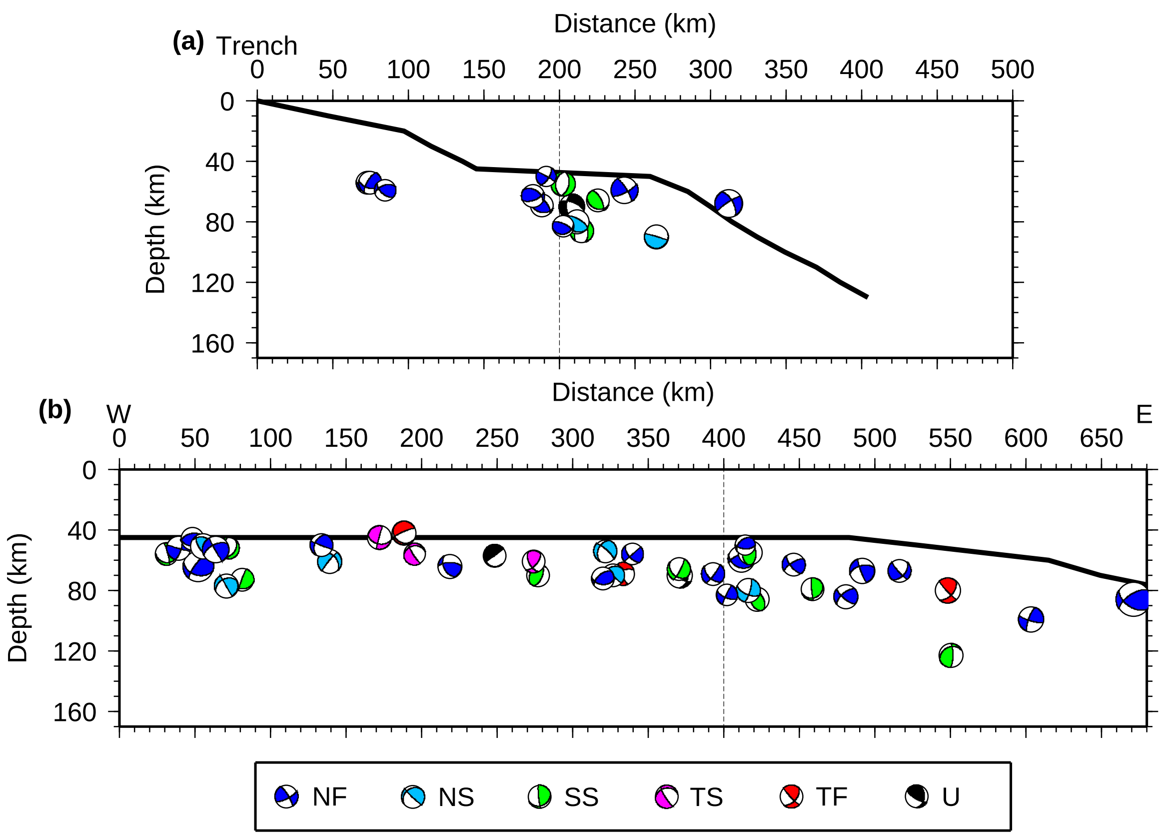

Figure 3.8: Cross-sections of CAP focal mechanisms along the (a) trench-normal and (b) trench-parallel lines in Figure 3.7. Focal mechanisms located within 50 km of the respective cross-section line are included and shown as viewed from the side. Mechanisms are colored by faulting type following *Zoback* (1992). The faulting types include normal faulting (NF), predominately normal with strike-slip component (NS), strike-slip faulting (SS), predominately thrust with strike-slip component (TS), thrust faulting (TF), and unknown (U). The majority of events shown exhibit normal (NF or NS) mechanisms. Heavy black lines indicate the top of the slab from the isodepth contours. Thin dashed lines mark the point of intersection of the two cross-sections.

3.4.5 1D Velocity Modeling

The shallow seismic structure of the eastern central Mexico subduction zone is examined in 1D using frequency-wave number forward modeling techniques with CAP focal mechanisms (Table 3.1). The sensitivity of observed waveforms to the subduction zone structure is tested using 15 different P- and S-wave velocity models, five of which are presented here: (1) *Furumura and Singh* (2002) velocity model for central Mexico without the slab (FSa) (Figure 3.9a); (2) *Furumura and Singh* (2002) velocity model including the slab (FSb) (Figure 3.9b); (3) New central Mexico (ncM) velocity model from *Dougherty et al.* (2012) (Figure 3.9c); (4) Composite velocity model comprised of the overriding plate structure from model FSa and the slab structure from model ncM (ncM_FSa) (Figure 3.9d); (5) Modified ncM velocity model with re-calculated P-wave velocities (ncMc) from this study (Figure 3.9e). These five models are the most relevant of those tested as they provide the closest approximations of the observed waveforms. The remaining ten models can be found in Figure 3.18. The FSa model does not include slab structure, while the other four models discussed here contain a multilayered, somewhat complex slab (Figure 3.9). The ncM, ncM_FSa, and ncMc models also include the USL (3 km thick, V_S of 2.6 km/s) that was imaged by the MASE array. The P-wave velocities in the ncMc model are calculated using the FSa V_P/V_S ratio of 1.7 and ncM S-wave velocities, with the thicknesses and depths of the layers held constant between the ncM and ncMc models (Figure 3.9e). The FSa crustal model tests the sensitivity of the observed waveforms to the crustal structure only, while the remaining four models test the waveform sensitivity to combined crustal and slab structure.

A comparison of the synthetics produced for each of these five models to the data for event M1 at three stations is shown in Figure 3.10. The waveforms have been bandpass filtered to 0.01–0.1 Hz in order to increase the signal-to-noise ratio and accentuate the major phases (e.g., P, sP, S). Overall, the ncMc model provides the most accurate prediction of the data on both vertical and horizontal components, with the best fits to P, sP, and SH phases at all distances (Figures 3.10 and 3.11). The FSa model provides a slightly improved fit to the sP and SV phases on the vertical component, but a poorer fit to all phases on the radial component (Figure 3.10). The ncM model provides a

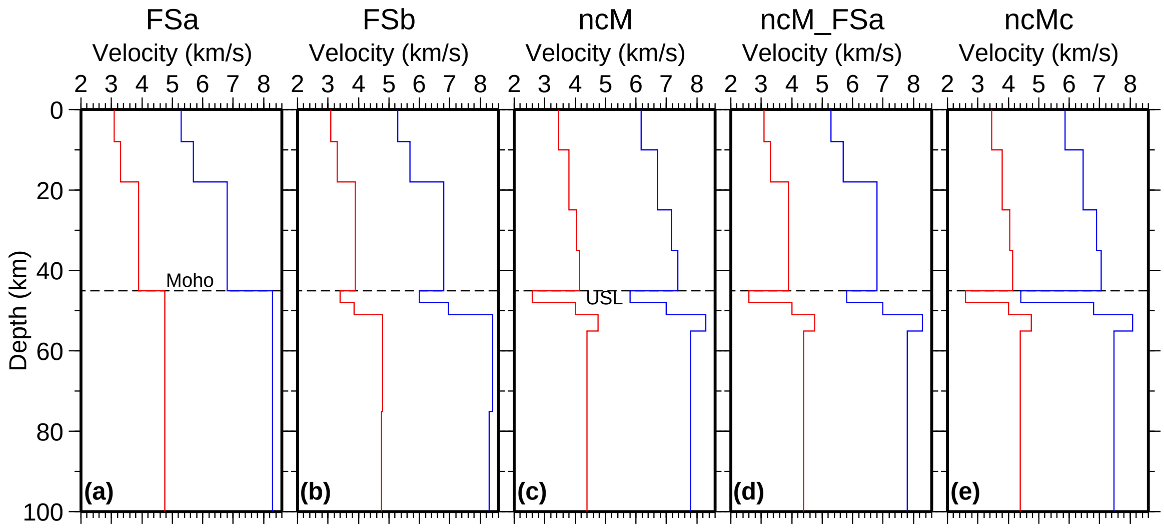

Figure 3.9: 1D P (blue) and S (red) wave velocity models tested in this study. (a) *Furumura and Singh* (2002) velocity model for central Mexico without the slab (FSa). The Moho depth is indicated by the black dashed line. (b) *Furumura and Singh* (2002) velocity model including the slab (FSb). (c) New central Mexico (ncM) velocity model from *Dougherty et al.* (2012). Ultra-slow velocity layer (USL) is indicated at the top of the subducted plate. (d) Composite velocity model comprised of the overriding plate structure from model FSa and the slab structure from model ncM (ncM_FSa). (e) Modified ncM velocity model with re-calculated P-wave velocities (ncMc) from this study.

comparable fit to the ncMc model for the major phases on the radial component, with a slightly worse fit on the vertical component (Figure 3.10). The uppermost slab structure in the ncMc model, particularly the USL, is likely responsible for reproducing the observed horizontal waveforms that the simpler FSa model fails to accurately predict. Additionally, the re-calculated P-wave velocities of the ncMc model using the V_P/V_S ratio of the FSa model can be credited for improved predictions of the vertical component waveforms over the ncM model.

3.4.6 2D Velocity Modeling

To further investigate the shallow structure of the subducted S Cocos plate along the transition from flat to normal subduction, we produce synthetic seismograms with a 2D finite-difference wave propagation algorithm for particular velocity and slab geometry models and compare these to the data for 16 events. As with the 1D velocity modeling, we use source parameters from the CAP focal mechanisms (Table 3.1) to generate the synthetics. Models for the 16 events tested are oriented along 17 different profiles throughout the study region, concentrated across the USL, possible USL,

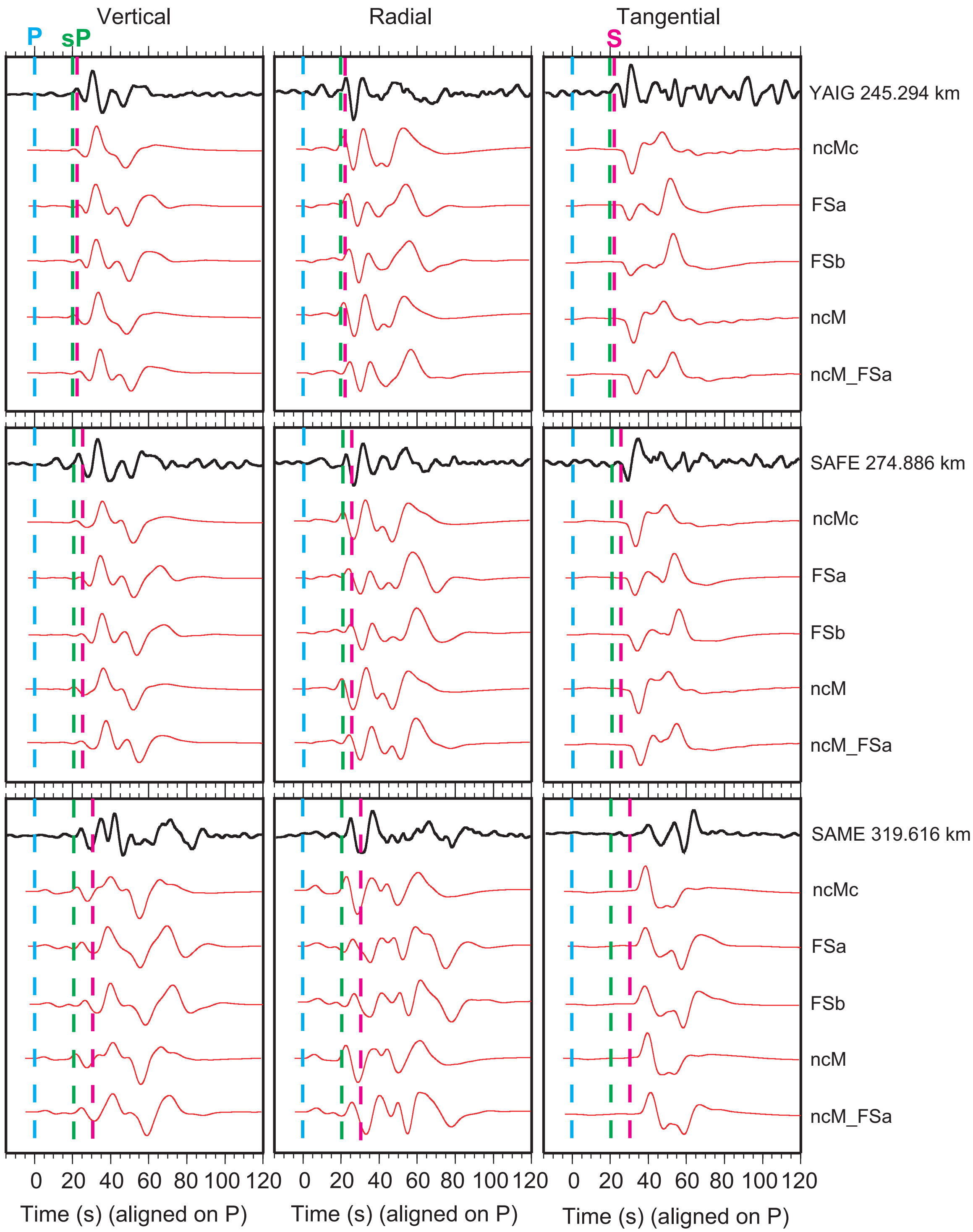

Figure 3.10: Comparison of 1D modeling results of event M1 for the five models tested at three stations. Waveforms are filtered to 0.01–0.1 Hz. Data are in black, synthetics are in red. P, sP, and S phases are indicated by dashed lines.

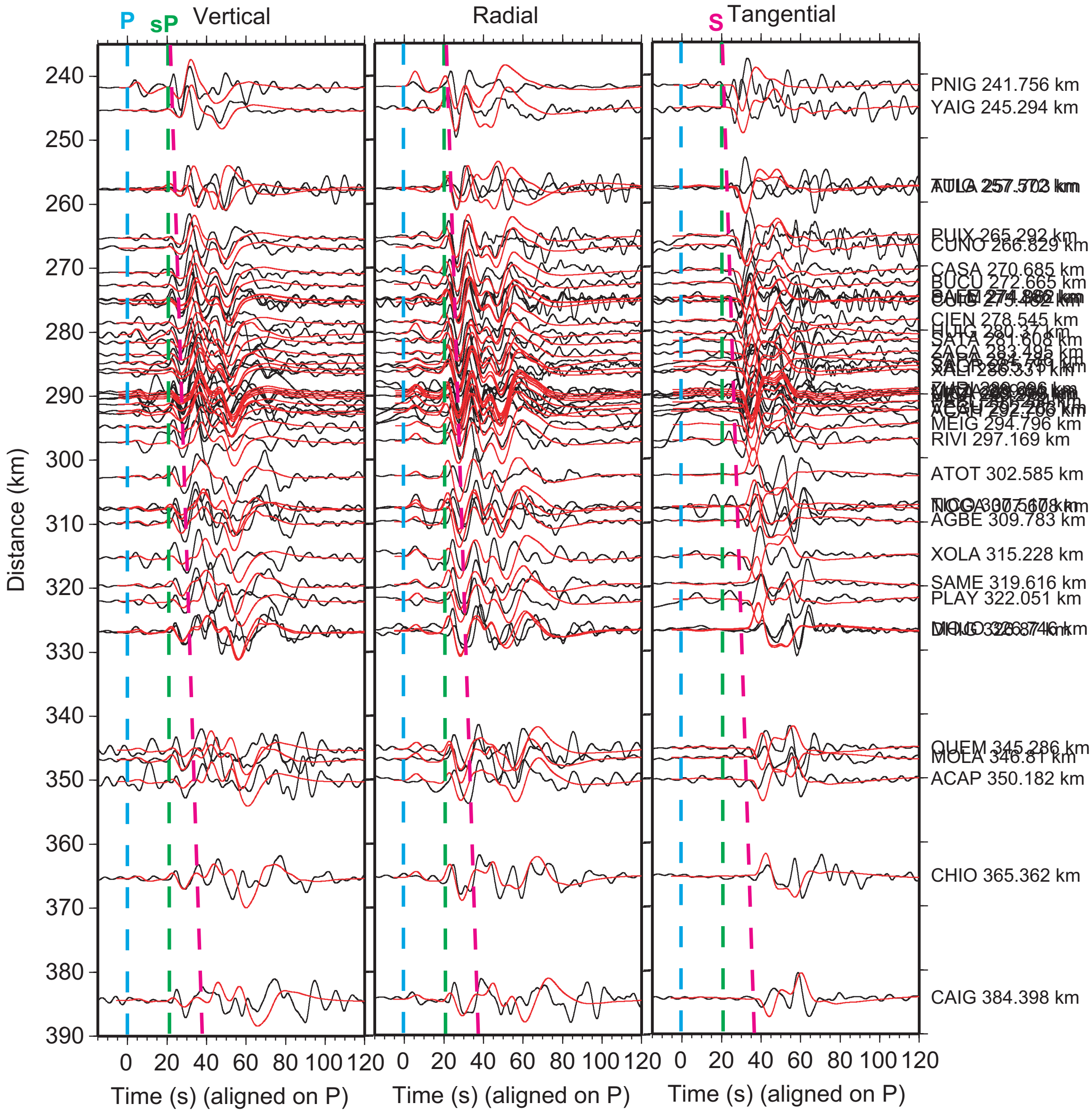

Figure 3.11: 1D modeling results of event M1 for the ncMc velocity model filtered to 0.01–0.1 Hz. Data from MASE and SSN stations are in black, synthetics are in red. P, sP, and S phases are indicated by dashed lines. See Figure 3.19 of the auxiliary material for results plotted without station overlap.

and no USL zones in order to examine the validity of their boundaries (Figure 3.12a). Note that for event V2 both a NW-SE oriented profile and an E-W profile are modeled. All of the models investigated consist of P- and S-wave velocities from the ncMc model with subducted slab geometries estimated from the isodepth contours (*Pérez-Campos et al.*, 2008; *Kim et al.*, 2010, 2011; *Melgar and Pérez-Campos*, 2011). The 2D modeling results for all of the events tested are summarized in Figure 3.12b, where profile lines are colored to indicate locations of confirmed presence of the USL, possible presence of the USL, and lack of the USL. In general, the USL is shown to be present (or possibly present) across the entire width of the previously defined possible USL zone, from the coast to its northernmost estimated extent, although the profile furthest from the coast indicates that only a small patch of the USL is present (event M2). Two parallel transects across this zone (events M9 and M3) are exceptions to this result, instead indicating that no USL is present. Additionally, the modeling results for the event M22 profile across this zone are inconclusive. Transects located to the north and east of the possible USL zone confirm that the USL is not present in these regions.

The preferred 2D velocity model along the E-W profile for event V2 is presented in Figure 3.13 as an example. Data along this transect were recorded by OXNET and SSN stations. The USL in this model ends at the approximate eastern boundary of the possible USL (USL?) zone. The synthetics produced from this model (i.e., end1) are compared to the data from three stations in Figure 3.14. The model predicts the P and sP phases reasonably well at all distances and the S-wave at shorter distances. A later large amplitude phase, presumed to be an S-wave multiple, is predicted reasonably well by the model at all stations.

In order to test the effect of the presence or absence of the USL and the location of its eastern lateral extent on the synthetic seismograms produced, we examine nine other models with the same velocity structure, including six which assess our model's sensitivity to the absolute location of the end of the USL: (1) USL continues across the entire width of model without an end (ncMc); (2) USL stops at approximate western boundary of the no USL zone (end2); (3) no USL present, thicker lower oceanic crust to compensate; (4) USL stops at approximate eastern boundary of the USL? zone shifted by 10 km to the west (end1+10); (5) USL? boundary shifted 25 km to the west

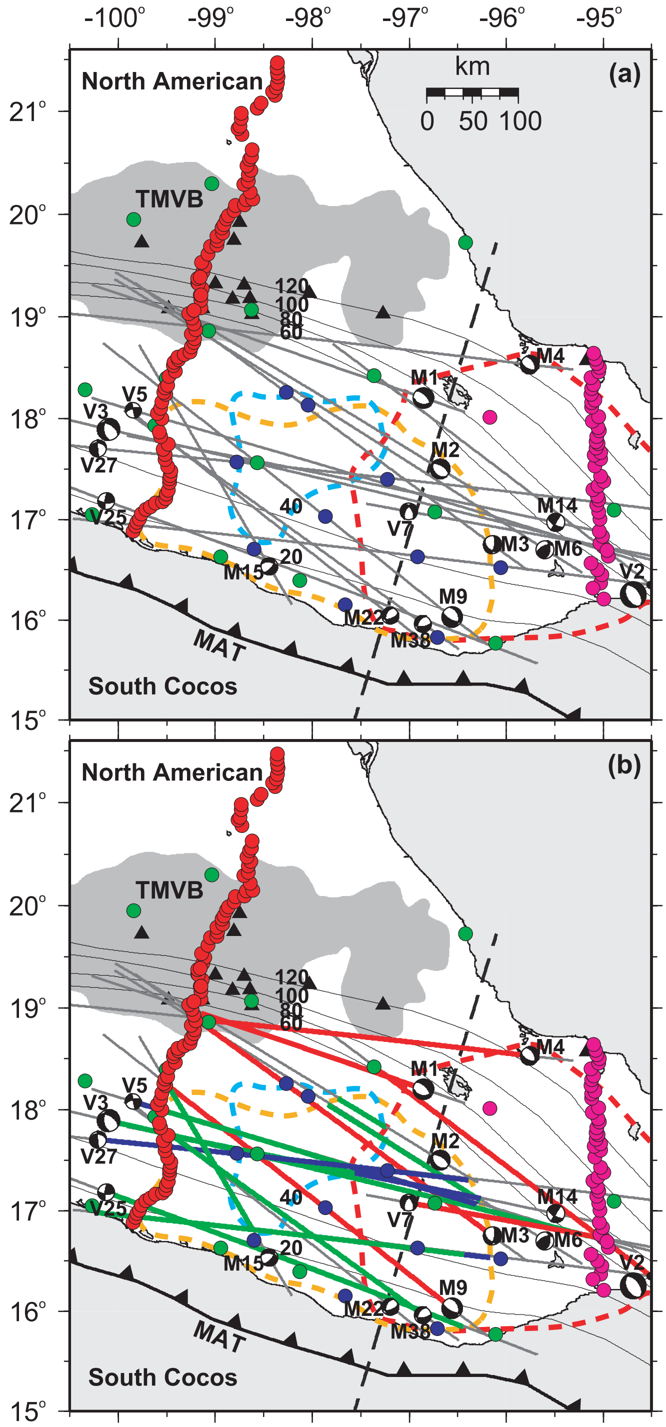

Figure 3.12: (a) Map of locations of 2D velocity model cross-sections (dark grey lines) for the sixteen events modeled (focal mechanisms). Focal mechanisms are from this study. Thick dashed lines mark the boundaries of the USL (cyan), possibly USL (orange), and no USL (red) zones from Figure 3.5. (b) Same as (a) with cross-section lines colored to reflect 2D modeling results. Confirmed presence of the USL is shown in green and possible presence of the USL is shown in blue. Red lines indicate that a model without the USL provides the best representation of the data.

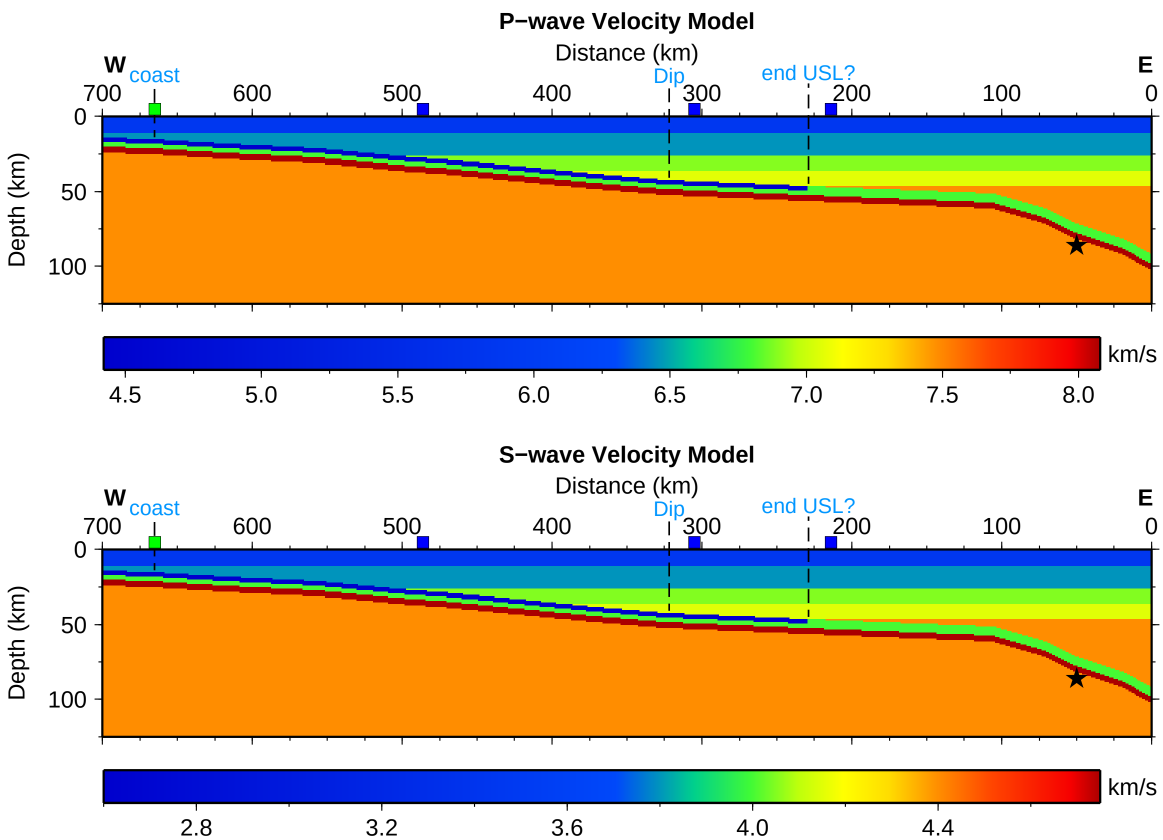

Figure 3.13: 2D velocity model of the shallow subduction zone structure across the OXNET (blue squares) and SSN (green square) arrays along the E-W profile for event V2 in Figure 3.12. P- and S-wave velocities are from the ncMc model. Subducted slab shape is estimated from the isodepth contours. Locations of the approximate end of the possible USL (USL?) zone, the sharp transition in slab dip, and the coastline are indicated for reference. The location of event V2 used in the modeling is shown by the black star.

(end1+25); (6) USL? boundary shifted 25 km to the east (end1−25); (7) USL? boundary shifted 30 km to the west (end1+30); (8) USL? boundary shifted 50 km to the west (end1+50); (9) USL? boundary shifted 50 km to the east (end1−50). A comparison of the synthetics produced for each of the nine models and the preferred (end1) model to the data at three stations is shown in Figure 3.14. A ∼40–53 sec segment of the waveform after the S-wave that includes the large amplitude, presumed S-wave multiple illustrates the greatest variance among the models, indicating that this phase is most sensitive to the USL. The synthetic waveform for each model is cross-correlated with the data for this segment. Due to the increased complexity of the waveforms observed on the radial component, we note that the correlation coefficients for all of the models are generally reduced relative to the vertical component and recommend weighing the vertical component results more heavily than the radial component. While there is some variance between the vertical and radial components, in general, the correlation coefficients indicate that the end1 (i.e., preferred) model synthetics are better representations of the data than the end2 and no USL models. The correlation coefficients for the majority of the stations located along the profile clearly indicate that the end1 model synthetics fit the data better than those produced by the complete USL (i.e., ncMc) model on both the vertical and radial components. In comparison to the shifted boundary models, overall the correlation coefficients indicate increased accuracy for synthetics produced with boundary shifts of 10–30 km to the west relative to those produced by the end1 model. On the other hand, boundary shifts of 25–50 km to the east produce worse fits to the data than the end1 model. These results suggest the confirmed presence of the USL to a location 30 km west of the eastern USL? boundary

---

Figure 3.14 *(following page)*: Comparison of 2D modeling results of event V2 along the E-W profile for ten different models at three stations, filtered to 0.01–0.1 Hz. Data are in black, synthetics are in red. Vertical (Z) and radial (R) components are shown. P (dashed line), sP (green arrow), and S (pink arrow) arrivals are indicated. The primary variance among the models was the USL: ncMc = USL continues across entire width of model without an end; end1 = USL stops at approximate eastern boundary of the USL? zone; end2 = USL stops at approximate western boundary of the no USL zone; noUSL = no USL present, thicker lower oceanic crust to compensate; end1+10, end1+25, end1+30, end1+50 = USL? boundary shifted 10 km, 25 km, 30 km, 50 km, respectively, to the west; end1−25, end1−50 = USL? boundary shifted 25 km, 50 km, respectively, to the east. Segment of waveform illustrating greatest variance among the models is shaded grey. Cross-correlation coefficients (X) for each model with the data for the selected segment are shown.

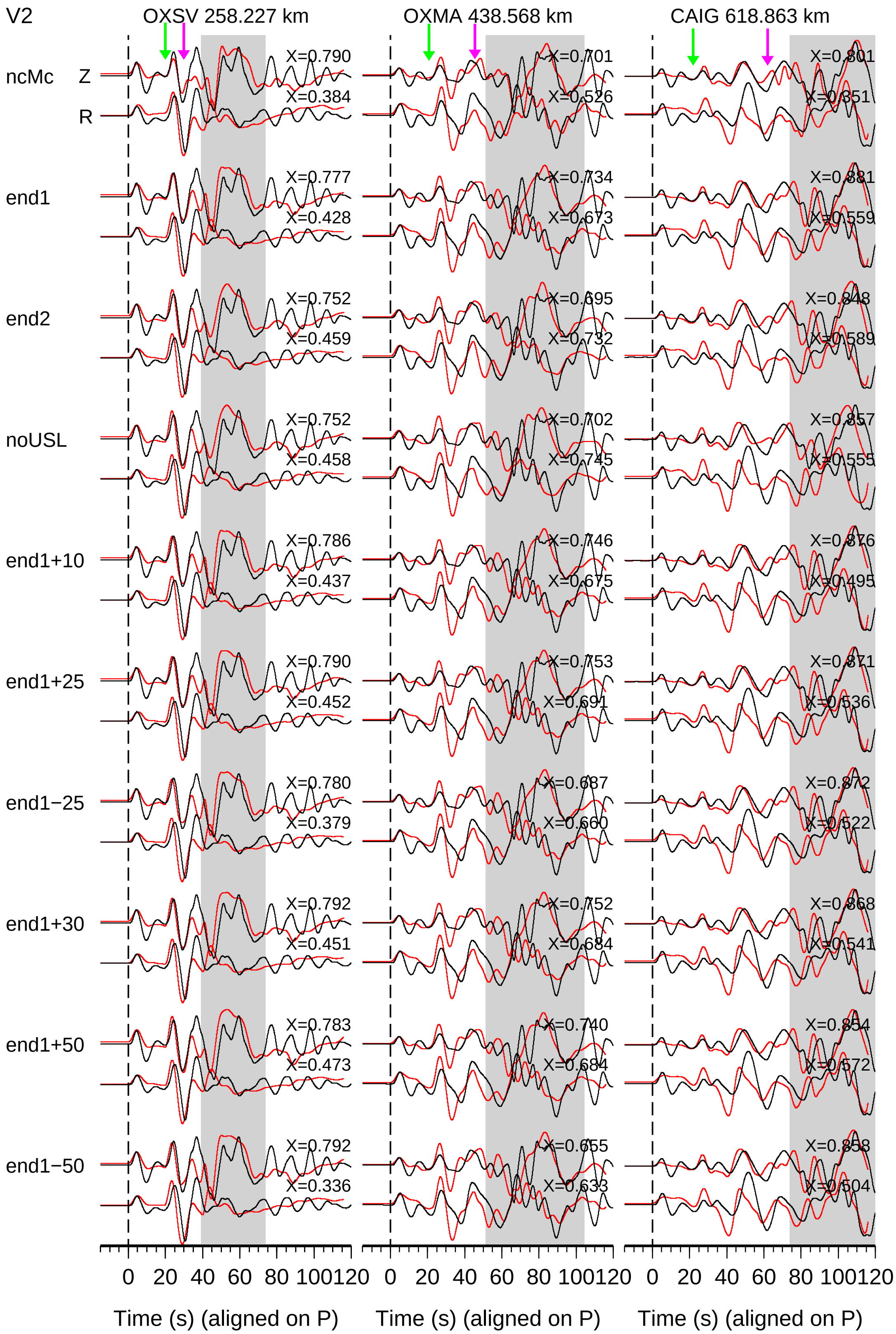
V2
OXSV 258.227 km
OXMA 438.568 km
CAIG 618.863 km
ncMc
Z
R
end1
end2
noUSL
end1+10
end1+25
end1−25
end1+30
end1+50
end1−50
X=0.790
X=0.384
X=0.701
X=0.526
X=0.801
X=0.351
X=0.777
X=0.428
X=0.734
X=0.673
X=0.881
X=0.559
X=0.752
X=0.459
X=0.695
X=0.732
X=0.848
X=0.589
X=0.752
X=0.458
X=0.702
X=0.745
X=0.857
X=0.555
X=0.786
X=0.437
X=0.746
X=0.675
X=0.876
X=0.495
X=0.790
X=0.452
X=0.753
X=0.691
X=0.871
X=0.536
X=0.780
X=0.379
X=0.687
X=0.660
X=0.872
X=0.522
X=0.792
X=0.451
X=0.752
X=0.684
X=0.868
X=0.541
X=0.783
X=0.473
X=0.740
X=0.684
X=0.854
X=0.572
X=0.792
X=0.336
X=0.655
X=0.633
X=0.858
X=0.504
0 20 40 60 80 100 120
Time (s) (aligned on P)

and the possible presence of the USL between this location and the USL? boundary (as indicated in Figure 3.12b).

The preferred 2D velocity model along the event M2 profile and a comparison of the synthetics produced for each of the models tested to the data are shown in Figures 3.20 and 3.21, respectively, as an additional example.

3.5 Discussion

The abrupt end of the TMVB coupled with the interruption of arc volcanism near the transition from flat to normal subduction in eastern central Mexico suggests a possible slab tear located within the subducted S Cocos plate. In this study, we provide further evidence for such a tear based on seismic observations, source mechanism analysis, and modeling of the velocity structure of the subduction zone. From estimating the lateral variation in slab dip using Wadati-Benioff zone seismicity, we find a sharp increase in slab dip indicative of a possible tear in the S Cocos plate. Due to the short distance over which this increase in dip occurs (~50 km), it is unlikely to be accommodated by a smooth contortion of the slab, as suggested by *Pardo and Suárez* (1995). The location of this sharp transition in slab dip near the end of the TMVB may have important implications for the observed gap in arc volcanism. With the increase in slab dip eastward from the TMVB, it would be expected that the arc volcanism would shift trenchward, following the slab, but the lack of observed volcanism instead suggests that a slab source for melt generation could be missing beneath this area. A tear in the S Cocos slab that begins downdip and extends trenchward to <100 km depth (i.e., the point of decompression melting) could explain the suggested lack of a slab source. Alternatively, the truncation of the S Cocos slab observed to the east by the Yucatán slab, which restricts flow in the mantle wedge, may also explain the unusual configuration of arc volcanism in the region (*Kim et al.*, 2011; *Chen and Clayton*, 2012).

Examination of the eastern lateral extent of the USL shows a complex pattern that cannot be mapped as a single linear feature, as was done by *Dougherty et al.* (2012) for the western extent. The observed boundary between the USL and no USL zones that is coincident with the end of the

TMVB suggests a change in plate structure here and could indicate a possible tear in the S Cocos slab. East of here there is a transitional, weakening USL zone, evident in the overlapping possible USL and no USL regions closer to the coast. This patchy petering out of the USL in the updip portion of the slab further implies that the possible slab tear is currently concentrated downdip, as the hydrous minerals and potential pore fluid of the USL would not be maintained across a break in the slab at shallower depths. This mapping of the USL extent contradicts similar mapping by *Song et al.* (2009), which showed no observed USL in the region of our USL zone. The events analyzed by *Song et al.* (2009) in this region of overlap were recorded by a single station prior to the MASE array deployment, while we utilize data from multiple arrays with events recorded by a minimum of 24 (and up to 94) stations. The increased quantity and quality of our data relative to that of *Song et al.* (2009) likely accounts for the discrepancy in results and favors our mapping of the USL. Additionally, the 2D finite-difference modeling confirmed the location of the USL across the entire width of the USL and possible USL zones, further solidifying our mapping.

The intraslab seismicity patterns observed across the study region provide further evidence for a possible tear in the S Cocos slab. The margin of a zone of decreased seismicity located to the west of the sharp transition in slab dip is coincident with both the end of the TMVB and the boundary between the USL and no USL zones. The decreased seismicity of this zone suggests a change in plate structure, and its coincidence with the TMVB and USL boundaries further suggests that this change could indicate a tear in the slab. If the slab was undergoing plate flexure along a smooth contortion instead, we would expect an increase in seismicity, not a decrease (*McCrory et al.*, 2012). The clustering of events within this zone (bins 12 and 13) may imply focusing of stress from a tear that is propagating updip from a deeper point, as has been observed for slab tears in other subduction zones (*Gutscher et al.*, 1999; *Miller et al.*, 2004; *Clark et al.*, 2008; *Meighan et al.*, 2013b). The abrupt increase in depth at the point of rotation of the downdip seismicity band near the end of the TMVB also suggests a structural change indicative of a possible slab tear.

Focal mechanisms of the intraslab seismicity elucidate the nature of the flat-to-normal transition in slab dip beyond that of the epicentral ISC catalog locations. The observed decrease in depth of events from the shallowly dipping to the more steeply dipping portion of the slab in both the GCMT and SSN CMT catalog data and the CAP focal mechanisms indicates a change in stress distribution across this region. The deeper events on the shallowly dipping segment may be due to a localized stress concentration as a result of the steeper adjacent segment (*Pacheco and Singh*, 2010) and/or downdip tearing of the slab. Both of these scenarios could produce a vertical column of seismicity like that suggested based on the cross-sections of the CAP focal mechanisms. Such a column has been observed along slab tears in the southern Lesser Antilles (*Clark et al.*, 2008), the northeast Caribbean (*Meighan et al.*, 2013b), and Tonga (*Millen and Hamburger*, 1998). In eastern central Mexico, the intraslab seismicity is generally sparse, making it difficult to conclude that a vertical column of seismicity exists here, yet the implications of the possibility are relevant to our discussion.

In addition to the patterns in their spatial distribution, the orientations of the focal mechanisms also provide evidence for a possible slab tear. While normal faulting mechanisms are generally predominant, the orientations of these mechanisms are highly variable near the sharp transition in slab dip, suggesting a complex stress distribution (*Pardo and Suárez*, 1995; *Rebollar et al.*, 1999). The observed concentration of strike-slip mechanisms in this region indicates further complexity of the stress field. Such variation in stress orientations suggests that the earthquakes are either accommodating the strain that is necessary for the slab to fail and tear or failure of the slab has already taken place, and the seismicity is the result of faulting as adjacent mantle is drawn into the gap (*Miller et al.*, 2004). The strike-slip focal mechanisms may be accommodating the shear motion that is thought to be associated with the slab-tearing process (*Burbach et al.*, 1984; *Rosenbaum et al.*, 2008; *Meighan et al.*, 2013b; *Vargas and Mann*, 2013). This range of earthquake mechanisms and orientations observed near the possible tear in the S Cocos slab is consistent with observations at slab tears in other subduction zones (e.g., *Russo et al.*, 1993; *Bilich et al.*, 2001). Additionally, the approximate alignment of steeply dipping focal planes for some CAP mechanisms along the strike of the change in dip line suggest tearing of the slab per *Gutscher et al.* (1999)'s classification of "tearing events".

The ∼50–75-km-wide offset between the eastern end of the TMVB and the sharp transition in slab dip suggests the existence of a downdip tear zone which encompasses the various seismic observations presented here. The western margin of this tear zone is defined by the termination of the TMVB and its coincidence with the boundary between the USL and no USL regions and the limit of an area of decreased intraslab seismicity, indicating that this margin is a marked structural boundary in the downdip portion of the slab. The eastern margin of the tear zone is delineated by the sharp transition in slab dip and, based on the spatial distribution and orientations of the focal mechanisms analyzed in this study, the locus of active tearing of the S Cocos slab is proposed to occur along here. The continuation of a weakening USL zone in the updip portion of the slab across this tear zone and the sharp transition in slab dip demonstrates that the presence of the USL is not controlled simply by geometry, consistent with observations in western central Mexico (*Dougherty et al.*, 2012). Rather, the presence of the USL is strongly controlled by the structure of the S Cocos slab, which is still continuous in the shallow updip region.

The lack of surficial expression of the possible tear (e.g., rifting or magmatism) implies that it is a less developed or young feature and supports the theory that it is currently localized to the downdip, aseismic portion of the slab. P-wave tomography shows a gap in the imaged slab at the eastern end of the TMVB at 380 km depth (*Gorbatov and Fukao*, 2005), which is interpreted as a tear in the slab. A similar observation has been made along the transition from flat to normal subduction in Chile, where a gap in fast velocities at depths of 220–340 km suggests a local tear in the downdip portion of the slab (*Pesicek et al.*, 2012). The lack of surface volcanism further implies that any asthenospheric mantle material which may be flowing through the tear is not rising to a shallow enough depth to have an effect on the overriding plate (*Miller et al.*, 2009).

The possible tear in the S Cocos slab may be the result of the subduction of several parallel ridges of seamounts off the coast of Oaxaca. Seamount subduction is a common process that is often related to large earthquake ruptures, although the role of seamounts as asperities or barriers to rupture propagation is controversial (see, e.g., *Cloos*, 1992; *Scholz and Small*, 1997; *Wang and Bilek*, 2011; *Kopp*, 2013; *Yang et al.*, 2013, and references therein). The subduction of seafloor heterogeneities, which induce an abrupt variation of the mechanical properties of the oceanic plate, may provide a preferred location to initiate a tear within the slab (*Chatelain et al.*, 1992; *Bonnardot et al.*, 2009; *Mason et al.*, 2010). These inhomogeneities may reduce the strength of the lithosphere, resulting in a weak zone along which a tear will propagate (*Hale et al.*, 2010). In the case of seamounts, this weak zone is located along the margin of the strengthened lithosphere (i.e., along the chain or ridge) (*Hale et al.*, 2010), where seamount parallel faults have been observed offshore central Mexico (*Kanjorski*, 2003). The eastern margin of the Puerto Escondido seamount cluster is located near 97.5°W at the MAT, coincident with the sharp transition in slab dip. This spatial correlation supports seamount subduction as a cause of the possible slab tear. In addition to (or instead of) this proposed cause, the accommodation of a considerable amount of strain in the slab due to the abrupt variation in geometry (i.e., sharp transition in slab dip) may promote tearing (*Miller et al.*, 2004, 2005; *Yang et al.*, 2009).

In conjunction with the tear in western central Mexico (*Dougherty et al.*, 2012; *Stubailo et al.*, 2012), the possible slab tear in the S Cocos plate proposed here may play an important role in the rollback process by allowing the slab to rollback in segments, resulting in observed along-trench variations in slab dip (Figure 3.15). As slab rollback begins on only a segment of the plate, the first slab tear develops, allowing mantle flow through the gap. Over time, slab rollback continues, steepening the initial segment and inducing rollback in another segment of the plate, where a second slab tear develops, allowing further mantle flow between the segments. This steepening of the slab during rollback pushes material laterally from underneath the slab around an edge and into the overlying mantle wedge (*Russo and Silver*, 1994; *Schellart*, 2004; *Jadamec and Billen*, 2010). This flow is presumably currently accommodated by the gap between the N Cocos and Rivera plates (*Soto et al.*, 2009). The proposed tears in the plate would significantly short-cut this process. Additionally, the toroidal flow through the tear introduces less dense and viscous asthenosphere material into the mantle wedge, promoting rapid rollback of the slab segment (*Schellart et al.*, 2007; *Soto et al.*, 2009).

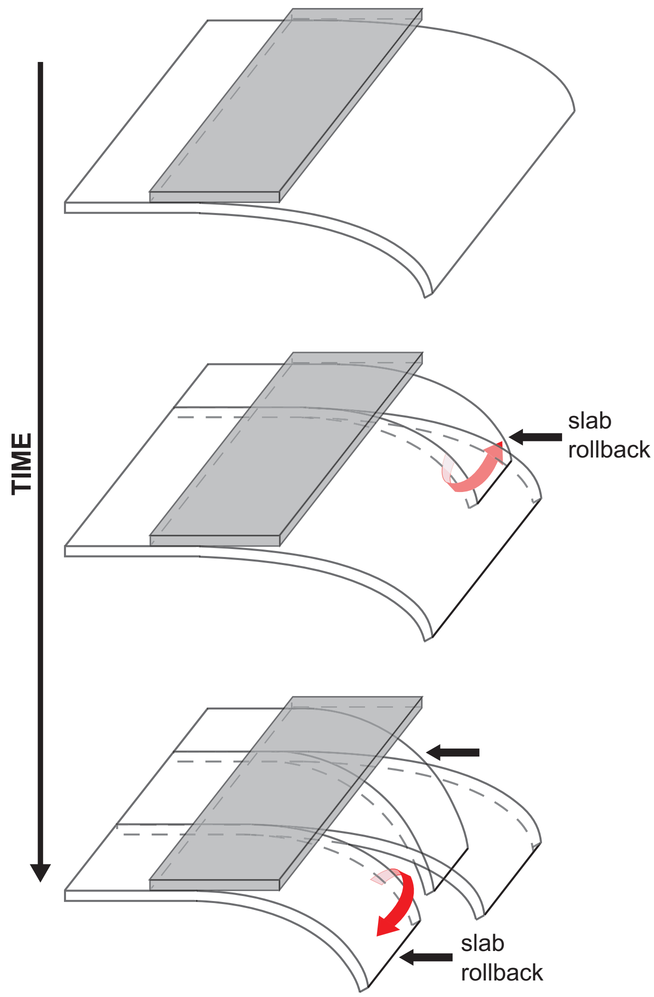

Figure 3.15: 3D schematic of the slab rollback process and plate tearing through time. (top) Start with a flat slab. (middle) Slab rollback begins on only a segment of the plate; first plate tear develops, allowing mantle flow through the gap (red arrow). (bottom) Slab rollback continues and a second segment of the plate begins rolling back; second plate tear develops, allowing further mantle flow between the segments.

3.6 Conclusions

The nature of the transition from flat to normal subduction in eastern central Mexico is interrogated using intraslab seismicity patterns, an analysis of P waveform complexities, and 1D and 2D waveform modeling techniques. The results show that the subducted S Cocos plate is a complicated, multilayered structure with a thin USL atop the slab. The lateral extent of this USL is marked by a boundary between the USL and no USL zones, followed by a diffuse weakening USL region closer to the coast. A sharp transition in slab dip near the abrupt end of the TMVB suggests a possible tear in the S Cocos slab. The coincidence of the boundary between the USL and no USL zones with the margin of a zone of decreased seismicity along this change in dip and the end of the TMVB implies a change in structure which we interpret as evidence of a possible tear. Additional observed intraslab seismicity patterns of clustering, sudden increase in depth, variable focal mechanism orientations and faulting types, and alignment of source mechanisms along the sharp transition in slab dip further support this conclusion. We propose the subduction of parallel ridges of seamounts and/or stress due to the abrupt change in geometry as potential causes of the possible slab tear in the S Cocos plate. Further imaging of the subduction zone structure with denser station coverage over the downdip aseismic portion of the slab may provide a clearer picture of the possible tear at depth.

Acknowledgments

MASE and VEOX data are available at the IRIS DMC under the network code TO. Researchers should contact Michael Brudzinski for OXNET data and Carlos M. Valdes Gonzalez for SSN waveform data. The SSN event catalog is accessible from the Servicio Sismológico Nacional website (http://www.ssn.unam.mx/). The SSN CMT catalog is available on the Mexican CMT Project website (http://laxdoru.igeofcu.unam.mx/cmt). The ISC Bulletin event catalog is accessible from the International Seismological Centre website (http://www.isc.ac.uk).

This study was supported in part by the Gordon and Betty Moore Foundation through the Tectonics Observatory at California Institute of Technology. This is contribution number 256 from the Caltech Tectonics Observatory. We are grateful to Michael Brudzinski, Enrique Cabral-Cano, and Alejandra Arciniega-Ceballos for making the OXNET waveform data available. We thank Arturo Iglesias for providing the Servicio Sismológico Nacional event catalog and Ting Chen for the slab isodepth contour lines. We also thank Editor Robert Nowack, the Associate Editor, Sebastiano D'Amico, and an anonymous reviewer for helpful comments, which improved the manuscript.

3.7 Supplemental Figures

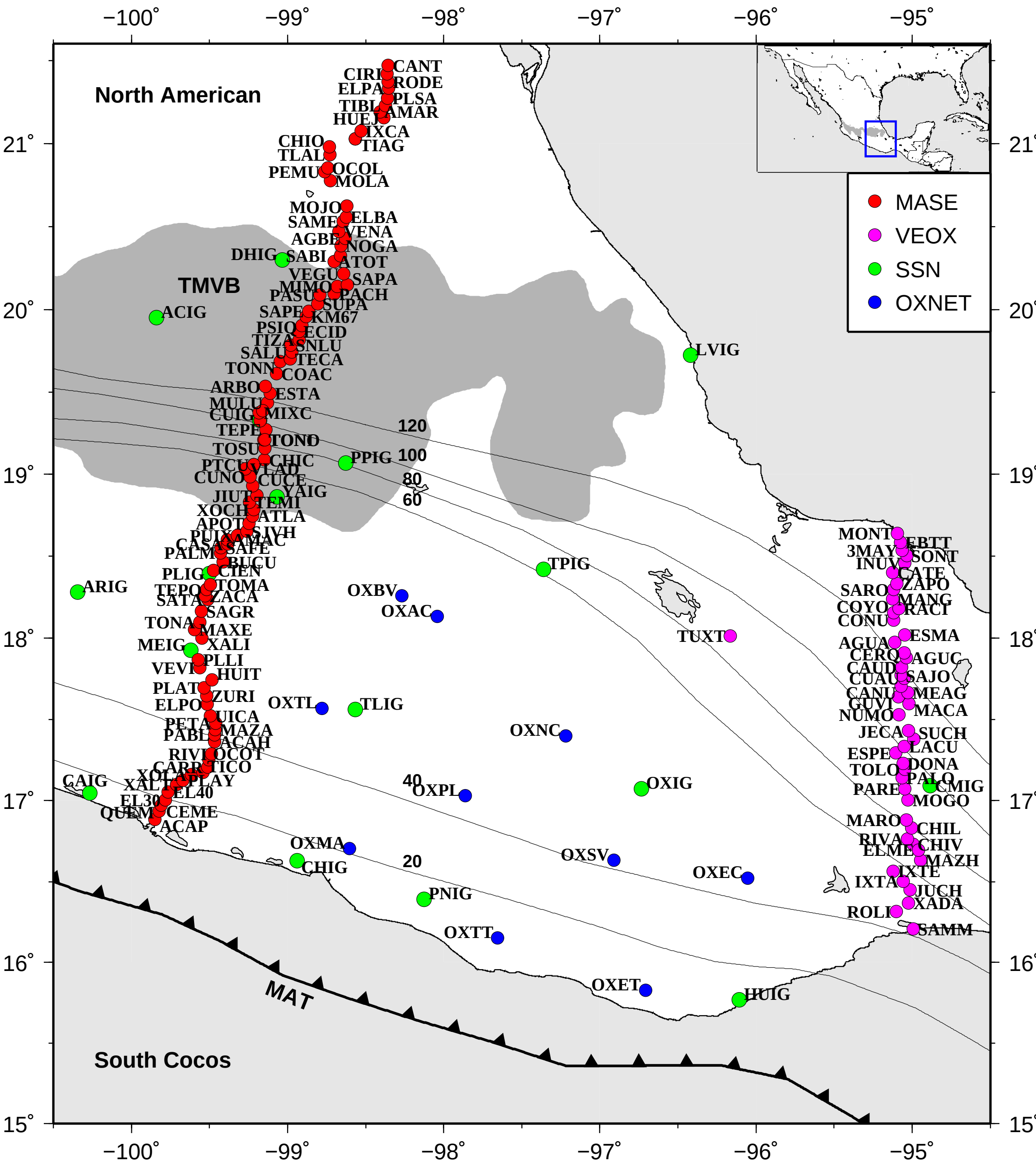

Figure 3.16: Map showing the locations of MASE, VEOX, SSN, and OXNET stations along with their respective station names. The dark grey shaded area indicates the Trans Mexican Volcanic Belt (TMVB). Slab isodepth contours based on local seismicity and teleseismic receiver functions (*Pérez-Campos et al.*, 2008; *Kim et al.*, 2010, 2011; *Melgar and Pérez-Campos*, 2011) are shown in thin lines.

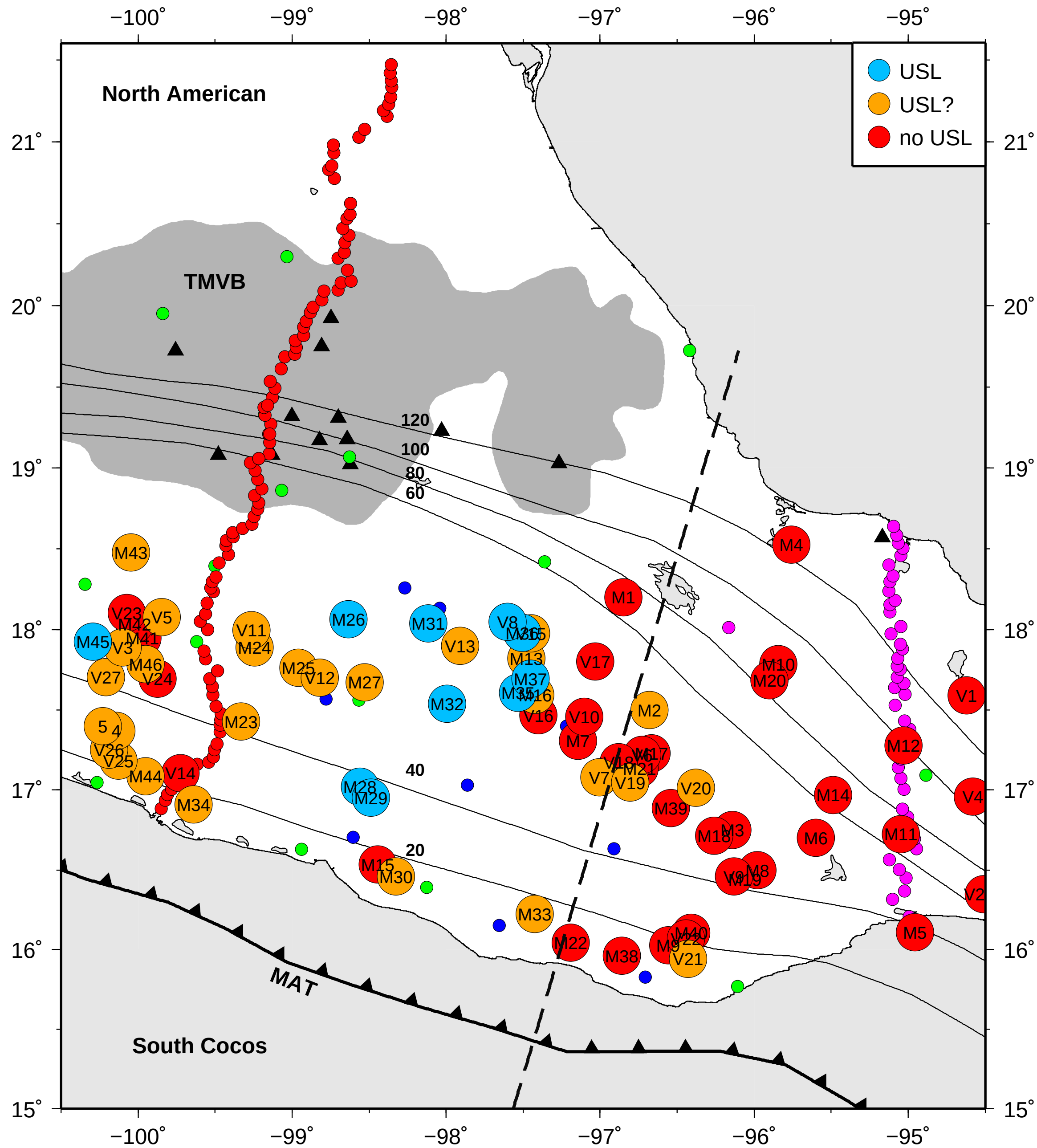

Figure 3.17: Enlarged map of the eastern lateral extent of the USL using MASE, VEOX, SSN, and OXNET P waveforms, including event labels. Events which indicate the presence of the USL are shown in cyan. Those which possibly indicate the USL is present are shown in orange. Red events indicate no USL is present.

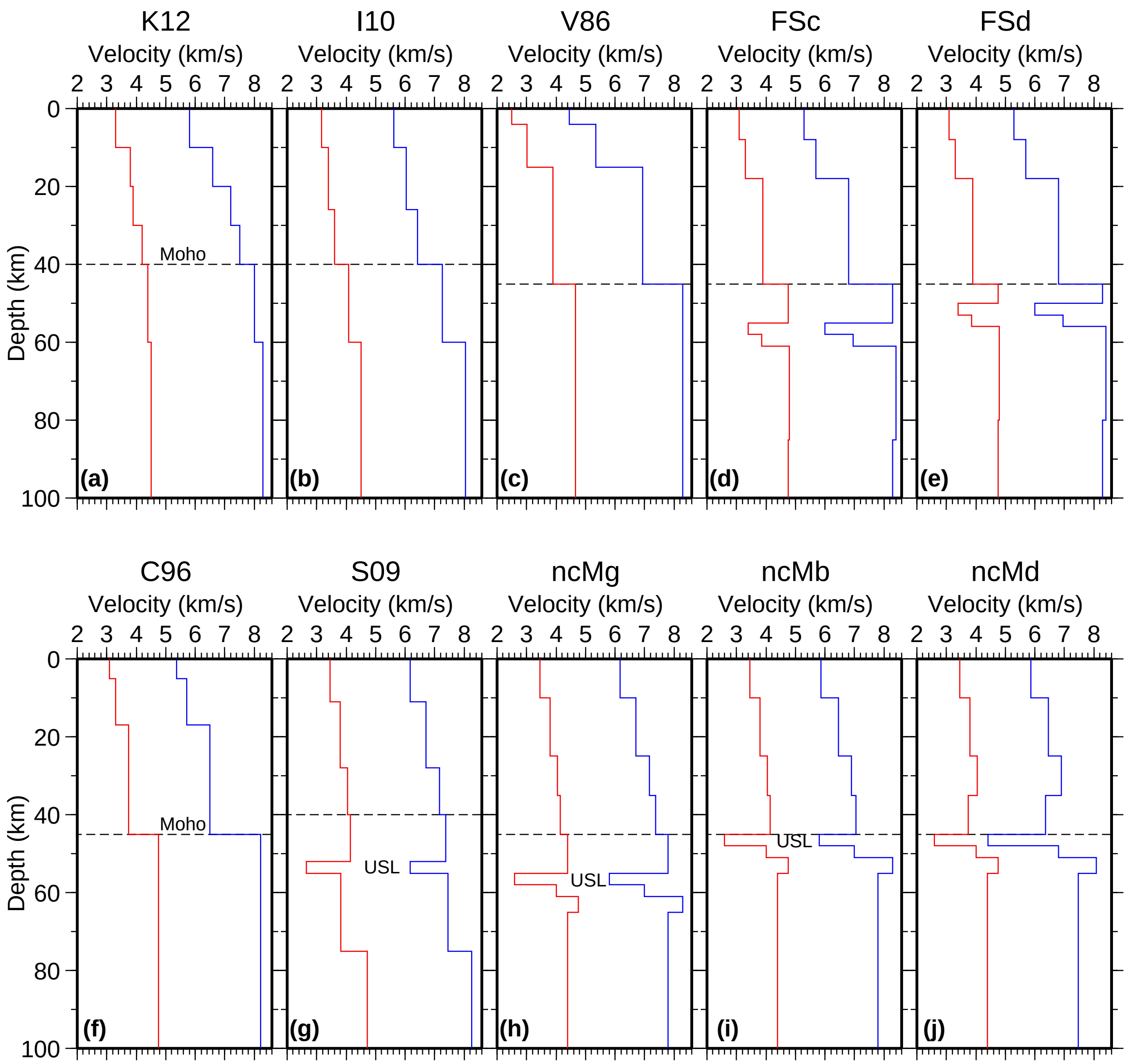

Figure 3.18: Additional 1D P (blue) and S (red) wave velocity models tested in this study. (a) Composite central Mexico velocity model from *Kim et al.* (2012) (K12). The Moho depth is indicated by the black dashed line. (b) Central Mexico velocity model from surface wave tomography study by *Iglesias et al.* (2010) (I10) using the MASE array. (c) Central Mexico velocity model from seismic refraction study by *Valdes et al.* (1986) (V86). (d) *Furumura and Singh* (2002) velocity model including the slab and 10 km of intervening mantle (FSc). (e) *Furumura and Singh* (2002) velocity model including the slab and 5 km of intervening mantle (FSd). (f) Central Mexico velocity model from group velocity dispersion study by *Campillo et al.* (1996) (C96). (g) Central Mexico velocity model from waveform modeling study along the MASE array by *Song et al.* (2009) (S09). Ultra-slow velocity layer (USL) is indicated at the top of the subducted plate. (h) New central Mexico velocity model from *Dougherty et al.* (2012) with a 10-km gap between the slab and overriding plate (ncMg). (i) Modified ncM velocity model with re-calculated P-wave velocities for the overriding plate (ncMb). (j) Modified ncM velocity model with re-calculated P-wave velocities for all layers and decreased P- and S-wave velocities in the lower crust of the overriding plate (ncMd).

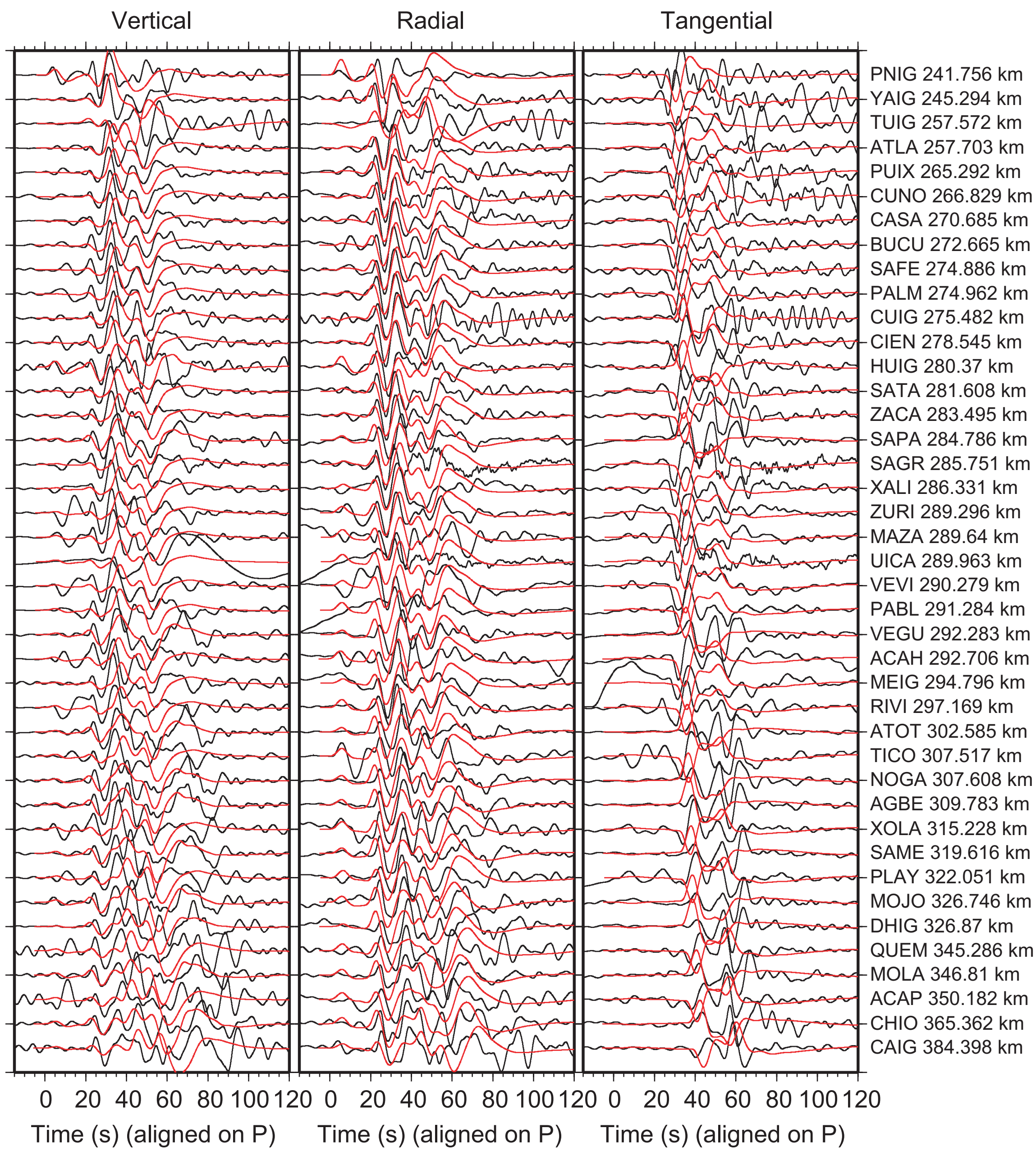

Figure 3.19: 1D modeling results of event M1 for the ncMc velocity model filtered to 0.01–0.1 Hz and plotted without station overlap. Data from MASE and SSN stations are in black, synthetics are in red.

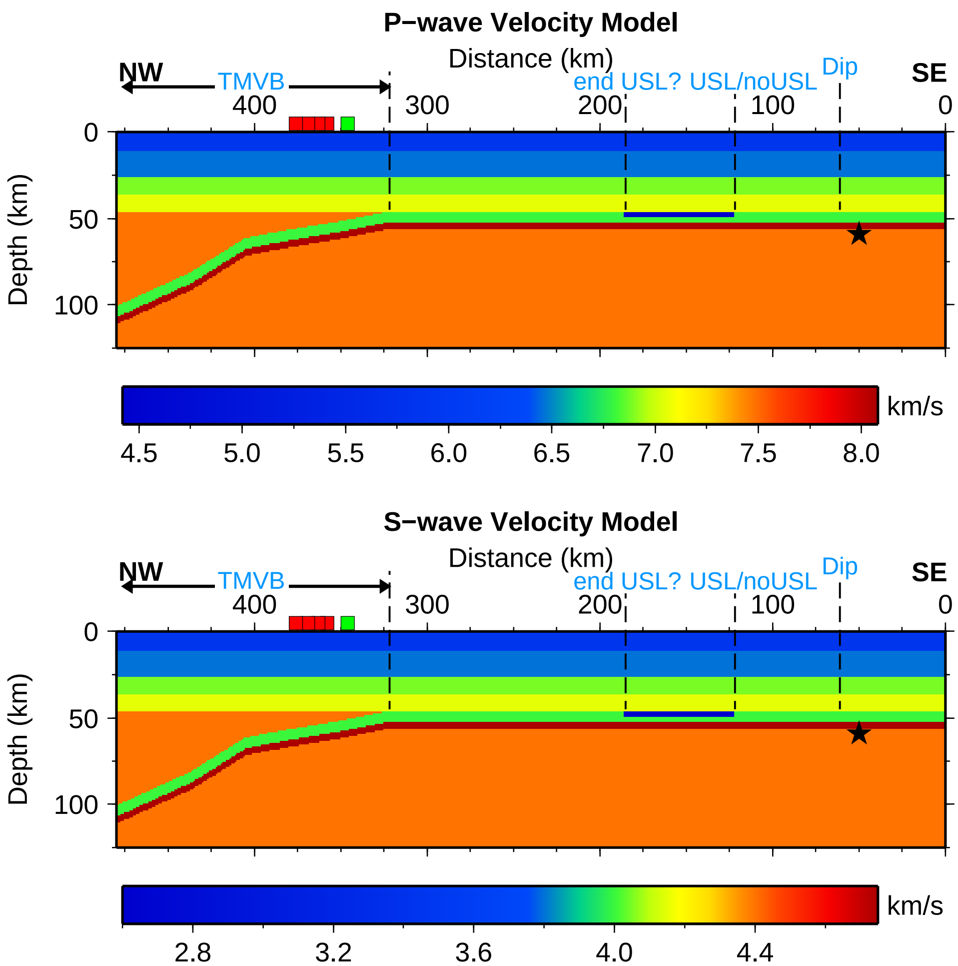

Figure 3.20: 2D velocity model of the shallow subduction zone structure across the SSN (green square) and MASE (red squares) arrays along the NW-SE profile for event M2 in Figure 3.12. P- and S-wave velocities are from the ncMc model. Subducted slab shape is estimated from the isodepth contours. Locations of the approximate end of the possible USL (USL?) zone, the intersection of the boundaries of the USL and no USL zones, the sharp transition in slab dip, and the TMVB are indicated for reference. The location of event M2 used in the modeling is shown by the black star.

Figure 3.21 *(following page)*: Comparison of 2D modeling results of event M2 along the NW-SE profile for twelve different models at three stations, filtered to 0.01–0.1 Hz. Data are in black, synthetics are in red. Vertical (Z) and radial (R) components are shown. P (dashed line), sP (green arrow), and S (pink arrow) arrivals are indicated. The primary variance among the models was the USL: ncMc = USL continues across entire width of model without an end; end1 = USL stops at approximate northern boundary of the USL zone; end2 = USL stops at approximate northern boundary of the USL? zone; bound1 = USL present between the northern boundary of the USL zone and the intersection of the USL and no USL zone boundaries; bound2 = USL present between the northern boundary of the USL? zone and the intersection of the USL and no USL zone boundaries (preferred model); noUSL = no USL present, thicker lower oceanic crust to compensate; end1+25, end1+50 = USL boundary shifted 25 km, 50 km, respectively, to the northwest; end1−25, end1−50 = USL boundary shifted 25 km, 50 km, respectively, to the southeast; end2−25 = USL? boundary shifted 25 km to the southeast; bound2−25 = intersection of the USL and no USL zone boundaries shifted 25 km to the southeast. Segment of waveform illustrating greatest variance among the models is shaded grey. Cross-correlation coefficients (X) for each model with the data for the selected segment are shown.

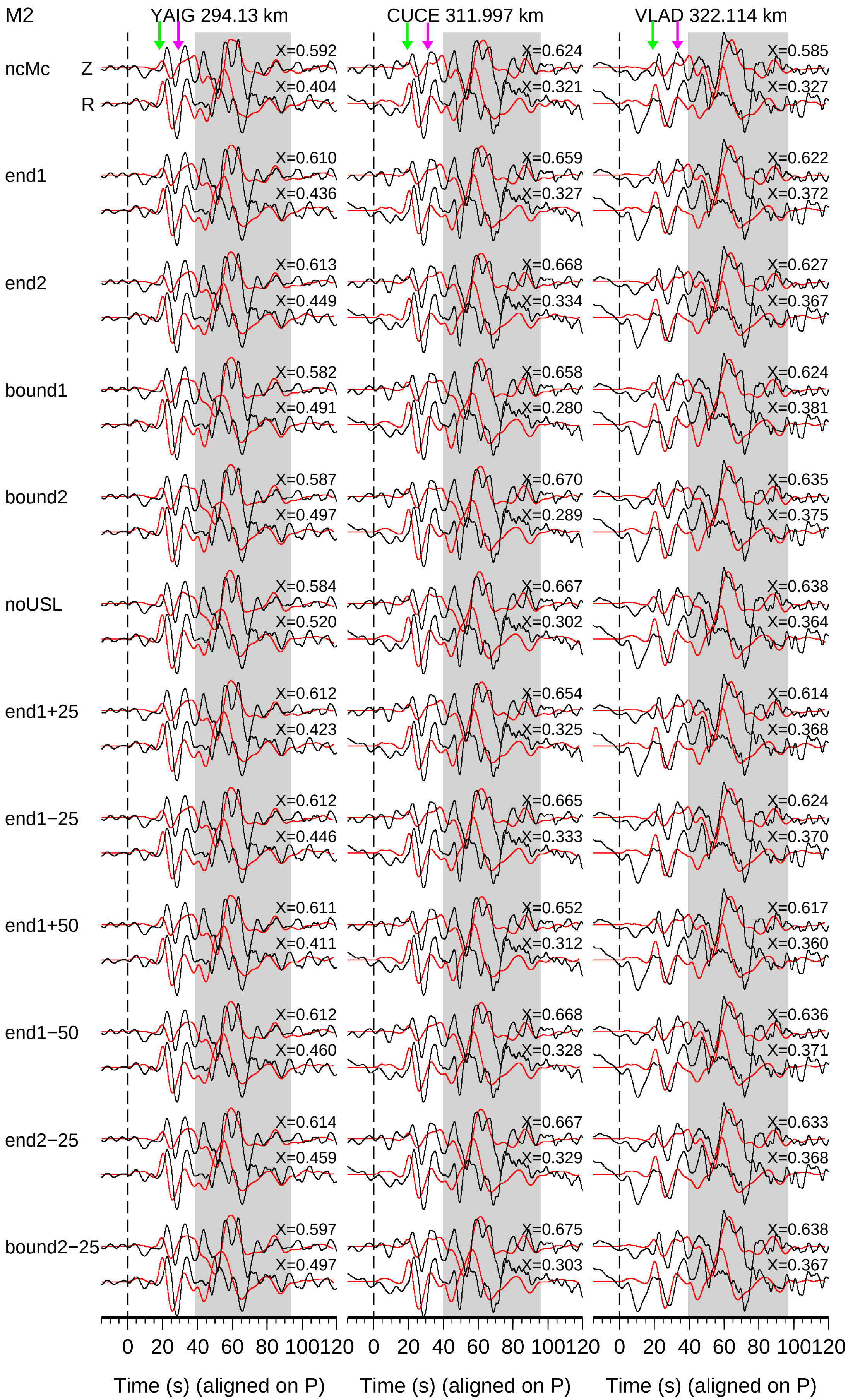
M2
YAIG 294.13 km
CUCE 311.997 km
VLAD 322.114 km
ncMc
Z
R
X=0.592
X=0.404
X=0.624
X=0.321
X=0.585
X=0.327
end1
X=0.610
X=0.436
X=0.659
X=0.327
X=0.622
X=0.372
end2
X=0.613
X=0.449
X=0.668
X=0.334
X=0.627
X=0.367
bound1
X=0.582
X=0.491
X=0.658
X=0.280
X=0.624
X=0.381
bound2
X=0.587
X=0.497
X=0.670
X=0.289
X=0.635
X=0.375
noUSL
X=0.584
X=0.520
X=0.667
X=0.302
X=0.638
X=0.364
end1+25
X=0.612
X=0.423
X=0.654
X=0.325
X=0.614
X=0.368
end1−25
X=0.612
X=0.446
X=0.665
X=0.333
X=0.624
X=0.370
end1+50
X=0.611
X=0.411
X=0.652
X=0.312
X=0.617
X=0.360
end1−50
X=0.612
X=0.460
X=0.668
X=0.328
X=0.636
X=0.371
end2−25
X=0.614
X=0.459
X=0.667
X=0.329
X=0.633
X=0.368
bound2−25
X=0.597
X=0.497
X=0.675
X=0.303
X=0.638
X=0.367
0 20 40 60 80 100 120
Time (s) (aligned on P)
0 20 40 60 80 100 120
Time (s) (aligned on P)
0 20 40 60 80 100 120
Time (s) (aligned on P)

References

Abt, D. L., K. M. Fischer, G. A. Abers, M. Protti, V. Gonzalez, and W. Strauch (2010), Constraints on upper mantle anisotropy surrounding the Cocos slab from SK(K)S splitting, *J. Geophys. Res.*, *115*, B06316, doi:10.1029/2009JB006710.

Alberto, C. A. O. (2010), Caracterización de la geometría de la zona benioff con una red densa de banda ancha en el istmo de Tehuantepec, Ph.D. thesis, Natl. Auton. Univ. of Mex., Mexico City.

Bandy, W., C. Mortera-Gutierrez, J. Urrutia-Fucugauchi, and T. W. C. Hilde (1995), The subducted Rivera-Cocos plate boundary: Where is it, what is it, and what is its relationship to the Colima rift?, *Geophys. Res. Lett.*, *22*, 3075–3078.

Bandy, W. L., T. W. C. Hilde, and C.-Y. Yan (2000), The Rivera-Cocos plate boundary: Implications for Rivera-Cocos relative motion and plate fragmentation, in *Cenozoic Tectonics and Volcanism of Mexico*, *Geol. Soc. Am. Spec. Pap.*, vol. 334, edited by H. Delgado-Granados, G. Aguirre-Díaz, and J. M. Stock, pp. 1–28, GSA, Boulder, Colorado.

Batiza, R., T. L. Smith, and Y. Niu (1989), Geological and petrologic evolution of seamounts near the EPR based on submersible and camera study, *Mar. Geophys. Res.*, *11*, 169–236.

Bilich, A., C. Frohlich, and P. Mann (2001), Global seismicity characteristics of subduction-to-strike-slip transitions, *J. Geophys. Res.*, *106*, 19,443–19,452.

Bonnardot, M.-A., M. Régnier, C. Christova, E. Ruellan, and E. Tric (2009), Seismological evidence for a slab detachment in the Tonga subduction zone, *Tectonophysics*, *464*, 84–99, doi:10.1016/j.tecto.2008.10.011.

Brudzinski, M. R., H. R. Hinojosa-Prieto, K. M. Schlanser, E. Cabral-Cano, A. Arciniega-Ceballos, O. Diaz-Molina, and C. DeMets (2010), Nonvolcanic tremor along the Oaxaca segment of the Middle America subduction zone, *J. Geophys. Res.*, *115*, B00A23, doi:10.1029/2008JB006061.

Burbach, G. V., C. Frohlich, W. D. Pennington, and T. Matumoto (1984), Seismicity and tectonics of the subducted Cocos plate, *J. Geophys. Res.*, *89*, 7719–7735.

Burkett, E. R., and M. I. Billen (2010), Three-dimensionality of slab detachment due to ridge-trench collision: Laterally simultaneous boudinage versus tear propagation, *Geochem. Geophys. Geosyst.*, *11*, Q11012, doi:10.1029/2010GC003286.

Cahill, T. A., and B. L. Isacks (1992), Seismicity and shape of the subducted Nazca plate, *J. Geophys. Res.*, *97*, 17,503–17,529.

Campillo, M., S. K. Singh, N. Shapiro, J. Pacheco, and R. B. Herrmann (1996), Crustal structure south of the Mexican volcanic belt, based on group velocity dispersion, *Geofís. Int.*, *35*, 361–370.

Chatelain, J.-L., P. Molnar, R. Prévot, and B. Isacks (1992), Detachment of part of the downgiong slab and uplift of the New Hebrides (Vanuatu) Islands, *Geophys. Res. Lett.*, *19*, 1507–1510.

Chen, T., and R. W. Clayton (2012), Structure of central and southern Mexico from velocity and attenuation tomography, *J. Geophys. Res.*, *117*, B09302, doi:10.1029/2012JB009233.

Clark, S. A., M. Sobiesiak, C. A. Zelt, M. B. Magnani, M. S. Miller, M. J. Bezada, and A. Levander (2008), Identification and tectonic implications of a tear in the South American plate at the southern end of the Lesser Antilles, *Geochem. Geophys. Geosyst.*, *9*, Q11004, doi:10.1029/2008GC002084.

Cloos, M. (1992), Thrust-type subduction-zone earthquakes and seamount asperities: A physical model for seismic rupture, *Geology*, *20*, 601–604.

D'Amico, S., B. Orecchio, D. Presti, L. Zhu, and R. B. Herrmann (2010), Broadband waveform inversion of moderate earthquakes in the Messina Straits, southern Italy, *Phys. Earth Planet. Inter.*, *179*, 97–106, doi:10.1016/j.pepi.2010.01.012.

D'Amico, S., B. Orecchio, D. Presti, A. Gervasi, L. Zhu, I. Guerra, G. Neri, and R. B. Herrmann (2011), Testing the stability of moment tensor solutions for small earthquakes in the Calabro-Peloritan Arc region (southern Italy), *Boll. Geofis. Teor. Appl.*, *52*, 283–298, doi:10.4430/bgta0009.

DeMets, C., and S. Traylen (2000), Motion of the Rivera plate since 10 Ma relative to the Pacific and North American plates and the mantle, *Tectonophysics*, *318*, 119–159.

DeMets, C., R. G. Gordon, and D. F. Argus (2010), Geologically current plate motions, *Geophys. J. Int.*, *181*, 1–80, doi:10.1111/j.1365-246X.2009.04491.x.

Dougherty, S. L., R. W. Clayton, and D. V. Helmberger (2012), Seismic structure in central Mexico: Implications for fragmentation of the subducted Cocos plate, *J. Geophys. Res.*, *117*, B09316, doi:10.1029/2012JB009528.

Dziewonski, A. M., T.-A. Chou, and J. H. Woodhouse (1981), Determination of earthquake source parameters from waveform data for studies of global and regional seismicity, *J. Geophys. Res.*, *86*, 2825–2852, doi:10.1029/JB086iB04p02825.

Ekström, G., M. Nettles, and A. M. Dziewonski (2012), The global CMT project 2004-2010: Centroid-moment tensors for 13,017 earthquakes, *Phys. Earth Planet. Inter.*, *200-201*, 1–9, doi: 10.1016/j.pepi.2012.04.002.

Ferrari, L. (2004), Slab detachment control on mafic volcanic pulse and mantle heterogeneity in central Mexico, *Geology*, *32*, 77–80, doi:10.1130/G19887.1.

Ferrari, L., T. Tagami, M. Eguchi, M. T. Orozco-Esquivel, C. M. Petrone, J. Jacobo-Albarrán, and M. López-Martínez (2005), Geology, geochronology and tectonic setting of late Cenozoic volcanism along the southwestern Gulf of Mexico: The Eastern Alkaline Province revisited, *J. Volcanol. Geotherm. Res.*, *146*, 284–306, doi:10.1016/j.jvolgeores.2005.02.004.

Ferrari, L., T. Orozco-Esquivel, V. Manea, and M. Manea (2011), The dynamic history of the Trans-Mexican Volcanic Belt and the Mexico subduction zone, *Tectonophysics*, *522-523*, 122–149, doi:10.1016/j.tecto.2011.09.018.

Franco, S. I., V. Kostoglodov, K. M. Larson, V. C. Manea, M. Manea, and J. A. Santiago (2005), Propagation of the 2001-2002 silent earthquake and interplate coupling in the Oaxaca subduction zone, Mexico, *Earth Planets Space*, *57*, 973–985.

Fryer, P., N. Becker, B. Appelgate, F. Martinez, M. Edwards, and G. Fryer (2003), Why is the Challenger Deep so deep?, *Earth Planet. Sci. Lett.*, *211*, 259–269.

Furumura, T., and S. K. Singh (2002), Regional wave propagation from Mexican subduction zone earthquakes: The attenuation functions for interplate and inslab events, *Bull. Seis. Soc. Am.*, *92*, 2110–2125, doi:10.1785/0120010278.

Gasparon, M., G. Rosenbaum, J. Wijbrans, and P. Manetti (2009), The transition from subduction arc to slab tearing: Evidence from Capraia island, northern Tyrrhenian sea, *J. Geodyn.*, *47*, 30–38.

Gómez-Tuena, A., M. T. Orozco-Esquivel, and L. Ferrari (2007), Igneous petrogenesis of the Trans-Mexican Volcanic Belt, in *Geology of Mexico*, *Spec. Pap. Geol. Soc. Am.*, vol. 422, edited by S. A. Alaniz-Alvarez and A. F. Nieto-Samaniego, pp. 129–181, GSA, Boulder, Colorado.

Gorbatov, A., and Y. Fukao (2005), Tomographic search for missing link between the ancient Farallon subduction and the present Cocos subduction, *Geophys. J. Int.*, *160*, 849–854, doi:10.1111/j.1365-246X.2005.02507.x.

Govers, R., and M. J. R. Wortel (2005), Lithosphere tearing at STEP faults: Response to edges of subduction zones, *Earth Planet. Sci. Lett.*, *236*, 505–523, doi:10.1016/j.epsl.2005.03.022.

Gutscher, M.-A., J. Malavieille, S. Lallemand, and J.-Y. Collot (1999), Tectonic segmentation of the North Andean margin: impact of the Carnegie Ridge collision, *Earth Planet. Sci. Lett.*, *168*, 255–270.

Hale, A. J., K.-D. Gottschaldt, G. Rosenbaum, L. Bourgouin, M. Bauchy, and H. Mühlhaus (2010), Dynamics of slab tear faults: Insights from numerical modelling, *Tectonophysics*, *483*, 58–70, doi:10.1016/j.tecto.2009.05.019.

Husker, A., and P. M. Davis (2009), Tomography and thermal state of the Cocos plate subduction beneath Mexico City, *J. Geophys. Res.*, *114*, B04306, doi:10.1029/2008JB006039.

Iglesias, A., R. W. Clayton, X. Pérez-Campos, S. K. Singh, J. F. Pacheco, D. García, and C. Valdés-González (2010), S wave velocity structure below central Mexico using high-resolution surface wave tomography, *J. Geophys. Res.*, *115*, B06307, doi:10.1029/2009JB006332.

International Seismological Centre (2011), *On-line Bulletin*, Int. Seis. Cent., Thatcham, United Kingdom, http://www.isc.ac.uk.

Isacks, B. L., and M. Barazangi (1977), Geometry of Benioff zones: Lateral segmentation and downwards bending of the subducted lithosphere, in *Island Arcs, Deep Sea Trenches and Back-Arc Basins*, *Maurice Ewing Series*, vol. 1, edited by M. Talwani and W. C. Pitman, pp. 99–114, American Geophysical Union, Washington, D. C.

Jadamec, M. A., and M. I. Billen (2010), Reconciling surface plate motions with rapid three-dimensional mantle flow around a slab edge, *Nature*, *465*, 338–341, doi:10.1038/nature09053.

Johnston, S. T., and D. J. Thorkelson (1997), Cocos-Nazca slab window beneath central America, *Earth Planet. Sci. Lett.*, *146*, 465–474.

Kanjorski, N. M. (2003), Cocos plate structure along the Middle America subduction zone off Oaxaca and Guerrero, Mexico: Influence of subducting plate morphology on tectonics and seismicity, Ph.D. thesis, Univ. of Calif., San Diego.

Kim, Y., R. W. Clayton, and J. M. Jackson (2010), Geometry and seismic properties of the subducting Cocos plate in central Mexico, *J. Geophys. Res.*, *115*, B06310, doi:10.1029/2009JB006942.

Kim, Y., R. W. Clayton, and F. Keppie (2011), Evidence of a collision between the Yucatán Block and Mexico in the Miocene, *Geophys. J. Int.*, *187*, 989–1000, doi:10.1111/j.1365-246X.2011.05191.x.

Kim, Y., M. S. Miller, F. Pearce, and R. W. Clayton (2012), Seismic imaging of the Cocos plate subduction zone system in central Mexico, *Geochem. Geophys. Geosyst.*, *13*, Q07001, doi:10.1029/2012GC004033.

Kim, Y., R. W. Clayton, P. D. Asimow, and J. M. Jackson (2013), Generation of talc in the mantle wedge and its role in subduction dynamics in central Mexico, *Earth Planet. Sci. Lett.*, *384*, 81–87, doi:10.1016/j.epsl.2013.10.006.

Klitgord, K. D., and J. Mammerickx (1982), Northern East Pacific Rise: Magnetic anomaly and bathymetric framework, *J. Geophys. Res.*, *87*, 6725–6750.

Kneller, E. A., and P. E. van Keken (2008), Effect of three-dimensional slab geometry on deformation in the mantle wedge: Implications for shear wave anisotropy, *Geochem. Geophys. Geosyst.*, *9*, Q01003, doi:10.1029/2007GC001677.

Kopp, H. (2013), Invited review paper: The control of subduction zone structural complexity and geometry on margin segmentation and seismicity, *Tectonophysics*, *589*, 1–16, doi:10.1016/j.tecto.2012.12.037.

Lin, J.-Y., S.-K. Hsu, and J.-C. Sibuet (2004), Melting features along the Ryukyu slab tear, beneath the southwestern Okinawa Trough, *Geophys. Res. Lett.*, *31*, L19607, doi:10.1029/2004GL020862.

Lonsdale, P. (2005), Creation of the Cocos and Nazca plates by fission of the Farallon plate, *Tectonophysics*, *404*, 237–264, doi:10.1016/j.tecto.2005.05.011.

Macías, J. L. (2007), Geology and eruptive history of some active volcanoes of Mexico, in *Geology of Mexico*, *Spec. Pap. Geol. Soc. Am.*, vol. 422, pp. 183–232, GSA, Boulder, Colorado.

Mammerickx, J., and K. D. Klitgord (1982), Northern East Pacific Rise: Evolution from 25 m.y. B.P. to the present, *J. Geophys. Res.*, *87*, 6751–6759.

Manea, V., and M. Gurnis (2007), Subduction zone evolution and low viscosity wedges and channels, *Earth Planet. Sci. Lett.*, *264*, 22–45, doi:10.1016/j.epsl.2007.08.030.

Manea, V. C., M. Manea, V. Kostoglodov, C. A. Currie, and G. Sewell (2004), Thermal structure, coupling and metamorphism in the Mexican subduction zone beneath Guerrero, *Geophys. J. Int.*, *158*, 775–784, doi:10.1111/j.1365-246X.2004.02325.x.

Manea, V. C., M. Manea, V. Kostoglodov, and G. Sewell (2006), Intraslab seismicity and thermal stress in the subducted Cocos plate beneath central Mexico, *Tectonophysics*, *420*, 389–408, doi: 10.1016/j.tecto.2006.03.029.

Manea, V. C., M. Manea, and L. Ferrari (2013), A geodynamical perspective on the subduction of Cocos and Rivera plates beneath Mexico and Central America, *Tectonophysics*, *609*, 56–81, doi:10.1016/j.tecto.2012.12.039.

MASE (2007), Meso America Subduction Experiment, Caltech, dataset, doi:10.7909/C3RN35SP.

Mason, W. G., L. Moresi, P. G. Betts, and M. S. Miller (2010), Three-dimensional numerical models of the influence of a buoyant oceanic plateau on subduction zones, *Tectonophysics*, *483*, 71–79, doi:10.1016/j.tecto.2009.08.021.

McClain, J. S., and M. A. Wright (1990), The morphology and structure of the West O'Gorman Fracture Zone, *Mar. Geophys. Res.*, *12*, 317–328.

McCrory, P. A., J. L. Blair, F. Waldhauser, and D. H. Oppenheimer (2012), Juan de Fuca slab geometry and its relation to Wadati-Benioff zone seismicity, *J. Geophys. Res.*, *117*, B09306, doi: 10.1029/2012JB009407.

Meighan, H. E., J. Pulliam, U. ten Brink, and A. M. López-Venegas (2013a), Seismic evidence for a slab tear at the Puerto Rico Trench, *J. Geophys. Res.*, *118*, doi:10.1002/jgrb.50227.

Meighan, H. E., U. ten Brink, and J. Pulliam (2013b), Slab tears and intermediate-depth seismicity, *Geophys. Res. Lett.*, *40*, 4244–4248, doi:10.1002/grl.50830.

Melgar, D., and X. Pérez-Campos (2011), Imaging the Moho and subducted oceanic crust at the Isthmus of Tehuantepec, Mexico, from receiver functions, *Pure Appl. Geophys.*, *168*, 1449–1460, doi:10.1007/s00024-010-0199-5.

Millen, D. W., and M. W. Hamburger (1998), Seismological evidence for tearing of the Pacific plate at the northern termination of the Tonga subduction zone, *Geology*, *26*, 659–662.

Miller, M. S., B. L. N. Kennett, and G. S. Lister (2004), Imaging changes in morphology, geometry, and physical properties of the subducting Pacific plate along the Izu-Bonin-Mariana arc, *Earth Planet. Sci. Lett.*, *224*, 363–370, doi:10.1016/j.epsl.2004.05.018.

Miller, M. S., A. Gorbatov, and B. L. N. Kennett (2005), Heterogeneity within the subducting Pacific slab beneath the Izu-Bonin-Mariana arc: Evidence from tomography using 3D ray tracing inversion techniques, *Earth Planet. Sci. Lett.*, *235*, 331–342, doi:10.1016/j.epsl.2005.04.007.

Miller, M. S., A. Gorbatov, and B. L. N. Kennett (2006), Three-dimensional visualization of a near-vertical slab tear beneath the southern Mariana arc, *Geochem. Geophys. Geosyst.*, *7*, Q06012, doi:10.1029/2005GC001110.

Miller, M. S., A. Levander, F. Niu, and A. Li (2009), Upper mantle structure beneath the Caribbean-South American plate boundary from surface wave tomography, *J. Geophys. Res.*, *114*, B01312, doi:10.1029/2007JB005507.

Nelson, S. A., E. Gonzalez-Caver, and T. K. Kyser (1995), Constraints on the origin of alkaline and calc-alkaline magmas from the Tuxtla Volcanic Field, Veracruz, Mexico, *Contrib. Mineral. Petrol.*, *122*, 191–211.

Nolet, G. (2009), Slabs do not go gently, *Science*, *324*, 1152–1153, doi:10.1126/science.1174664.

Pacheco, J. F., and S. K. Singh (2010), Seismicity and state of stress in Guerrero segment of the Mexican subduction zone, *J. Geophys. Res.*, *115*, B01303, doi:10.1029/2009JB006453.

Pardo, M., and G. Suárez (1995), Shape of the subducted Rivera and Cocos plates in southern Mexico: Seismic and tectonic implications, *J. Geophys. Res.*, *100*, 12,357–12,373.

Pérez-Campos, X., Y. Kim, A. Husker, P. M. Davis, R. W. Clayton, A. Iglesias, J. F. Pacheco, S. K. Singh, V. C. Manea, and M. Gurnis (2008), Horizontal subduction and truncation of the Cocos Plate beneath central Mexico, *Geophys. Res. Lett.*, *35*, L18303, doi:10.1029/2008GL035127.

Pesicek, J. D., E. R. Engdahl, C. H. Thurber, H. R. DeShon, and D. Lange (2012), Mantle subducting slab structure in the region of the 2010 M8.8 Maule earthquake (30-40°S), Chile, *Geophys. J. Int.*, *191*, 317–324, doi:10.1111/j.1365-246X.2012.05624.x.

Peyton, V., V. Levin, J. Park, M. Brandon, J. Lees, E. Gordeev, and A. Ozerov (2001), Mantle flow at a slab edge: Seismic anisotropy in the Kamchatka region, *Geophys. Res. Lett.*, *28*, 379–382.

Protti, M., F. Gündel, and K. McNally (1994), The geometry of the Wadati-Benioff zone under southern Central America and its tectonic significance: results from a high-resolution local seismograph network, *Phys. Earth Planet. Inter.*, *84*, 271–287.

Rebollar, C. J., V. H. Espíndola, A. Uribe, A. Mendoza, and A. Pérez-Vertti (1999), Distributions of stresses and geometry of the Wadati-Benioff zone under Chiapas, Mexico, *Geofís. Int.*, *38*, 95–106.

Rosenbaum, G., M. Gasparon, F. P. Lucente, A. Peccerillo, and M. S. Miller (2008), Kinematics of slab tear faults during subduction segmentation and implications for Italian magmatism, *Tectonics*, *27*, TC2008, doi:10.1029/2007TC002143.

Russo, R. M., and P. G. Silver (1994), Trench-parallel flow beneath the Nazca plate from seismic anisotropy, *Science*, *263*, 1105–1111.

Russo, R. M., R. C. Speed, E. A. Okal, J. B. Shepherd, and K. C. Rowley (1993), Seismicity and tectonics of the southeastern Caribbean, *J. Geophys. Res.*, *98*, 14,299–14,319.

Schellart, W. P. (2004), Kinematics of subduction and subduction-induced flow in the upper mantle, *J. Geophys. Res.*, *109*, B07401, doi:10.1029/2004JB002970.

Schellart, W. P., J. Freeman, D. R. Stegman, L. Moresi, and D. May (2007), Evolution and diversity of subduction zones controlled by slab width, *Nature*, *446*, 308–311, doi:10.1038/nature05615.

Scholz, C. H., and C. Small (1997), The effect of seamount subduction on seismic coupling, *Geology*, *25*, 487–490.

Singh, S. K., and F. Mortera (1991), Source time functions of large Mexican subduction earthquakes, morphology of the Benioff zone, age of the plate, and their tectonic implications, *J. Geophys. Res.*, *96*, 21,487–21,502.

Singh, S. K., and M. Pardo (1993), Geometry of the Benioff zone and state of stress in the overriding plate in central Mexico, *Geophys. Res. Lett.*, *20*, 1483–1486.

Song, T. A., D. V. Helmberger, M. R. Brudzinski, R. W. Clayton, P. Davis, X. Pérez-Campos, and S. K. Singh (2009), Subducting slab ultra-slow velocity layer coincident with silent earthquakes in southern Mexico, *Science*, *324*, 502–506.

Soto, G. L., J. F. Ni, S. P. Grand, E. Sandvol, R. W. Valenzuela, M. G. Speziale, J. M. G. González, and T. D. Reyes (2009), Mantle flow in the Rivera-Cocos subduction zone, *Geophys. J. Int.*, *179*, 1004–1012, doi:10.1111/j.1365-246X.2009.04352.x.

Stubailo, I., C. Beghein, and P. M. Davis (2012), Structure and anisotropy of the Mexico subduction zone based on Rayleigh-wave analysis and implications for the geometry of the Trans-Mexican Volcanic Belt, *J. Geophys. Res.*, *117*, B05303, doi:10.1029/2011JB008631.

Suckale, J., S. Rondenay, M. Sachpazi, M. Charalampakis, A. Hosa, and L. H. Royden (2009), High-resolution seismic imaging of the western Hellenic subduction zone using teleseismic scattered waves, *Geophys. J. Int.*, *178*, 775–791.

ten Brink, U. (2005), Vertical motions of the Puerto Rico Trench and Puerto Rico and their cause, *J. Geophys. Res.*, *110*, B06404, doi:10.1029/2004JB003459.

Valdes, C. M., W. D. Mooney, S. K. Singh, R. P. Meyer, C. Lomnitz, J. H. Luetgert, C. E. Helsley, B. T. R. Lewis, and M. Mena (1986), Crustal structure of Oaxaca, Mexico, from seismic refraction measurements, *Bull. Seis. Soc. Am.*, *76*, 547–563.

Vargas, C. A., and P. Mann (2013), Tearing and breaking off of subducted slabs as the result of collision of the Panama arc-indenter with northwestern South America, *Bull. Seis. Soc. Am.*, *103*, 2025–2046, doi:10.1785/0120120328.

VEOX (2010), Veracruz-Oaxaca Subduction Experiment, Caltech, dataset, doi: 10.7909/C3MW2F2C.

Verma, S. P. (2006), Extension-related origin of magmas from a garnet-bearing source in the Los Tuxtlas volcanic field, Mexico, *Int. J. Earth Sci.*, *95*, 871–901.

Wang, K., and S. L. Bilek (2011), Do subducting seamounts generate or stop large earthquakes?, *Geology*, *39*, 819–822, doi:10.1130/G31856.1.

Wortel, M. J. R., and W. Spakman (2000), Subduction and slab detachment in the Mediterranean-Carpathian Region, *Science*, *290*, 1910–1917.

Yang, H., Y. Liu, and J. Lin (2013), Geometrical effects of a subducted seamount on stopping megathrust ruptures, *Geophys. Res. Lett.*, *40*, 1–6, doi:10.1002/grl.50509.

Yang, T., S. P. Grand, D. Wilson, M. Guzman-Speziale, J. M. Gomez-Gonzalez, T. Dominguez-Reyes, and J. Ni (2009), Seismic structure beneath the Rivera subduction zone from finite-frequency seismic tomography, *J. Geophys. Res.*, *114*, B01302, doi:10.1029/2008JB005830.

Yogodzinski, G. M., J. M. Lees, T. G. Churikova, F. Dorendorf, G. Wöerner, and O. N. Volynets (2001), Geochemical evidence for the melting of subducting oceanic lithosphere at plate edges, *Nature*, *409*, 500–504.

Zandt, G., and E. Humphreys (2008), Toroidal mantle flow through the western U.S. slab window, *Geology*, *36*, 295–298, doi:10.1130/G24611A.1.

Zhao, L.-S., and D. V. Helmberger (1994), Source estimation from broadband regional seismograms, *Bull. Seis. Soc. Am.*, *84*, 91–104.

Zhu, L., and D. V. Helmberger (1996), Advancement in source estimation techniques using broadband regional seismograms, *Bull. Seis. Soc. Am.*, *86*, 1634–1641.

Zoback, M. L. (1992), First- and second-order patterns of stress in the lithosphere: The world stress map project, *J. Geophys. Res.*, *97*, 11,703–11,728.

Appendix

This appendix presents a summary map of the lateral extent of the ultra-slow velocity layer (USL) in central Mexico that was not included in the published papers (Figure 3.22). The events which occurred in western central Mexico and were analyzed in Chapter 2 are re-plotted here such that the status of the USL at each epicentral location is indicated. This is done to be consistent with the data presentation for eastern central Mexico shown in Chapter 3. The status of the USL at each epicentral event location can be either present, possibly present, or not present. Note that there are no events in western central Mexico which indicate the USL is possibly present; all events indicate that the USL is either there or not. Shaded contours of the USL and no USL zones in the west are drawn for comparison with the zones previously identified in the east. Additionally, the contour of the possible USL zone in the east is extended west of the MASE line to include events which were not contoured to be within the zone previously. A small no USL zone is also identified and contoured in this region west of the MASE line.

Overall, the USL and possible USL zones are located within the flat slab region, extending laterally across the shallow portions of the transitions from flat to normal subduction located on either side. These zones do not reach the more steeply dipping regions to the northwest and southeast, where the no USL zones are concentrated. The small no USL zone near the MASE line may reflect the lateral heterogeneity of the layer. Interestingly, the strongest presence of the USL is identified $\sim$50 km to the west and to the east of the MASE line, while a weaker USL is located along the array, where the layer was first identified and imaged (*Pérez-Campos et al.*, 2008; *Song et al.*, 2009; *Kim et al.*, 2010).

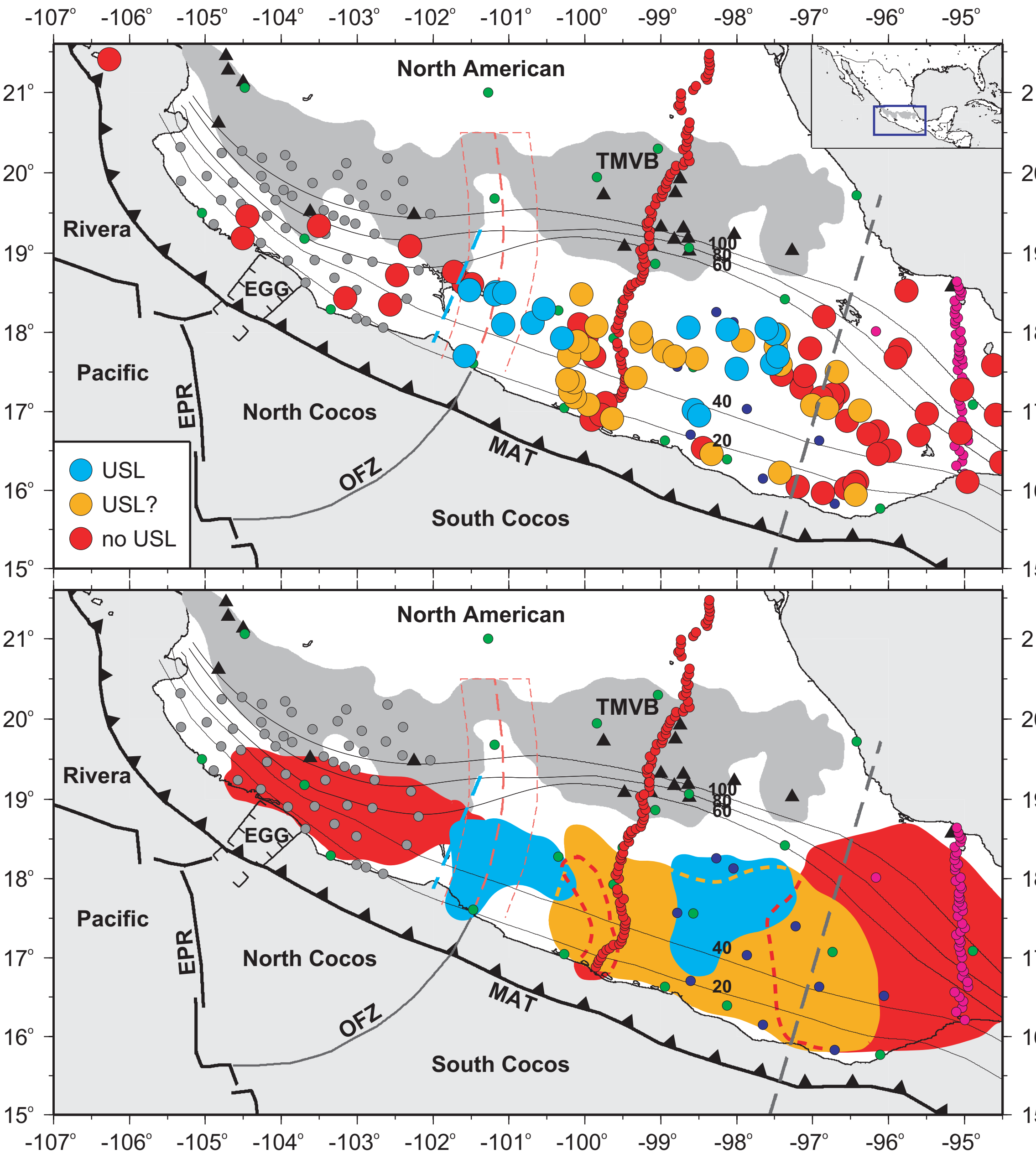

Figure 3.22: Summary map of the lateral extent of the USL in central Mexico using MARS (grey dots), MASE (red dots), VEOX (pink dots), SSN (green dots), and OXNET (blue dots) P waveforms. (top) Events which indicate the presence of the USL are shown in blue. Those which possibly indicate the USL is present are shown in orange. Red events indicate no USL is present. (bottom) Shaded contours of USL, possible USL, and no USL zones. The boundary between bins 13 and 14 of Figure 3.3, demarking the significant change in slab dip in the east, is denoted by the dark grey dashed line. The approximate location of the western edge of the USL atop the slab proposed in Figure 2.7 is indicated by the blue dashed line. The projected path of the Orozco Fracture Zone (OFZ) beneath the North American plate is shown as a thick, red dashed line, with thinner red dashed lines to either side delineating the estimated 100-km width of the fracture zone (*Blatter and Hammersley*, 2010). The dark grey shaded area indicates the Trans Mexican Volcanic Belt (TMVB), and the black triangles denote active volcanoes. Slab isodepth contours based on local seismicity and teleseismic receiver functions (*Pérez-Campos et al.*, 2008; *Kim et al.*, 2010, 2011; *Melgar and Pérez-Campos*, 2011) are shown in thin lines. Other abbreviations shown in the map are EPR, East Pacific Rise; MAT, Middle America Trench; EGG, El Gordo Graben.

Chapter 4

Seismic structure in southern Peru: Evidence for a smooth contortion between flat and normal subduction of the Nazca plate

4.1 Abstract

Rapid changes in slab geometry are typically associated with fragmentation of the subducted plate; however, continuous curvature of the slab is also possible. The transition from flat to normal subduction in southern Peru is one such geometrical change. The morphology of the subducted Nazca plate along this transition is explored using intraslab earthquakes recorded by temporary regional seismic arrays. Observations of a gradual increase in slab dip coupled with a lack of any gaps or vertical offsets in the intraslab seismicity suggest a smooth contortion of the slab. Concentrations of focal mechanisms at orientations which are indicative of slab bending are also observed along the change in slab geometry. The presence of a thin ultra-slow velocity layer (USL) atop the horizontal Nazca slab is identified and located. The lateral extent of this USL is coincident with the margin of the projected linear continuation of the subducting Nazca Ridge, implying a causal relationship. Waveform modeling of the 2D structure in southern Peru using a finite-difference algorithm provides constraints on the velocity and geometry of the slab's seismic structure and confirms the absence of any tears in the slab. The seismic and structural evidence suggests smooth contortion of the Nazca

plate along the transition from flat to normal subduction. The slab is estimated to have experienced 10% strain in the along-strike direction across this transition.

4.2 Introduction

The transition from flat to normal subduction may be accommodated by either a tear in the slab, as has been suggested in western (*Bandy et al.*, 2000; *Dougherty et al.*, 2012; *Stubailo et al.*, 2012) and eastern (*Dougherty and Clayton*, 2014) central Mexico, or a smooth contortion, such as that imaged in central Chile (*Pesicek et al.*, 2012). Here, we investigate the slab morphology across such a transition in southern Peru, where the Nazca plate is subducting beneath the South American plate at a convergence rate of $\sim$7.1 cm/yr along an azimuth of N77°E (*DeMets et al.*, 2010) (Figure 4.1). In the flat subduction region located north of $\sim$15°S, the slab dips at $\sim$30° near the trench to a depth of 100 km, then continues horizontally for $\sim$300 km before dipping steeply into the mantle (*Hasegawa and Sacks*, 1981; *Cahill and Isacks*, 1992). In the normal subduction region to the south, the slab dips at a constant $\sim$30° to at least 300 km depth (*Hasegawa and Sacks*, 1981; *Cahill and Isacks*, 1992). Previous studies of this transition region have suggested both tearing (e.g., *Barazangi and Isacks*, 1976, 1979; *Yamaoka et al.*, 1986) and continuous curvature (e.g., *Hasegawa and Sacks*, 1981; *Bevis and Isacks*, 1984; *Boyd et al.*, 1984; *Grange et al.*, 1984a; *Cahill and Isacks*, 1992; *Phillips and Clayton*, 2014) of the subducted Nazca plate. The approximate spatial coincidence of the subducting Nazca Ridge (*Barazangi and Isacks*, 1976, 1979) and the regional scale inflection in the shape of the western edge of the South American plate (*Bevis and Isacks*, 1984) with the transition in slab dip (Figure 4.2) has been used to identify possible causes of tearing or contortion, respectively, of the plate. The Nazca Ridge has been proposed to act as a line of weakness along which the slab may tear (*Barazangi and Isacks*, 1976, 1979; *Vogt et al.*, 1976); however, its location 150–200 km north of the bend in slab isodepth contours (*Cahill and Isacks*, 1992), coupled with its southward migration from 11°S since it intersected the trench $\sim$11.2 Ma (*Hampel*, 2002) make such tearing unlikely. Lateral flexure, on the other hand, may be part of the geometrical response of subduction of the Nazca plate beneath the concave shape of the overriding South American plate

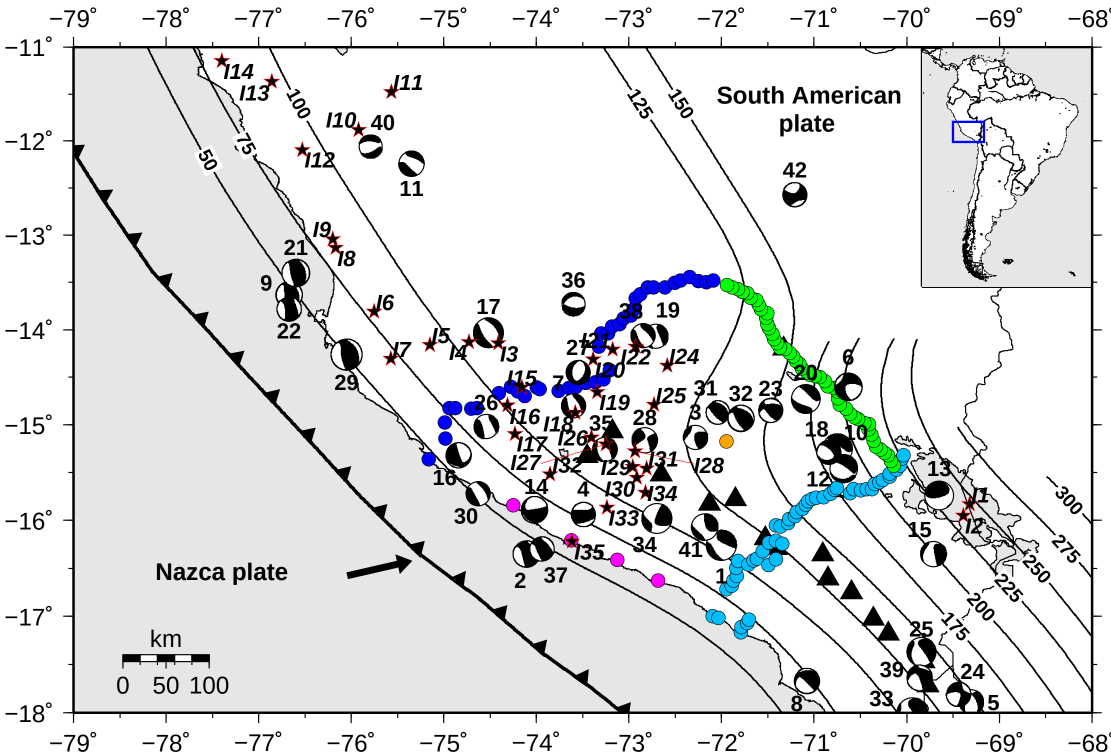

Figure 4.1: Map showing the locations of PeruSE and CAUGHT (orange dots) stations along with events (stars, focal mechanisms) used in this study. The PE (light blue dots), PF (green dots), PG (blue dots), and PH (pink dots) lines of the PeruSE array are shown. Focal mechanisms are from the Global Centroid Moment Tensor (GCMT) catalog (Table 4.1). Events from the International Seismological Centre (ISC) Bulletin event catalog are indicated by italicized labels. The black triangles denote Holocene volcanoes; note the lack of volcanism in the flat slab region. Slab isodepth contours from *Cahill and Isacks* (1992) are shown in thin lines. The convergence direction of the Nazca plate relative to the South American plate near the Peru-Chile Trench is indicated by the black arrow (*DeMets et al.*, 2010). See Figure 4.2 for station names.

(*Bevis and Isacks*, 1984).

A recent deployment of broadband seismometers in southern Peru overlying the transition from flat to normal subduction presents the opportunity to provide further constraints on the nature of this transition as either a smooth contortion or plate tear. Receiver functions along this array suggest a continuous slab with no clear breaks (*Phillips and Clayton*, 2014). In order to test this conclusion and expand on investigations of this region, we use regional earthquakes recorded by the Peru Subduction Experiment (PeruSE) (*PeruSE*, 2013) and Central Andes Uplift and Geodynamics of High Topography (CAUGHT) (*Ward et al.*, 2013) seismic arrays to study the fine-scale structure of the southern Peru subduction zone along the flat-to-normal transition (Figure 4.1). We

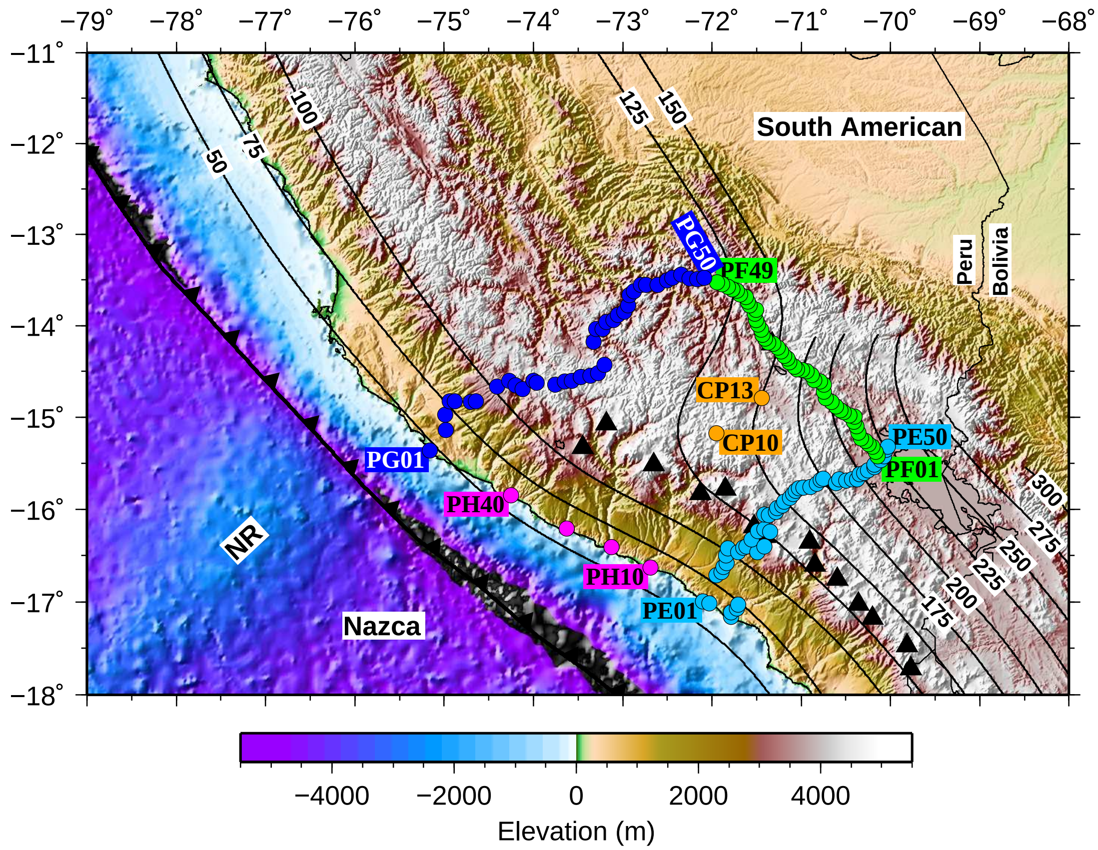

Figure 4.2: Topographic-bathymetric map illustrating the Nazca Ridge (NR) and the high elevation of the Andes. Station and volcano locations are as in Figure 4.1. Stations are numbered sequentially along each line (i.e., PE, PF, PG, and PH) of the PeruSE array with names for endpoint stations indicated. Station names for the two CAUGHT stations (orange dots) are also shown. Topography (*Farr et al.*, 2007) and bathymetry (*Smith and Sandwell*, 1997) data are from the SRTM30_PLUS version 2.0 dataset (http://topex.ucsd.edu/WWW_html/srtm30_plus.html).

analyze seismicity patterns and focal mechanism orientations for any indications of fragmentation or contortion of the subducted plate. We also explore structural features, such as a thin ultra-slow velocity layer (USL) atop the flat slab, that might constrain the slab morphology. Additionally, we perform 2D waveform modeling to image the structure of the subducted Nazca and overriding South American plates in this region, including any potential tears.

4.3 Data Analysis

4.3.1 Data

The seismic data used in this study were recorded by the PeruSE and CAUGHT arrays. The PeruSE array consisted of 100 broadband seismic instruments deployed progressively from July 2008 to February 2013 in four lines (i.e., PE, PF, PG, and PH), comprising a rectangular distribution of 154 stations (Figures 4.1 and 4.2), with each site occupied for ~2 years. The PE, PF, and PG lines each consisted of 50 stations with an average station spacing of ~6 km. The PE and PG lines were oriented perpendicular to the trench over the normal and flat subduction regions, respectively. The PF line was oriented parallel to the trench over the downdip flat-to-normal transition. The PH line consisted of 4 stations along the coast. The goal of this experiment was to image the structure of the Peruvian subduction zone in the flat slab, transitional, and normal dipping regions. The CAUGHT array consisted of 50 broadband seismic instruments deployed from November 2010 to August 2012 in a 2D geometry in the Central Andes of northern Bolivia and southern Peru (*Ward et al.*, 2013). Two stations of this array that are located within the interior of the box defined by the PeruSE array (Figure 4.2) are utilized in this study.

We analyze seismograms from 76 regional intraslab earthquakes recorded by these arrays. These events have magnitudes within the range of 4.0 to 6.4 and occur at depths between 46 and 258 km (Table 4.1). The locations of these events are shown in Figure 4.1. Earthquakes whose hypocenters are taken from the International Seismological Centre (ISC) Bulletin event catalog (*International Seismological Centre*, 2011) have identifiers that begin with 'I' (Figure 4.1, Table 4.1). All other events are from the Global Centroid Moment Tensor (GCMT) catalog (*Dziewonski et al.*, 1981; *Ekström et al.*, 2012).

Table 4.1. Events used in southern Peru and their source parameters.

Event ID	Date	Lat (°)	Lon (°)	Depth (km)	Mag	Mechanism Strike/Dip/Rake	Source[a]
1	2008/07/08	-16.26	-72	126	6.2	177/44/-23	1
2	2008/09/20	-16.35	-74.11	52	5.4	303/37/44	1
3	2008/10/15	-15.13	-72.28	134	5	257/58/13	1
4	2008/11/27	-15.94	-73.49	80	5	54/39/52	1
5	2008/12/22	-17.89	-69.3	152	5	333/54/-135	1
6	2009/03/15	-14.6	-70.63	211	5.7	167/63/-25	1
7	2009/06/02	-14.8	-73.6	101	4.9	323/45/-108	1
8	2009/06/13	-17.67	-71.08	95	5.2	237/25/12	1
9	2009/06/15	-13.63	-76.67	52	5.4	330/31/67	1
10	2009/07/12	-15.25	-70.75	197	6.1	101/26/-112	1
11	2009/08/01	-12.24	-75.35	115	5.2	273/48/-135	1
12	2009/09/05	-15.46	-70.68	210	5.8	74/25/-136	1
13	2009/09/30	-15.74	-69.65	258	5.9	315/9/146	1
14	2009/12/24	-15.89	-74.02	71	5.5	165/22/176	1
15	2010/03/22	-16.35	-69.71	218	5.3	235/27/-23	1
16	2010/03/23	-15.32	-74.84	63	5.2	81/22/8	1
17	2010/05/23	-14.03	-74.52	109	6.1	321/37/-97	1
18	2010/06/09	-15.29	-70.84	197	5	78/35/-140	1
19	2010/08/10	-14.07	-72.71	116	5	186/38/-59	1
20	2010/09/13	-14.73	-71.09	171	5.8	93/51/-136	1
21	2010/09/22	-13.4	-76.6	64	5.7	339/30/82	1
22	2010/11/03	-13.78	-76.67	60	5	314/44/40	1
23	2010/11/28	-14.85	-71.47	142	5	256/49/31	1
24	2010/12/15	-17.81	-69.44	157	5.1	8/71/-160	1
25	2011/06/08	-17.37	-69.84	150	5.9	208/32/-27	1
26	2011/07/24	-15.02	-74.54	98	5	308/46/-136	1
27	2011/11/30	-14.45	-73.55	115	5.1	27/46/-72	1
28	2012/01/11	-15.16	-72.83	111	5.2	333/73/-171	1
29	2012/01/30	-14.26	-76.05	46	6.4	323/31/64	1
30	2012/02/12	-15.72	-74.63	81	4.9	316/34/-107	1
31	2012/04/19	-14.87	-72.04	138	4.9	307/30/81	1
32	2012/04/21	-14.93	-71.79	136	5.4	293/36/55	1
33	2012/05/14	-18	-69.94	119	6.3	203/25/-25	1
34	2012/06/07	-15.98	-72.7	120	6.2	110/56/173	1
35	2012/07/13	-15.26	-73.26	117	5.1	175/33/-70	1
36	2012/07/15	-13.73	-73.6	89	4.8	246/33/-119	1
37	2012/09/06	-16.3	-73.94	72	5.1	302/43/54	1
38	2012/09/20	-14.06	-72.85	88	4.9	168/49/-56	1
39	2012/09/29	-17.64	-69.86	146	5.3	252/40/-3	1
40	2012/11/04	-12.06	-75.79	118	4.8	280/48/-59	1
41	2012/11/04	-16.07	-72.18	134	5.5	94/51/-174	1
42	2012/12/30	-12.57	-71.21	51	5	24/71/-9	1
I1	2011/07/14	-15.831	-69.323	233	4.9	—	2
I2	2011/07/14	-15.95	-69.39	236	4.5	—	2
I3	2010/03/19	-14.142	-74.412	104	4.7	—	2
I4	2010/06/26	-14.13	-74.73	94	4.3	—	2

Table 4.1. (continued).

Event ID	Date	Lat (°)	Lon (°)	Depth (km)	Mag	Mechanism Strike/Dip/Rake	Source[a]
I5	2009/01/18	-14.161	-75.15	81	4.7	—	2
I6	2012/05/06	-13.809	-75.752	75	5.1	—	2
I7	2012/03/12	-14.306	-75.573	61	4.7	—	2
I8	2012/01/28	-13.13	-76.17	61	4.1	—	2
I9	2012/06/27	-13.04	-76.2	96	4.4	—	2
I10	2011/09/23	-11.88	-75.923	90	4.5	—	2
I11	2008/12/01	-11.477	-75.569	100	4.7	—	2
I12	2012/05/17	-12.095	-76.526	100	4.4	—	2
I13	2012/12/29	-11.37	-76.86	96	4.6	—	2
I14	2012/12/31	-11.15	-77.401	74	4.9	—	2
I15	2010/08/21	-14.607	-74.156	91	4.1	—	2
I16	2011/07/24	-14.797	-74.31	97	4.9	—	2
I17	2011/05/07	-15.097	-74.233	60	5	—	2
I18	2011/02/17	-14.875	-73.58	98	4.2	—	2
I19	2009/04/25	-14.654	-73.341	87	4.2	—	2
I20	2010/02/28	-14.31	-73.389	83	4.2	—	2
I21	2010/08/11	-14.207	-73.173	86	4.7	—	2
I22	2008/08/06	-14.174	-72.928	94	4.8	—	2
I24	2009/06/20	-14.377	-72.587	86	4.7	—	2
I25	2008/08/20	-14.787	-72.73	99	4.2	—	2
I26	2010/07/11	-15.132	-73.406	103	4.8	—	2
I27	2010/05/30	-15.205	-73.251	104	4.4	—	2
I28	2012/11/30	-15.278	-72.932	103	4.6	—	2
I29	2010/12/27	-15.439	-72.956	102	4	—	2
I30	2008/07/05	-15.557	-72.915	98	4.3	—	2
I31	2012/04/20	-15.46	-72.81	87	4.5	—	2
I32	2008/12/05	-15.519	-73.85	59	4.2	—	2
I33	2011/10/15	-15.866	-73.241	85	4	—	2
I34	2012/02/24	-15.712	-72.821	119	4.7	—	2
I35	2012/02/02	-16.221	-73.615	70	5	—	2

[a]Sources are 1) location, focal mechanism, M_w, and depth from the Global CMT (GCMT) catalog (*Dziewonski et al.*, 1981; *Ekström et al.*, 2012); 2) location, m_b, and depth from the International Seismological Centre (ISC) Bulletin event catalog (*International Seismological Centre*, 2011).

4.3.2 Seismicity

Intraslab seismicity across the study region is examined for any changes, gaps, or patterns that could elucidate the nature of the transition from flat to normal subduction of the Nazca plate. Epicentral locations of 40–300-km-depth earthquakes from the 1960–2013 ISC Bulletin event catalog are shown in Figure 4.3. An abrupt decrease in intermediate depth seismicity can be observed northwest of the PG line of stations, coincident with both the transition to flat subduction and the intersection of

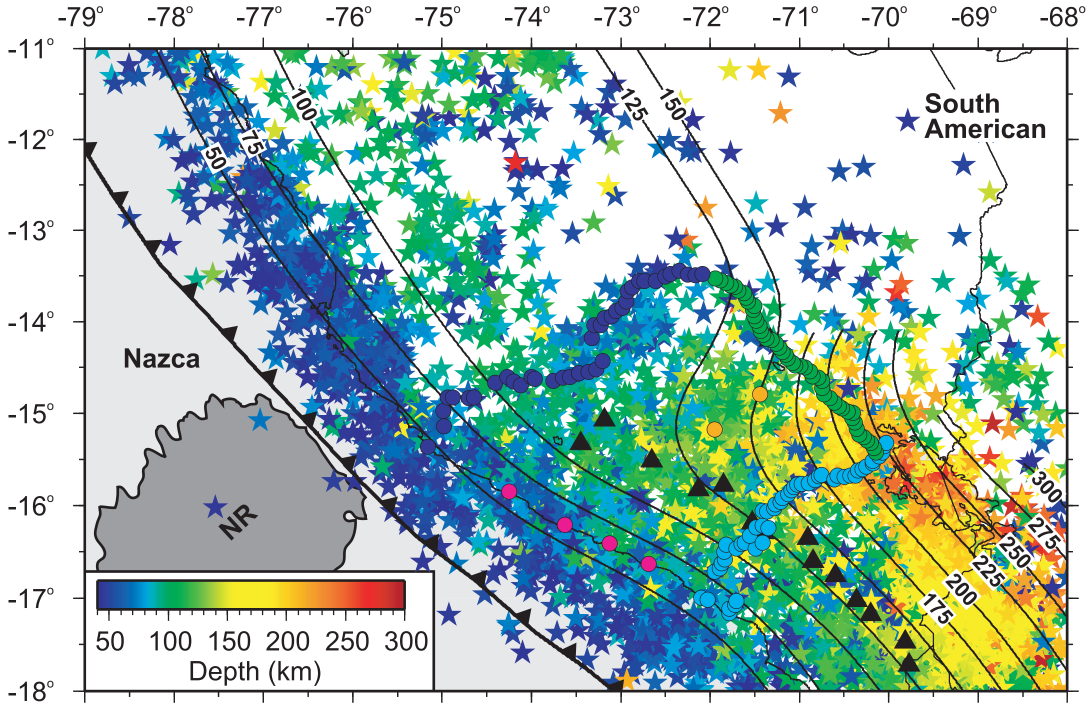

Figure 4.3: Seismicity pattern across the study region. Map of epicenters (stars) for 40–300-km-depth earthquakes from the 1960–2013 International Seismological Centre (ISC) Bulletin event catalog (*International Seismological Centre*, 2011). Epicenters are color-coded by event depth. The dark grey shaded area indicates the Nazca Ridge (NR). Dots are seismic stations (see Figures 4.1 and 4.2). Note the abrupt decrease in intermediate depth seismicity northwest of the PG line of stations, coincident with both the transition from normal (SE) to flat (NW) subduction and the intersection of the NR with the trench. The relative abundance of shallow seismicity within the South American plate overlying the flat slab region should also be noted.

the Nazca Ridge with the Peru-Chile Trench. This decrease in seismicity is indicative of a structural change between the normal dipping region to the southeast and the horizontal slab to the northwest. Additionally, there is a pronounced gap in the intermediate depth seismicity downdip from the Nazca Ridge, which could have implications for the nature of this structural change. This seismicity gap has also been noted by previous authors (*Gutscher et al.*, 1999a; *Hampel*, 2002). The relative abundance of lower crustal seismicity within the South American plate overlying the flat slab region should also be noted for its potential indication of the level of interaction between the two plates. A cluster of seismicity between ∼55 km and ∼85 km depth near the PG line, centered at ∼14°S, 72.85°W (Figure 4.3), may reflect bending of the slab. A cross-section of the seismicity through this cluster is shown in Figure 4.19 of the auxiliary material.

Focal mechanisms of intraslab earthquakes in southern Peru are also analyzed for details of the Nazca slab structure. Source mechanisms of 60–275-km-depth events from the 1976–2013 GCMT catalog are mapped in Figure 4.4. There is a general predominance of normal faulting events below ~80 km depth, as would be expected for earthquakes which occur in the oceanic lithosphere, as these are typically attributed to bending of the slab and/or slab pull (e.g., *Schneider and Sacks*, 1987; *Suárez et al.*, 1990). The decreased seismicity northwest of the PG line that was noted for the ISC catalog data above is also evident here. Southeast of ~15.5°S, the events are concentrated in a narrow coast-parallel band between the 100-km and 125-km isodepth contours that only widens near the concave bend in the trench (Figure 4.4) located just south of 18°S (see inset map in Figure 4.1). There is a downdip gap in seismicity between this narrow band and events located northeast of the 175-km isodepth contour. A linear ENE-WSW-oriented concentration of events can also be observed along the sharp bend in isodepth contours through the center of the array, extending continuously from the coast to the 225-km isodepth contour. This concentration of events may have important implications for the morphology of the slab across this region.

The orientations of focal planes across this zone are examined for any information that they can provide about stress within the slab, which could clarify the accommodation mechanism of the flat-to-normal transition. In the horizontal subduction region to the northwest, the normal faulting events primarily exhibit downdip extension. Within the ENE-WSW concentration of events along the change in dip, there are several thrust and oblique faulting events, especially between the 125-km and 150-km isodepth contours (Figure 4.4). The orientations of some of these events show N-S and NW-SE compression. Focal planes for normal faulting mechanisms located near the intersection of the PE and PF lines and slightly to the southeast between the 225-km and 275-km isodepth contours are oriented nearly E-W, indicating NNW-SSE extension. The cluster of shallower seismicity near the PG line noted from the ISC catalog data consists of normal faulting events at various orientations, including those that signify N-S and NW-SE extension. A second cluster of seismicity near the PG line, centered at ~14.25°S, 73.5°W, is comprised of normal faulting mechanisms showing primarily NW-SE extension.

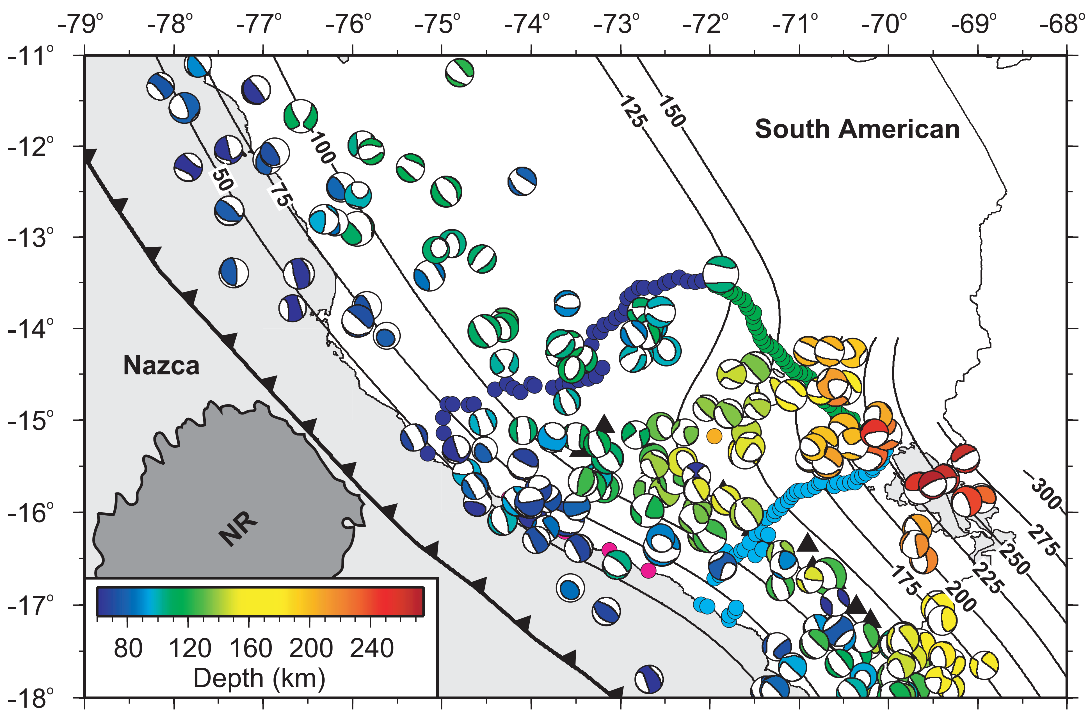

Figure 4.4: Focal mechanisms for intermediate depth earthquakes which occurred in the study region. Map of focal mechanisms from the 1976–2013 Global CMT (GCMT) catalog (*Dziewonski et al.*, 1981; *Ekström et al.*, 2012). Mechanisms are color-coded by event depth and primarily exhibit normal faulting. Note the linear ENE-WSW-oriented concentration of events along the sharp bend in isodepth contours through the center of the array.

4.3.3 Slab Dip

The lateral variation in slab dip across the transition from flat to normal subduction in southern Peru is examined in detail to assess if this change in geometry is accommodated by a smooth contortion of the slab or if there is an abrupt transition which could be indicative of a possible tear. Epicenters for earthquakes from the 1960–2013 ISC Bulletin event catalog are mapped and divided into seventeen 25-km-wide trench-normal bins (Figure 4.5a). Bin 1 overlies the flat slab region across the northwestern extent of the PG line, and bin 17 overlies the normal dipping region along the southeast margin of the PE line. Cross-sections of the seismicity in each bin illustrate variations in the Wadati-Benioff zone across the region and are used to estimate the slab dip in each bin. Examples from bins 5, 13, and 14 are shown in Figure 4.5b-d. Hypocenter locations for earthquakes from the relocated 1960–2008 EHB Bulletin event catalog (*International Seismological Centre*, 2011) are overlain for comparison. There are no systematic differences between the ISC and EHB locations that would affect estimates of slab dip. In general, the ISC data form a scatter envelope around the EHB locations. Thus, the dip angle is estimated by visually selecting ISC hypocenter locations that are downdip of the trench and not within the overriding plate (as defined by teleseismic receiver functions (*Phillips et al.*, 2012; *Phillips and Clayton*, 2014)), then performing a linear regression of the selected locations. The estimated slab dip in bins 5–17 is shown in Figure 4.5e. In order to focus more closely on the transition from flat to normal subduction, results for bins 1–4 are not shown in Figure 4.5e, since, as in bins 5–7, the estimated slab dip in these bins is 0°. The errors on the dip estimates (calculated from the standard deviation in dip) are weighted by the number of earthquakes in each bin, such that fewer events in a bin produces a larger error, with values ranging from ±0.96° (bin 17) to ±3.34° (bin 5). The slab is flat beneath the PG line with its dip gradually increasing in 3° or 5° increments across the transition zone to 19° by bin 13 (Figure 4.5). Between bins 13 and 14, there is the largest incremental increase in slab dip of 8°, followed by an approximately constant dip (27–28°) across the remainder of the bins to the southeast (Figure 4.5).

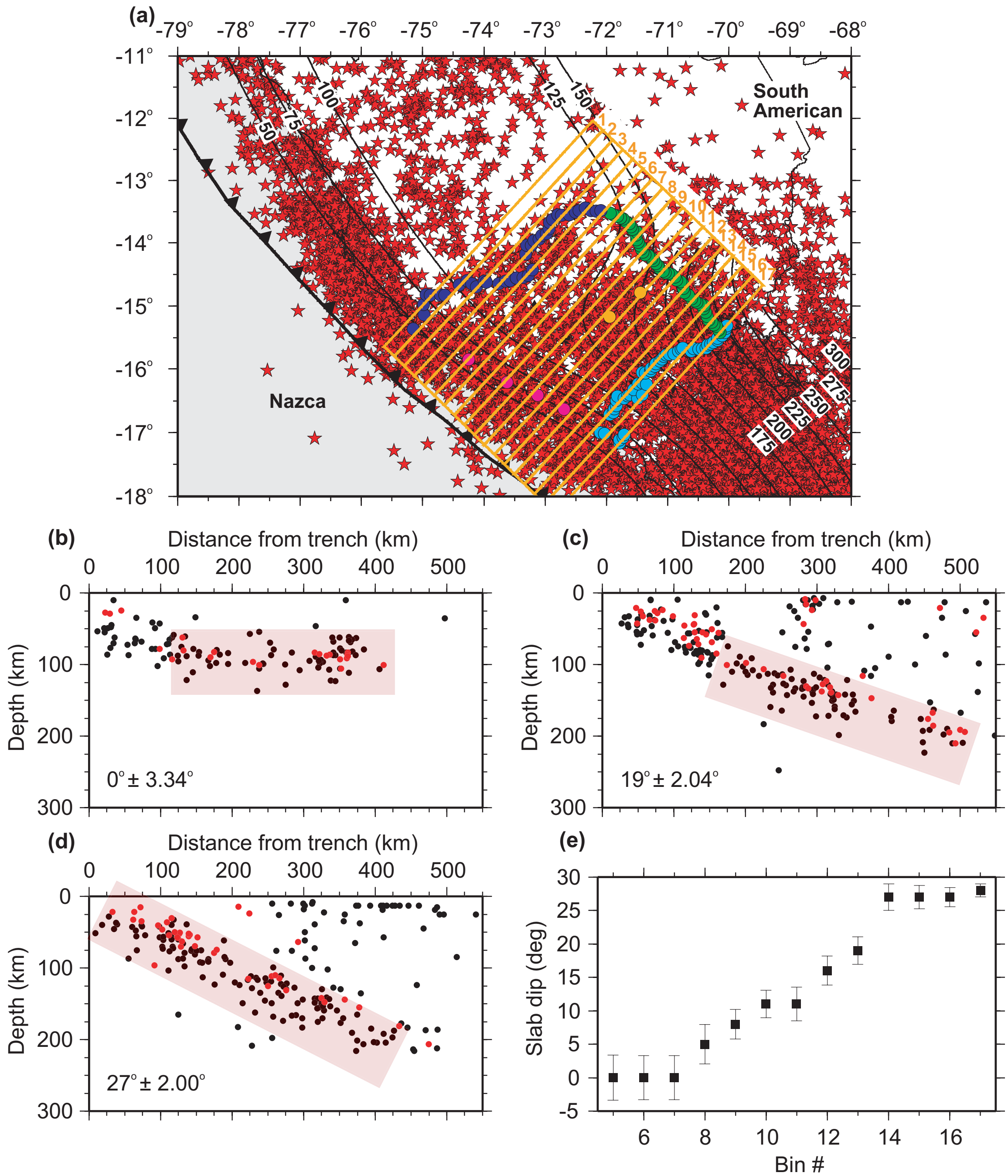

Figure 4.5: Seismicity and slab dip across the transition from flat to normal subduction. (a) Map showing epicenters (stars) for earthquakes from the 1960–2013 ISC Bulletin event catalog (*International Seismological Centre*, 2011). Data in seventeen 25-km-wide bins roughly perpendicular to the trench are analyzed for changes in slab dip across this region. Cross-sections of seismicity (black dots) in bins (b) 5, (c) 13, and (d) 14 are shown along with their respective estimated slab dips. Pink shaded regions reflect the slope of the linear regression and encompass the slab seismicity used to estimate dip. Hypocenter locations for earthquakes from the relocated 1960–2008 EHB Bulletin event catalog (*International Seismological Centre*, 2011) (red dots) are shown for reference. Note the 8° change in slab dip between bins 13 and 14. (e) Plot of slab dip across the data bins. Error bars are weighted by the number of events in each bin, such that fewer events produces a larger error.

4.3.4 Slab Transition

In addition to the along-dip direction, lateral variations in seismicity in the along-strike direction are also analyzed for any gaps or vertical offsets that could indicate plate tearing rather than continuous curvature. Epicenters for earthquakes from the 1960–2013 ISC Bulletin event catalog are mapped and divided into twenty-two 25-km-wide trench-parallel bins that encompass the PeruSE array (Figure 4.6). These trench-parallel (or horizontal) bins are referred to with a preceding 'h' (e.g., bin h1) to distinguish them from the trench-normal bins in Figure 4.5. Bin h1 is located along and just downdip of the trench, while bin h22 is located 50–75 km northeast of the PF line. Note the marked decrease in seismicity in the northwestern portions of bins h19–h22 that expands in lateral extent in the downdip direction. Hypocenter locations from the relocated 1960–2008 EHB Bulletin event catalog are also included in the along-strike seismicity analysis to provide further constraints on the slab location and morphology. For events which can be found in both the ISC and EHB catalogs, only the EHB hypocenter is used. Cross-sections of the ISC and EHB seismicity in each bin illustrate variations in the Wadati-Benioff zone across the region and are used to delineate the transition from flat to normal subduction. Examples from bins h11–h15, located 250–375 km from the trench, are shown in Figure 4.7. No gaps or vertical offsets in the Wadati-Benioff zone seismicity can be observed in the cross-sections. Rather, a continuous transition from horizontal to 28° dipping slab is observed.

A weighted least-squares piecewise-linear regression fit to the slab seismicity in each cross-section is performed using the Shape Language Modeling toolkit (*D'Errico*, 2009) in order to approximate the slab morphology across the transition. Events located within the overriding plate and any deep outliers (determined visually) are weighted to 0. Individual ISC hypocenters offset from the main concentration of slab seismicity and/or from the overall slab trend approximated from the EHB hypocenters are weighted to 0.25–0.75, depending on the degree of offset, with the largest offset events weighted the lowest. All other events are weighted to 1. The fits for bins h11–h15 are shown in Figure 4.7. Due to the marked decrease in seismicity in the northwestern portions of bins h19–h22, there is insufficient data to perform piecewise-linear regression fits in these bins. The complete

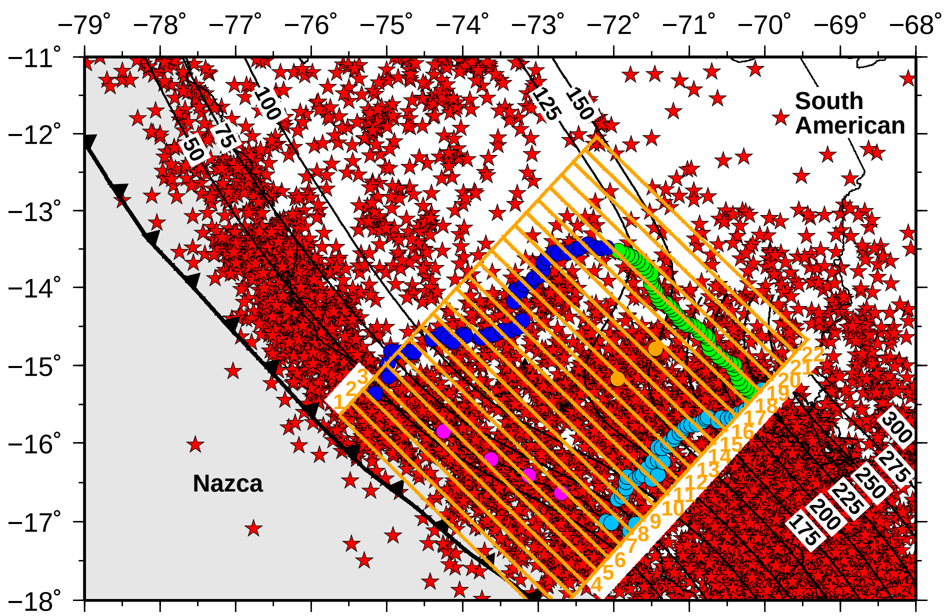

Figure 4.6: Map showing epicenters (stars) for earthquakes from the 1960–2013 ISC Bulletin event catalog as in Figure 4.5a. Data in twenty-two 25-km-wide bins roughly parallel to the trench are used to constrain the transition from flat to normal subduction across this region. These trench-parallel (or horizontal) bins are referred to with a preceding 'h' to distinguish them from the trench-normal bins in Figure 4.5. Note the marked decrease in seismicity in the northwestern portions of bins h19–h22.

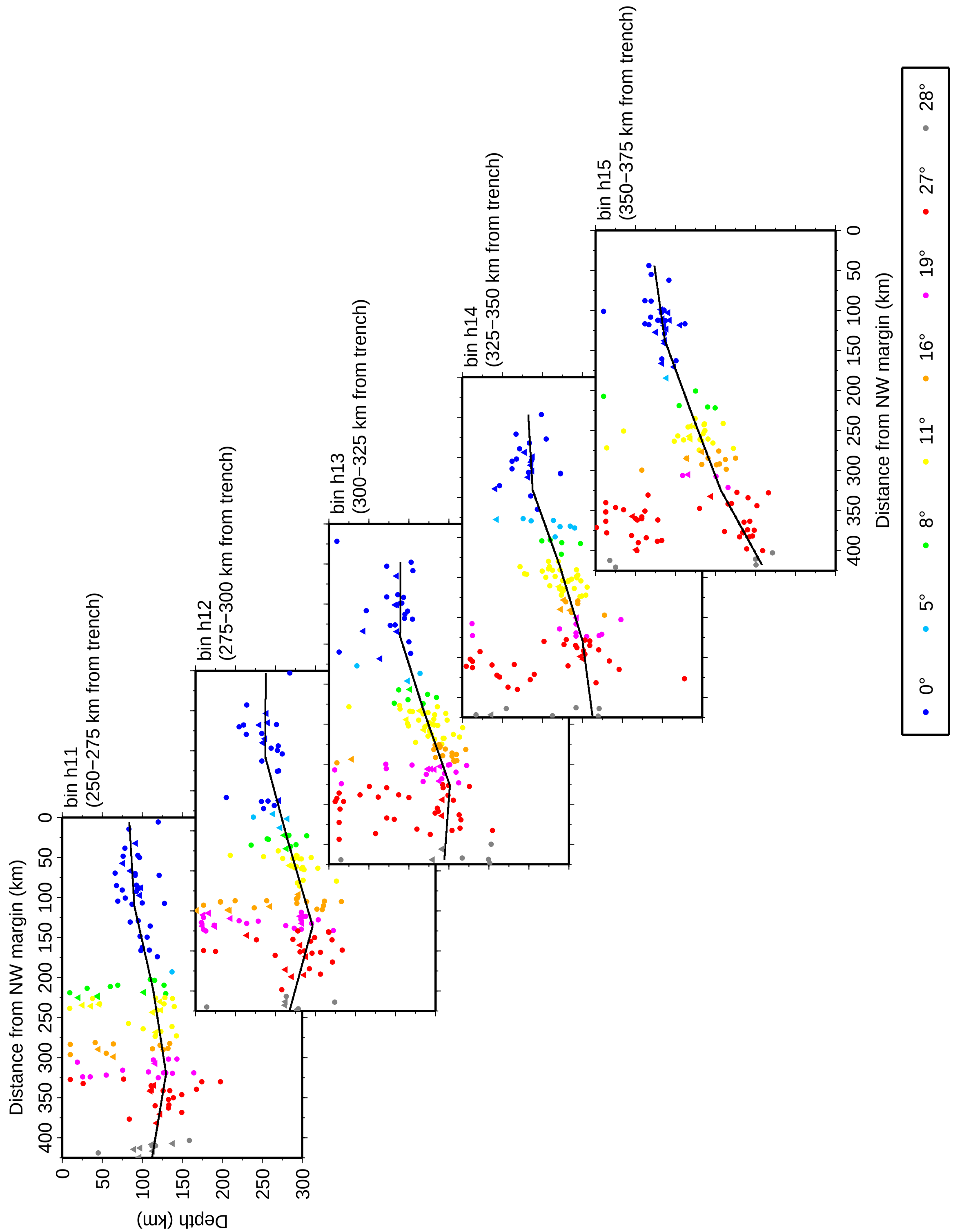

Figure 4.7: Cross-sections of seismicity from the ISC (dots) and EHB (triangles) catalogs in trench-parallel bins h11–h15 (see Figure 4.6 for bin locations). Hypocenter locations are colored to reflect slab dip as estimated in Figure 4.5. Weighted piecewise-linear regression fits to the slab seismicity in each cross-section are shown (black lines). Note the smooth transition from horizontal to 28° dipping slab without any gaps or vertical offsets in the seismicity. See Figure 4.20 of the auxiliary material for the complete set of seismicity cross-sections (bins h1–h18).

set of seismicity cross-sections (i.e., bins h1–h18), including fits, can be found in Figure 4.20 of the auxiliary material. Consistent with the lack of gaps and vertical offsets observed in the seismicity, the fits in each cross-section do not show any sharp changes in the slab shape. The fit for bin h17 is an exception to this, where an abrupt step can be observed due to a poorly constrained regression from sparse data in this bin (Figure 4.20). As such, bin h17 is excluded from further analyses.

The weighted piecewise-linear regression fits to the slab seismicity in trench-parallel cross-sections h1–h18 (with h17 removed; Figure 4.8a) are used to estimate a 3D slab surface in an attempt to image the flat-to-normal transition. The gridfit function of *D'Errico* (2005) is used to approximate the slab surface on a 425-km-by-450-km grid that extends to ∼210 km depth from the seventeen seismicity fits. Each fit is placed at the midpoint of its 25-km-wide bin for determining its distance from the trench in the grid. For example, bin h1 encompasses 0–25 km from the trench, so its fit is placed at 12.5 km from the trench. The resultant 3D slab surface is shown in Figure 4.8b. Observed vertical oscillations, or waviness, of the slab surface are likely artificial and are the result of 25-km-wide gaps between the location of each seismicity fit. An increase in the smoothing parameter applied to the surface estimate by two orders of magnitude significantly reduces the amplitude of the waviness of the surface; however, it also results in a shallowing that is inconsistent with the seismicity. As such, the slab surface as shown in Figure 4.8b, with very little smoothing applied, is a more accurate representation of the data. The addition of interpolated lines located at the midpoints between each seismicity fit, effectively reducing the 25-km-wide gaps to 12.5-km-wide gaps, increases the frequency of the waviness of the surface, further supporting the relative accuracy of the slab surface as shown in Figure 4.8b. An anomalous rise in the northwestern corner (∼0–150 km from the NW margin) of the slab surface in the downdip region (∼325–450 km from the trench) should also be noted. Possible implications of this feature will be discussed in section 4.4.

4.3.5 Ultra-slow Velocity Layer

Investigation of a fine-scale structural feature, such as an USL, can provide further information on the nature of the transition from flat to normal subduction. The existence of such a layer is searched

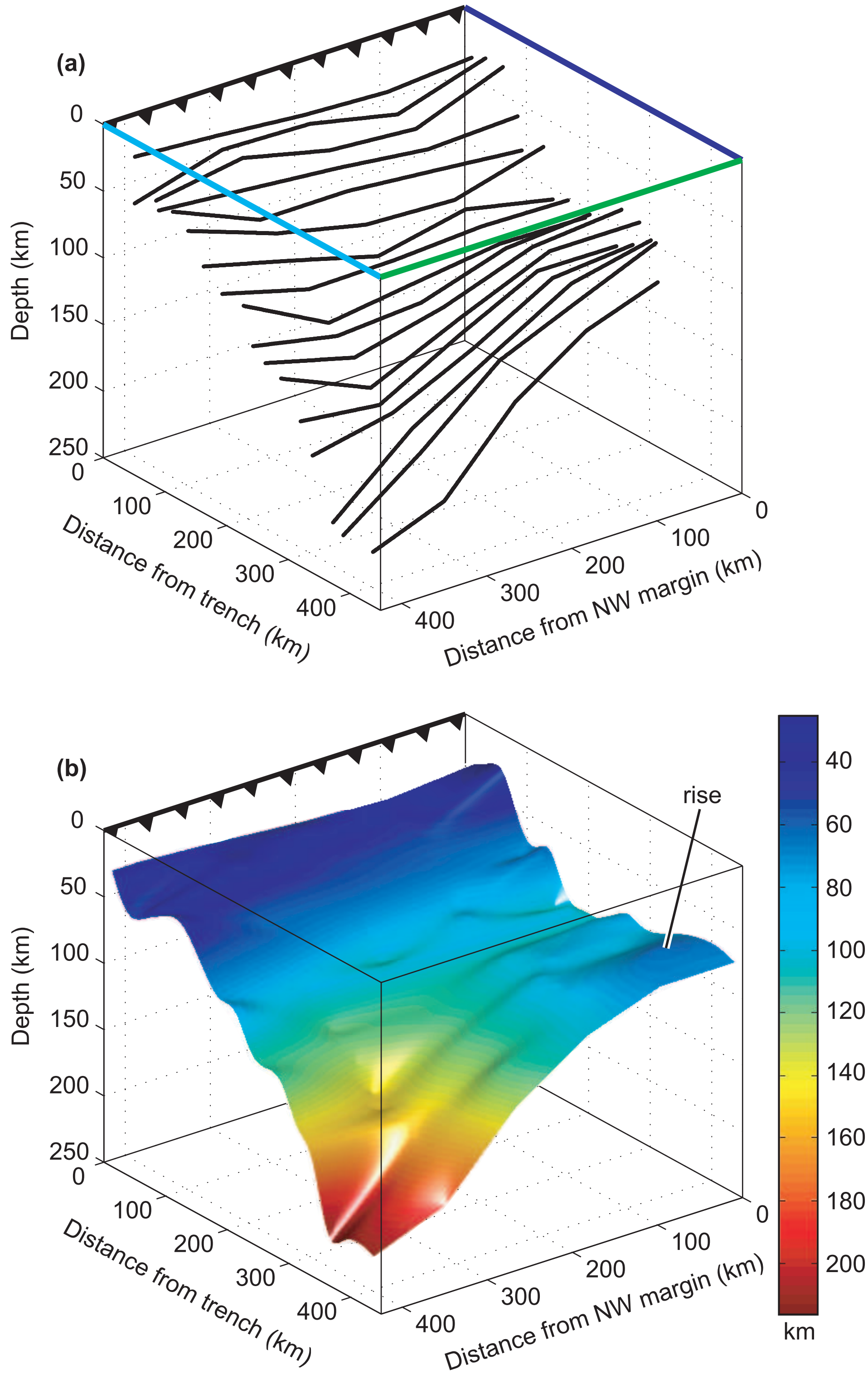

Figure 4.8: 3D perspective view (looking west) of the transition from flat to normal subduction as constrained by seismicity. (a) Weighted piecewise-linear regression fits to the slab seismicity in trench-parallel cross-sections h1–h18 shown in 3D. The fit for bin h17 is excluded due to a poorly constrained regression from sparse data in this bin (see Figure 4.20 of the auxiliary material). At the surface, the boundaries of the box are colored to reflect their correspondence with the approximate locations of the PG (blue), PF (green), and PE (light blue) lines of the PeruSE array (Figure 4.6). (b) 3D slab surface generated from seismicity fits in (a). Note the anomalous rise in the northwestern corner of the slab surface in the downdip region, which may be due to decreased seismicity in this region (Figure 4.6). Trench location is indicated by barbed line.

for in southern Peru, with potentially important implications for slab tearing if its lateral extent is coincident with other possible tear indicators. The USL as explored here was first imaged atop the flat Cocos slab in central Mexico as a 3–5-km-thick layer at a depth of 45–50 km with a V_P of 5.4–6.2 km/s and a V_S of 2.0–3.4 km/s (*Song et al.*, 2009; *Kim et al.*, 2010). Its anomalously low shear wave velocity suggests a relationship with fluids, specifically free water or hydrous minerals, in the subduction zone; however, the exact nature of the USL is not known. *Song et al.* (2009) proposed that the USL represents a fluid-saturated portion of the oceanic crust, forming a high pore fluid pressure (HPFP) layer that is sealed by some low permeability layer, such as fine-grained blueschist, directly above it. Thermal modeling of the central Mexico subduction zone found a high pore pressure ratio of 0.98 along the subduction interface (*Manea et al.*, 2004), consistent with *Song et al.* (2009)'s HPFP layer. *Kim et al.* (2010), on the other hand, proposed that the USL is highly heterogeneous upper crust that is composed of mechanically weak hydrous minerals (talc) that might be under high pore pressure. With or without free fluid, *Kim et al.* (2013) demonstrate that a talc-rich ultramafic layer is required to explain the observed USL velocities and suggest that this talc originates from the mantle wedge during the slab flattening process. Similarly, *Manea et al.* (2013) propose that the USL represents a remnant of mantle wedge that experienced significant serpentinization since the slab flattened. The hydrous minerals and/or high pore pressure of the USL characterize it as a low strength layer, which may be responsible for the flat subduction geometry (*Manea and Gurnis*, 2007; *Kim et al.*, 2010) and the observed decoupling of the flat Cocos slab from the overriding North American plate (*Singh and Pardo*, 1993; *Franco et al.*, 2005) in central Mexico.

The presence of the USL atop the Nazca slab is identified by the existence of complex P waveforms (*Song et al.*, 2009) recorded by the PeruSE and CAUGHT arrays. As described by *Dougherty et al.* (2012) for the case of the Cocos slab, these complex P waveforms consist of three locally converted S-to-P phases (A, B, C) that arrive within 4 sec after the P-wave (Figure 4.9). Phase A converts at the bottom of the USL and appears as a negative pulse at local stations. Phase B arrives immediately after phase A as a positive pulse, indicative of an S-to-P wave that converted at the top of the USL. Phase C converts at the base of the high velocity layer, arriving before phase A and ~1.0–1.5 sec after the direct P-wave (*Song and Kim*, 2012). These three phases are searched for in the seismograms of the intraslab earthquakes analyzed in this study. P waveforms in these seismograms are categorized as complex, possibly complex, or simple based on the existence or absence and nature of phases A, B, and C. Examples of these waveforms from event 17 recorded at PeruSE stations are shown in Figure 4.9. The waveforms have been bandpass filtered to 0.01–0.6 Hz, with the shorter periods in the frequency band allowing for the identification of the three S-to-P phases. When all three of the phases are readily observed, the waveform is deemed complex. If one of the phases is not easily identified due to an uncharacteristic pulse shape and/or amplitude, but the other two phases are clearly visible, then the waveform is possibly complex. Simple waveforms lack the shoulder in the direct P pulse representative of the C phase and also have uncharacteristically shaped and/or low amplitude A and B phases, indicating that there is no HVL or USL present, respectively. The arrival times of the possible A and B phases in the simple waveforms are also inconsistent with the presence of the USL (i.e., they arrive too early).

The lateral extent of the USL in southern Peru is mapped by examining the status of the layer at each epicentral event location (Figure 4.10). We identify seven events which indicate the presence of the USL from their P waveforms. Another 14 events possibly indicate the presence of the USL. The presence of the USL is undetermined for three events due to low signal-to-noise ratio, and the remaining 52 events in our dataset indicate that no USL is present at their locations. In general, the events which suggest (or possibly suggest) the existence of the USL are concentrated in the flat slab region along and northwest of the PG line, while those that suggest the USL is lacking are concentrated to the southeast, where the slab dip is increasing and normal subduction occurs. There is no overlap between the USL or possible USL locations and the no USL events. It should also be noted that the events which indicate the presence of the USL are all located directly downdip from the Nazca Ridge where it intersects the trench. The projected linear continuation of the Nazca Ridge is indicated in Figure 4.10. The width of this linear extension is constrained by the current width of the ridge near the trench (Figure 4.10). Previous authors have identified the Tuamotu Plateau on the Pacific plate as the conjugate feature to the Nazca Ridge (e.g., *Pilger*, 1981; *Pilger*

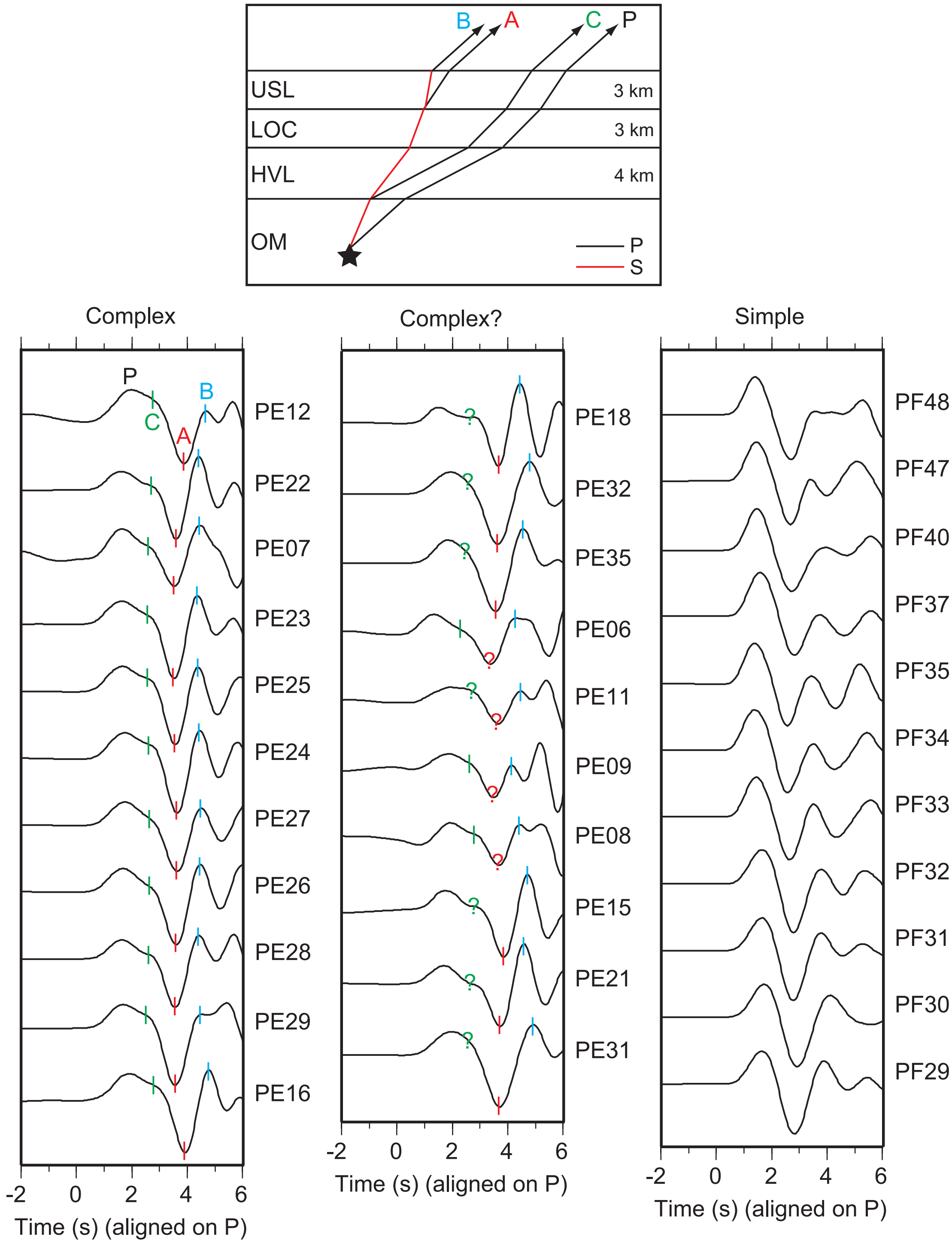

Figure 4.9: (top) Schematic cross-section illustrating the raypaths of the P-wave and the three S-to-P phases (A, B, C) that comprise the complex P waveform. Abbreviations are USL, ultra-slow velocity layer; LOC, lower oceanic crust; HVL, high velocity layer; OM, oceanic mantle. Approximate layer thicknesses for the USL, LOC, and HVL are indicated. (bottom) Examples of (left) complex, (middle) possibly complex, and (right) simple P waveforms from event 17 recorded on the vertical component by PeruSE stations and filtered to 0.01–0.6 Hz. S-to-P phases A, B, and C are indicated by red, blue, and green tick marks, respectively. All three of these phases are visible in the complex waveforms within 4 sec of the P-wave. Question marks on the possibly complex waveforms indicate a phase that is not easily identified due to an uncharacteristic pulse shape and/or amplitude. Simple waveforms lack the shoulder in the direct P pulse indicative of the C phase and also have uncharacteristically shaped and/or low amplitude A and B phases, indicating there is no HVL or USL present, respectively. Modified from *Dougherty et al.* (2012).

and Handschumacher, 1981; *Woods and Okal*, 1994) and used its size and location to approximate the downdip continuation of the Nazca Ridge beneath South America (e.g., *Pilger*, 1981; *von Huene et al.*, 1996; *Gutscher et al.*, 1999a; *Hampel*, 2002). A recent geochronological and geochemical study of lavas from the Nazca Ridge, however, indicated that the ridge formed at a hotspot located well to the east (i.e., at least 500 km) of the Pacific-Farallon spreading center (*Ray et al.*, 2012), and, as such, the Tuamotu Plateau cannot be its conjugate feature. Note the coincidence of the approximate boundary between the USL or possible USL locations and the no USL locations with the southeast margin of the projected continuation of the Nazca Ridge. Shaded contours of the USL, possible USL, and no USL zones further clarify our observations (Figure 4.10).

The locations of the S-to-P conversion points from the top of the Nazca slab are also mapped in order to illustrate where the slab is sampled to produce complex, possibly complex, and simple P waveforms (Figure 4.11). These S-to-P conversion point locations are approximated as 10% of the distance from the source to the receiver along a direct path. Conversion point locations for simple P waveforms indicate where no USL is present (Figure 4.11a), while those for possibly complex waveforms indicate where the USL is possibly present (USL?; Figure 4.11b). The complex P waveform conversion point locations denote where the USL is present (Figure 4.11c). The intermingling of S-to-P conversion points indicative of the USL or possible USL with those that signify no USL northwest of the PG line in the flat slab region suggests that the USL is likely laterally heterogeneous, consistent with previous observations in central Mexico (*Song et al.*, 2009; *Kim et al.*, 2010; *Dougherty et al.*, 2012). Other observations of patterns in USL, possible USL, and no USL locations, as noted for Figure 4.10 above, also apply here.

4.3.6 2D Velocity Modeling

The shallow seismic structure of the southern Peru subduction zone is examined in 2D using a finite-difference wave propagation algorithm with GCMT focal mechanisms (Table 4.1). The P- and S-wave velocities from three different models (Figure 4.12) are coupled with subducted slab geometries estimated from two different sets of isodepth contours (Figure 4.13) in an effort to constrain the

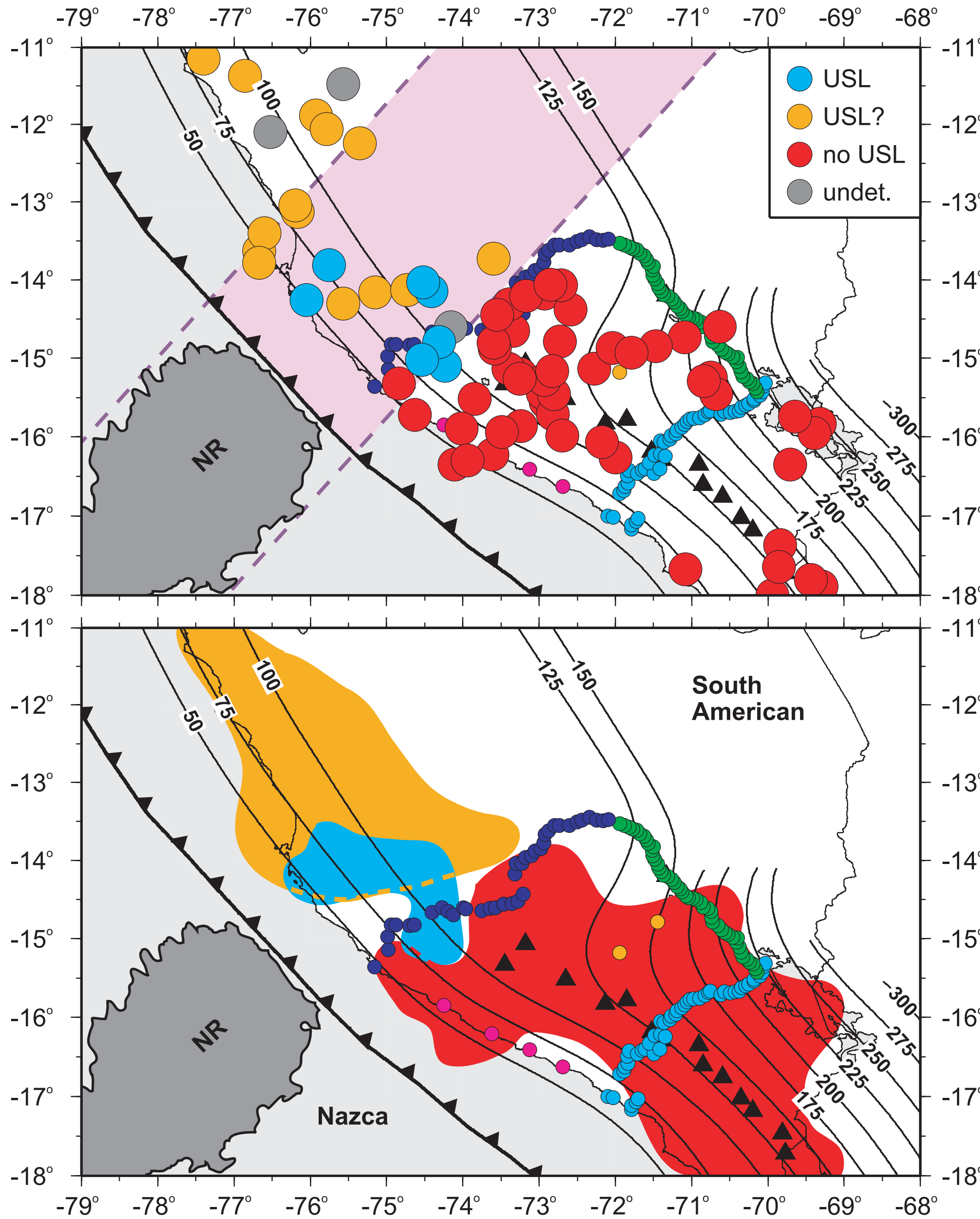

Figure 4.10: Mapping the lateral extent of the USL using PeruSE P waveforms. (top) Events which indicate the presence of the USL are shown in blue. Those which possibly indicate the USL is present are shown in orange. Red events indicate no USL is present. The presence of the USL is undetermined for grey events. The projected linear continuation of the NR is indicated by the purple shaded region. Note the transition from USL and possible USL events to no USL events along the SE margin of this feature. (bottom) Shaded contours of USL, possible USL, and no USL zones.

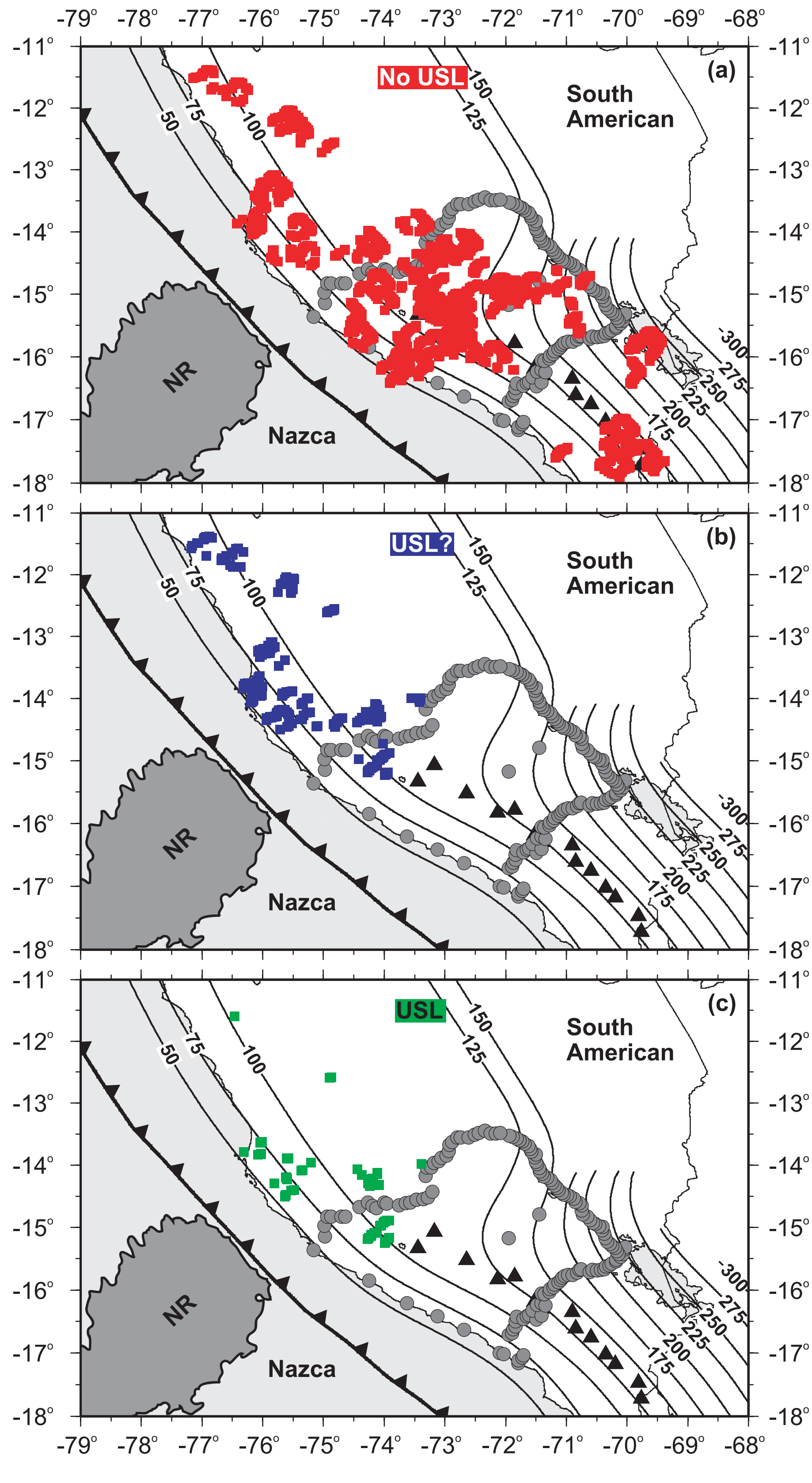

Figure 4.11: Approximate locations of S-to-P conversion points from the top of the Nazca slab for waveforms recorded at PeruSE stations. Conversion points for waveforms which indicated (a) no USL is present, (b) possible USL presence, and (c) USL is present are shown. Compare the locations of these conversion points to the zones in Figure 4.10.

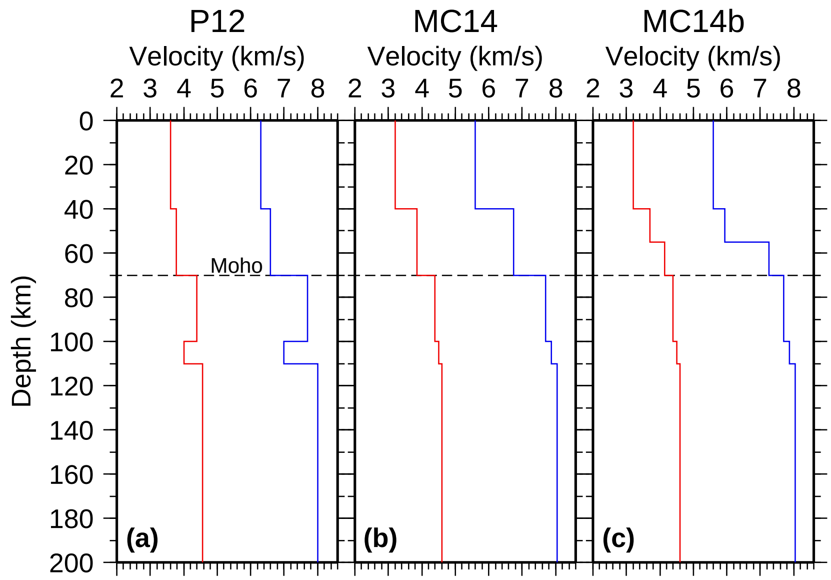

Figure 4.12: 1D P (blue) and S (red) wave velocity models tested in this study. (a) Southern Peru velocity model from receiver function study by *Phillips et al.* (2012) (P12). The Moho depth is indicated by the black dashed line. (b) Simplified southern Peru velocity model from surface wave study by *Ma and Clayton* (2014) (MC14). (c) Variation on MC14 velocity model with lower crust of the overriding plate subdivided into two layers (MC14b).

structure and morphology of the Nazca slab. The three velocity models tested are: (1) southern Peru velocity model from receiver function study by *Phillips et al.* (2012) (P12) (Figure 4.12a); (2) simplified southern Peru velocity model from surface wave study by *Ma and Clayton* (2014) (MC14) (Figure 4.12b); (3) variation on MC14 velocity model with the lower crust of the overriding plate subdivided into two layers (MC14b) (Figure 4.12c). *Phillips et al.* (2012)'s receiver function results are used to constrain the depths of the crustal and mantle discontinuities in the MC14 and MC14b models. A simplified 1D average of S-wave velocities from 2D cross-sections in *Ma and Clayton* (2014) is used to generate the MC14 and MC14b models. The corresponding P-wave velocities are calculated using an average V_P/V_S ratio of 1.75 (*Phillips and Clayton*, 2014). These models exclude the low velocity zone imaged in portions of the overriding plate (*Ma and Clayton*, 2014) for simplicity. Additionally, the well-established isodepth contours of *Cahill and Isacks* (1992) are tested in comparison to the more recent contours of Slab1.0 (*Hayes et al.*, 2012) in order to ascertain which might be a better representation of the actual slab geometry. Both sets of contours are derived from hypocenter locations.

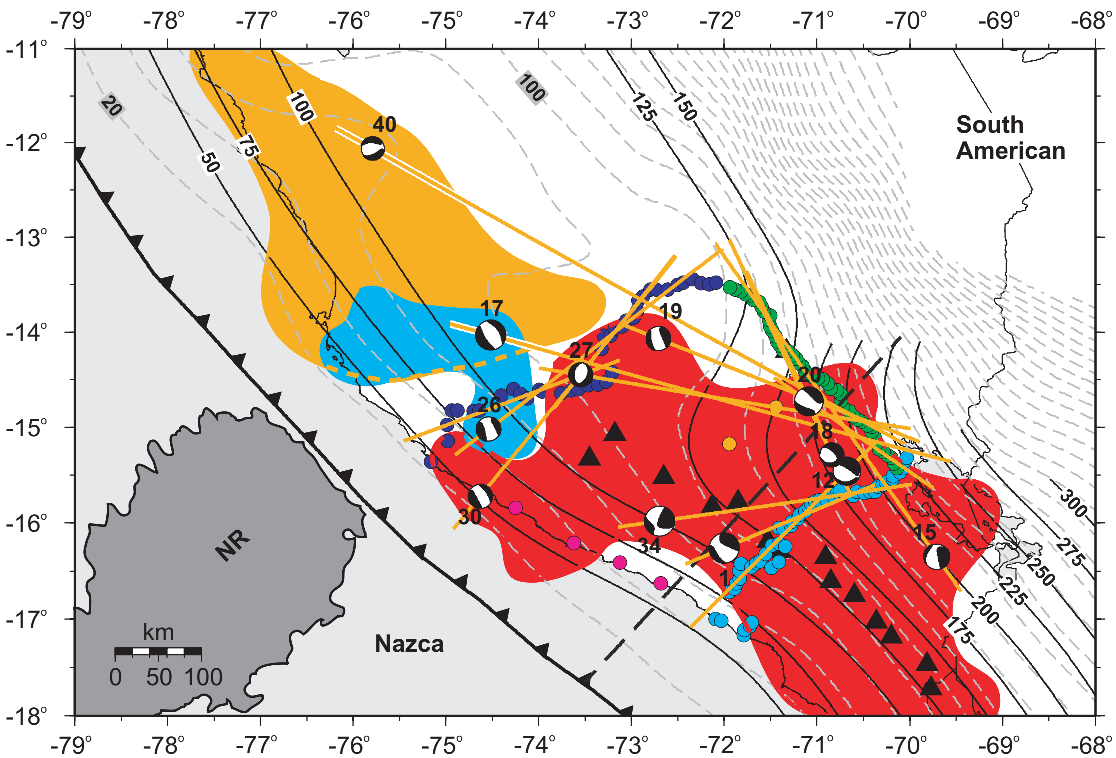

Figure 4.13: Map of locations of 2D velocity model cross-sections (orange lines) for the twelve events modeled (focal mechanisms). The USL (blue), possibly USL (orange), and no USL (red) zones from Figure 4.10 are shown. The boundary between bins 13 and 14 of Figure 4.5, demarking the largest change in slab dip (8°), is denoted by the black dashed line. Slab isodepth contours from Slab1.0 (*Hayes et al.*, 2012) are shown in grey dashed lines. The 20-km and 100-km contours are labeled for reference. Model parameters and results for each 2D profile can be found in Table 4.2.

We generate synthetic seismograms for particular 2D velocity and slab geometry models and compare them to the data for 12 events. These models are oriented along 15 different profiles throughout the study region, concentrated across the transition between flat and normal subduction in order to examine the nature of this change in slab dip (Figure 4.13, Table 4.2). Note that for event 20 both a N26°W-oriented profile and a S56°E profile are modeled. Three different profiles (i.e., N39°E, S81°E, and S70°W) are also modeled for event 27. For each 2D model, we test for the presence of any of four possible slab structural features that may exist along the profile, depending on its location. These features include a 3-km-thick USL (V_S of 2.6 km/s) at the top of the slab, the projected downdip extension of the Nazca Ridge, a tear in the slab located along the southeast margin of the projected Nazca Ridge, and a tear in the slab located along the largest transition (i.e., 8°) in dip (Figure 4.13, Table 4.2). The USL is limited to only those regions encompassed by the USL and possible USL zones as defined in Figure 4.10. The projected continuation of the Nazca Ridge is modeled to be only as wide as its current expression near the trench (∼250 km) and 18 km thick across its center (*Couch and Whitsett*, 1981; *Woods and Okal*, 1994). Each of the two possible slab tears are modeled as 20-km and 50-km-wide gaps in the plate, centered at their respective feature of interest (i.e., ridge margin or change in dip).

The 2D modeling results for all of the events tested are summarized in Table 4.2, with the best-fitting velocities and slab geometry for each profile indicated, along with the status (i.e., confirmed presence, not present, or inconclusive) of any structural features tested. In general, the P12 velocity model produces synthetics that are better representations of the observed data than the MC14 or MC14b models, although there is some discrepancy between the vertical and radial components along four profiles in which the MC14 model provides a better fit to the radial component data than the P12 model. The MC14 model only provides the best fit to the data on both vertical and radial components for events 17 and 40. Similarly, the MC14b model is the best-fitting model only for the S81°E profile of event 27. All three of these events are located in same general area of our study region, along and northwest of the PG line, and their respective profiles are oriented within a ∼20° azimuth window (Figure 4.13, Table 4.2). However, the data from a nearby event (i.e.,

Table 4.2: Model parameters and results for each 2D profile in southern Peru.

Event ID	Profile azimuth (°)	Profile length (km)	1D Velocity model[a]	Slab geometry[b]	Feature(s) tested[c]	Results[d]
1	N68E	245	P12(Z), MC14(R)	S1	n/a	—
12	S46W	300	P12	S1	n/a	—
15	N36W	480	P12(Z), MC14(R)	S1	dip tear	No tear
17	S73E	600	MC14	S1	USL, ridge, ridge tear, dip tear	USL: inconclusive, ridge: confirmed, no tears
18	N26W	330	P12	CI	dip tear	No tear
19	S68E	385	P12	CI	dip tear	No tear
20	N26W	220	P12	S1	n/a	—
	S56E	230	P12(Z), MC14(R)	S1	dip tear	No tear
26	N53E	390	P12	S1	USL	Possibly confirmed
27	N39E	230	P12	S1	n/a	—
	S81E	450	MC14b	S1	dip tear	No tear
	S70W	275	P12	S1	USL	Confirmed
30	N40E	415	P12	CI	USL	No USL
34	N82E	355	P12(Z), MC14(R)	S1	dip tear	No tear
40	S60E	750	MC14	CI	USL, ridge, ridge tear, dip tear	USL: confirmed, ridge: inconclusive, no tears

[a]Best fitting 1D velocity model when applied in 2D. P12 is from *Phillips et al.* (2012); MC14 and MC14b are from *Ma and Clayton* (2014). Variable results between vertical (Z) and radial (R) components are indicated.

[b]Slab geometry which most accurately predicts the observed waveforms when coupled with the best fitting 1D velocity model(s). Possible geometries are estimated from the slab isodepth contours of *Cahill and Isacks* (1992) (CI) and Slab1.0 (*Hayes et al.*, 2012) (S1).

[c]Slab structural feature(s) tested along each profile, which include: an ultra-slow velocity layer at the top of the slab (USL), the projected downdip extension of the Nazca Ridge (ridge), a tear in the slab located along the SE margin of the projected Nazca Ridge (ridge tear), and a tear in the slab located along the sharpest transition in dip (dip tear).

[d]Modeling results for each slab feature tested. The presence of each feature is confirmed, denied (e.g., no tear), or inconclusive.

19) whose profile is located within this same azimuth window is best fit by the P12 model. The only observed commonality among the four profiles with variable results between the vertical and radial components is that they all sample the northeastern end of the PE line, which may have implications for the structure of the subduction zone in this corner of the array. Out of the 15 model profiles tested, the slab geometry estimated from the *Cahill and Isacks* (1992) isodepth contours most accurately predicts the observed waveforms along just four profiles. These four profiles (i.e., events 18, 19, 30, and 40) all sample the northern region of the array, near the intersection of the PF and PG lines. Other profiles which sample this same region, however, support the Slab1.0 (*Hayes et al.*, 2012) isodepth contours as a better representation of the slab geometry. Overall, tests of the four possible slab structural features indicate that there is no tear present along either the southeast margin of the projected Nazca Ridge or along the sharpest increase in slab dip, while the presence of the downdip extension of the Nazca Ridge is likely confirmed and the existence of the USL is possible.

The 2D velocity model along the event 26 profile using the preferred P12 velocities is presented in Figure 4.14 as an example. The model is shown with the slab geometry estimated from the isodepth contours of both *Cahill and Isacks* (1992) (Figure 4.14a) and Slab1.0 (*Hayes et al.*, 2012) (Figure 4.14b) for comparison. Data along this transect were recorded by the PG line. This model tests the presence and location of the USL using the lateral extent of the USL zone and its possible extension to the boundary of the no USL zone as shown in Figure 4.13. The synthetics produced from this model, using both possible slab geometries, are compared to the data from three stations in Figure 4.15. A ∼65–70 sec segment of the synthetic waveform that includes the P- and S-wave arrivals is cross-correlated with the data for this segment. The results of this cross-correlation clearly indicate that the Slab1.0 (*Hayes et al.*, 2012) geometry is a better representation of the slab shape along this profile than that derived from *Cahill and Isacks* (1992) (CI). The results from models with the addition of the USL and those that use the MC14 and MC14b velocities are also shown. These models all include the slab geometry estimated from Slab1.0 (*Hayes et al.*, 2012). The lower cross-correlation coefficients for the MC14 and MC14b models relative to those for the P12 model on both the vertical and radial components demonstrate that, out of the three velocity models tested, the P12 velocities are the most accurate representation of the slab structure along this profile. Relative to the model without the USL (P12 in Figure 4.15), the model that includes the USL within the lateral extent of the USL zone, as sampled by this profile (P12_USL; Figure 4.14b), produces improved fits to the data on the radial component at all stations and on the vertical component at some stations. Extending the width of the USL to the boundary of the no USL zone (P12_USL2; Figure 4.14b) produces worse fits to the data relative to the model without the USL on the vertical component at all stations and on the radial component at most stations. Note that stations PG33 and PG35 (Figure 4.15) are the only two stations along the profile which show improved fits on the radial component for the P12_USL2 model. This comparison of modeling results suggests possible confirmation of the presence of the USL, limited to the extent of the USL zone.

The 2D velocity model along the S56°E profile for event 20 using the preferred slab geometry estimated from the isodepth contours of Slab1.0 (*Hayes et al.*, 2012) is shown in Figure 4.16 as an additional example. The model is shown with the P12 (Figure 4.16a) and MC14 (Figure 4.16b) velocities for comparison. The data along this transect were recorded by the PF and PE lines. This model tests the presence of a tear in the slab along the largest transition in dip. As was described for the event 26 model above, the synthetics produced from this model are compared to the data at three stations in Figure 4.17, with cross-correlations between a segment of the synthetic and the data used to assess the quality of fit. Here, the segment used is ∼58–65 sec and still includes the P- and S-wave arrivals. Out of the three sets of velocities tested (i.e., P12, MC14, and MC14b), synthetics produced using the P12 velocities provide the most accurate (overall) prediction of the data on the vertical component, while the same is true for the MC14 velocities on the radial component. Due to this variation between the vertical and radial components, we compare models produced with both of these velocities to those produced with the addition of a tear or with an alternative slab geometry in the following. Consistent with the event 26 results, the cross-correlation coefficients for the event 20 models clearly indicate that the Slab1.0 (*Hayes et al.*, 2012) geometry is a better representation of the slab shape than that derived from *Cahill and Isacks* (1992) (CI). Using this

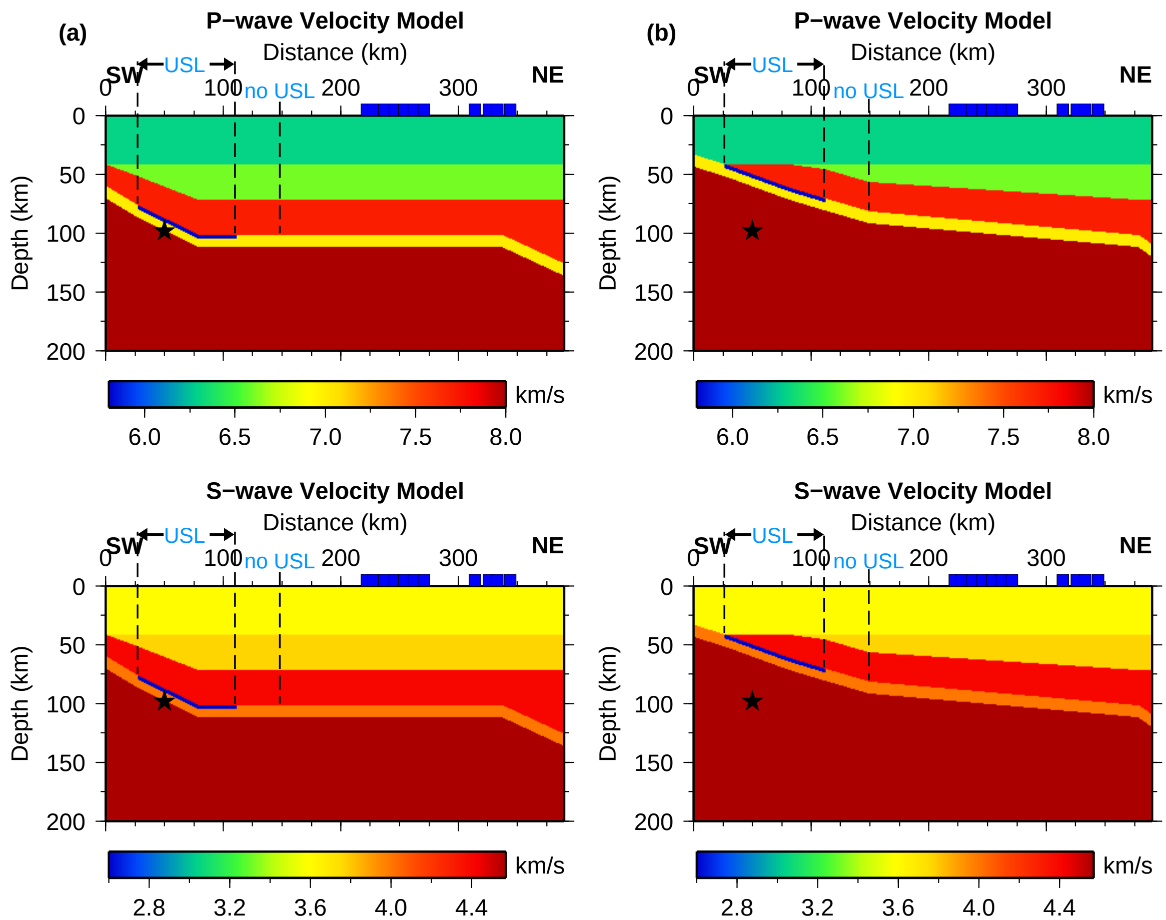

Figure 4.14: 2D velocity models of the subduction zone structure along the PG line (blue squares) for event 26 (Figure 4.13, Table 4.2). P- and S-wave velocities are from the P12 model. Subducted slab shape is estimated from the isodepth contours of (a) *Cahill and Isacks* (1992) and (b) Slab1.0 (*Hayes et al.*, 2012). Note the large variation in slab geometry between (a) and (b). Locations of the USL zone and approximate boundary of the no USL zone are indicated for reference. The location of event 26 used in the modeling is shown by the black star.

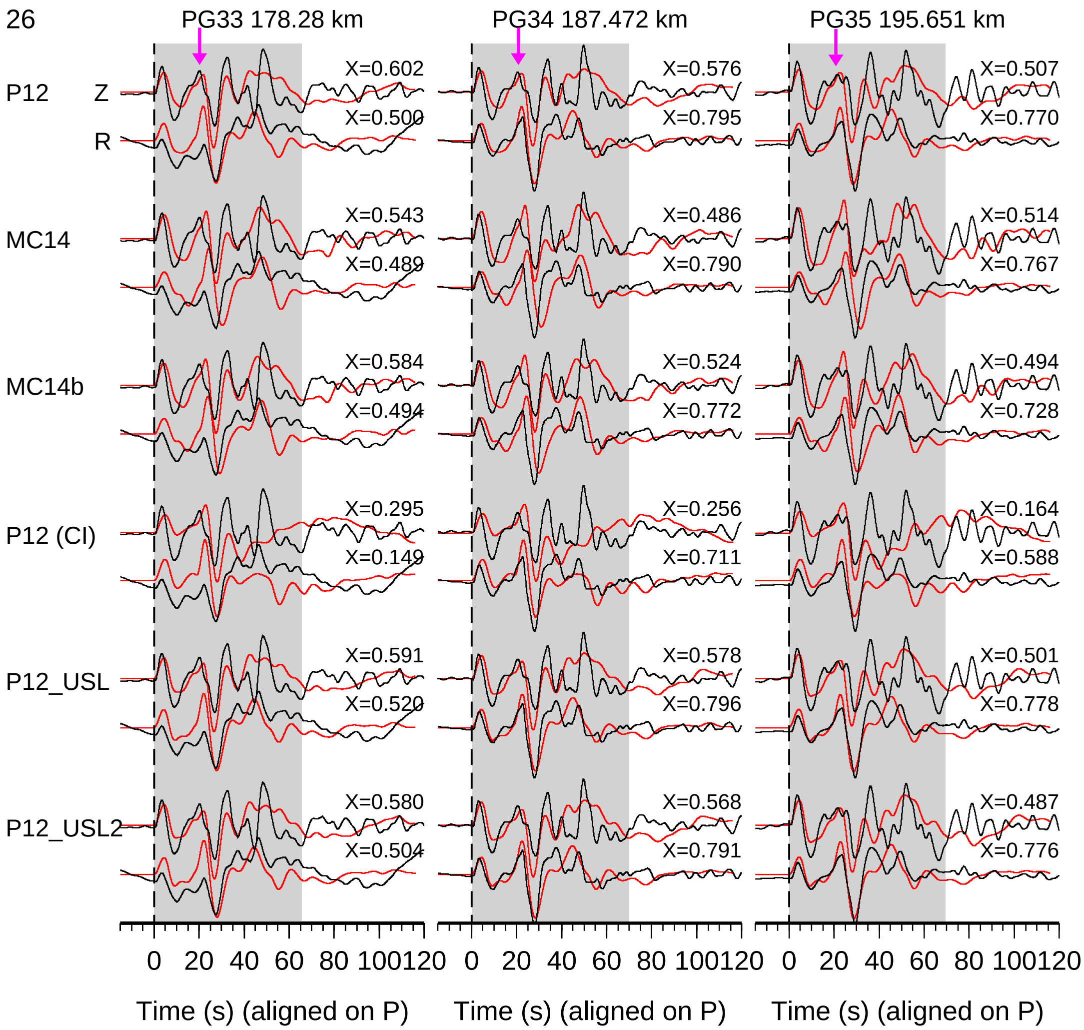

Figure 4.15: Comparison of 2D modeling results of event 26 for six different models at three stations, filtered to 0.01–0.1 Hz. Data are in black, synthetics are in red. Vertical (Z) and radial (R) components are shown. P (dashed line) and S (pink arrow) arrivals are indicated. The top three rows show results using each of the 1D velocity models tested in this study coupled with slab geometry estimated from the Slab1.0 (*Hayes et al.*, 2012) isodepth contours. The P12 (CI) model uses P12 velocities coupled with slab geometry estimated from the *Cahill and Isacks* (1992) (CI) contours. The P12_USL and P12_USL2 models both consist of P12 velocities coupled with slab shape estimated from Slab1.0 and the addition of an USL at the top of the slab. The USL is constrained to the USL zone in P12_USL and extends to the boundary of the no USL zone in P12_USL2 (Figure 4.14b). Cross-correlation coefficients (X) for each model with the data for the grey shaded segment of the waveform are shown. See Table 4.2 for summary of modeling results.

preferred Slab1.0 (*Hayes et al.*, 2012) geometry, models with the addition of 20-km (i.e., P12_dt20 and MC14_dt20) and 50-km (i.e., P12_dt50 and MC14_dt50) wide gaps in the slab centered at the location of the largest transition in slab dip (Figure 4.16) are compared to those without any tearing (i.e., P12 and MC14 in Figure 4.17). The P12_dt20 and MC14_dt20 models provide overall worse fits to the data on both the vertical and radial components than the corresponding models that do not include a tear. The P12_dt50 and MC14_dt50 models both provide slightly improved fits to the data on the vertical component and significantly worse fits on the radial component, which more than counterbalance any improvement on the vertical. As such, these modeling results suggest that there is no tear in the slab along the 8° increase in slab dip.

4.4 Discussion

The transition from flat to normal subduction in southern Peru suggests either tearing or continuous curvature of the subducted Nazca plate to accommodate this change in geometry. In this study, we provide evidence that supports a smooth contortion of the slab based on seismic observations, source mechanism analysis, and modeling of the velocity structure of the subduction zone. Observations of intraslab seismicity reveal a zone of decreased seismicity in the flat slab region, the margin of which is coincident with both the transition to a steeper dip and the intersection of the Nazca Ridge with the Peru-Chile Trench. The decreased seismicity of this zone suggests a change in plate structure, which, coupled with the seismic gap over the projected downdip continuation of the Nazca Ridge, is likely due to the ridge itself. The southward migration of the Nazca Ridge from 11°S since ~11.2 Ma, when it first intersected the trench (*Hampel*, 2002), could explain the observed decrease in seismicity in the flat slab region to the northwest, where the ridge was subducting in the past. Decreased coupling in the seismogenic zone along the current intersection of the Nazca Ridge with the trench implies aseismic creep (*Pritchard and Fielding*, 2008; *Perfettini et al.*, 2010; *Chlieh et al.*, 2011) and may explain the observed downdip gap in intraslab seismicity. While relatively narrow zones of decreased seismicity have been used to suggest plate-tearing in other subduction zones (e.g., *Dougherty and Clayton*, 2014), the broad zone of decreased intermediate depth seismicity observed here is most

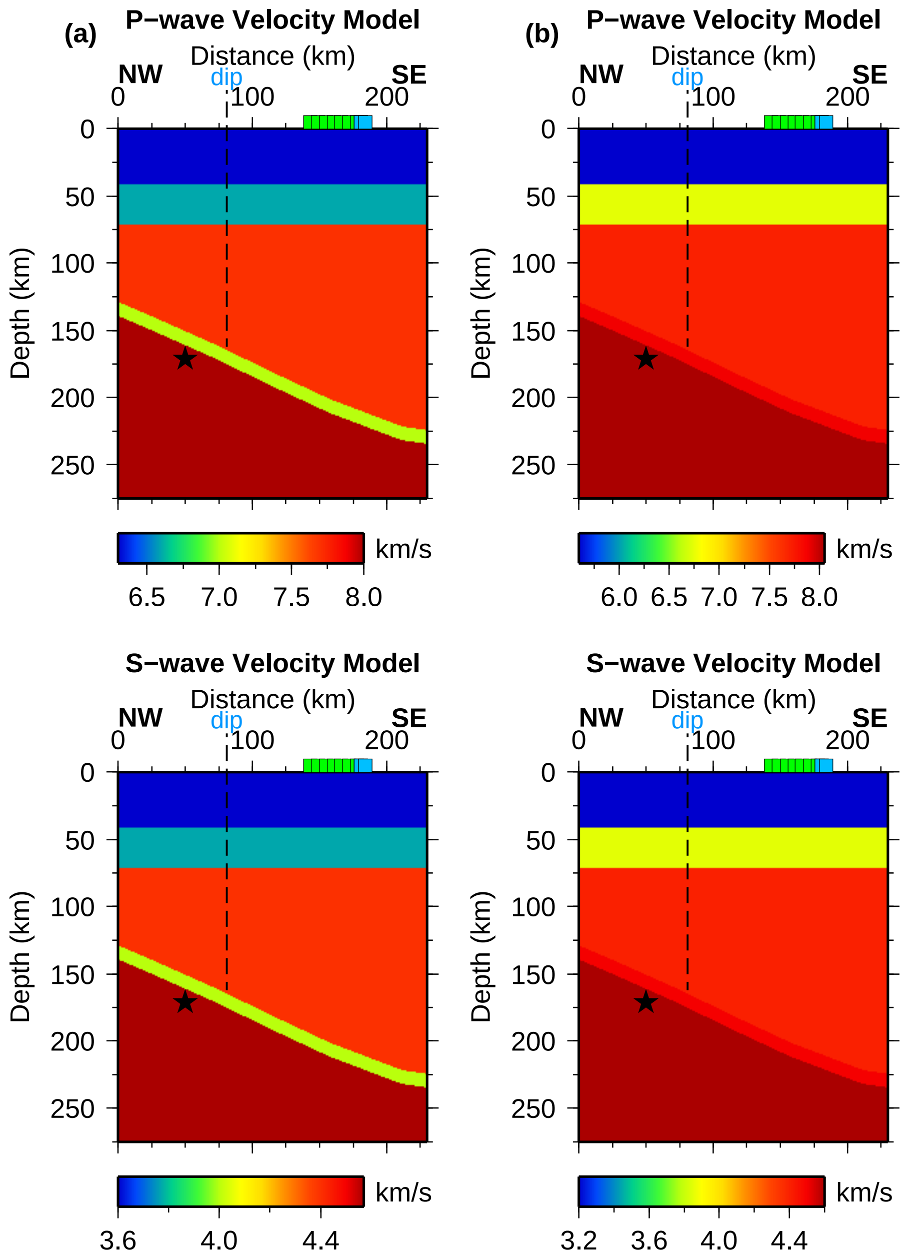

Figure 4.16: 2D velocity models of the subduction zone structure along the PF (green squares) and PE (light blue squares) lines for the S56°E-oriented profile for event 20 (Figure 4.13, Table 4.2). P- and S-wave velocities are from the (a) P12 and (b) MC14 models. Subducted slab shape is estimated from the isodepth contours of Slab1.0 (*Hayes et al.*, 2012). Location of the largest change in slab dip is indicated for reference. The location of event 20 used in the modeling is shown by the black star.

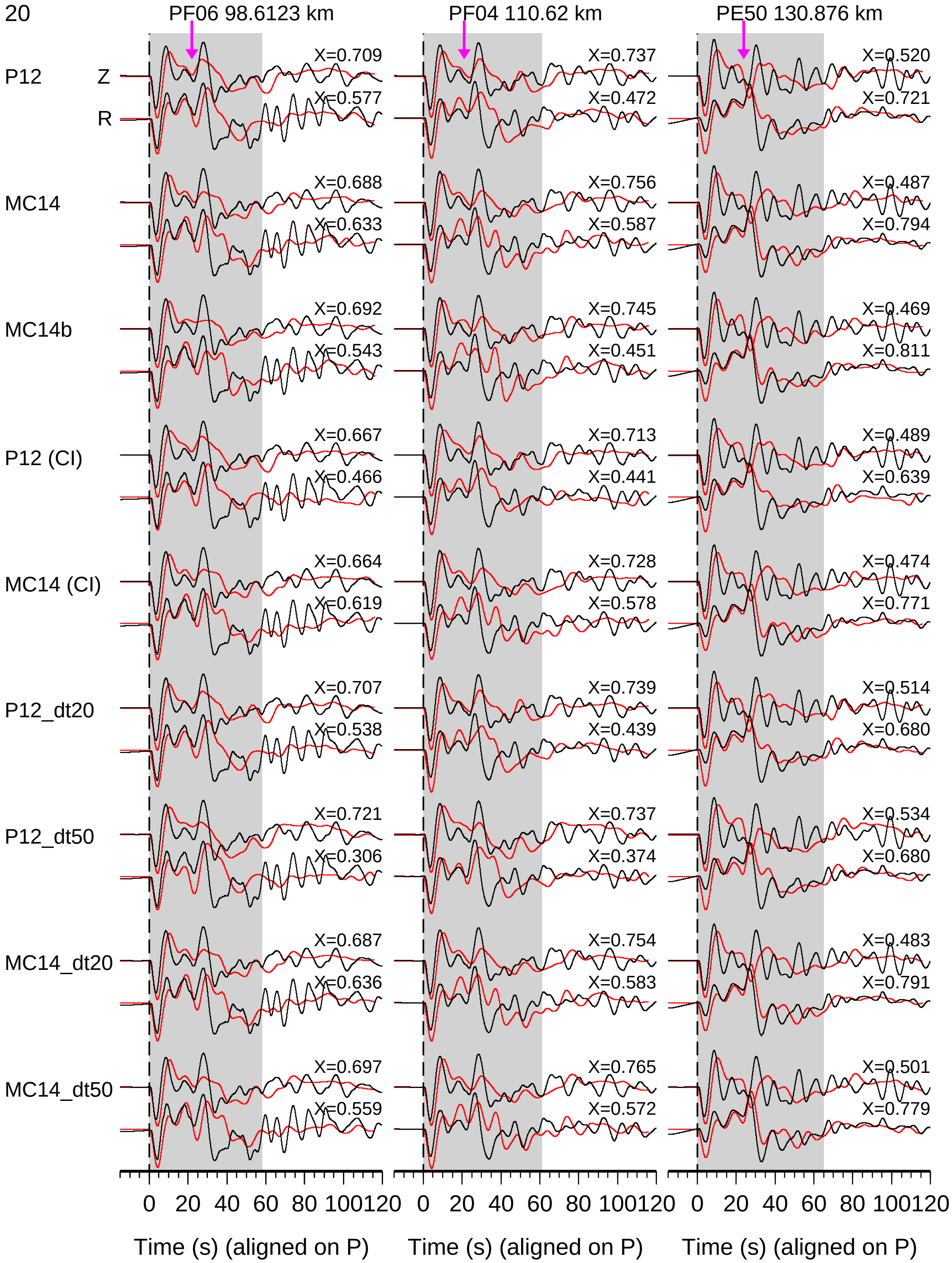

Figure 4.17: Comparison of 2D modeling results of event 20 for nine different models at three stations, filtered to 0.01–0.1 Hz. Data are in black, synthetics are in red. Vertical (Z) and radial (R) components are shown. P (dashed line) and S (pink arrow) arrivals are indicated. The top three rows show results using each of the 1D velocity models tested in this study coupled with slab geometry estimated from the Slab1.0 (*Hayes et al.*, 2012) isodepth contours. The P12 (CI) and MC14 (CI) models use P12 and MC14 velocities, respectively, coupled with slab geometry estimated from the *Cahill and Isacks* (1992) (CI) contours. The P12_dt20 and P12_dt50 models both consist of P12 velocities coupled with slab shape estimated from Slab1.0 and the addition of 20-km and 50-km-wide, respectively, tears (t) in the slab centered at the largest change in dip (d) (Figure 4.16a). Corresponding models using MC14 velocities instead of P12 are also tested (MC14_dt20, MC14_dt50). Cross-correlation coefficients (X) for each model with the data for the grey shaded segment of the waveform are shown. See Table 4.2 for summary of modeling results.

likely due to the subduction of the aseismic Nazca Ridge, not a tear. This is supported by the confirmed projected continuation of the ridge and the lack of slab tear from the 2D finite-difference modeling. The abundant lower crustal seismicity observed within the overriding South American plate in the flat slab region has been suggested to indicate strong coupling between the two plates in this region (e.g., *Barazangi and Isacks*, 1976; *Gutscher*, 2002). If these plates are strongly coupled, however, a higher rate of seismicity would be expected in the flat slab than that observed. In fact, the largest amount of overriding plate seismicity in our study region occurs above the projected linear continuation of the Nazca Ridge, which exhibits low coupling with the South American plate at the trench. This suggests instead that the elevated geometry (∼1.5 km high at the crest (*Woods and Okal*, 1994)) of the subducted Nazca Ridge is imparting increased stress on the base of the overriding plate where the flat slab underplates South America, resulting in increased lower crustal seismicity. This interpretation is consistent with the observed uplift of the Fitzcarrald arch in the Amazonian foreland basin, which is attributed to the projected continuation of the Nazca Ridge (*Espurt et al.*, 2007). The observed cluster of seismicity near the PG line, centered at ∼14°S, 72.85°W, may imply focusing of stress related to the changing slab geometry (*Suárez et al.*, 1990). Its shallower depth range, ∼15–45 km above the estimated slab surface at ∼100 km, suggests possible upwarping of the slab as a flexural response to resubduction downdip and/or lateral contortion. Alternatively, there may be some other (unidentified) localized anomaly responsible for this seismicity cluster; however, shear wave velocities down to 120 km depth reveal no such feature (*Ma and Clayton*, 2014).

Focal mechanisms of the intraslab seismicity elucidate the nature of the flat-to-normal transition in slab dip beyond that of the epicentral ISC catalog locations. The linear ENE-WSW-oriented concentration of events observed along the sharp bend in isodepth contours through the center of the array implies a focusing of stress and increase in seismicity in this region, consistent with plate flexure along a smooth contortion as seen here and elsewhere (*Grange et al.*, 1984b; *McCrory et al.*, 2012). Thrust and oblique faulting mechanisms located at the point of sharpest curvature of the isodepth contours and exhibiting N-S and NW-SE compression indicate the flexural response of the slab around this bend (*Yamaoka et al.*, 1986; *Creager et al.*, 1995; *Kirby et al.*, 1995). Normal faulting mechanisms with NNW-SSE extension located near the intersection of the PE and PF lines to the southeast show further response of the slab to the smooth contortion between flat and normal subduction (*Schneider and Sacks*, 1987; *Tavera and Buforn*, 2001). The N-S and NW-SE extensional mechanisms of the cluster of seismicity near event 38 in Figure 4.1 support our hypothesis that this seismicity may be due to along-strike bending of the slab as the result of a lateral contortion, wherein the more steeply dipping region is sinking and exerting lateral slab-pull on the horizontal section (*Schneider and Sacks*, 1987). Additionally, the lack of observed "tearing events" consisting of steeply dipping focal planes aligned along the strike of a possible tear location (*Gutscher et al.*, 1999b) imply that there is no tear present in southern Peru. The absence of compressional mechanisms in the flat slab region also argues against strong coupling between the Nazca and South American plates, as noted for the ISC data above.

From estimating the lateral variation in slab dip using Wadati-Benioff zone seismicity, we find a gradual increase in slab dip indicative of a smooth contortion in the Nazca plate. Further exploration of this seismicity in the trench-parallel direction reveals no gaps or vertical offsets which might indicate tearing of the plate, consistent with the continuous slab identified from receiver functions (*Phillips and Clayton*, 2014) and imaged tomographically (*Engdahl et al.*, 1995). This is contrary to what has been observed along the flat-to-normal transition in northern Peru/southern Ecuador, where both a gap and vertical offset in seismicity suggest a slab tear (*Gutscher et al.*, 1999b). The 3D surface generated from piecewise-linear regression fits to the seismicity clearly indicates the continuous curvature of the slab from flat to normal subduction in southern Peru, consistent with the confirmed absence of tearing in the 2D modeling results. The anomalous rise in the northwestern corner of the downdip region of the slab surface may be due to decreased seismicity in this region, resulting in fits that are less constrained through this area, producing an anomalous shallowing of the surface. An alternative explanation is that this rise may reflect the flexural bulge of the plate suggested from the observed cluster of shallower seismicity in this region. Such a bulge, however, was not identified from receiver functions (*Phillips and Clayton*, 2014).

Examination of the lateral extent of the USL shows that it is restricted to the flat slab region in the northwest portion of our study area. The observed boundary between the USL (or possible USL) and no USL zones that is coincident with the southeast margin of the projected continuation of the Nazca Ridge suggests a change in plate structure here, as was identified from the observed decrease in seismicity. Similar boundaries in central Mexico were used in conjunction with coincident sharp transitions in slab dip to suggest tearing of the subducted plate (*Dougherty et al.*, 2012; *Dougherty and Clayton*, 2014). In southern Peru, however, this boundary is within the horizontal subduction region and is ∼100 km northwest of where the slab ceases to be flat and begins to gradually increase in dip. The lack of a coincident sharp transition in slab dip here suggests that this boundary is not indicating a tear in the slab, but rather is related to a structural change caused by the subduction of the Nazca Ridge. The confirmed absence of a slab tear here from 2D modeling further reinforces this conclusion. The concentration of the USL zone immediately downdip from where the Nazca Ridge intersects the trench suggests that this low strength layer may be responsible for the observed low coupling and gap in intermediate depth seismicity within the projected continuation of the ridge. Such decoupling of the flat slab from the overriding plate has also been observed in central Mexico (*Singh and Pardo*, 1993; *Franco et al.*, 2005) and is attributed to the USL there (*Kim et al.*, 2010). The possibly confirmed presence of the USL zone from 2D modeling also supports this theory; however, further modeling along different profiles and/or using different events would provide additional constraints on the presence of the USL. Previous studies have noted increased hydration of the oceanic lithosphere within the Nazca Ridge evidenced by decreased seismic velocities (*Couch and Whitsett*, 1981; *Ma and Clayton*, 2014) and increased receiver function amplitudes (*Phillips and Clayton*, 2014). This hydration may support the formation of the USL by providing additional free-fluid and/or hydrous minerals to the subduction zone. A possible mechanism for the formation of the USL in this region can be suggested if its composition as a talc-rich ultramafic layer that originated from the mantle wedge (*Kim et al.*, 2013) is assumed.

We propose that the initial subduction of the Nazca Ridge at 11°S introduced additional water to the subduction zone as the slab dehydrated. This increased the localized concentration of water in the mantle wedge, resulting in the production of talc (*Kim et al.*, 2013) overlying the subducted ridge. Talc formation decreases the viscosity of the wedge, which may facilitate flattening of the slab (*Manea and Gurnis*, 2007; *Kim et al.*, 2013). In Peru, the flattening of the Nazca slab is estimated to have begun ∼10–12 Ma (*Ramos and Folguera*, 2009), consistent with the initial subduction of the Nazca Ridge ∼11.2 Ma (*Hampel*, 2002). Partly based on this temporal coincidence, the buoyancy of the ridge is often suggested as a cause of flat subduction in this region (e.g., *Pilger*, 1981; *Soler and Bonhomme*, 1990; *Gutscher et al.*, 1999a); however, geodynamical modeling has demonstrated that the buoyancy of the ridge alone is insufficient to cause flattening of the slab (*van Hunen et al.*, 2004; *Espurt et al.*, 2008; *Gerya et al.*, 2009). Further discussion of possible causes of flat subduction is given in *Gutscher* (2002), *van Hunen et al.* (2004), and *Pérez-Gussinyé et al.* (2008). As the Nazca Ridge migrates southward, continued dehydration introduces an increased concentration of water to a new section of mantle wedge, resulting in talc formation there. Once the ridge migrates, the flux of water into the section of mantle wedge overlying its former location decreases, which decreases or stops talc production. Translating this process into the distribution of the USL, the increased hydration of the Nazca Ridge causes localized formation of the USL along its downdip continuation. Southward migration of the ridge results in a weak or dissipating USL to the northwest due to decreased hydration of the mantle wedge. This interpretation is consistent with the observed USL zone located downdip from the current position of the Nazca Ridge and the possible USL zone located in the flat slab region to the northwest.

The 2D velocity modeling also provides valuable insights into the structure and morphology of the slab along the transition from flat to normal subduction, which can most accurately be described as consisting, overall, of P12 velocity material with Slab1.0 (*Hayes et al.*, 2012) geometry. The failure of the MC14 and MC14b velocities to provide better fits to the data may be the result of oversimplification of the velocity structure imaged by *Ma and Clayton* (2014) for this study. A more complex velocity model that includes the imaged lateral heterogeneity and low velocity zone in the overriding plate (*Ma and Clayton*, 2014) may be more representative of the subduction zone structure. Additionally, the preference of slab geometries estimated from the isodepth contours of Slab1.0 (*Hayes et al.*, 2012) over *Cahill and Isacks* (1992) is puzzling. The *Cahill and Isacks*

(1992) contours are more consistent with the observed Wadati-Benioff zone seismicity than those of Slab1.0 (*Hayes et al.*, 2012), especially in the flat slab region. *Hayes et al.* (2012) even acknowledges their difficulty in fitting the true subduction interface in this region, as evidenced by anomalous short-wavelength features and large misfits. The slab surface as determined from receiver functions (*Phillips et al.*, 2012; *Phillips and Clayton*, 2014) is also more consistent with the *Cahill and Isacks* (1992) contours.

In an effort to understand why smooth contortion of the slab along flat-to-normal transitions occurs in some places and plate tearing in others, we examine the lateral strain of the smoothly contorting Nazca slab in southern Peru and compare it with that of the likely torn Cocos slab in western and eastern central Mexico. Slab dip estimates for western central Mexico (*Dougherty et al.*, 2012), eastern central Mexico (*Dougherty and Clayton*, 2014), and southern Peru (this study) are used to approximate the slab surface in each region along a trench-parallel cross-section (Figure 4.18a). It should be noted that there are only four dip estimates for western central Mexico, while eastern central Mexico and southern Peru have 21 and 17 data points, respectively. Also, the dip estimates for western central Mexico were made from seismicity in 50-km-wide bins, while those in the other two regions utilized 25-km-wide bins. Comparison of the approximate slab surfaces in Figure 4.18a clearly demonstrates the gradual transition from flat to normal subduction in southern Peru relative to the abrupt transitions in both regions of central Mexico. *Dougherty et al.* (2012) and *Dougherty and Clayton* (2014) both noted sharp increases in slab dip of 14°, while the largest increase in slab dip that we observe in southern Peru is only 8° and is preceded by several smaller increases of 3° and 5° across the slab transition. The incremental normal strain between each bin in which a dip estimate is obtained is shown in Figure 4.18b for all three regions. This strain is calculated as the fractional change in length, where the original length is the bin width (i.e., 25 km or 50 km). The largest incremental strain occurs at the sharpest gradient in the slab surface in all three regions, with nearly all of the strain in the Cocos slab concentrated here, while strain in the Nazca slab is distributed over a larger area. In order to compare the overall strain among the three regions on the same length scale, we select a 150-km-wide segment of the eastern central Mexico and southern Peru slabs centered around the midpoint of the largest gradient in the slab surface. The normal strains over this segment are calculated to be ∼10% in southern Peru and ∼15% in both regions of central Mexico. Other studies also find 10% along-strike strain in this region of southern Peru (*Schneider and Sacks*, 1987; *Creager et al.*, 1995). In central Mexico, *Burbach and Frohlich* (1986) estimate a lateral strain of ∼15% in the west and ∼6% in the east. The discrepancy between our calculated strain and that of *Burbach and Frohlich* (1986) in eastern central Mexico may be due to the small amount of seismicity in this region that is used in their strain estimation, yielding a less well constrained value. The difference in strain of 5% between southern Peru and central Mexico may partly explain why tearing occurs in the Cocos slab, but not in the Nazca slab; however, other factors are likely also responsible.

Tearing of the young, ∼15 Ma in the west and ∼18 Ma in the east (*Ferrari et al.*, 2012), Cocos slab and not of the much older, ∼45 Ma (*Müller et al.*, 2008), Nazca slab is counterintuitive, even with an increase in strain of 5%. Young slabs are warmer and generally show less resistance against bending relative to their older counterparts (*van Hunen et al.*, 2002), suggesting that a smooth contortion would be more likely to occur in a young slab, while an older slab would be more likely to fail and tear. One possible explanation is that rollback of the Cocos slab since the late Miocene (*Ferrari et al.*, 2012) imposed stresses on the slab which resulted in tearing along pre-existing lines of weakness in the subducting plate located at the transitions from flat to normal subduction (*Dougherty and Clayton*, 2014), where the slab was previously contorted. These lines of weakness include the projected extension of the Orozco Fracture Zone in the west (*Bandy et al.*, 2000; *Dougherty et al.*, 2012; *Stubailo et al.*, 2012) and parallel ridges of seamounts in the east (*Dougherty and Clayton*, 2014). The absence of similar rollback and of a coincident line of weakness at the slab transition in southern Peru supports the Nazca slab remaining continuous.

4.5 Conclusions

The nature of the transition from flat to normal subduction in southern Peru is investigated using intraslab seismicity patterns, focal mechanism orientations, an analysis of P waveform complexities,

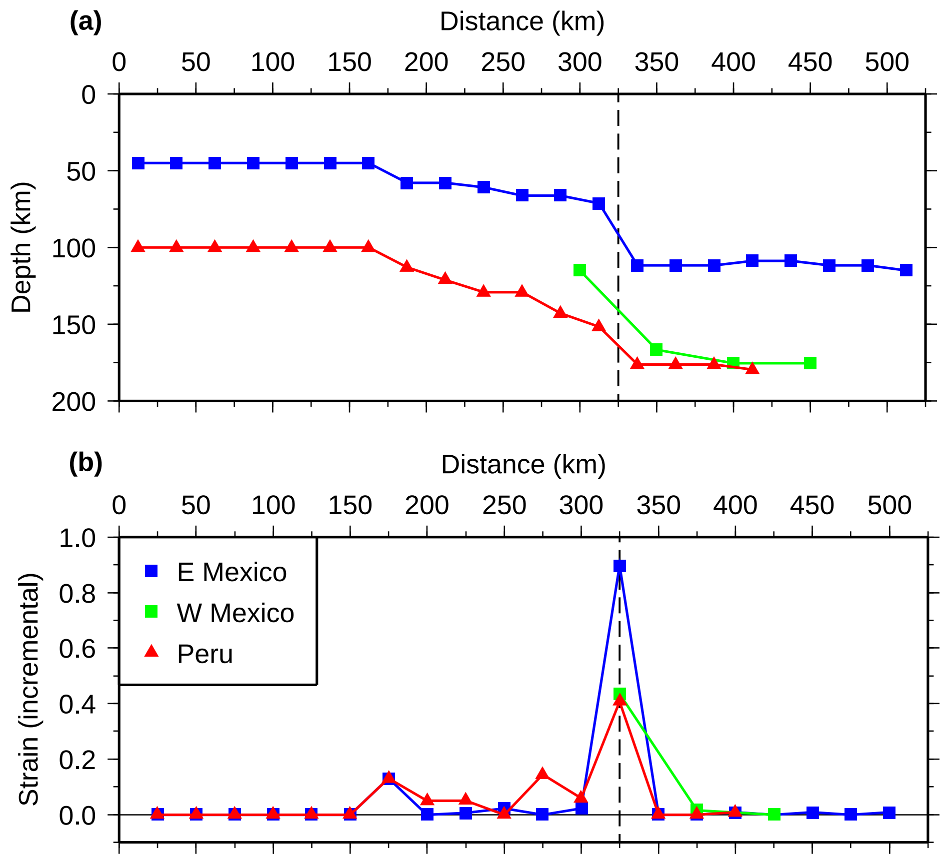

Figure 4.18: Slab strain along the transition from flat to normal subduction in three regions. (a) Depth to the top of the slab using slab dip estimates for eastern central Mexico (*Dougherty and Clayton*, 2014), western central Mexico (*Dougherty et al.*, 2012), and southern Peru (this study). Slabs are aligned along midpoint of largest gradient in depth (black dashed line). Note the gradual transition from flat (left) to normal (right) subduction in southern Peru relative to the abrupt transitions in both regions of central Mexico. (b) Incremental strain between each bin in which a dip estimate is obtained. Bins in eastern central Mexico and southern Peru are 25 km wide; those in western central Mexico are 50 km wide.

and 2D waveform modeling techniques. The results show that the subducted Nazca plate is a complicated structure with a possible thin USL atop the horizontal slab. The lateral extent of this USL is coincident with the margin of the projected continuation of the subducting Nazca Ridge, implying a change in structure which we interpret as a causal relationship between these features. A gradual increase in slab dip with no sharp transitions suggests smooth contortion of the Nazca plate. The lack of any gaps or vertical offsets in the intraslab seismicity coupled with the concentration and orientation of focal mechanisms indicative of slab bending further support this conclusion. The absence of a tear in the slab along either the Nazca Ridge or the largest increase in slab dip is also confirmed with 2D waveform modeling. Further modeling of the subduction zone structure in the flat slab region may provide additional constraints on the presence of the USL.

4.6 Supplemental Figures

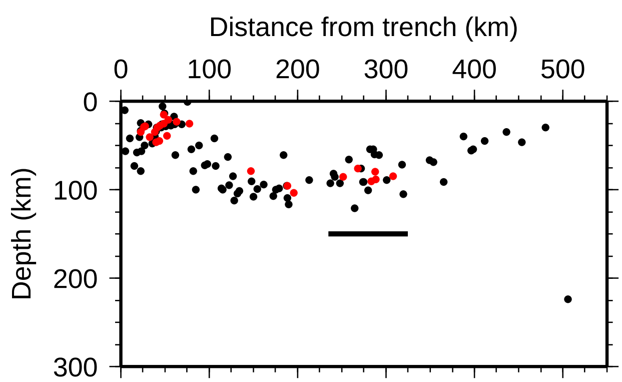

Figure 4.19: Trench-normal cross-section of seismicity from the 1960–2013 ISC Bulletin event catalog (*International Seismological Centre*, 2011) (black dots) in bin 3 of Figure 4.5. Hypocenter locations for earthquakes from the relocated 1960–2008 EHB Bulletin event catalog (*International Seismological Centre*, 2011) (red dots) are shown for reference. A black horizontal bar marks the location of the shallower cluster of seismicity centered at ∼14°S, 72.85°W that was noted for Figure 4.3.

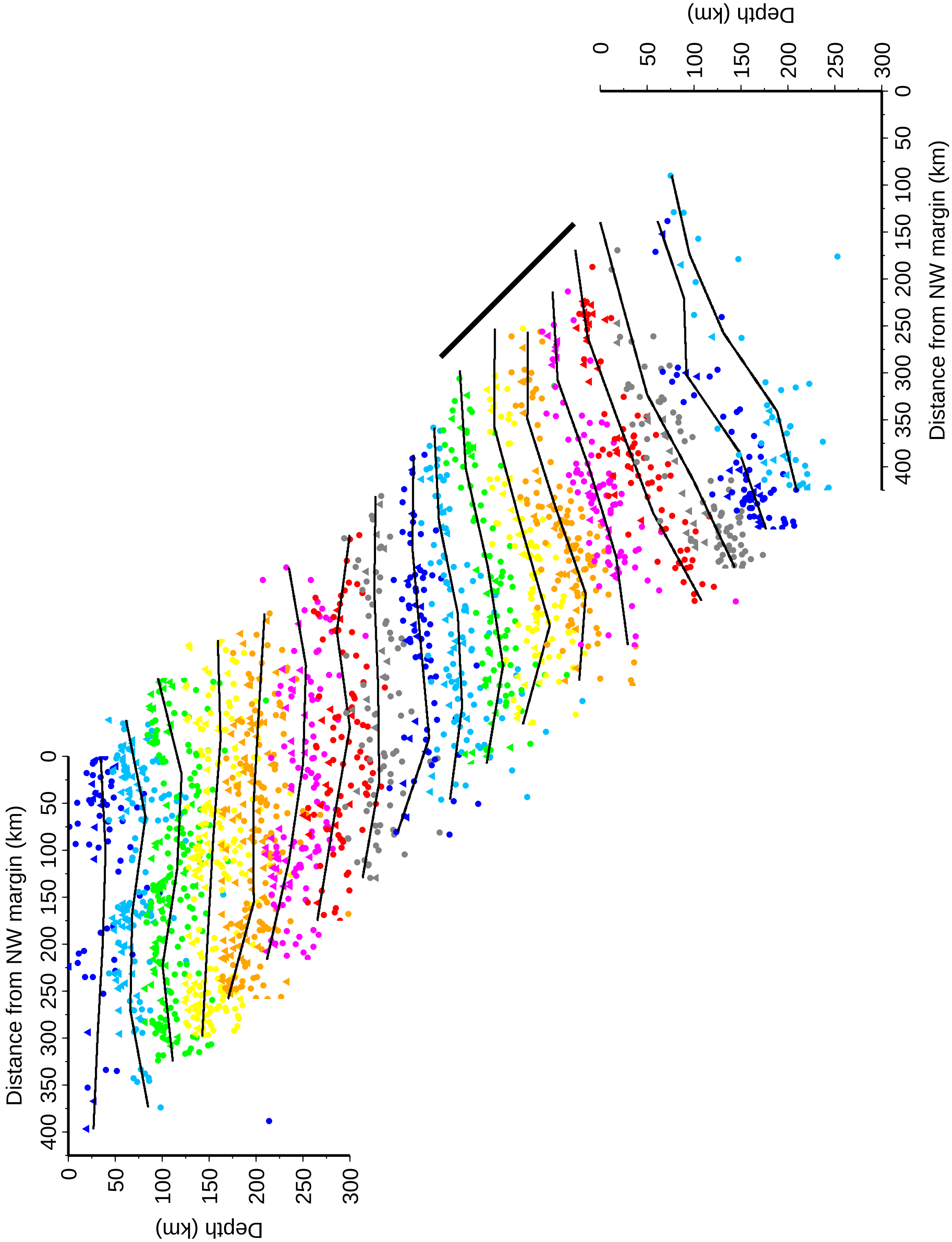

Figure 4.20: Perspective view (updip) of cross-sections of slab seismicity from the ISC (dots) and EHB (triangles) catalogs in trench-parallel bins h1 (top) to h18 (bottom; see Figure 4.6 for bin locations). Events within the overriding plate are not shown. All events within a particular bin are shown as a single color. Variations in color between bins are used to distinguish cross-sections. Weighted piecewise-linear regression fits to the slab seismicity in each cross-section are shown (black lines). Cross-sections for bins h11–h15 shown in Figure 4.7 are marked by a heavy black line. Note the abrupt step in the fit for bin h17 due to a poorly constrained regression from sparse data in this bin.

References

Bandy, W. L., T. W. C. Hilde, and C.-Y. Yan (2000), The Rivera-Cocos plate boundary: Implications for Rivera-Cocos relative motion and plate fragmentation, in *Cenozoic Tectonics and Volcanism of Mexico*, *Geol. Soc. Am. Spec. Pap.*, vol. 334, edited by H. Delgado-Granados, G. Aguirre-Díaz, and J. M. Stock, pp. 1–28, GSA, Boulder, Colorado.

Barazangi, M., and B. L. Isacks (1976), Spatial distribution of earthquakes and subduction of the Nazca plate beneath South America, *Geology*, *4*, 686–692.

Barazangi, M., and B. L. Isacks (1979), Subduction of the Nazca plate beneath Peru: evidence from spatial distribution of earthquakes, *Geophys. J. R. astr. Soc.*, *57*, 537–555.

Bevis, M., and B. L. Isacks (1984), Hypocentral trend surface analysis: Probing the geometry of Benioff zones, *J. Geophys. Res.*, *89*, 6153–6170.

Boyd, T. M., J. A. Snoke, I. S. Sacks, and A. R. B. (1984), High-resolution determination of the Benioff zone geometry beneath southern Peru, *Bull. Seis. Soc. Am.*, *74*, 559–568.

Burbach, G. V., and C. Frohlich (1986), Intermediate and deep seismicity and lateral structure of subducted lithosphere in the circum-Pacific region, *Rev. Geophys.*, *24*, 833–874.

Cahill, T., and B. L. Isacks (1992), Seismicity and shape of the subducted Nazca Plate, *J. Geophys. Res.*, *97*, 17,503–17,529.

Chlieh, M., H. Perfettini, H. Tavera, J.-P. Avouac, D. Remy, J.-M. Nocquet, F. Rolandone, F. Bondoux, G. Gabalda, and S. Bonvalot (2011), Interseismic coupling and seismic potential along the Central Andes subduction zone, *J. Geophys. Res.*, *116*, B12405, doi:10.1029/2010JB008166.

Couch, R., and R. M. Whitsett (1981), Structures of the Nazca Ridge and the continental shelf and slope of southern Peru, in *Nazca Plate: Crustal Formation and Andean Convergence*, *Geol. Soc. Am. Mem.*, vol. 154, edited by L. D. Kulm, J. Dymond, E. J. Dasch, D. M. Hussong, and R. Roderick, pp. 569–586, GSA, Boulder, Colorado.

Creager, K. C., L.-Y. Chiao, J. P. Winchester, and E. R. Engdahl (1995), Membrane strain rates in the subducting plate beneath South America, *Geophys. Res. Lett.*, *22*, 2321–2324.

DeMets, C., R. G. Gordon, and D. F. Argus (2010), Geologically current plate motions, *Geophys. J. Int.*, *181*, 1–80, doi:10.1111/j.1365-246X.2009.04491.x.

D'Errico, J. (2005), *Surface fitting using gridfit*, MATLAB Central File Exchange, http://www.mathworks.com/matlabcentral/fileexchange/8998-surface-fitting-using-gridfit, accessed 18 April 2014.

D'Errico, J. (2009), *SLM - Shape Language Modeling*, MATLAB Central File Exchange, http://www.mathworks.com/matlabcentral/fileexchange/24443-slm-shape-language-modeling, accessed 17 April 2014.

Dougherty, S. L., and R. W. Clayton (2014), Seismicity and structure in central Mexico: Evidence for a possible slab tear in the South Cocos plate, *J. Geophys. Res.*, *119*, 3424–3447, doi:10.1002/2013JB010883.

Dougherty, S. L., R. W. Clayton, and D. V. Helmberger (2012), Seismic structure in central Mexico: Implications for fragmentation of the subducted Cocos plate, *J. Geophys. Res.*, *117*, B09316, doi:10.1029/2012JB009528.

Dziewonski, A. M., T.-A. Chou, and J. H. Woodhouse (1981), Determination of earthquake source parameters from waveform data for studies of global and regional seismicity, *J. Geophys. Res.*, *86*, 2825–2852, doi:10.1029/JB086iB04p02825.

Ekström, G., M. Nettles, and A. M. Dziewonski (2012), The global CMT project 2004-2010: Centroid-moment tensors for 13,017 earthquakes, *Phys. Earth Planet. Inter.*, *200-201*, 1–9, doi:10.1016/j.pepi.2012.04.002.

Engdahl, E. R., R. D. van der Hilst, and J. Berrocal (1995), Imaging of subducted lithosphere beneath South America, *Geophys. Res. Lett.*, *22*, 2317–2320.

Espurt, N., P. Baby, S. Brusset, M. Roddaz, W. Hermoza, V. Regard, P.-O. Antoine, R. Salas-Gismondi, and R. Bolaños (2007), How does the Nazca Ridge subduction influence the modern Amazonian foreland basin?, *Geology*, *35*, 515–518, doi:10.1130/G23237A.1.

Espurt, N., F. Funiciello, J. Martinod, B. Guillaume, V. Regard, C. Faccenna, and S. Brusset (2008), Flat subduction dynamics and deformation of the South American plate: Insights from analog modeling, *Tectonics*, *27*, TC3011.

Farr, T. G., P. A. Rosen, E. Caro, R. Crippen, R. Duren, S. Hensley, M. Kobrick, M. Paller, E. Rodriguez, L. Roth, D. Seal, S. Shaffer, J. Shimada, J. Umland, M. Werner, M. Oskin, D. Burbank, and D. Alsdorf (2007), The Shuttle Radar Topography Mission, *Rev. Geophys.*, *45*, RG2004, doi:10.1029/2005RG000183.

Ferrari, L., T. Orozco-Esquivel, V. Manea, and M. Manea (2012), The dynamic history of the Trans-Mexican Volcanic Belt and the Mexico subduction zone, *Tectonophysics*, *522-523*, 122–149, doi:10.1016/j.tecto.2011.09.018.

Franco, S. I., V. Kostoglodov, K. M. Larson, V. C. Manea, M. Manea, and J. A. Santiago (2005), Propagation of the 2001-2002 silent earthquake and interplate coupling in the Oaxaca subduction zone, Mexico, *Earth Planets Space*, *57*, 973–985.

Gerya, T. V., D. Fossati, C. Cantieni, and D. Seward (2009), Dynamic effects of aseismic ridge subduction: numerica modelling, *Eur. J. Mineral.*, *21*, 649–661.

Grange, F., P. Cunningham, J. Gagnepain, D. Hatzfeld, P. Molnar, L. Ocola, A. Rodrígues, S. W. Roecker, J. M. Stock, and G. Suárez (1984a), The configuration of the seismic zone and the downgoing slab in southern Peru, *Geophys. Res. Lett.*, *11*, 38–41.

Grange, F., D. Hatzfeld, P. Cunningham, P. Molnar, S. W. Roecker, G. Suárez, A. Rodrígues, and L. Ocola (1984b), Tectonic implications of the microearthquake seismicity and fault plane solutions in southern Peru, *J. Geophys. Res.*, *89*, 6139–6152.

Gutscher, M.-A. (2002), Andean subduction styles and their effect on thermal structure and interplate coupling, *J. South Am. Earth Sci.*, *15*, 3–10.

Gutscher, M.-A., J.-L. Olivet, D. Aslanian, J.-P. Eissen, and R. Maury (1999a), The "lost Inca Plateau": cause of flat subduction beneath Peru?, *Earth Planet. Sci. Lett.*, *171*, 335–341.

Gutscher, M.-A., J. Malavieille, S. Lallemand, and J.-Y. Collot (1999b), Tectonic segmentation of the North Andean margin: impact of the Carnegie Ridge collision, *Earth Planet. Sci. Lett.*, *168*, 255–270.

Hampel, A. (2002), The migration history of the Nazca Ridge along the Peruvian active margin: a re-evaluation, *Earth Planet. Sci. Lett.*, *203*, 665–679.

Hasegawa, A., and I. S. Sacks (1981), Subduction of the Nazca plate beneath Peru as determined from seismic observations, *J. Geophys. Res.*, *86*, 4971–4980.

Hayes, G. P., D. J. Wald, and R. L. Johnson (2012), Slab1.0: A three-dimensional model of global subduction zone geometries, *J. Geophys. Res.*, *117*, B01302.

International Seismological Centre (2011), *On-line Bulletin*, Int. Seis. Cent., Thatcham, United Kingdom, http://www.isc.ac.uk.

Kim, Y., R. W. Clayton, and J. M. Jackson (2010), Geometry and seismic properties of the subducting Cocos plate in central Mexico, *J. Geophys. Res.*, *115*, B06310, doi:10.1029/2009JB006942.

Kim, Y., R. W. Clayton, P. D. Asimow, and J. M. Jackson (2013), Generation of talc in the mantle wedge and its role in subduction dynamics in central Mexico, *Earth Planet. Sci. Lett.*, *384*, 81–87, doi:10.1016/j.epsl.2013.10.006.

Kirby, S. H., E. A. Okal, and E. R. Engdahl (1995), The 9 June 94 Bolivian deep earthquake: An exceptional event in an extraordinary subduction zone, *Geophys. Res. Lett.*, *22*, 2233–2236.

Ma, Y., and R. W. Clayton (2014), The crust and uppermost mantle structure of Southern Peru from ambient noise and earthquake surface wave analysis, *Earth Planet. Sci. Lett.*, *395*, 61–70.

Manea, V., and M. Gurnis (2007), Subduction zone evolution and low viscosity wedges and channels, *Earth Planet. Sci. Lett.*, *264*, 22–45, doi:10.1016/j.epsl.2007.08.030.

Manea, V. C., M. Manea, V. Kostoglodov, C. A. Currie, and G. Sewell (2004), Thermal structure, coupling and metamorphism in the Mexican subduction zone beneath Guerrero, *Geophys. J. Int.*, *158*, 775–784, doi:10.1111/j.1365-246X.2004.02325.x.

Manea, V. C., M. Manea, and L. Ferrari (2013), A geodynamical perspective on the subduction of Cocos and Rivera plates beneath Mexico and Central America, *Tectonophysics*, *609*, 56–81, doi:10.1016/j.tecto.2012.12.039.

McCrory, P. A., J. L. Blair, F. Waldhauser, and D. H. Oppenheimer (2012), Juan de Fuca slab geometry and its relation to Wadati-Benioff zone seismicity, *J. Geophys. Res.*, *117*, B09306, doi: 10.1029/2012JB009407.

Müller, R. D., M. Sdrolias, C. Gaina, and W. R. Roest (2008), Age, spreading rates, and spreading symmetry of the world's ocean crust, *Geochem. Geophys. Geosyst.*, *9*, Q04006.

Pérez-Gussinyé, M., A. R. Lowry, J. P. Morgan, and A. Tassara (2008), Effective elastic thickness variations along the Andean margin and their relationship to subduction geometry, *Geochem. Geophys. Geosyst.*, *9*, Q02003.

Perfettini, H., J.-P. Avouac, H. Tavera, A. Kositsky, J.-M. Nocquet, F. Bondoux, M. Chlieh, A. Sladen, L. Audin, D. L. Farber, and P. Soler (2010), Seismic and aseismic slip on the Central Peru megathrust, *Nature*, *465*, 78–81.

PeruSE (2013), Peru Subduction Experiment, Caltech, dataset, doi:10.7909/C3H41PBZ.

Pesicek, J. D., E. R. Engdahl, C. H. Thurber, H. R. DeShon, and D. Lange (2012), Mantle subducting slab structure in the region of the 2010 M8.8 Maule earthquake (30-40°S), Chile, *Geophys. J. Int.*, *191*, 317–324, doi:10.1111/j.1365-246X.2012.05624.x.

Phillips, K., and R. W. Clayton (2014), Structure of the subduction transition region from seismic array data in southern Peru, *Geophys. J. Int.*, *196*, 1889–1905.

Phillips, K., R. W. Clayton, P. Davis, H. Tavera, R. Guy, S. Skinner, I. Stubailo, L. Audin, and V. Aguilar (2012), Structure of the subduction system in souther Peru from seismic array data, *J. Geophys. Res.*, *117*, B11306, doi:10.1029/2012JB009540.

Pilger, R. H. (1981), Plate reconstructions, aseismic ridges, and low-angle subduction beneath the Andes, *Geol. Soc. Am. Bull.*, *92*, 448–456.

Pilger, R. H., and D. W. Handschumacher (1981), The fixed-hotspot hypothesis and origin of the Easter-Sala y Gomez-Nazca trace, *Geol. Soc. Am. Bull.*, *92*, 437–446.

Pritchard, M. E., and E. J. Fielding (2008), A study of the 2006 and 2007 earthquake sequence of Pisco, Peru, with InSAR and teleseismic data, *Geophys. Res. Lett.*, *35*, L09308.

Ramos, V. A., and A. Folguera (2009), Andean flat-slab subduction through time, in *Ancient Orogens and Modern Analogues*, *Geol. Soc. London Spec. Pub.*, vol. 327, edited by J. B. Murphy, J. D. Keppie, and A. J. Hynes, pp. 31–54, GSL.

Ray, J. S., J. J. Mahoney, R. A. Duncan, J. Ray, P. Wessel, and D. F. Naar (2012), Chronology and geochemistry of lavas from the Nazca Ridge and Easter Seamount Chain: an ∼30 myr hotspot record, *J. Petrol.*, *53*, 1417–1448, doi:10.1093/petrology/egs021.

Schneider, J. F., and I. S. Sacks (1987), Stress in the contorted Nazca plate beneath southern Peru from local earthquakes, *J. Geophys. Res.*, *92*, 13,887–13,902.

Singh, S. K., and M. Pardo (1993), Geometry of the Benioff zone and state of stress in the overriding plate in central Mexico, *Geophys. Res. Lett.*, *20*, 1483–1486.

Smith, W. H. F., and D. T. Sandwell (1997), Global seafloor topography from satellite altimetry and ship depth soundings, *Science*, *277*, 1957–1962.

Soler, P., and M. G. Bonhomme (1990), Relation of magmatic activity to plate dynamics in central Peru from Late Cretaceous to present, in *Plutonism from Antarctica to Alaska*, *Geol. Soc. Am. Spec. Pap.*, vol. 241, edited by S. M. Kay and C. W. Rapela, pp. 173–192, GSA, Boulder, Colorado.

Song, T. A., and Y. Kim (2012), Anisotropic uppermost mantle in young subducted slab underplating Central Mexico, *Nature Geosci.*, *5*, 55–59, doi:10.1038/NGEO1342.

Song, T. A., D. V. Helmberger, M. R. Brudzinski, R. W. Clayton, P. Davis, X. Pérez-Campos, and S. K. Singh (2009), Subducting slab ultra-slow velocity layer coincident with silent earthquakes in southern Mexico, *Science*, *324*, 502–506.

Stubailo, I., C. Beghein, and P. M. Davis (2012), Structure and anisotropy of the Mexico subduction zone based on Rayleigh-wave analysis and implications for the geometry of the Trans-Mexican Volcanic Belt, *J. Geophys. Res.*, *117*, B05303, doi:10.1029/2011JB008631.

Suárez, G., J. Gagnepain, A. Cisternas, D. Hatzfeld, P. Molnar, L. Ocola, S. W. Roecker, and J. P. Viodé (1990), Tectonic deformation of the Andes and the configuration of the subducted slab in central Peru: results from a microseismic experiment, *Geophys. J. Int.*, *103*, 1–12.

Tavera, H., and E. Buforn (2001), Source mechanism of earthquakes in Peru, *J. Seis.*, *5*, 519–539.

van Hunen, J., A. P. van den Berg, and N. J. Vlaar (2002), On the role of subducting oceanic plateaus in the development of shallow flat subduction, *Tectonophysics*, *352*, 317–333.

van Hunen, J., A. P. van den Berg, and N. J. Vlaar (2004), Various mechanisms to induce present-day shallow flat subduction and implications for the younger Earth: a numerical parameter study, *Phys. Earth Planet. Int.*, *146*, 179–194.

Vogt, P. R., A. Lowrie, D. R. Bracey, and R. N. Hey (1976), *Subduction of Aseismic Oceanic Ridges: Effects on Shape, Seismicity, and Other Characteristics of Consuming Plate Boundaries*, *Geol. Soc. Am. Spec. Pap.*, vol. 172, GSA, Boulder, Colorado.

von Huene, R., I. A. Pecher, and M.-A. Gutscher (1996), Development of the accretionary prism along Peru and material flux after subduction of Nazca Ridge, *Tectonics*, *15*, 19–33.

Ward, K. M., R. C. Porter, G. Zandt, S. L. Beck, L. S. Wagner, E. Minaya, and H. Tavera (2013), Ambient noise tomography across the Central Andes, *Geophys. J. Int.*, *194*, 1559–1573.

Woods, M. T., and E. A. Okal (1994), The structure of the Nazca ridge and Sala y Gomez seamount chain from the dispersion of Rayleigh waves, *Geophys. J. Int.*, *117*, 205–222.

Yamaoka, K., Y. Fukao, and M. Kumazawa (1986), Spherical shell tectonics: Effects of sphericity and inextensibility of the geometry of the descending lithosphere, *Rev. Geophys.*, *24*, 27–53.

Chapter 5

Further evidence for P-wave complexity in a region with slow slip events

Note: This chapter was written in 2009 and, consequently, the locations of non-volcanic tremor and slow slip events may be out of date. The figures and text will be updated to reflect any changes in the course of preparing this chapter to be submitted for publication in the future.

5.1 Abstract

A recent study of subduction beneath central Mexico indicates that there is a relationship between the location of slow slip events (SSEs) and the location of intraslab earthquakes that generate complex P-waves. Simple P waveforms indicate normal slab conditions with no occurrences of SSEs, whereas complex P waveforms imply the presence of a thin ultra-slow velocity layer (USL) on top of the slab and the occurrence of SSEs. Here, we further test this hypothesis in a region of southwest Japan that experiences SSEs and has a dense set of local stations. We estimate the location of a possible USL along the Philippine Sea slab surface and find this region of low velocity to be coincident with locations of SSEs that have occurred in southwest Japan. We interpret the source of the possible USL layer as fluids dehydrated from the subducting plate.

5.2 Introduction

The geometry of the subducted 15–27 Ma (*Okino et al.*, 1994) Philippine Sea (PHS) plate beneath the Eurasian (EUR) plate in southwest Japan is very similar to that of the subducted 10–23 Ma (*Pardo and Suárez*, 1995; *Manea et al.*, 2004) Cocos plate beneath the North American (NAM) plate in central Mexico. Both of these young plates exhibit large lateral variations in slab dip, with segments that subduct nearly horizontally abutting segments that dip much more steeply. The PHS slab dips ~10° towards the north beneath the island of Shikoku and ~45° towards the west beneath the neighboring island of Kyushu (*Nakanishi*, 1980; *Zhao et al.*, 2000; *Shiomi et al.*, 2004). The Cocos slab dips ~10–15° near the trench and then becomes subhorizontal beneath central Mexico (*Pardo and Suárez*, 1995; *Pérez-Campos et al.*, 2008). To the north, the Cocos slab dips ~30–50°, while to the south, it dips ~25–30° (*Pardo and Suárez*, 1995). The subduction zone in southwest Japan, however, has the added component of a second subducting plate. While the PHS plate shallowly subducts beneath the EUR plate in this region, the Pacific (PAC) plate subducts beneath the PHS plate at much greater depth (Figure 5.1).

In both the Japanese and Mexican subduction zones, SSEs have been noted to occur in the regions where the slab is dipping shallowly and where the dip of the slab is changing from nearly horizontal to a steeper dip (e.g., *Obara and Hirose*, 2006). By correlating locations of SSEs with epicenters of earthquakes that produced complex P waveforms, *Song et al.* (2009) suggested that there is a relationship between the presence of an ultra-slow velocity layer (USL) on top of the Cocos slab and location of SSEs. The locations of SSEs that have occurred in southwest Japan are shown in Figure 5.1. These episodic events are spatially and temporally correlated with the occurrence of non-volcanic tremor (NVT) in the region (*Obara et al.*, 2004; *Obara and Hirose*, 2006; *Ito et al.*, 2007). The source areas for these coincident events are estimated to occur at depths of 30 to 40 km over a 600-km-long belt parallel to the strike of the subducting PHS plate (*Obara*, 2002; *Obara and Hirose*, 2006; *Ito et al.*, 2007) (Figure 5.1). The SSEs and NVT occur in the transition zone from locked to aseismic slip in the downdip portion of the slab (*Obara and Hirose*, 2006; *Ito et al.*, 2007). These events are thought to be coupling phenomena related to stress accumulation along the upper

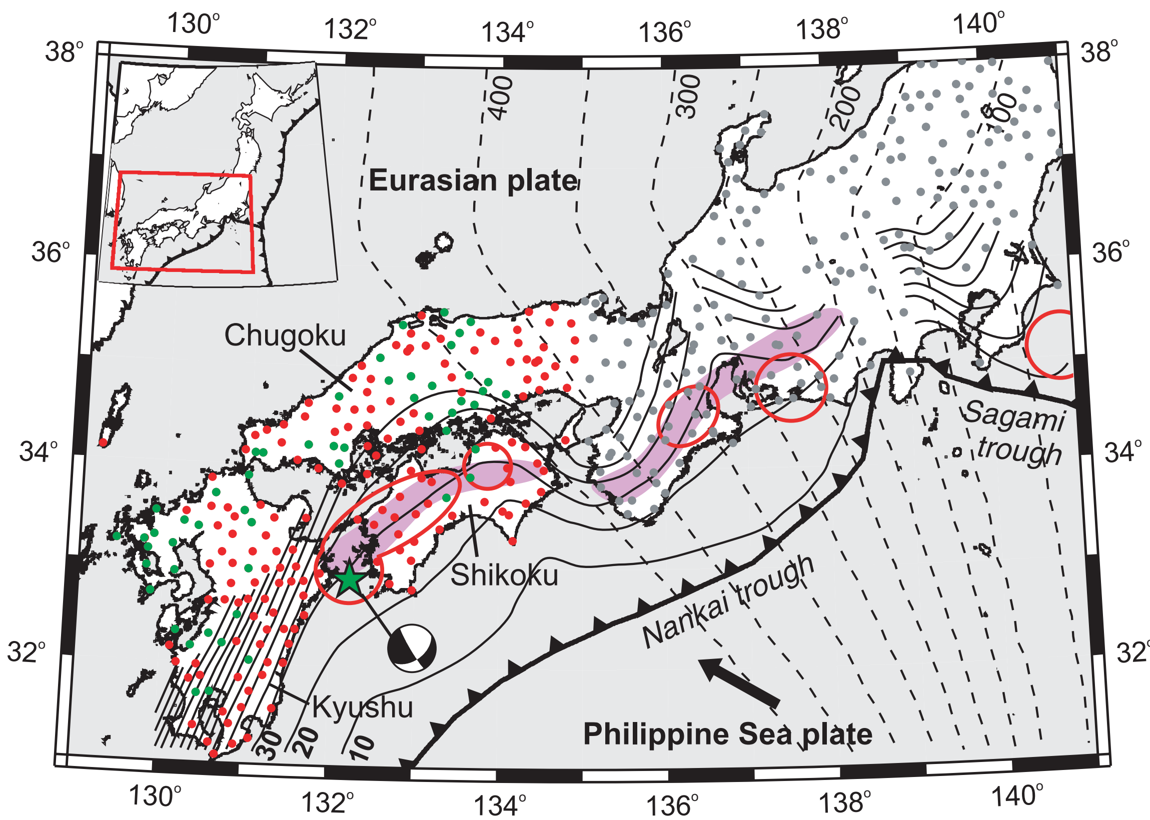

Figure 5.1: Hi-net stations in southwest Japan which recorded complex (green dots) or simple (red dots) P waveforms for the oblique-normal earthquake shown. Stations not sampled in this study are indicated by grey dots. The locations of slow slip events (red outlines) (*Hirose and Obara*, 2005; *Obara and Hirose*, 2006) and non-volcanic tremor (purple belt) (*Obara*, 2002) are indicated. The isodepth contours of the Pacific slab (*Zhao and Hasegawa*, 1993; *Nakajima and Hasegawa*, 2006) are shown by dashed lines with an interval of 50 km, while those of the Philippine Sea slab (*Wang et al.*, 2004) are shown by solid lines with an interval of 10 km. The convergence direction of the Philippine Sea plate near the Nankai trough is indicated by the black arrow (*Seno et al.*, 1993).

portion of the subducting plate, which result in an increase in the stress field updip where megathrust earthquakes occur (*Obara et al.*, 2004; *Ito et al.*, 2007). Although not completely understood, it is thought that the source of these phenomena is fluid generated by dehydration of the slab (e.g., *Obara*, 2002; *Seno and Yamasaki*, 2003; *Kodaira et al.*, 2004; *Wang et al.*, 2006). NVT could be generated by hydrofracturing during fluid migration (*Seno and Yamasaki*, 2003; *Wang et al.*, 2006; *Schwartz and Rokosky*, 2007), while at the same time, this fluid could alter the frictional properties at the slab interface, decreasing the coupling and resulting in SSEs (*Kodaira et al.*, 2004; *Obara et al.*, 2004; *Obara and Hirose*, 2006).

Several studies have provided evidence for the existence of a zone of high pore-fluid pressure along the upper boundary of the subducted PHS plate at depths of ∼25–45 km (e.g., *Honda and Nakanishi*, 2003; *Kodaira et al.*, 2004; *Wang et al.*, 2006; *Matsubara et al.*, 2009) that could cause a reduction in the effective normal stress on the plate interface, promoting SSEs. This high pore-fluid pressure zone is characterized by high-V_P/V_S (1.80–1.88) (*Matsubara et al.*, 2009), high Poisson's ratio (0.30–0.35) (*Honda and Nakanishi*, 2003; *Kodaira et al.*, 2004; *Wang et al.*, 2006), and low V_S (3.7–4.1 km/s) (*Honda and Nakanishi*, 2003; *Wang et al.*, 2006; *Matsubara et al.*, 2009). Seismic tomography reveals a region of strong low V_S, high-V_P/V_S anomaly along the top of the subducted PHS slab beneath the western Shikoku region (*Matsubara et al.*, 2009), which may indicate the presence of an USL similar to that found in central Mexico.

5.3 Data and Method

The P-wave complexities that *Song et al.* (2009) and *Song and Kim* (2012) identified as relating to the presence of an USL are locally comprised of three distinct S-to-P phases (A, B, C) that arrive within 4 sec after the P-wave (Figure 5.2). Phase A converts at the bottom of the USL and appears as a negative pulse at local stations. Phase B arrives immediately after phase A as a positive pulse, indicative of an S-to-P wave that converted at the top of the USL. Phase C converts at the base of the high velocity layer (*Dougherty et al.*, 2012; *Song and Kim*, 2012), arriving before phase A and ∼1.0–1.5 sec after the direct P-wave. At teleseismic distances, the complex P-wave of interest is an underside reflection from the USL in which an upgoing S-wave converts to a downgoing P-wave, resulting in the phase $s_{USL}P$ (Figure 5.3). This $s_{USL}P$ phase arrives ~3.5–4 sec after the direct P-wave.

These complex P waveforms are searched for on both local and teleseismic recordings of a selection of shallow (~40–70 km), moderate magnitude (M5–7) intraslab earthquakes that occurred in southwest Japan between 2001 and 2003. The densely distributed Japanese Hi-net array, which is a high-sensitivity network comprised of more than 600 three-component, short-period (1 s) borehole seismometers (*Obara et al.*, 2005), is the source of the local data analyzed in this study. For teleseismic distances, data from global broadband seismometers and short-period monitoring arrays are analyzed. Each short-period monitoring array consists of a dense distribution of stations over a very small area, so the seismograms from each station within an array are stacked to produce a single record with very high signal-to-noise ratio, easing the identification of seismic phases.

5.4 Results

For the selection of earthquakes analyzed, one event had particularly good data coverage both locally and teleseismically. This M5.7 oblique-normal earthquake occurred on 25 April 2001 at a depth of 46 km in the southwest Japan region, beneath the Bungo channel (Figure 5.1) (from the Global Centroid Moment Tensor catalog (*Dziewonski et al.*, 1981; *Ekström et al.*, 2012)). Recordings of this earthquake display some complex P waveforms on local Hi-net stations (Figure 5.2) and teleseismically on individual broadband seismometers and on short-period monitoring arrays (Figure 5.3).

The locally converted S-to-P phases are visible in the complex waveforms recorded at Hi-net stations within 4 sec of the direct P-wave, while no such phases are observed in the simple waveforms (Figure 5.2). The prominence of each of the three local phases can be seen to vary with source-receiver distance and azimuth, with the strongest arrivals of all three phases occurring at stations located more than 140 km from the source in an azimuth range of ~230°–253° (Figure 5.2). The variability of these waveforms is expected from small changes in slab geometry in this transition

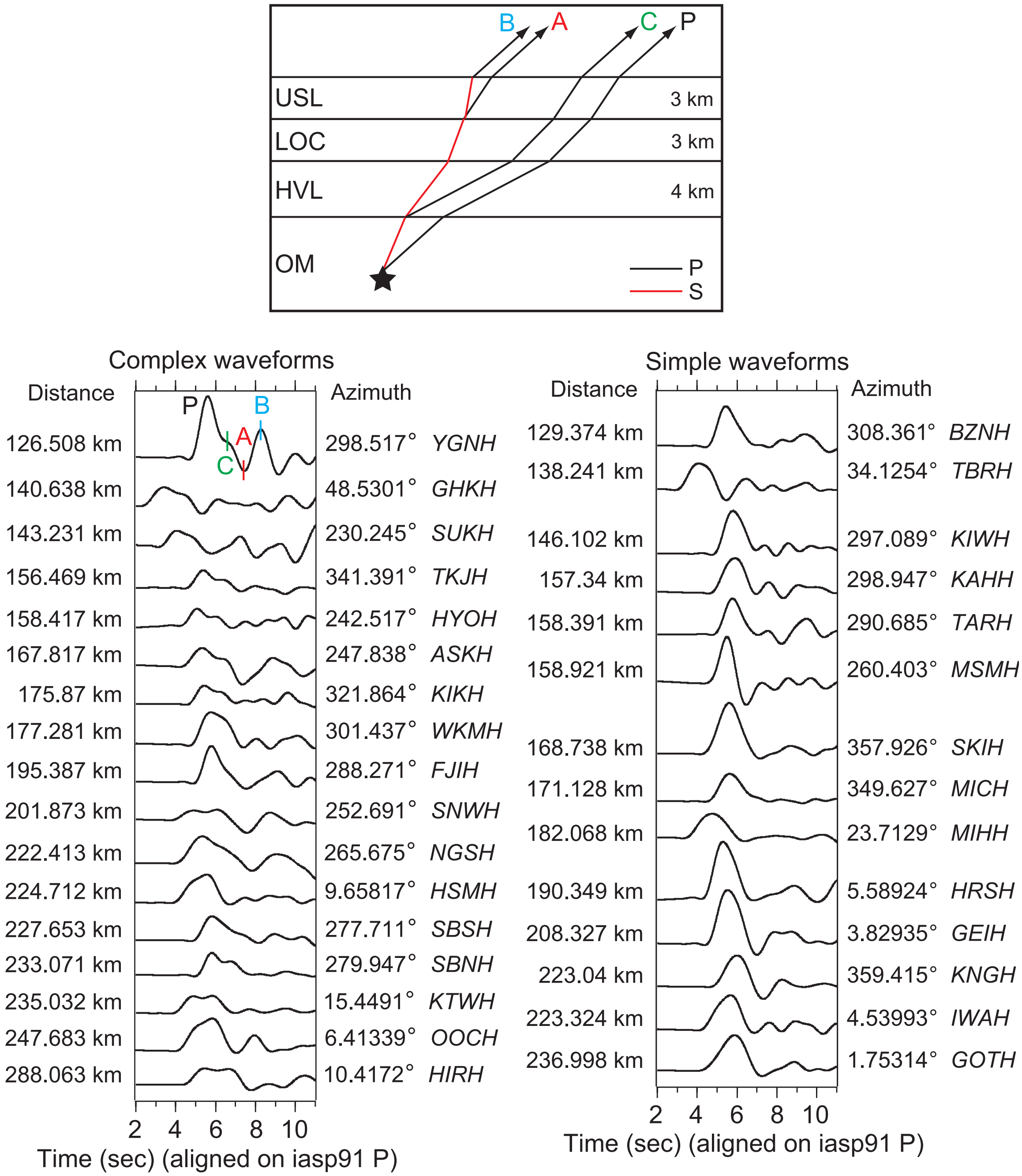

Figure 5.2: (top) Schematic cross-section illustrating the raypaths of the P-wave and the three local S-to-P phases (A, B, C) that comprise the complex P waveform. Abbreviations are USL, ultra-slow velocity layer; LOC, lower oceanic crust; HVL, high velocity layer; OM, oceanic mantle. Approximate layer thicknesses for the USL, LOC, and HVL are indicated. Modified from *Dougherty et al.* (2012). (bottom) Examples of (left) complex and (right) simple P waveforms recorded on the vertical component by the Hi-net array and filtered to 1–30 sec. S-to-P phases A, B, and C are indicated by red, blue, and green tick marks, respectively, on a single waveform as an example. The locally converted S-to-P phases are visible in the complex waveforms within 4 sec of the direct P-wave, while no such phases are observed in the simple waveforms. Station names are shown in italics.

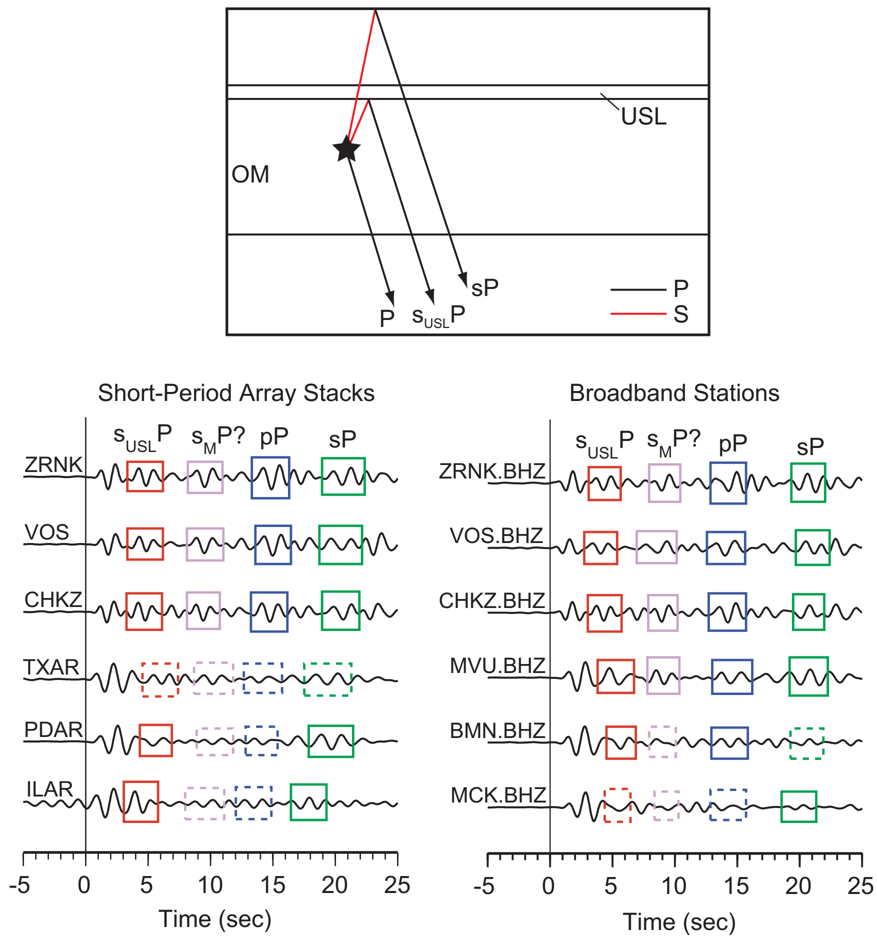

Figure 5.3: (top) Schematic diagram illustrating the raypaths of the teleseismic P-wave, the depth phase sP, and the underside reflection $s_{USL}P$ from the USL. Abbreviations are as in Figure 5.2. (bottom) Teleseismic records from (left) stacking data at six short-period arrays and from (right) broadband stations located in the vicinity of the arrays, filtered to 0.5–1 Hz. Array and station names are indicated. The arrival of the $s_{USL}P$ phase (red box) ∼3.5–4 sec after the direct P-wave is indicated. The arrivals of the depth phases pP (blue box) and sP (green box), along with a possible underside reflection from the Moho of the overriding plate ($s_M P$; purple box) are also shown. Possible arrivals that are not distinct are indicated by dashed boundaries. The locations of the short-period arrays and broadband stations are shown in Figure 5.4.

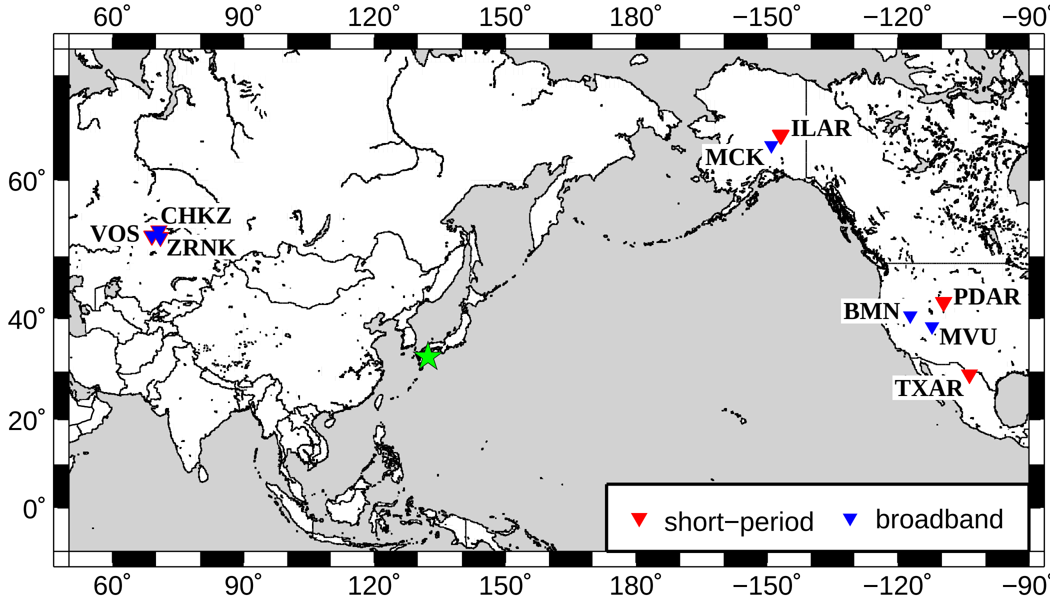

Figure 5.4: Map showing the locations of the short-period arrays (red inverted triangles) and broadband stations (blue inverted triangles) used in this study. Array and station names are indicated. For the CHKZ, ZRNK, and VOS arrays, note that the corresponding broadband stations are co-located and have the same name (see Figure 5.3). The event location is indicated by the green star.

region from subhorizontal to normal subduction.

The teleseismic underside reflection $s_{USL}P$ is clearly identifiable in five of six short-period array stacks presented in Figure 5.3; data from the sixth array indicates a possible $s_{USL}P$ phase that is not easily distinguished. Observations of this phase on broadband stations located in the vicinity of these short-period arrays (Figures 5.3 and 5.4) demonstrate that the appearance of this phase is not limited to short-period instruments. Consistent with the estimation of *Song et al.* (2009), this $s_{USL}P$ phase arrives ~3.5–4 sec after the direct P-wave in both the short-period and broadband data at these teleseismic distances.

The locations of the S-to-P conversion points and underside reflection bounce points at the top of the PHS slab are estimated using the TauP Toolkit (*Crotwell et al.*, 1999) with the iasp91 velocity model (*Kennett and Engdahl*, 1991). A possible region for the USL is proposed based on the locations of conversion points for Hi-net stations that recorded complex and simple P waveforms and bounce points for teleseismic short-period arrays and broadband stations that recorded the

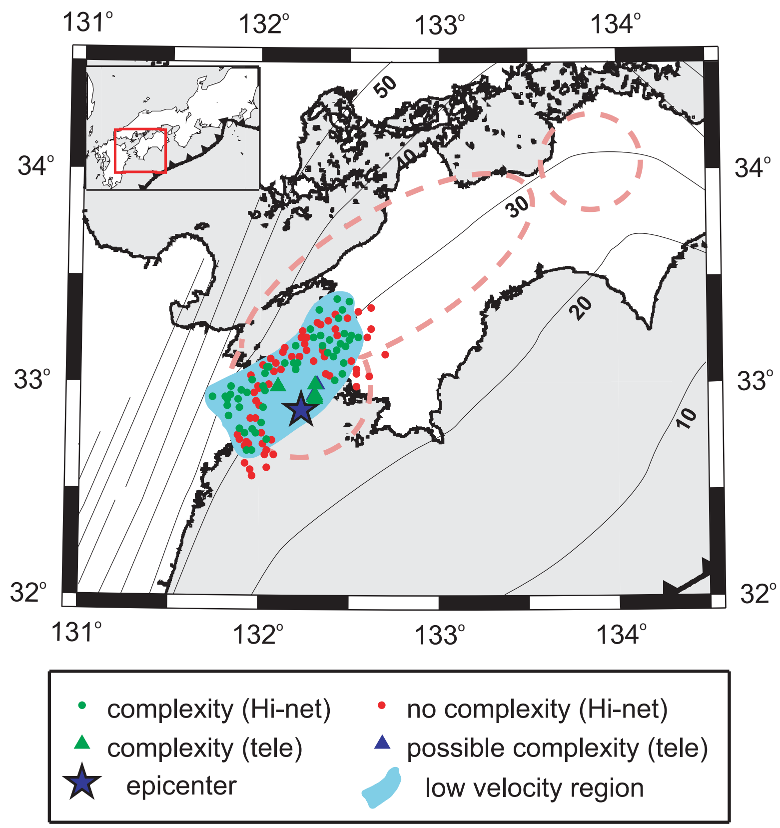

Figure 5.5: Local S-to-P conversion points and underside reflection bounce points from the top of the Philippine Sea slab for Hi-net stations that recorded complex (green dots) and simple (red dots) P waveforms and for teleseismic short-period arrays and broadband stations that recorded the $s_{USL}P$ phase (triangles), respectively. Bounce points for $s_{USL}P$ arrivals that are not distinct are indicated by blue triangles. A possible region for the USL (light blue) is proposed based on the locations of these conversion and bounce points. The locations of slow slip events (pink dashed outlines) and the Philippine Sea slab isodepth contours (thin black lines) are as in Figure 5.1.

$s_{USL}P$ phase (Figure 5.5). The intermingling of S-to-P conversion points for stations that recorded complex P waveforms and those that recorded simple P waveforms indicates that the proposed USL in southwest Japan is likely laterally heterogeneous, consistent with the observations of *Song et al.* (2009) for central Mexico.

5.5 Discussion and Conclusions

Observations of complex P waveforms both locally and teleseismically for an intraslab earthquake that occurred in a region of southwest Japan known to produce SSEs provides further evidence for the proposed relationship between the location of SSEs and the presence of an USL on top of the slab. Using the locations of S-to-P conversion points and underside reflection bounce points at the top of the PHS slab for complex P waveforms, we are able to estimate the location of a possible USL along the slab surface. This region of very low velocity is spatially coincident with locations of SSEs that have occurred in southwest Japan and may represent part of the subducted oceanic crust that is fluid-saturated, forming a high pore-fluid pressure layer (*Song et al.*, 2009). This layer would be expected to greatly reduce the effective normal stress on the plate interface, decreasing the coupling, and promoting SSEs. The source of this fluid is thought to be dehydration of hydrous minerals in the subducted oceanic crust. A low permeability layer consisting of fine-grained blueschist located directly above the high pore-fluid pressure layer is proposed to seal in the fluid (*Song et al.*, 2009). Lateral variations in the amount of fluid released from the slab could produce the laterally heterogeneous structure of the proposed USL. This is consistent with the undulating variation from thicker, more hydrated regions to thinner, less hydrated regions that was modeled for the low velocity layer on top of the Tonga-Fiji slab (*Savage*, 2012). Alternatively, the proposed USL may occur in isolated patches of variable size, similar to the asperity model of stress distribution on the fault plane (*Lay et al.*, 1982; *Bilek and Lay*, 2002). Waveform modeling of such an asperity-like structure for the USL could provide further insights into its heterogeneity.

A seismic explosion survey conducted by *Ueno et al.* (2009) in the Tokai region of southwest Japan used wide-angle seismic reflections and 2D forward modeling by the finite-difference method to show the existence of a thin (∼2–3 km) low velocity ($V_P \sim 4$ km/s) layer in the upper part of the PHS slab. Their model results suggest that SSEs occur within this layer. Regional variations in the strength of reflections from this layer imply that it is laterally heterogeneous (*Ueno et al.*, 2009), consistent with our observations. Further fine-scale seismic modeling of the subduction zone in southwest Japan is needed in order to provide constraints on the thickness and velocity of the possible USL at the top of the PHS slab.

The spatial correlation of locations of SSEs in both southwest Japan and central Mexico with regions where the subducted plate is dipping shallowly may be related to the geometry of the plate itself. When the slab is subducting at a very low angle and nearly underplating the overriding plate at a shallow depth, the fine-grained blueschist cap layer which creates a low permeability barrier for the fluid-saturated USL below (*Song et al.*, 2009) may exist for a long distance perpendicular to the trench. Thus, the fluid released by dehydration of the subducted oceanic crust may disperse and/or become trapped along the slab surface over a broad region, creating a high pore-fluid pressure zone in which SSEs could occur. This is contrary to the case of a more steeply subducting slab in which fluid is released at depths beyond the stability field of blueschist (e.g., *Hacker et al.*, 2003), effectively preventing the formation of a high pore-fluid pressure layer due to the lack of a low permeability seal.

5.6 Future Work

Waveform modeling of the fine-scale seismic structure of the subduction zone in southwest Japan using a 2D finite-difference algorithm can be performed in order to provide constraints on the thickness, velocity, and lateral extent of the possible USL atop the PHS slab. Additional modeling of the potential asperity-like structure proposed for the USL will explore the nature of its observed lateral heterogeneity. This study can further be strengthened through the analysis of more recent events which have occurred in this region.

References

Bilek, S., and T. Lay (2002), Tsunami earthquakes possibly widespread manifestations of frictional conditional stability, *Geophys. Res. Lett.*, *29*, 1673, doi:10.1029/2002GL015215.

Crotwell, H. P., T. J. Owens, and J. Ritsema (1999), The TauP Toolkit: Flexible seismic travel-time and ray-path utilities, *Seis. Res. Lett.*, *70*(2), 154–160.

Dougherty, S. L., R. W. Clayton, and D. V. Helmberger (2012), Seismic structure in central Mexico: Implications for fragmentation of the subducted Cocos plate, *J. Geophys. Res.*, *117*, B09316, doi:10.1029/2012JB009528.

Dziewonski, A. M., T.-A. Chou, and J. H. Woodhouse (1981), Determination of earthquake source parameters from waveform data for studies of global and regional seismicity, *J. Geophys. Res.*, *86*, 2825–2852, doi:10.1029/JB086iB04p02825.

Ekström, G., M. Nettles, and A. M. Dziewonski (2012), The global CMT project 2004-2010: Centroid-moment tensors for 13,017 earthquakes, *Phys. Earth Planet. Inter.*, *200-201*, 1–9, doi: 10.1016/j.pepi.2012.04.002.

Hacker, B. R., G. A. Abers, and S. M. Peacock (2003), Subduction factory, 1, Theoretical mineralogy, densities, seismic wave speeds, and H_2O contents, *J. Geophys. Res.*, *108*, 2029, doi: 10.1029/2001JB001127.

Hirose, H., and K. Obara (2005), Repeating short- and long-term slow slip events with deep tremor activity around the Bungo channel region, southwest Japan, *Earth Planets Space*, *57*, 961–972.

Honda, S., and I. Nakanishi (2003), Seismic tomography of the uppermost mantle beneath southwestern Japan: Seismological constraints on modelling subduction and magmatism for the Philippine Sea slab, *Earth Planets Space*, *55*, 443–462.

Ito, Y., K. Obara, K. Shiomi, S. Sekine, and H. Hirose (2007), Slow earthquakes coincident with episodic tremors and slow slip events, *Science*, *315*, 503–506.

Kennett, B. L. N., and E. R. Engdahl (1991), Travel times for global earthquake location and phase association, *Geophys. J. Int.*, *105*, 429–465.

Kodaira, S., T. Iidaka, A. Kato, J. Park, T. Iwasaki, and Y. Kaneda (2004), High pore fluid pressure may cause silent slip in the Nankai Trough, *Science*, *304*, 1295–1298.

Lay, T., H. Kanamori, and L. Ruff (1982), The asperity model and the nature of large subduction zone earthquakes, *Earthquake Pred. Res.*, *1*, 3–71.

Manea, V. C., M. Manea, V. Kostoglodov, C. A. Currie, and G. Sewell (2004), Thermal structure, coupling and metamorphism in the Mexican subduction zone beneath Guerrero, *Geophys. J. Int.*, *158*, 775–784.

Matsubara, M., K. Obara, and K. Kasahara (2009), High-V_P/V_S zone accompanying non-volcanic tremors and slow-slip events beneath southwestern Japan, *Tectonophysics*, *472*, 6–17, doi: 10.1016/j.tecto.2008.06.013.

Nakajima, J., and A. Hasegawa (2006), Anomalous low-velocity zone and linear alignment of seismicity along it in the subducted pacific slab beneath Kanto, Japan: Reactivation of subducted fracture zone?, *Geophys. Res. Lett.*, *33*, L16309, doi:10.1029/2006GL026773.

Nakanishi, I. (1980), Precursors to ScS phases and dipping interface in the upper mantle beneath southwestern Japan, *Tectonophysics*, *69*, 1–35.

Obara, K. (2002), Nonvolcanic deep tremor associated with subduction in southwest Japan, *Science*, *296*, 1679–1681.

Obara, K., and H. Hirose (2006), Non-volcanic deep low-frequency tremors accompanying slow slips in the southwest Japan subduction zone, *Tectonophysics*, *417*, 33–51.

Obara, K., H. Hirose, F. Yamamizu, and K. Kasahara (2004), Episodic slow slip events accompanied by non-volcanic tremors in southwest Japan subduction zone, *Geophys. Res. Lett.*, *31*, L23602, doi:10.1029/2004GL020848.

Obara, K., K. Kasahara, S. Hori, and Y. Okada (2005), A densely distributed high-sensitivity seismograph network in Japan: Hi-net by National Research Institute for Earth Science and Disaster Prevention, *Review of Scientific Instruments*, *76*, 021301, doi:10.1063/1.1854197.

Okino, K., Y. Shimakawa, and S. Nagaoka (1994), Evolution of the Shikoku Basin, *J. Geomag. Geoelec.*, *46*, 463–479.

Pardo, M., and G. Suárez (1995), Shape of the subducted Rivera and Cocos plates in southern Mexico: Seismic and tectonic implications, *J. Geophys. Res.*, *100*, 12,357–12,373.

Pérez-Campos, X., Y. Kim, A. Husker, P. M. Davis, R. W. Clayton, A. Iglesias, J. F. Pacheco, S. K. Singh, V. C. Manea, and M. Gurnis (2008), Horizontal subduction and truncation of the Cocos plate beneath central Mexico, *Geophys. Res. Lett.*, *35*, L18303, doi:10.1029/2008GL035127.

Savage, B. (2012), Seismic constraints on the water flux delivered to the deep earth by subduction, *Geology*, *40*, 235–238, doi:10.1130/G32499.1.

Schwartz, S. Y., and J. M. Rokosky (2007), Slow slip events and seismic tremor at circum-Pacific subduction zones, *Rev. Geophys.*, *45*, RG3004, doi:10.1029/2006RG000208.

Seno, T., and T. Yamasaki (2003), Low-frequency tremors, intraslab and interplate earthquakes in Southwest Japan—from a viewpoint of slab dehydration, *Geophys. Res. Lett.*, *30*(22), 2171, doi:10.1029/2003GL018349.

Seno, T., S. Stein, and A. E. Gripp (1993), A model for the motion of the Philippine Sea plate consistent with NUVEL-1 and geological data, *J. Geophys. Res.*, *98*, 17,941–17,948, doi: 10.1029/93JB00782.

Shiomi, K., H. Sato, K. Obara, and M. Ohtake (2004), Configuration of the subducting Philippine Sea plate beneath southwest Japan revealed from receiver function analysis based on the multivariate autoregressive model, *J. Geophys. Res.*, *109*, B04308, doi:10.1029/2003JB002774.

Song, T. A., and Y. Kim (2012), Anisotropic uppermost mantle in young subducted slab underplating Central Mexico, *Nature Geosci.*, *5*, 55–59, doi:10.1038/NGEO1342.

Song, T. A., D. V. Helmberger, M. R. Brudzinski, R. W. Clayton, P. Davis, X. Pérez-Campos, and S. K. Singh (2009), Subducting slab ultra-slow velocity layer coincident with silent earthquakes in southern Mexico, *Science*, *324*, 502–506.

Ueno, T., T. Takeda, K. Obara, and Y. Asano (2009), Seismic explosion survey around slow events in the Tokai region, Japan, *Eos Trans. AGU*, *90*(52), Abstract T11C–1837.

Wang, K., I. Wada, and Y. Ishikawa (2004), Stress in the subducting slab beneath southwest Japan and relation with plate geometry, tectonic forces, slab dehydration, and damaging earthquakes, *J. Geophys. Res.*, *109*, B08,304, doi:10.1029/2003JB002888.

Wang, Z., D. Zhao, O. P. Mishra, and A. Yamada (2006), Structural heterogeneity and its implications for the low frequency tremors in Southwest Japan, *Earth Planet. Sci. Lett.*, *251*, 66–78.

Zhao, D., and A. Hasegawa (1993), P-wave tomographic imaging of the crust and upper mantle beneath the Japan Islands, *J. Geophys. Res.*, *98*, 4333–4353.

Zhao, D., K. Asamori, and H. Iwamori (2000), Seismic structure and magmatism of the young Kyushu subduction zone, *Geophys. Res. Lett.*, *27*, 2057–2060.

Chapter 6

Conclusions

In this thesis, I investigate the seismic structure along transitions from flat to normal subduction located in central Mexico, southern Peru, and southwest Japan. I explore the nature of the flat-to-normal transitions in central Mexico and southern Peru to determine whether these changes in geometry are accommodated by slab tears or smooth contortions. In southwest Japan, I explore the spatial coincidence of a thin ultra-slow velocity layer (USL) with locations of slow slip events (SSEs) and the possible causal relationship between the two. The results of these studies can be summarized in the following.

In western central Mexico, the results of 1D and 2D waveform modeling techniques and an analysis of P waveform complexities show that the subducted Cocos plate is a complicated, multilayered structure with a thin USL atop the slab. The western lateral extent of this USL is approximately coincident with the western margin of the projected Orozco Fracture Zone (OFZ) region, implying a structural boundary which I interpret as a tear in the Cocos plate. Recent tectonic observations in the region of variable plate motions to either side of the OFZ and a possible small-scale rift-rift-rift triple junction overlying the landward projection of the OFZ have suggested that the Cocos plate is fragmenting along this fracture zone. On the basis of my seismic results and these tectonic observations, I propose a slab tear model, wherein the Cocos slab is currently fragmenting into a North Cocos plate and a South Cocos plate along the projection of the OFZ by a pivoting subduction process similar to that which occurred when the Rivera plate separated from the proto-Cocos plate. This ongoing fragmentation event presents the opportunity to observe and study a young tearing process in action.

In eastern central Mexico, intraslab seismicity patterns, an analysis of P waveform complexities, and 1D and 2D waveform modeling techniques are used to interrogate the nature of the flat-to-normal transition. The eastern lateral extent of the thin USL atop the slab is marked by a boundary between the USL and no USL zones, followed by a diffuse weakening USL region closer to the coast. A sharp transition in slab dip near the abrupt end of the Trans Mexican Volcanic Belt (TMVB) suggests a possible tear in the South Cocos slab. The coincidence of the boundary between the USL and no USL zones with the margin of a zone of decreased seismicity along this change in dip and the end of the TMVB implies a change in structure which I interpret as evidence of a possible tear. Additional observed intraslab seismicity patterns of clustering, sudden increase in depth, variable focal mechanism orientations and faulting types, and alignment of source mechanisms along the sharp transition in slab dip further support this conclusion. I propose the subduction of parallel ridges of seamounts and/or stress due to the abrupt change in geometry as potential causes of the possible slab tear in the South Cocos plate. Further imaging of the subduction zone structure with denser station coverage over the downdip aseismic portion of the slab may provide a clearer picture of the possible tear at depth.

The morphology of the Nazca slab along the flat-to-normal transition in southern Peru is investigated using intraslab seismicity patterns, focal mechanism orientations, an analysis of P waveform complexities, and 2D waveform modeling techniques. The results show that the subducted Nazca plate is a complicated structure with a possible thin USL atop the horizontal slab. The lateral extent of this USL is coincident with the margin of the projected continuation of the subducting Nazca Ridge, implying a change in structure which I interpret as a causal relationship between these features. A gradual increase in slab dip with no sharp transitions suggests smooth contortion of the Nazca plate. The lack of any gaps or vertical offsets in the intraslab seismicity coupled with the concentration and orientation of focal mechanisms indicative of slab bending further support this conclusion. The absence of a tear in the slab along either the Nazca Ridge or the largest increase in slab dip is also confirmed with 2D waveform modeling. Further modeling of the subduction zone structure in the flat slab region may provide additional constraints on the presence of the USL.

In southwest Japan, local and teleseismic recordings of complex P waveforms are used to examine the fine-scale seismic structure of the subducted Philippine Sea plate along the transition from flat to normal subduction. Observations of such waveforms both locally and teleseismically for an intraslab earthquake located beneath the Bungo channel yield a possible region for a thin USL along the Philippine Sea slab surface. The spatial coincidence of this region of very low velocity with the locations of SSEs provides further evidence for the proposed causal relationship between the occurrence of SSEs and the presence of an USL atop the slab. I interpret the source of the possible USL in this region as fluids dehydrated from the subducting plate, forming a high pore-fluid pressure layer. Future 2D waveform modeling of the seismic structure of the subduction zone in southwest Japan will be performed in order to provide constraints on the thickness, velocity, and lateral extent of the possible USL here and to explore the nature of its observed lateral heterogeneity. This study can further be strengthened through the analysis of more recent events which have occurred in this region.

Update to Chapters 2 and 3

The description of simple P waveforms as written in Chapters 2 and 3 has been updated since these chapters were published. The new description (see section 4.3.5) clarifies that the lack of the C phase in these waveforms indicates that there is no high velocity layer present, while uncharacteristically shaped and/or low amplitude A and B phases indicate that there is no USL present. Additionally, the arrival times of the possible A and B phases in the simple waveforms are inconsistent with the presence of the USL.